# Convective Episodes near the Intertropical Discontinuity in Summertime West Africa: Representation in Models and Implications for Dust Uplift

Alexander James Roberts

Submitted in accordance with the requirements for the degree of
Doctor of Philosophy

The University of Leeds
School of Earth and Environment
August 2014

*"the merit of all things lies in their difficulty"*

ALEXANDRE DUMAS

# Declaration of Authorship

The candidate confirms that the work submitted is his own, except where the work which has formed part of jointly authored publications has been included. The contribution of the candidate and the other authors has been explicitly indicated below. The candidate confirms that appropriate credit has been given within the thesis where reference has been made to the work of others.

The candidates jointly authored publications that share content with this thesis are:

Publication (1) Roberts, A. and P. Knippertz (2012), Haboobs: convectively generated dust storms in West Africa, Weather, 67(12), 311-316

Publication (2) Roberts, A. and P. Knippertz (2014), The formation of a large summertime Saharan dust plume: Convective and synoptic-scale analysis, J. Geophys. Res. Atmos., 119(4), pp. 1766–1785.

Publication (3) Roberts, A., P. Knippertz and J.H. Marsham (submitted 2014), Disagreements in Low-level moisture between (Re)analyses over Summertime West Africa, Mon. Weather Rev.

Publication (1) is an invited contribution to the non-specialist journal Weather, and is based on a presentation written and given by the candidate at the 2011 Royal Meteorological Society student conference. It consists of an overview of the subject of haboobs and, as such, its content is incorporated into the Chapter 2 of the thesis. A first draft of publication (1) was written by the candidate, additionally, Peter Knippertz made suggestions to improve the clarity and content, and made small changes to the structure, content and wording of the article. All figures were prepared by the candidate. Figure 5 (Figure 2.10 in the thesis) is redrawn from a schematic previously used by Peter Knippertz.

Publication (2) is a case study of a large summertime Saharan dust plume. Its findings form the content of Chapter 4. Information from the paper's Introduction and Data and Model Setup sections are included in the Chapters 2 and 3 of the thesis respectively. A first draft of publication (2) was prepared by the candidate. Additional input from Peter Knippertz was given in the form of discussion of content and structure as well as editorial advice such as small changes to the text's structure and wording. All figures were prepared by the candidate. High resolution SEVIRI dust images used in Figures 1, 4 and 12 of the publication were provided on request by Helen Brindley and Jonathan Murray at Imperial College London.

Publication (3) investigates the differences between the distribution of low-level moisture over West Africa in 7 reanalysis and operational analysis products over 11 consecutive monsoon seasons. Its findings form the content of Chapter 5 of the thesis. Parts of the Introduction and Data and Methods sections are included in Chapters 2 and 3 of the thesis. The experimental design, structure and content of this publication are attributable to the candidate. A first draft was prepared by the candidate and suggestions from Peter Knippertz and John Marsham to improve the structure and clarity of the article were implemented. Small changes to the structure, content and wording were also made by Peter Knippertz and John Marsham. All figures were prepared by the candidate.

Further recognition should be afforded to Peter Knippertz who is responsible the initial proposal without which there would be no PhD project.

# Acknowledgements

Firstly I would like to thank Peter Knippertz. As my supervisor, he has given excellent advice and support throughout this process. From him I have learnt a great deal about how to conduct research. I feel that this will serve me well in the future. Thanks also go to John Marsham for providing invaluable help throughout the project and for taking up the mantle of lead supervisor after Peter's move to Karlsruhe. Peter's continued contact and visits to Leeds, combined with John's dedication have made the transition very smooth, allowing me to stay focussed on research. I would also like to thank them both for their constructive insight during the preparation of the papers published/submitted during this process. I am grateful to my co-supervisor Andrew Ross and Alan Blyth (the sole member of my research support group) for helpful comments and advice given during meetings.

This work is funded by the Natural Environment Research Council (NERC ref NE/I528750/1) and I am grateful for them for making this project possible. Additional support has been provided by the European Research Council (ERC) "Desert Storms" project (ref 25753). Thanks also go to Helen Brindley and Jonathan Murray at Imperial College London for producing high resolution SEVIRI dust imagery on request. This has been used in the JGR: Atmospheres case-study paper and Chapter 4 of this manuscript. I would also like to express how valuable I have found ICAS coffee, Chatmosphere, group lunch on a Thursday and Monday night ICAS football.

On a more personal note I wish to thank my family for their continual support, especially my lovely wife Vicky. She is my best friend and has been a constant source of love and support. On top of this she has funded some spectacular holidays and furnished me with a beautiful baby daughter. Finally I wish to thank my daughter, Beatrix, her arrival provided a very real deadline towards which to work, and made sure I finished this manuscript on time.

# Abstract

This study focusses on the production of mesoscale convective systems (MCSs) close to the intertropical discontinuity (ITD), including their associated dust uplift processes and representation in global and high-resolution, limited-area models. Findings from this work include a detailed description of the synoptic-scale meteorology important for the formation of a large, rare Saharan MCS and the spectacular dust plume which it created in June 2010. Results are presented from a high resolution simulation of this event using the Weather Research and Forecasting (WRF) model. Important dynamical processes which govern the triggering and development of the MCS are discussed as well as the mechanisms for dust uplift with which it is associated. Also highlighted from the simulation is the strong dependence of simulations on initial conditions and the disagreement at particular times between some operational analysis and reanalysis products (referred to here as (re)analysis products). (Re)Analyses are ostensibly representing the atmosphere at the same time and with the same observations as each other. Despite this, disagreement with respect to low-level moisture distribution between (re)analyses is shown to be large at times. Disagreement is as a result of different representations of the West African monsoon (WAM) flow and is greatest during the retreat after a northward excursions. It is also found that extreme disagreement events are linked to the occurrence of rainfall and anomalously high aerosol optical depth (AOD) values north of the zonal-mean ITD (ITD$\Phi$). The seasonal patterns of rainfall in the Sahara and disagreement between (re)analysis products are shown to be similar, suggesting a link between the occurrence of convective storms and the representation of the West African Monsoon. There is also a spatio-temporal connection between anomalous rainfall events and anomalously high AOD values. Analysis of the synoptic-scale meteorology reveals a statistically significant

925 hPa geopotential dipole present during extreme rainfall events. This has been used to produce a preliminary version of an anomalous rainfall in the Sahara (ARS) index.

# Contents

# List of Figures

# List of Tables

# Abbreviations

**AEJ** African Easterly Jet

**AEW** African Easterly Wave

**AI** Aerosol Index

**AMMA** African Monsoon Multidisciplinary Analysis

**AOD** Aerosol Optical Depth

**AR5** Assessment Report 5

**ARS Index** Anomalous Rainfall in Sahara Index

**BT** Brightness Temperature

**CAPE** Convective Available Potential Energy

**CCN** Cloud Condensation Nuclei

**CFL condition** Courant-Friedrichs-Lewy condition

**CFSR** Climate Forecast System Reanalysis

**CIN** Convective Inhibition

**DCAPE** Downdraught Convective Available Potential Energy

**DEM** Digital Elevation Model

**DUP** Dust Uplift Potential

**ECMWF** European Centre for Medium-Range Weather Forecasts

**EL** Equilibrium Level

$\boldsymbol{\theta_e}$ Equivalent Potential Temperature

**EUMETSAT** European Organisation for the Exploitation of Meteorological Satellites

$\boldsymbol{geo_{200}}$ 200 hPa Geopotential

$\boldsymbol{geo_{925}}$ 925 hPa Geopotential

$\boldsymbol{geo'_{200}}$ 200 hPa Geopotential Anomaly

$\boldsymbol{geo'_{925}}$ 925 hPa Geopotential Anomaly

**GERB** Geostationary Earth Radiation Satellite

**GFS** Global Forecast System

**GRIB** Meteorological binary gridded data format

**GTS** Global Telecommunications System

**HYSPLIT** Hybrid Single Particle Integrated Trajectory

**IN** Ice Nuclei

**IPCC** Intergovernmental Panel on Climate Change

**IR** InfraRed radiation

**ITCZ** Intertropical Convergence Zone

**ITD** Intertropical Discontinuity

**ITD$\Phi$** Zonal-Mean Intertropical Discontinuity

**LCL** Lifting Condensation Level

**LFC** Level of Free Convection

**MCC** Mesoscale Convective Complex

**MCM** Meninococcal Meningitis

**MCS** Mesoscale Convective System

**MERRA** Modern Era Retrospective-analysis for Research and Applications

**MIDAS** Met Office Integrated Data Archive System

**MM5** fifth generation Pennsylvania State University - NCAR Mesoscale Model

**MODIS** Moderate Resolution Imaging Spectroradiometer

**MSG** Meteosat Second Generation

$\boldsymbol{mslp}$ Mean Sea-Level Pressure

**MYJ** Mellor-Yamada-Janic PBL Scheme

**NASA** National Aeronautics and Space Administration

**NASCube** North African Sand Storm Survey

**NBL** Nocturnal Boundary Layer

**NCAR** National Center for Atmospheric Research

**NCEP** National Center for Environmental Prediction

**NH** Northern Hemisphere

**NLLJ** Nocturnal Low-Level Jet

**NWP** Numerical Weather Prediction

**OLR** Outgoing Longwave Radiation

**OMI** Ozone Measuring Instrument

**PBL** Planetary Boundary Layer

**pgf** pressure gradient force

$\boldsymbol{q_{925}}$ 925 hPa Specific Humidity

$\boldsymbol{Re}$ Reynolds number, the ratio of inertial to viscous forces

**RGB** Red-Green-Blue

**RMSD** Root Mean Square Difference

$\boldsymbol{Ro}$ Rossby number, ratio of inertial to rotational forces

**SAL** Saharan Air Layer

**SAMUM** Saharan Mineral Dust Experiment

**SEVIRI** Spinning Enhanced Visual and InfraRed Imager

**SHL** Saharan Heat Low

**SOP** Special Observing Period

**SRTM** Shuttle Radar Topography Mission

$\boldsymbol{stream_{925}}$ 925 hPa streamlines based on u and v winds at the same pressure level

**TCI** TMI/TRMM Combined Instrument

**TKE** Turbulent Kinetic Energy

**TMI** TRMM Microwave Imager

**TOMS** Total Ozone Mapping Spectrometer

**TRMM** Tropical Rainfall Measuring Mission

**UTC** Coordinated Universal Time

**UV** Ultraviolet radiation

**VIRS** Visual and InfraRed Scanner

$\boldsymbol{\theta_v}$ Virtual Potential Temperature

**WAM** West African Monsoon

**WPS** WRF Preprocessing System

**WRF model** Weather Research and Forecasting model

**YSU** Yonsei University

# Chapter 1

# Introduction

## 1.1 Motivation

In West Africa, mesoscale convective systems (MCSs) are responsible for a large proportion of the total annual rainfall. When they are triggered in the Sahara or northern Sahel they are able to produce dust storms. Dust uplift occurs along the turbulent leading edges of evaporatively generated pools of cold air and are known as haboobs. The primary control on the spatial and temporal distribution of MCSs is the availability of low-level moisture. During the boreal summer the West African monsoon (WAM) moves north bringing moist air from over the Gulf of Guinea and the Atlantic Ocean. The northern edge of the monsoonal flow is known as the intertropical discontinuity (ITD). South of the ITD, where the monsoon flow is sufficiently deep and there is favourable shear due to the presence of mid-level African Easterly Jet (AEJ), small convective cells can develop into MCSs. The ITD is a very mobile boundary. Occasionally northward excursions allow monsoon air to reach much further into the West African interior than is climatologically expected. This allows for the production of MCSs in an environment which is normally arid and has scant vegetative cover. The cold pools which are produced are then able to further displace the ITD, lift mineral dust and produce rainfall in regions where, even during the monsoon season, precipitation is rare.

A large proportion of the Sahelian population are reliant on rain-fed agriculture. Therefore, variation in the behaviour of the WAM and the associated rains can have a huge impact

on the lives of the people who live there. This variability occurs on decadal to sub-seasonal time scales and causes many issues, the most obvious of which is limited food and water security. An additional problem is that Sahelian nations are becoming increasingly vulnerable to such issues due to rapid population growth, limiting their ability to adapt to the problems raised by natural variability.

Many climatological and meteorological features of the WAM are poorly understood, especially when compared to the important meteorological processes over wealthier parts of the world. In recent years much work has been focussed on both improving the predictability of this system but also the complex synoptic- and mesoscale meteorology which can influence its behaviour. Despite the fact that the horizontal scale of MCSs starts at a few kilometres they can grow to be hundreds of kilometres across. At the larger end of this spectrum they can begin to influence the synoptic-scale meteorology of the region including the position of the ITD. The triggering and growth of MCSs is complex, as are the interactions between convectively generated cold pools and the monsoon flow. Few modelling studies have focused on the behaviour of MCSs and cold pools in this region. There are still many uncertainties associated with the mechanisms of formation, factors important for development and the impacts that MCSs have both on meso- and synoptic-scales. Therefore, more work is needed to understand the important, dynamical processes of MCSs triggered in the Sahara and northern Sahel.

The interactions between meso- and synoptic-scale meteorology also highlight issues with global models. Currently all global models are run at grid spacings which are not able to resolve processes important for the development of convective storms. This means that they have to be represented through the use of convective parametrisations. As parameterisations are simplifications of real behaviour, some key processes such as updraughts and downdraughts are not well represented. For reanalysis and operational analysis products, assimilation of observation data is meant to constrain short-term parametrised forecasts. However, the meteorological observation network in large parts of West Africa is very sparse. With insufficient observations and convective storms playing an important role in the region's meteorology, it is probable that the global analyses and forecasts are sometimes not a good representation of the atmosphere.

As mentioned earlier, MCSs have a role in the emission of mineral dust through the generation of haboobs. Other important processes for dust uplift are low-level jets and

dry convection (including dust devils). However, there is a large degree of uncertainty as to the efficiency of each mechanism to lift dust away from the surface, making it available for long-range transport. Such a lack of understanding of the dust uplift processes in a source region as large as the Sahara is a major problem. By understanding the processes responsible for its emission and transport, the uncertainty associated with the effects of airborne mineral dust can be reduced

Airborne dust has impacts on many processes both close to, and thousands of km from, source regions. Dust impacts on the radiative balance of the planet by directly absorbing and reflecting longwave and shortwave radiation. These influences are known as direct effects (Stocker et al., 2013). Atmospheric aerosols also modify the physical properties of clouds. This can be through changing the brightness, longevity or environment in which clouds develop. These modifications to cloud behaviour, in turn, influence the radiative balance, producing what are known as indirect effects (Denman et al., 2007). The scale of these effects as well as the amount of dust which is transported away from the Sahara is poorly defined. As such, atmospheric aerosols, of which Saharan mineral dust is the largest natural component, represent a large uncertainty within the climate system. This is a problem, as without knowing the current effects of dust it is very difficult to estimate the impact of dust in a changing climate, both on the climate itself but also for people whose lives are impacted directly by lifted dust.

As well as atmospheric effects, when dust is deposited it can have influence the ecosystems. Fertilisation of oligotrophic regions of the World's oceans by mineral dust (specifically due to its iron content) can allow for the growth of phytoplankton blooms in regions isolated from riverine fluxes of nutrients. The growth of plankton blooms following deposition is important due to: (1) changes to surface albedo, (2) nitrogen fixation and (3) atmospheric carbon dioxide uptake (Shao et al., 2011). The importance of Saharan mineral dust has also been suggested for the fertilisation of terrestrial regions such as the Floridian Peninsula and the Amazon rainforest (Bristow et al., 2010; Prospero et al., 2010; Toon, 2003).

Mineral dust has also been shown to have more direct impacts on humans. Specifically: (1) physical damage to lung tissue and exacerbation of existing respiratory disorders associated with inhalation of fine mode dust ($\leq 4$ $\mu$m) (Derbyshire, 2007), (2) aggravation of cerebrovascular and cardiovascular conditions, even in regions to which dust has been

transported thousands of km (Alessandrini et al., 2013; Goudie, 2009), (3) potential transport of pathogens including a link between the Sahelian dusty season and the occurrence of meninococcal meningitis outbreaks (Sultan et al., 2005), (4) increased risk during road and air travel due to reduced visibility and strong turbulent winds associated with dust storms (Fujita and Byers, 1977; Nofal et al., 1996; Winter, 2009) ad (5) damage to both pastoral and arable agriculture, particularly as across large parts of West Africa the population is dependent on subsistence farming Sterk (2003).

Further open questions about airborne mineral dust include how efficiently it acts for the nucleation of cloud ice, the impact that it has on the production of rainfall, the processes and effects of atmospheric ageing, the relative importance of dust uplift processes and their representation in models and how dust uplift and transport will be affected by a changing climate.

The relative lack of understanding of meteorology in this part of the world is partly due to the sparse observation network. Atmospheric models are used to fill in gaps in observations and represent a major source of information for improving the understanding of both dust uplift and in a wider context, the behaviour of the WAM. However, models struggle in this part of the world due to the lack of constraining observations and the presence of features on many different spatial and temporal scales, not all of which are able to be represented in coarse resolution global models. In particular, MCSs and their cold pools strongly influence the behaviour of the WAM system, however, they are heavily dependent on sub grid-scale processes that have to be parameterised in global models. Therefore, there needs to be a greater understanding of the production of MCSs, especially close to the edge of the monsoon flow. The behaviour of the WAM system is important to millions of people, as such, work toward a greater understanding of the processes driving it and improving their representation in models is valuable for operational forecasting and researchers studying both local and global phenomena.

## 1.2 Aims and objectives

This project aims to investigate the production of MCSs close to the ITD. Focussing on northward excursions of the monsoon flow leading to the triggering and development of MCS further north than might normally be expected. The synoptic- and meso-scale

features of such events are investigated including the lifting and transport of dust. The representation of the WAM is also investigated in global operational analysis and reanalysis products highlighting periods of disagreement and the conditions present at such times. The synoptic-scale meteorology leading to the triggering of convective storms further north is also investigated.

### Structure of the thesis

Chapter 2 provides an overview of the relevant literature. This includes the climate and meteorology of West Africa, important processes for the production of convective storms and cold pools and dust uplift and transport processes. Chapter 3 gives details of the different tools that have been used in the study. Including both in-situ and satellite observations, a numerical weather prediction (NWP) model and a number of global operational and reanalysis products.

Chapter 4 presents findings of a case study looking at the formation of a large summertime Saharan dust plume. Observations, reanalysis and a high resolution simulation using the Weather Research and Forecasting model (WRF) are used to investigate the multi-scale dynamics which produced a northward surge of the monsoon flow, followed by the production of a large MCS and an associated haboob. This chapter aims to provide an understanding of the: (1) meteorological processes which lead to the formation of this event, (2) the mechanisms for development of the MCS and the production of a very large dust plume and (3) the meteorology which is responsible for winds capable of raising surface sediments.

Chapter 5 investigates the disagreement between low-level moisture distribution in a number of operational and reanalysis products which are associated with surges of the WAM. This chapter builds on preliminary work from Chapter 4 which highlighted the sensitivity of the high resolution limited area model to initialisation data. This chapter aims to: (1) quantify the scale of disagreement between moisture fields across commonly used global products (2) identify the regions and periods which are most likely to display disagreement, (3) identify which years from those studied and which parts of the monsoon season display strongest disagreement (4) identify important meteorological features during disagreement

events and (5) establish if there is a link between periods of disagreement and the lifting of dust.

Chapter 6 investigates the synoptic-scale meteorology associated with anomalously rainy periods in the Sahara. Both Chapters 4 and 5 illustrate the connection between northward surges of the monsoon flow and triggering of convection in the Sahara and northern Sahel. This chapter aims to: (1) identify periods which have anomalously heavy rainfall in the Sahara and northern Sahel, (2) link these events with the lifting of dust over the Sahara, (3) identify common synoptic-scale meteorological conditions leading to the production of anomalous events and (4) suggest a method for the prediction of heavy rainfall episodes in the summertime Sahara not relying on convective parameterisations.

Lastly Chapter 7 gives a summary of the results and provides suggestions for further work.

# Chapter 2

# Literature Review

## 2.1 West African Climate

### General circulation

The climate of West Africa can be simplistically understood by looking at the global atmospheric circulation as shown by Warner (2004) (Figure 2.1). The intertropical convergence zone (ITCZ) is a region encircling the Earth and marks the region where the trade winds converge and air is forced to rise. This air becomes horizontally divergent aloft, spreading away from the latitude of the ITCZ. In a climatological sense this rising air makes up the upward limb of the Hadley cell (Figure 2.1). The downward limb occurs at about 30° north and south, suppressing convection by adiabatic warming and drying of the descending air. This produces atmospheric stability. Inhibition of convective clouds increases the levels of solar radiation incident on the surface and suppresses the production of precipitation. The resultant arid conditions across the northern part of the African continent have led to the formation of the Sahara desert. Along the Gulf of Guinea coast (approximately 5° N) there is much more precipitation with a general trend of increasing aridity to the north.

### West African Monsoon

Despite what is shown in Figure 2.1 the circulation of the atmosphere and the distribution of precipitation is much more complex. During the northern hemisphere (NH) winter the

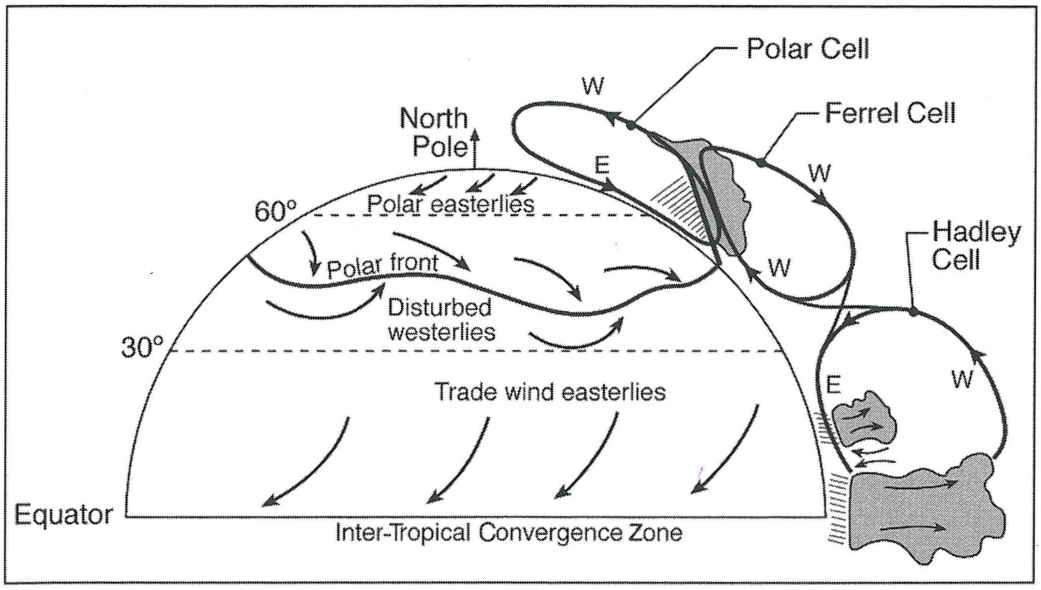


FIGURE 2.1: Schematic of the global atmospheric circulation associated with uneven heating of the Earth's surface (Warner, 2004). Note the large-scale convection driving surface winds toward the intertropical convergence zone (ITCZ) and a descending limb at approximately 30°.

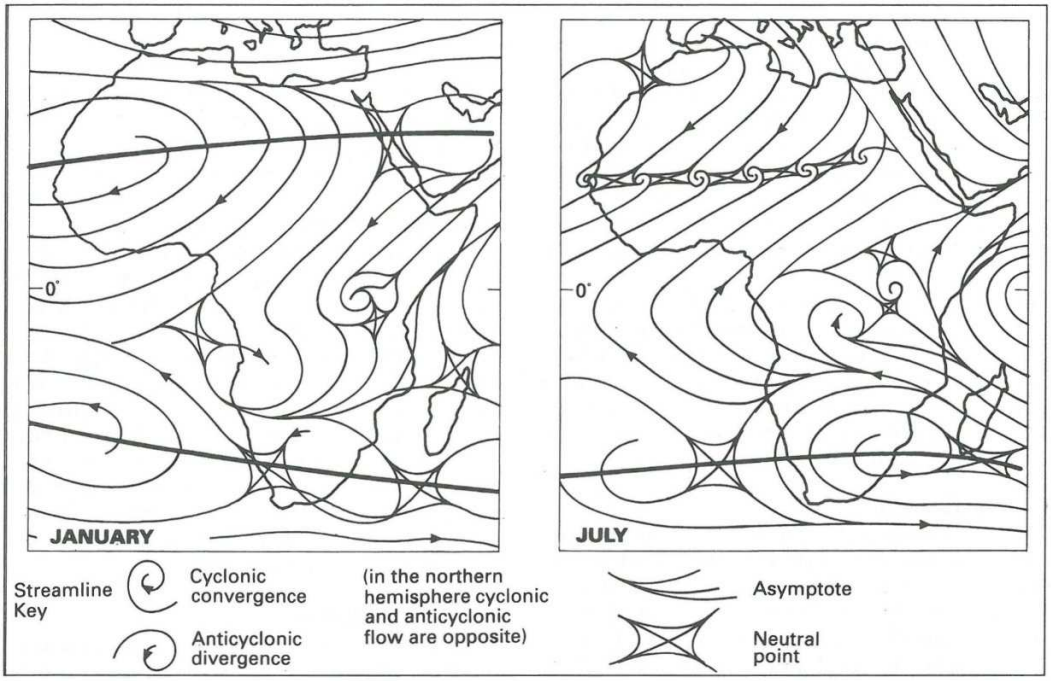


FIGURE 2.2: Schematic showing the streamlines for low-level wind during the northern hemisphere (NH) winter and summer (Buckle, 2004). In January the climatological flow over West Africa is almost entirely northeasterly, while in July there is a convergence zone across much of West Africa where the Harmattan and West African monsoon (WAM) flows meet.

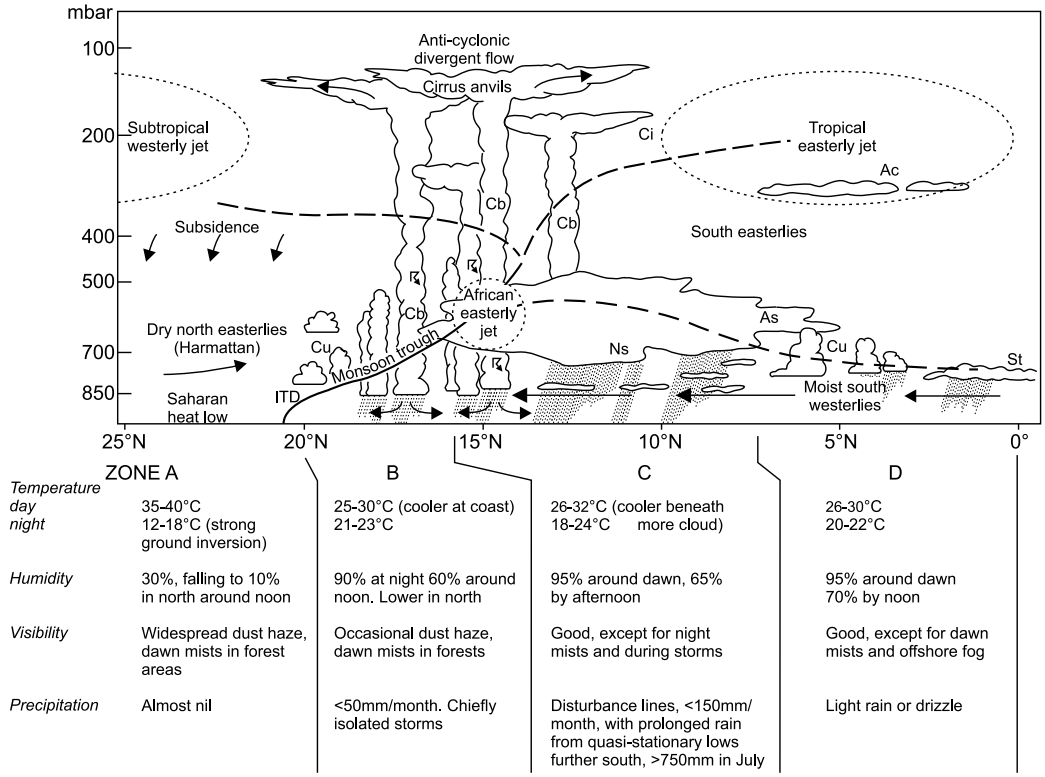


FIGURE 2.3: A schematic showing a north-south cross section of the atmosphere over West Africa during August to illustrate the main features of the West African monsoon (WAM) front. The surface confluence of the monsoon flow and Harmattan winds (intertropical discontinuity; ITD) is shown to reach north of 20 °N, this is a northerly position for the ITD which is able to move a considerable distance north and south influenced by meteorology. Other important features for the WAM system include a heat low over the Sahara, mesoscale convective systems (labelled Cb) where the monsoon flow is deep enough, the mid-level African easterly jet (AEJ) and upper level subtropical and tropical easterly jets. Adapted from Buckle 2004 using information from Lebel et al. 2010.

winds over the Saharan and Sahel are generally northeasterly (Figure 2.2). This wind air is known as the Harmattan. As the seasons change and the Earth's axis of rotation points the NH toward the Sun, the ITCZ moves north. The large scale convective circulation (Hadley cell labelled on Figure 2.1) drives moist air from the Gulf of Guinea and the Atlantic over West Africa. This flow of cooler, moister air is known as the West African Monsoon (WAM). The surface boundary between the WAM and the Harmattan winds is known as the intertropical discontinuity (ITD). The ITD is a dynamic front driven by a number of synoptic- and mesoscale meteorological processes. South of the ITD where the monsoon flow is sufficiently deep a band of intense rainfall is produced. This is especially important for the people living in the semi-arid Sahel, many of whom depend on rain-fed agriculture. The movement of the WAM flow inland can be seen in Figure 2.2, a convergent region across West Africa is produced where the Harmattan and WAM meet.

In the summer the Sahel and Guinea coast regions are no longer under the northeasterly Harmattan air but are strongly influenced by the WAM and ITD. A semi permanent low pressure feature is produced by strong heating of the lower atmosphere. This is known as the Saharan heat low (SHL). During the summer months the SHL is strengthened due to intensifying insolation.

Figure 2.3 shows some of the important features of the ITD region during August when the WAM has reached its furthest extent inland. The important climatological features present include: (1) a strong monsoonal flow from the south turning southwesterly and interacting with the Harmattan flow from the northeast, (2) a strongly baroclinic region where the two air masses meet, the surface front being the ITD with the front sloping back towards the Guinea coast with height, (3) a stronger SHL and deepening of the mixed boundary layer over the Sahara driven by the increased solar heating, (4) a high-level tropical easterly jet at the top of the troposphere, (5) a low to mid level jet called the African Easterly Jet (AEJ). This is produced by the strong meridional baroclinicity between the intensely heated Sahara and the Guinea coast region. Above the lower troposphere a pressure gradient is produced opposite to that at the surface. The influence of the Earth's rotation (Coriolis Force) turns the resultant flow to the right to form an easterly jet in the low to mid troposphere.

These features describe the general situation and provide the environment in which weather systems develop. Unlike this temporally averaged view of the atmosphere there is a great deal of variation and complexity which makes studying the meteorology of this region difficult and interesting.

## 2.2 West African Meteorology

### 2.2.1 Basics of convection

One of the most important features of West African meteorology is the production of convective storms. The cycle of a thunderstorm can be considered by looking at a single convective cloud's life cycle. As a single-cell convective storm develops it will progress through three separate stages (Figure 2.4) (Byers, 1949): (1) the cumulus phase, (2) the mature phase, (3) the dissipation phase.

### Cumulus phase

The cumulus phase of a convective cell is produced when buoyant, near-surface air rises to form a cumulus cloud (Figure 2.4a). Cooling due to expansion of the air parcel causes water vapour to condense into cloud droplets. As droplet formation occurs, latent heat is released, causing the parcel to cool less rapidly with height compared to the environment. This further encourages convection creating updraughts of increasing strength with height (Byers, 1949). During this early stage the updraughts within the cell are balanced by slow downward movement in the surrounding environment (Byers, 1949; Mapes, 1993). If latent heating within the parcel continues to make the parcel cool less rapidly than the surroundings convection will continue. A small cumulus with limited vertical extent can, with continued buoyancy, continue to grow into a cumulonimbus. At the top of the troposphere the stable tropopause prevents further vertical motion causing the top of the cloud to begin to spread (Figure 2.4b).

### Mature phase

As convective cells reach the mature stage they undergo rapid droplet growth. This is facilitated by three processes: (1) ice crystal growth, (2) collision/coalescence and (3) entrainment of sub-saturated air.

Firstly, there is a ubiquitous scarcity of particles suitable for ice nucleation (ice nuclei; IN) away from the surface (Phillips et al., 2007). However, cloud condensation nuclei (CCN) which allow for cloud droplet formation are much more common. The reduced pressure and temperature, a rising parcel reaches, coupled with the shortage of IN can lead to supersaturation with respect to ice being significantly higher than supersaturation with respect to liquid water. Under these conditions, there can be a high rate of deposition of water vapour from the atmosphere onto a limited number of IN. This promotes evaporation of liquid water from surrounding supercooled cloud droplets because the vapour pressure over ice is higher than over liquid water. Evaporated water from droplets is then able to deposit onto the surface rapidly growing of ice particles.

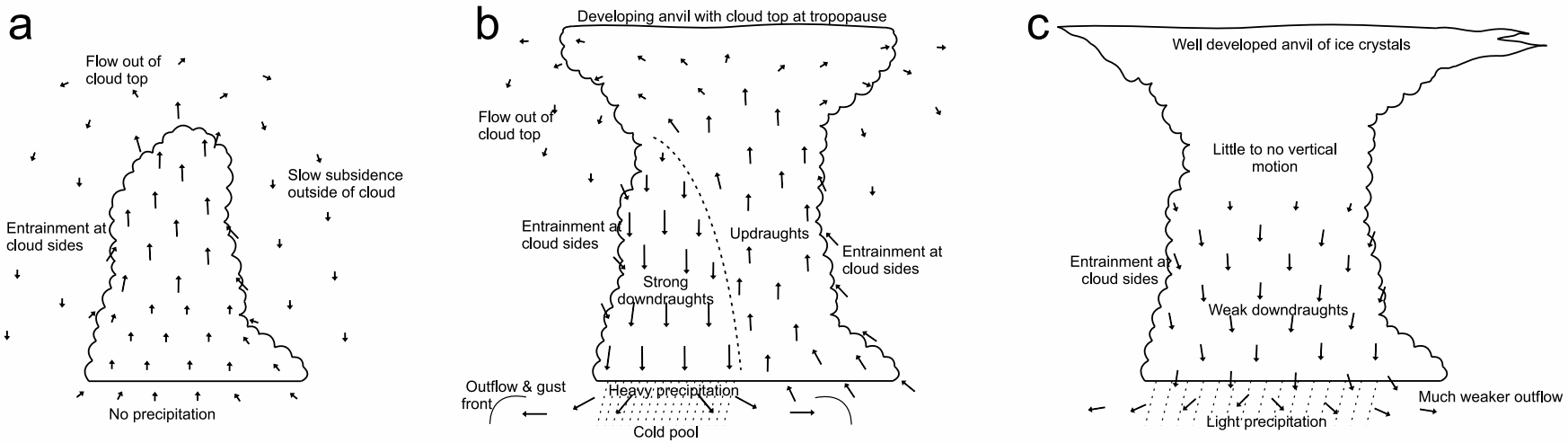


FIGURE 2.4: The three stages of cumulus development showing (a) the cumulus phase with updraughts throughout the entire cloud and flow out of the top of the cloud balanced by slow subsidence outside the cell, (b) the mature stage with well developed updraughts and downdraughts (produced by phase changes of hydrometeors, specifically evaporation in subsaturated conditions) and a strong outflow from the base of the cloud and (c) the dissipating stage, where downdraughts overcome updraughts, precipitation becomes weaker and downdraught strength is diminished.

Ice crystals are able to grow much larger and more rapidly than liquid water droplets in cumulus clouds. This is known as the Bergeron Findeisen process.

Secondly, different sized droplets and crystals within a cell allow for rapid growth by collision and coalescence as larger droplets and crystals fall more quickly and so collide with smaller droplets (Vohl et al., 2007). The probability that two droplets will coalesce also increases with droplet radius (Rangno and Hobbs, 2005; Vohl et al., 2007).

Lastly, when sub-saturated environmental air is entrained into the cloud, the relative humidity in the vicinity is reduced (Jonas, 1991). The equilibrium relationship means that water evaporating from cloud droplets forces the smallest droplets to evaporate entirely (Jonas, 1991). As convection continues the formation of new small droplets is suppressed due to the presence of fewer larger droplets limiting the supersaturation. This leads to fewer, larger droplets, creating further heterogeneity in droplet size. This feeds back into the second process as it further enhances the collision and coalescence growth of cloud droplets.

These processes are important for precipitation production as diffusional growth of droplets would take much longer than the lifetime of a single-cell cumulonimbus. The rapid growth of cloud droplets and ice crystals within convective cells also leads to the heavy precipitation associated with convective storms.

The large number of hydrometeors falling through subsaturated air within the mature convective cell creates strong downdraughts (Figure 2.4b). A feature of a convective cell in the mature phase is the presence of both updraughts and downdraughts. The formation of downdraughts by precipitation can be understood by considering interaction between the air and falling hydrometeors. As they fall, the evaporation of water droplets and melting of ice causes latent cooling of the air within the cloud (Atlas and Williams, 2003; Kamburova and Ludlam, 1966; Knupp and Cotton, 1985). This air contracts and becomes negatively buoyant, allowing downward motion. Additionally, frictional drag exerted on the air by the falling hydrometeors helps to drive downward motion (Byers, 1949; Rotunno et al., 1988). Once downdraughts reach the surface they can form pools of colder, denser air compared to the surrounding environment.

### Dissipating phase

The production of downdraughts in a single-cell convective storm interferes with the updraughts that feed the storm moist low-level air. This moves storms into the dissipating stage (Figure 2.4c). The lack of upward motion within the cell reduces the efficiency of cloud droplet and ice crystal formation and therefore precipitation intensity. A reduction in precipitation then leads to a weakening of the downdraughts. The weaker downdraughts mean that the outflow from the base of the storm is much weaker than during the mature phase.

### Atmospheric instability

A precursor for the development of a convective storm is atmospheric instability. As mentioned before, the release of latent heat can mean that the rate of cooling of a rising parcel is less than that of the surrounding environment. However, for a parcel to reach the stage where condensation can occur and latent heat is released it must first be raised to its lifting condensation level (LCL).

Below the LCL it is likely that the lapse rate of the dry ascending parcel is greater than that of the environment. This means that if perturbed upwards, the parcel will be negatively buoyant. The energy needed to overcome this negative buoyancy is known as the convective inhibition (CIN). If the atmospheric profile is such that a parcel raised through it never becomes positively buoyant due to additional latent heating, the atmosphere is stable. However, if the latent heating means that at some point the parcel does become positively buoyant, the atmosphere is described as being conditionally unstable. The height at which the parcel becomes buoyant is known as the level of free convection (LFC). At some higher altitude the parcel will become negatively buoyant again due to changes in the relative lapse rates of the parcel and the environment, this is known as the equilibrium level (EL) (often close to the tropopause). The energy available to the parcel between the LFC and the EL is known as the convective available potential energy (CAPE) and gives information about the amount of energy available to drive convective storm development.

#### Triggers

In order for a convective cell to be initiated, CIN must be overcome and the parcel must be forced to the LFC. The processes responsible for this initial perturbation are known as triggers. There are a number of mechanisms that can initiate a convective storm, these include: (1) surface heating driven turbulence in the lower atmosphere, (2) topographical effects, where terrain deflects the flow creating upslope winds, lee-side convergence or gravity waves (Houze, 2004), (3) convergence at low-levels, examples of which include: gust fronts from thunderstorm outflows, cold fronts, sea or lake breezes and drylines (Johnson and Mapes, 2001), (4) surface inhomogeneities such as variable land surface covering, creating surface temperature and moisture anomalies, leading to the production of buoyant parcels, (5) strong changes in wind speed and direction with height (vertical shear) these can produce near surface rolls, the upward limb of which can be strong enough to trigger convective storms, (6) the right entrance and left exit regions of jets (in the NH) create divergence aloft and are known to encourage vertical motion helping to trigger convection (Johnson and Mapes, 2001), jet curvature can produce a similar effect.

### 2.2.2 Downdraughts and cold pools

As shown above (Figure 2.4b), once a storm has matured it will produce strong downdraughts due to its production of large amounts of hydrometeors. The result of these downdraughts is that a significant pool of colder and therefore denser air will form below the precipitating clouds. This air will begin to spread out horizontally, driven by a pressure gradient associated with the enhanced density of the cold pool which creates hydrostatic imbalance.

As cold pool air spreads out, it takes the form of a type of flow seen in many different naturally occurring phenomena, that of a density current. Density currents, sometimes known as gravity or buoyancy currents are horizontal flows that are formed when gravity acts on two fluids with different densities out of hydrostatic equilibrium (Benjamin, 1968; Simpson, 1997). They are described in more detail in Section 2.3. As the cold air spreads away from its parent storm, ambient air is lifted above its leading edge. This process is an important factor in the organisation of convective systems.

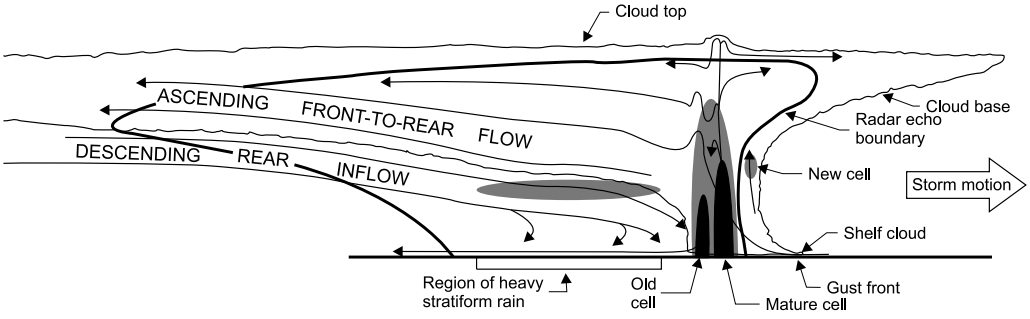


FIGURE 2.5: Schematic of a cross section through a mesoscale convective system (MCS) orientated parallel to the direction of storm motion. Note that the linear nature cannot be seen in this representation (redrawn from Houze et al. 1989).

### 2.2.3 Convective organisation

The simple, single-cell model of convective storms already discussed gives a good idea of the basic processes within a cumulonimbus cloud. However, this suggests that convective storms are always short-lived. In reality convective storms can last for much longer periods, with extreme examples persisting over a day rather than a few hours. The key to this longevity is the decoupling of updraughts and downdraughts within a storm. This can happen in two ways: (1) formation of a supercell storm where rotation imparted on the storm separates updraughts and downdraughts and (2) formation of a multicellular system of storms such as a squall line or mesoscale convective system (MCS). In this case vertical shear produces conditions in which convective cells are repeatedly generated along the leading edge of the system. Shear helps to modify the behaviour of the cold pool outflow creating preferential uplift along one side of a convective cell. This triggers new cells on this side of the system, producing a linearly organised group of convective cells that moves over time. This can be seen in Figure 2.5 which also shows features common for MCSs such as: a shelf cloud above the gust front of the cold pool, an ascending front-to-rear flow, a descending rear inflow jet and a region of heavy stratiform rain behind the main line of convective cells. It is the repeated generation of new cells that produces a convective system which is longer lived with a linear structure (Doswell, 2001).

Cold pools are also important because of the strong turbulent winds along their leading edges (gust fronts). The winds at a gust front can be structure damaging and where surface conditions allow, are capable of lifting surface sediments. When dust is raised by a

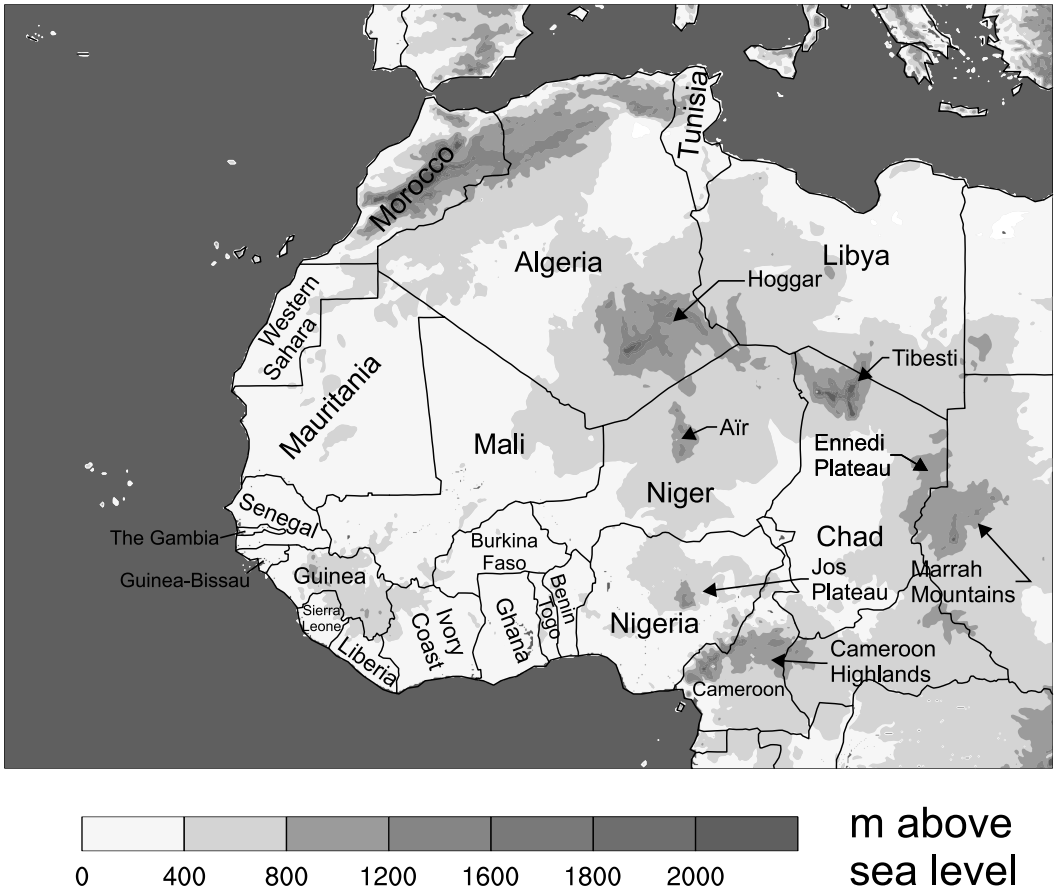


FIGURE 2.6: Terrain height of West Africa. Important convective triggering regions are labelled.

convective cold pool it is known as a haboob. Haboobs are a major dust uplift mechanism in West Africa and are discussed in more detail in section 2.6

### MCSs in West Africa

Multicellular storms can produce very high rates of precipitation and it has been shown that they account for over 80% of the annual rainfall in Africa between 5° and 18° north (Mohr et al., 1999). Similarly to the features needed to produce single cell convective storms, MCSs require: (1) adequate CAPE to produce strong convective cells once parcels reach the LFC (Johnson and Mapes, 2001; Laing and Fritsch, 2000), (2) a trigger for the initial vertical motion strong enough to overcome the CIN (Fritsch and Forbes, 2001; Johnson and Mapes, 2001) and (3) vertical wind shear to help to separate updraughts and downdraughts to produce long-lived systems.

In West Africa features responsible for the triggering of MCSs have been shown to include: (1) terrain, especially the Tibesti, Hoggar, Aïr and Marrah Mountains, the Cameroon highlands and the Ennedi and Jos Plateaus (Figure 2.6), (2) the exit and entrance regions of the AEJ which produce mid-level divergence (Johnson and Mapes, 2001), (3) heterogeneity of soil moisture, this is often controlled by previous storm activity (Birch et al., 2013; Taylor et al., 2012), (4) processes causing low-level convergence or uplift such as cold pool outflows of convective storms and (5) synoptic-scale features which favour convection such as African Easterly Waves (AEWs; westward propagating horizontal equatorial waves on the AEJ) (Berry and Thorncroft, 2005).

Also discussed in the literature are Mesoscale Convective Complexes (MCCs). MCCs are a group of convective cells arranged so that their anvil clouds merge and create a single round cloud shield (Fritsch and Forbes, 2001). The distinction between MCCs and MCSs is in fact an artefact of studying storms using satellite imagery. The round anvil clouds of MCCs often mask the linear structure of the convective systems beneath (Doswell, 2001). Storms that are classified as MCCs are generally very large (round cloud shield colder than $-32°$C covering over 100 000 km$^2$ and an area colder than $-52°$C covering over 50 000 km$^2$; Maddox (1980)) and long-lived ($\geq$ 6 hours). However, the processes that are important for their production are the same as for MCSs.

### 2.2.4 Position of the intertropical discontinuity (ITD)

As mentioned earlier the depth of the monsoon flow in some part dictates the regions over which MCSs are produced. Therefore, northward surges of the WAM help to produce MCSs close enough to the arid northern Sahel and Sahara for haboobs to be formed (Figure 2.7).

Factors that influence the behaviour of the monsoon flow and produce northward excursions include: (1) westward propagating AEWs on the AEJ (Berry and Thorncroft, 2005; Cuesta et al., 2010; Knippertz and Todd, 2010), (2) interactions between the tropics and the mid-latitudes such as the mid-latitude low pressure systems or the formation of tropical plumes (Knippertz, 2008; Knippertz and Martin, 2005; Knippertz and Todd, 2010;

Vizy and Cook, 2009) and (3) feedbacks between mesoscale and synoptic-scale meteorology such as convective cold pool strengthening of the monsoonal flow (Cuesta et al., 2010; Flamant et al., 2007).

When MCSs are positioned just south of the ITD they can have a significant impact on the behaviour of the monsoonal front. Flamant et al. (2007), Flamant et al. (2009) and Cuesta et al. (2010) have shown that the production of cold pools in this region, which flowed northwards, produced significant movement of the monsoon front over a localised area. In the case of Cuesta et al. (2010) the effect was also associated with the southerly sector of an AEW and circulation linked to the SHL. It produced wet conditions for the usually arid region in the Hoggar Mountains (Figure 2.6). It has also been suggested that modification of the ITD by a density current might help to strengthen the monsoon flow to the point where it is structurally similar to a density current (Bou Karam et al., 2008), making the ITD and the cold pool indistinguishable from one another (Figure 2.7).

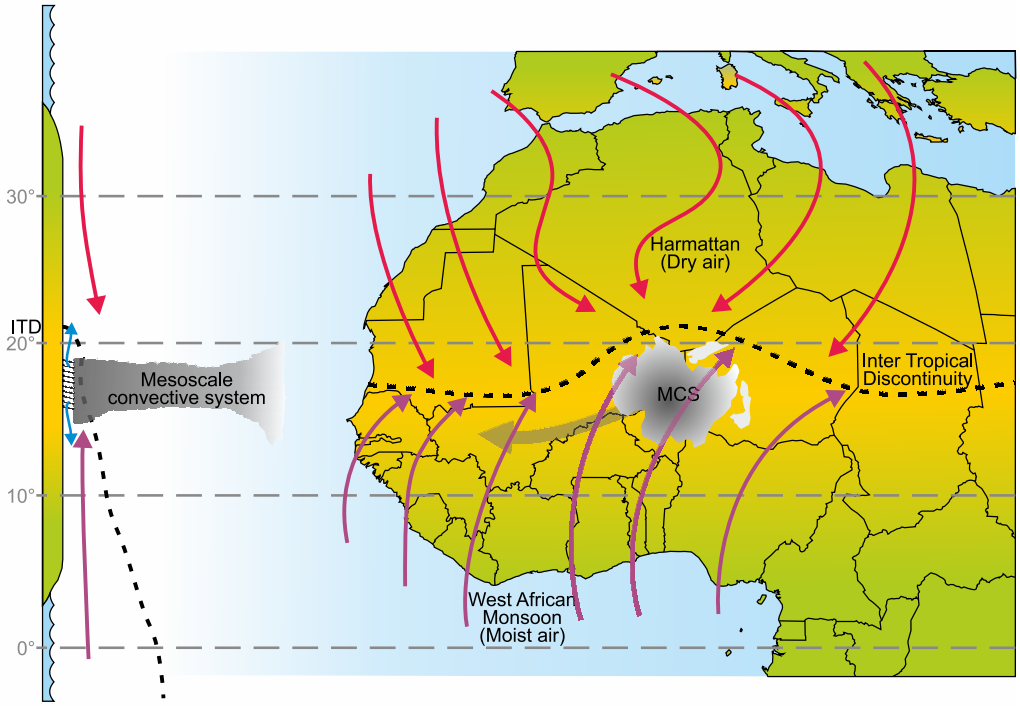


FIGURE 2.7: A schematic of the near-surface winds associated with the West African monsoon (WAM). The Harmattan winds are in red and WAM winds in purple, the dashed black line indicates the interface between the two. Also shown is a mesoscale convective system (MCS) within a northward bulge of the intertropical discontinuity (ITD), and the flow of cold pool air shown with blue arrows on the left hand side of the figure (Roberts and Knippertz, 2012).

## 2.3 Modelling density currents

As mentioned in Section 2.2.2 cold pools produced by convective storms take the form of density currents as the denser cold air spreads away from the parent storm. Examples of atmospheric density currents include convective storm outflows, katabatic winds, sea breezes and to some extent steep cold fronts. Previous studies have explored the anatomy of density driven flows under laboratory conditions to provide a basis for researching their behaviour in nature (Simpson, 1997; Simpson and Britter, 1980).

The main features of these flows can be seen in Figure 2.8 and include: (1) a well defined turbulent head along their leading edge and a laminar following flow, (2) a raised nose due to friction with the surface, making the dense fluid over-run some of the less dense ambient fluid, (3) turbulent lobes and clefts produced as the over-run fluid rises through the head of the flow (Britter and Simpson, 1978; Simpson, 1997).

As long as the fluids have a sufficient density difference and the kinematic viscosity of the flow is sufficiently small, the Reynolds number ($Re$) will exceed 10 000 and the flow will take the form of a density current (Simpson, 1997). Typically thunderstorm outflows have $Re$ values of $10^6$ and so conform to the density current structure shown here.

Assuming conditions are met for a density current to form, the initial speed of the current's leading edge can be estimated using the equation $U = Fr(g'h)^{\frac{1}{2}}$ (Simpson, 1997). $Fr$ is the internal Froude number of the flow (ratio of inertial to buoyancy forces) a value of 1.16 is used here Huppert and Simpson (1980). $g'$ is the reduced gravity of the flow ($g' = \frac{\Delta\rho}{\rho}g$; where $\Delta\rho$ is the change in density, $\rho$ is the density of the environmental fluid and $g$ is gravitational acceleration). $h$ is the initial depth of the dense fluid. A typical thunderstorm cold pool outflow might have a temperature perturbation of between 5 and 10 °C. For environmental temperatures and pressures (including conditions similar to those found in the Sahara) this produces a density perturbation of between 1.5 and 3 %. Using these density perturbations and initial flow heights between 500 and 2000 m the initial speed of the density current edge is predicted to range between 10 and 30 $ms^{-1}$ (this is slightly higher than observed atmospheric density currents that tend to range from 10 to 20 $ms^{-1}$; Idso et al., 1972; Miller et al., 2008; Simpson, 1997; Sutton, 1925). However, this might be explained by the fact that after the initial, early spreading stage of a density current (where its flow speed is constant) it enters a second phase where the

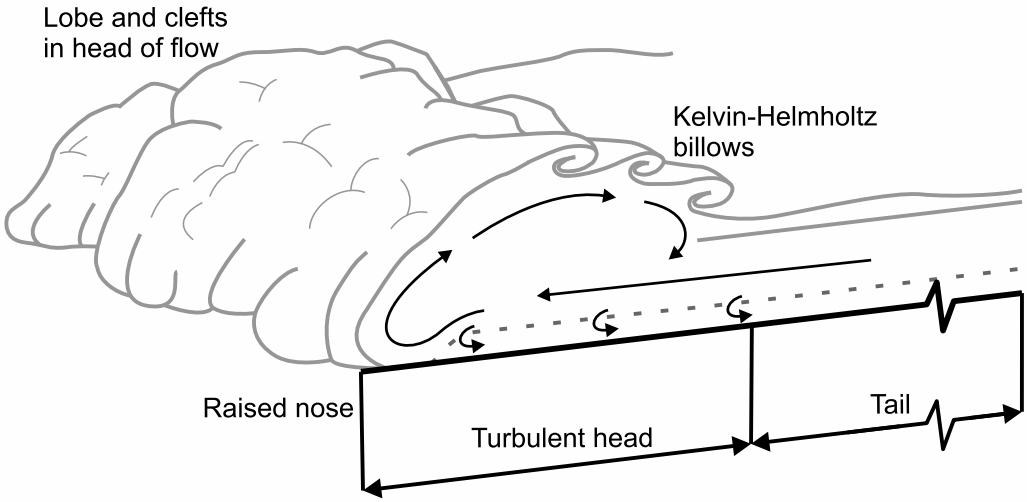


FIGURE 2.8: A schematic showing the main features observed in density currents: notably, a turbulent leading edge with a well-defined head region with lobe and cleft structures thought to be produced by over-run environmental fluid rising through the head. Also shown is the laminar flow of the tail region, the raised nose of the density current and Kelvin-Helmholtz billows created by strong shear. The arrows denote the circulations that are generally assumed within the head. (Adapted from Figures 2.6 and 11.3 from Simpson, 1997)

distance covered by the leading edge of the current varies with $t^{\frac{1}{2}}$, where $t$ is time (for axisymmetric flows, the distance covered by the edge of two-dimensional flows instead varies with $t^{\frac{2}{3}}$) (Huppert and Simpson, 1980; Simpson, 1997).

The modelling of density currents provides a method of learning about haboobs as a dust uplift process. The analogy of a convective cold pool to a density current is useful due to the largely predictable nature of their behaviour.

Early work on density currents was conducted by the production gravity driven flows in water tanks (Britter and Simpson, 1978; Huppert and Simpson, 1980; Rottman and Simpson, 1983; Simpson, 1997; Simpson and Britter, 1980). Usually, a tank is filled with water and a dyed fluid of enhanced density (saline) is released into it via a raised lock gate. The dense fluid slumps to produce the gravity driven flow.

Many of the investigations into the behaviour of density currents more recently have been conducted with the use of computer simulations (D'Alessio et al., 1996; Hallworth et al., 2001; Liu and Moncrieff, 1996; Moncrieff and Liu, 1999; Simpson, 1997; Zemach and Ungarish, 2013), however, laboratory studies are still used to investigate the behaviour of these flows (Hallworth et al., 2001; Maxworthy et al., 2002; Tan et al., 2010)

Additional areas of interest are the behaviour of density currents when the ambient fluid is moving and sheared (Liu and Moncrieff, 1996; Moncrieff and Liu, 1999), the role of stability (Holyer and Huppert, 1983; Tan et al., 2010) and density currents in rotating frames of reference (Hallworth et al., 2001).

It has been shown by Liu and Moncrieff (1996) that a density current flowing in a uniform background flow will have a raised (lowered) head when travelling against (with) the uniform ambient flow and a reduced (enhanced) front speed compared to no background flow. In sheared conditions it is found that weak or moderate shear in the direction of density current travel elevates the flows head. Shear in the opposite direction has little effect on the density current shape compared to no shear. These different behaviours can be seen in Figure 2.9 which shows a schematic of the modified behaviour of the head of a density current in no wind, uniform background wind and sheared wind. The processes which increase flow speed and head height have been shown to be influential in the formation of new cells along the leading edge of MCSs (Moncrieff and Liu, 1999) (Figure 2.5). This is due to the enhanced speed and height of updraughts produced along the leading edge of the convective cold pool.

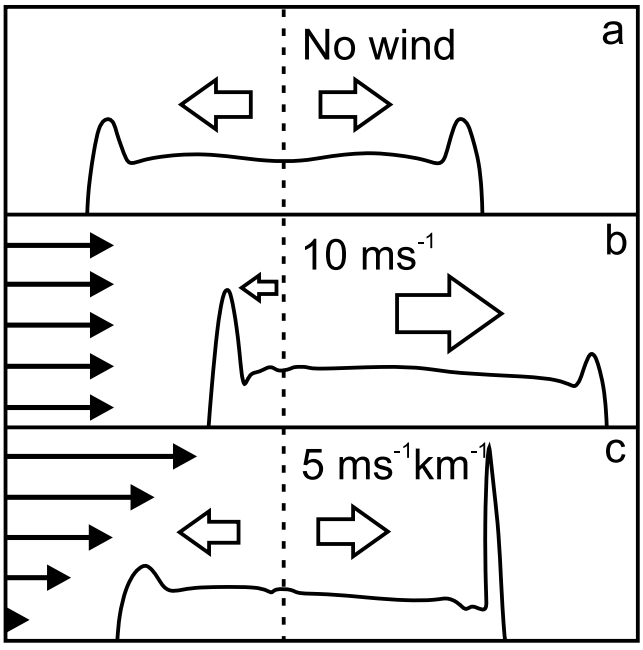


FIGURE 2.9: A schematic showing the structure of a density current head in (a) no background wind, (b) uniform 10 $ms^{-1}$ winds and (c) linearly sheared conditions with zero winds at the surface and increasing at 5 $ms^{-1}km^{-1}$. Also shown are the background wind (black arrows), arrows to give an indication of the speed of the density current (white arrows) and the starting point of the flows (dashed line). Based on findings from Liu and Moncrieff (1996).

In the work of Simpson (1997) and Tan et al. (2010) the influence of a density current flowing through a stratified environment is shown. In Simpson (1997) it is noted that if the depth of a density current is greater than four times the depth of the stable layer then this layer is mixed into the current and the system almost behaves as if the stable layer does not exist. However, when the ratio between stable layer depth and density current depth is less than one in four, the system can be described as being partially blocked. The stable layer is no longer mixed into the density current but neither is it simply able to flow over the top of it. Instead fluid builds up at the front of the current and an internal bore is produced, if the density current flow speed is smaller than the wave speed for the bore (based on density difference, the depth of the stable layer and the behaviour of the wave dictated by the amplitude of the bore compared to stable layer depth) then bores will be intermittently generated that propagate ahead of the density current (Simpson, 1997; Tan et al., 2010). This interaction with stable layers and the production of waves on an internal boundary is important due to the development of both strong NBLs and convective cold pools across the Sahel and Sahara. Bores can also be generated by intrusive density currents moving between two layers where the dense near-surface layer is shallow (Simpson, 1997).

The behaviour of density currents in rotating frames of reference is important due to the fact that sometimes MCSs have been observed to produce haboobs which are very large (Roberts and Knippertz, 2012). The size of these flows means that they are likely to be influenced by Coriolis force turning the flow to the right (in the NH; Figure 2.10) from the radial flow of a smaller axisymmetric density current. To establish if Coriolis force is a significant factor in the behaviour of a flow, it is usual to calculate its Rossby number ($Ro$). $Ro$ is a dimensionless number that gives a measure of the ratio of inertial forces and rotational forces.

$$Ro = \frac{U}{Lf} \tag{2.1}$$

Where $U$ is the characteristic velocity of the flow, $L$ is the length scale and $f$ is the Coriolis parameter. If a flow has $Ro << 1$ then rotational forces dominate and the flow will be deflected to the right (NH), however, if $Ro >> 1$ then inertial forces dominate and the flow follows the pressure gradient. The behaviour of a density current when it is influenced by rotational effects is different to a flow unaffected by rotation. Instead of the flow slowing down with time until viscous forces become more dominant (at which

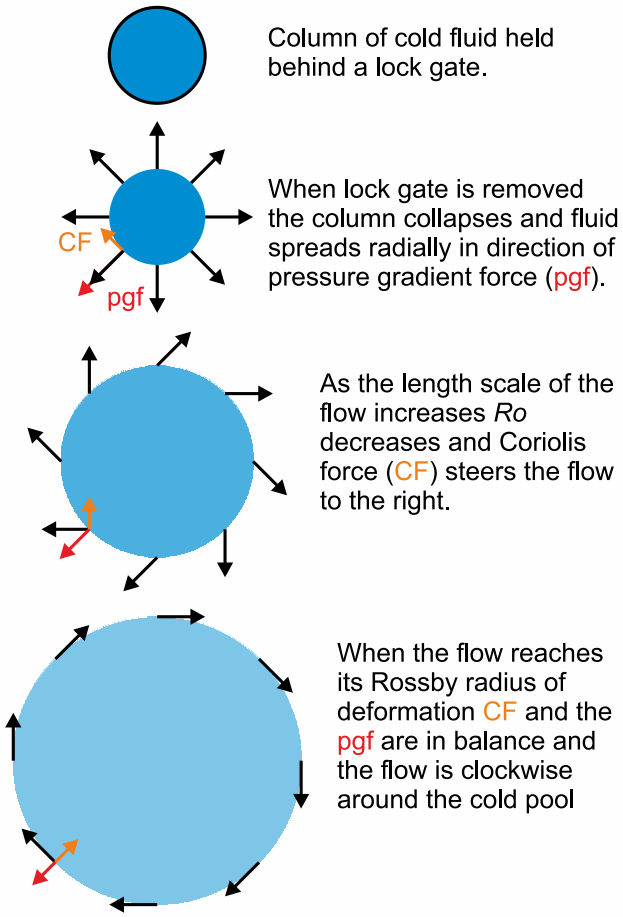


FIGURE 2.10: Schematic showing the change in behaviour of an axisymmetric density driven flow, from radial spreading after release to a point where the pressure gradient force is matched by the Coriolis Force and the flow is perpendicular to the pressure gradient. The strength of the blue colour denotes the depth of the fluid: lightening indicates thinning (Roberts and Knippertz, 2012).

point its leading edge slows more rapidly with time), the influence of rotation produces a current with a flow which becomes less radial. When the density current reaches a stage where it is dominated by rotational forces, it has been shown that the leading edge of the flow decelerates rapidly (Hallworth et al., 2001) A series of contractions and relaxations have been observed in laboratory experiments which lead to A maximum radius having been reached, a series of contractions and relaxations have been observed in laboratory experiments, the density current behaves like a meso-high with anti-cyclonic rotation and features consistent with horizontal shear instability have also been observed (Hallworth et al., 2001; Kawashima, 2010).

## 2.4 Field campaigns

To better understand the complex behaviour of the West African climate system there have been a number of field campaigns in recent years. These have been aimed at different aspects of the region but have all attempted to improve our understanding by gathering observations in this otherwise poorly observed part of the world. The largest, recent field campaigns discussed here are: (1) the African Monsoon Multidisciplinary Analysis (AMMA), (2) the Saharan Mineral Dust Experiment (SAMUM-1 and SAMUM-2) and (3) the Fennec campaign. This is by no means an exhaustive list of the field campaigns that have been undertaken in recent years. The cost associated with campaigns of this type is high, therefore, the size longevity and number of these campaigns highlights that quality data in such a data sparse region has great scientific value.

### AMMA

The AMMA field campaign focussed on gathering data to help improve the understanding of the WAM. The scope of AMMA as a project was broad, focussing on areas such as meteorological phenomena connected to the monsoon system (Lafore et al., 2011), atmospheric composition (Mari et al., 2011) and the social and economic impacts the WAM (Polcher et al., 2011). It included the use of existing and reactivated observation infrastructure (2001–2009), which were enhanced from 2005 to 2007 along with the implementation of additional land and sea-based instrumentation (Lebel et al., 2010; Parker et al., 2007). Within these nested periods was a special observing period (SOP) in 2006 during which there was a further enhancement of observations including the use of research aircraft and weather balloons (radiosondes) (Parker et al., 2008). AMMA Publications of particular interest for this study are Cuesta et al. (2010); Flamant et al. (2007) and Flamant et al. (2009) which detail the impact of convective cold pools and AEW on the position of the monsoon flow and the structure of the monsoon/Harmattan interface. Important findings include the influence that convective scale processes an have on the large-scale meteorological structures over West Africa such as the the position of the ITD and the strength of the SHL. Also of interest are Burton et al. (2013) which investigates the diurnal behaviour (including dust lifting) associated with the Harmattan and monsoon front and Lavaysse et al. (2010) which details the periodic pulsations in SHL strength.

### SAMUM

The SAMUM experiments in 2006 and 2008 focussed on the lifting and transport of Saharan dust. SAMUM-1 was based in southern Morocco and SAMUM-2 on Cape Verde in 2006 and 2008 respectively. The aim of the project was to evaluate the properties and transport processes for airborne mineral dust (Ansmann et al., 2011). In the first phase, freshly lifted dust and aged dust plumes were observed using lidar and research aircraft and their microphysical properties, chemical composition and optical properties were determined. During the second phase, the properties of aged dust plumes transported away from the Sahara were retrieved. The value of which is to determine the effects of ageing on dust (Ansmann et al., 2011). Additionally the properties of smoke from biomass burning over West Africa were studied. The meteorology of dust uplift processes was also investigated including gust fronts from convective storms (Knippertz et al., 2007), dry convective plumes and dust devils (Ansmann et al., 2009) and other synoptic-scale processes (Knippertz et al., 2009a). Other SAMUM publications of particular interest for this study are Knippertz et al., (2009b) and Reinfried et al. (2009) which both focus on modelling of convective cold pools produced by convective storms over the Atlas Mountains. Of particular interest are the influences of model physics on cold pool evolution (Knippertz et al., 2009b) and the need for explicit representation of convection to form cold pools similar to those seen in satellite imagery (Reinfried et al., 2009).

### Fennec

The Fennec campaign was based across the Sahara with ground instrumentation deployed across Algeria and Mauritania and research flights out of Morocco and the Canary Islands during 2011 and 2012. A main aim of Fennec was to gather data about the meteorology of the central Sahara, especially attempting to improve understanding of the very deep boundary layer, the behaviour of the SHL and meteorological processes responsible for the lifting of mineral dust (Washington et al., 2012). The observations made were by: (1) eight automatic weather stations positioned across the SHL region (Hobby et al., 2013), (2) super sites at Bordj Badji Mokhtar in Algeria (Marsham et al., 2013a) and Zouerat in Mauritania (Todd et al., 2013) which were equipped an array of tools including; flux towers, sodar, lidar and radiosondes and (3) research aircraft that conducted over 200

hours of scientific flying (Washington et al., 2012). Currently the observations taken as part of Fennec have not been utilised for a modelling study, therefore is represents a significant gap in the current literature. The Saharan - West African Monsoon Multiscale Ananlysis (SWAMMA) project (start date July 2014) partially aims to fill this gap in the the literature by conducting UK Met Office Unified Model runs over West Africa including convection permitting simulations and interactive dust some of which are focussed on the 2011 and 2012 monsoon seasons. Areas to be investigated include the connections between moist convection and dust, the balance of dynamic, convective and radiative WAM processes and the seasonal evolution of the WAM.

## 2.5 Dust sources

### 2.5.1 Geomorphology

The surface of the Sahara desert is dominated by aeolian and palaeo-fluvial landforms (Ballantine et al., 2005; Shaw, 1997). This is visible in the landform map produced by Ballantine et al. (2005) (see Figure 2.11). This shows many features which are the remnants of alluvial fans and lake beds dating back to the Holocene when the Sahara was far less arid than it is today (Drake and Bristow, 2006).

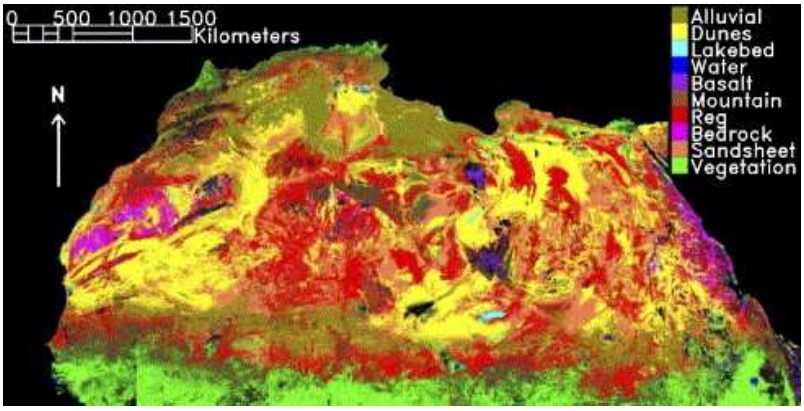


FIGURE 2.11: A landform map of North Africa produced from Moderate Resolution Imaging Spectrometer (MODIS) imagery by Ballantine et al. (2005), note the large areas covered by landforms produced by fluvial of aeolian processes suggesting the dominant geomorphological processes.

In the past, much of the work undertaken on Saharan geomorphology and its link to dust uplift has focussed on particular regions. One such area is the Bodélé depression (Bristow

et al., 2009; Drake and Bristow, 2006; Washington and Todd, 2005), which forms part of the bed of the palaeolake, Lake Megachad. Lake Megachad was an enormous body of fresh water that has since diminished in extent to the present day Lake Chad. It was part of a group of megalakes in North and West Africa that reached their peak sizes sometime before 7000 years ago (Drake and Bristow, 2006).

During this period there were four main lakes covering approximately 10% of what is now the Saharan surface (Drake and Bristow, 2006). The four lakes were (Figure 2.12): (1) Lake Megachad, positioned south of the Tbesti Mountains covering much of present day Chad, (2) Lake Megafezzan, situated in what is now Libya, northwest of the Tbesti mountains and east of the Hoggar Massif, (3) the Ahnet Moyer Megalake, west of the Hoggar Massif in what is now the lowlands of central Algeria and (4) the Basin of Chotts, south of the easternmost Atlas Mountains, straddling the Algerian-Tunisian border.

As well as large amounts of sediment deposited as part of lake beds, large palaeo-river systems also provide fine easily lifted surface sediments. This includes alluvial fans and wadis created as rivers flowed away from the mountainous regions of the Sahara (see Figure 2.11) into the basins in the continent's interior.

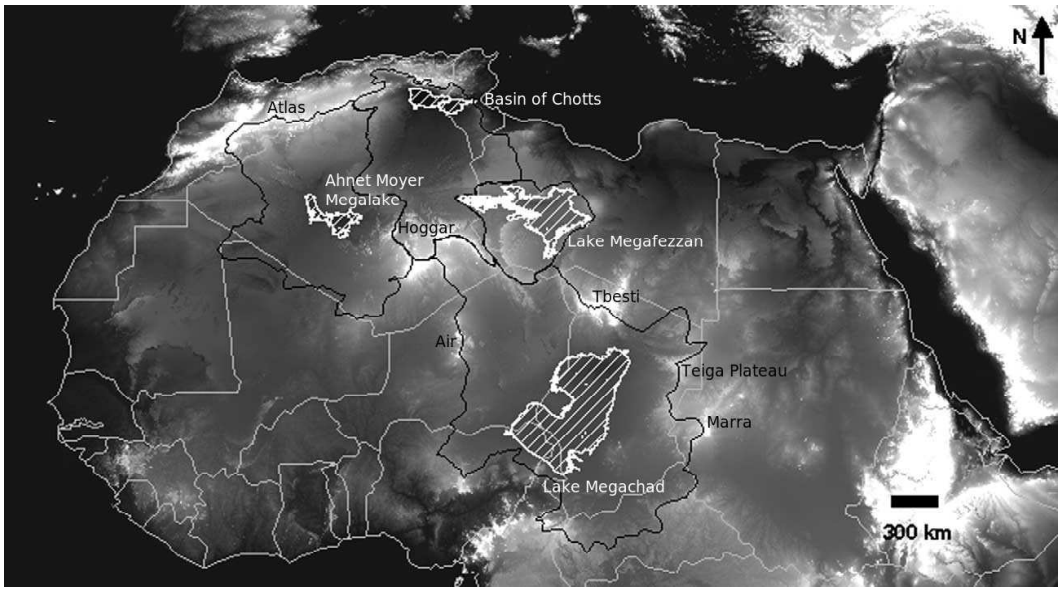


FIGURE 2.12: A map showing the position of palaeolakes at their largest known sizes from palaeo-shorelines and sediments, plotted on top of an altitude map from the Shuttle Radar Topography Mission (SRTM) digital elevation model (DEM). The lighter the colour the greater the height of the surface (from Drake and Bristow 2006).

As the region became more arid starting about 10 000 years ago (Kröpelin et al., 2008), the major sedimentary processes changed from being driven by water, to being controlled by the wind. This can be seen in Figure 2.11, large areas of the desert surface are covered by aeolian landforms such as: dunes, regs (desert pavements capping the underlying sediments, formed by aeolian erosion and deposition; Breed et al. 1997; Warner 2004), sandsheets and bedrock stripped of its overlying sediments. The modification of the vast fluvial landscape by aeolian processes highlights the importance of dust deflation, transportation and deposition in both the formation of and the current landform processes in the Sahara. Despite the identification of palaeo-processes and landforms that provide dust for deflation there is still some uncertainty as to the importance of source regions compared to one another and dust source regions are not well defined. Because of this much effort has been spent attempting to identify the most important dust sources in the West Africa.

### 2.5.2 Dust source identification

#### Direct measurement

Early methods for defining the source areas of dust were dependent on first-hand observations. These were outlined in Middleton and Goudie (2001) and include: (1) observation data from meteorological stations; (2) back trajectories and (3) mineral analysis to identify source regions.

The sparse nature of meteorological monitoring stations in the Sahara and sometimes lack of long-term records, mean that the value of such observations is limited (Middleton and Goudie, 2001). Also, with observations of this nature it is often impossible to determine whether dust has been actively deflated near the observer or merely advected from a different source.

A way to combat these problems is to identify the back trajectory of the dusty parcel of air. This can be done by examining numerical weather prediction model (NWP) output to produce back trajectories for different vertical levels (Petzold et al., 2009), or through the application of a 3D trajectory and dispersion models such as the Hybrid Single Particle Integrated Trajectory (HYSPLIT) model (Coz et al., 2009; Escudero et al., 2011).

Trajectory methods allow regions that frequently produce dust to be highlighted over a period of time as a common source of dust transported to observation stations. However, this method is only really applicable to identify a general, large-scale pattern (Middleton and Goudie, 2001). This is because it is difficult to determine how long dust had been suspended for, the lack of representation of moist and dry convection in trajectory models and the poor representation of near surface pressure fields in models. The uncertainty of near surface pressure is associated with a lack of observations to constrain the initialisation data for models. In fact, the representation of the SHL can be very different across products, as shown in Marsham et al. (2011).

Mineral analysis of airborne dust might provide an alternative. It has been shown that the ratio of Illite to Kaolinite can provide a fingerprint of the source region of lifted dust (Formenti et al., 2011). Currently the problem with this method is that it can only still be used for the identification of large regional sources. Improving the accuracy would require knowing a detailed mineralogy of the Saharan substrate. Unfortunately, this is a poorly researched area and the exact chemical profiles for desert soils has not been created (Middleton and Goudie, 2001). Considering the poor understanding of mineralogy the sparsity of dust and meteorological observations it is no surprise that when Herrmann et al. (1999) tried to evaluate previous studies using these methods of identification there was very little agreement between different studies or methods of source region identification.

**Satellite identification**

A major step forward in the identification of mineral dust sources was the use of remote sensing instruments mounted on satellites. A number of different platforms have been used to identify dust sources or study the optical properties of deflated Sahraran dust. Here the most widely used tools are discussed along with findings related to them, these products are: (1) the Total Ozone Mapping Spectrometer (TOMS) (Torres et al., 2002, 1998) and Ozone Monitoring Instrument (OMI) (Torres et al., 2007), (2) the Spinning Enhanced Visible and InfraRed Imager (SEVIRI) instrument mounted on the Meteosat Second Generation (MSG) satellite (Brindley et al., 2012) and (3) the Moderate Resolution Imaging Spectrometer (MODIS) DeepBlue algorithm (Hsu et al., 2004).

TOMS has been used more consistently than any other instrument to try to identify dust deflation sites and to try to study the climatology of Saharan dust (Goudie and Middleton, 2001; Mahowald et al., 2003; Middleton and Goudie, 2001; Schwanghart and Schutt, 2008; Washington et al., 2003). The reason for this is the long time period over which TOMS has been collecting data (1978–2006). TOMS was replaced by OMI from 2006–present. Multi-spectral UltraViolet (UV) observations from both TOMS and OMI allow for the identification of the mean structure of dust emission and transport without problems caused by variable surface reflectivity or a short temporal coverage (Washington et al., 2003). The studies mentioned in connection with TOMS above are all in agreement that the single largest dust source in the Sahara is the Bodélé Depression (Figure 2.13) where dust emission is consistently high for most of the year. This corroborates some surface observations that suggested that the Bodélé region is a major source. However, as well as the Bodélé a large area of Western Africa covering the parts of Mauritania, Mali and Algeria was also highlighted as a major Saharan dust source (Figure 2.13). The nature of this source is not clear due to the large spatial extent and lack of a clear geomorphological feature such as a palaeolake (Figure 2.12).

Despite the successful use of TOMS data to identify dust source regions in the Sahara the TOMS and OMI datasets do have some shortcomings for mineral dust source detection. The use of UV wavelengths of light and the calculation of aerosol densities by absorption by particles compared to molecular scattering by the air means that there is a height bias due to the change in density of air with height. Therefore absorbing aerosols higher in the atmosphere produce a clearer signal, whilst the signal strength from near surface particles is diminished (Torres et al., 2002).

More recent work on dust sources in the Sahara has used different satellite tools, notably the MSG mounted SEVIRI (Schepanski et al., 2007, 2012). A combination of infrared (IR) brightness temperature (BT) and BT differences are used to produce red, blue, green (RGB) dust images, the details of their production are discussed in Section 3.2. The fact that the MSG is a geostationary satellite as opposed to polar orbiting satellite means that the temporal scale on which images can be taken is much higher. SEVIRI images are available every 15 minutes compared to every one or two days for products such as TOMS and MODIS. This, coupled with a wide field of view covering the whole of the Sahara means that SEVIRI has been very useful for identifying dust sources.

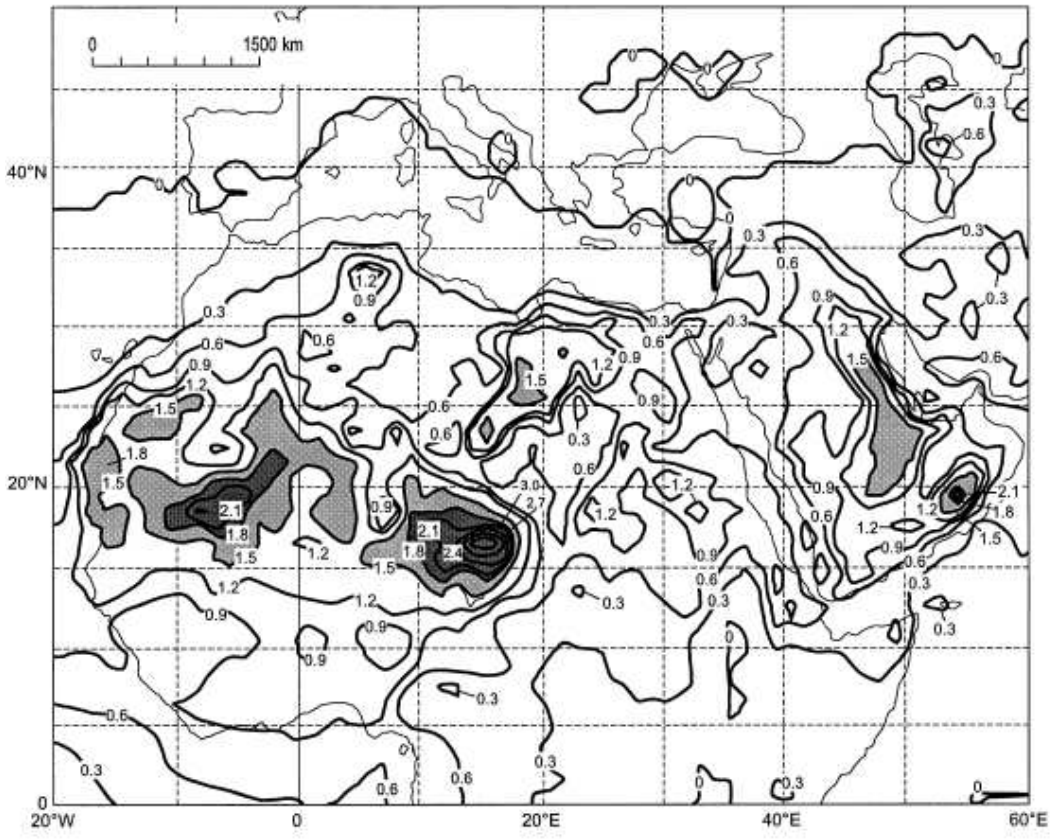


FIGURE 2.13: A map showing the annual mean Total Ozone Mass Spectrometer (TOMS) aerosol index (AI; defined as $-100([\log_{10}(\frac{I_{340nm}}{I_{380nm}})_{meas}] - [\log_{10}(\frac{I_{340nm}}{I_{380nm}})_{calc}])$ where $I$ denotes radiance; Hsu et al., 1999) over the Northern half of the African continent using TOMS data (1980-93, 1997-2000). Note the high AI values over the Bodélé Depression and a less well defined area to the West (Middleton and Goudie, 2001).

Schepanski et al. (2007) used SEVIRI data to produce a dust source map for West Africa and compared it to the aerosol indices from TOMS measurements. The SEVIRI map had more clearly defined areas of emission over the western Saharan source region, making the source area smaller and positioning it further east. This is likely to have been due to the removal of airborne transport of dust from the signal and at least some of the height bias.

MODIS, specifically the use of the Deep Blue algorithm (Hsu et al., 2004), can also be used to detect atmospheric aerosols using multiple near UV channels. The use of near-UV instead of the UV wavelengths used by TOMS and OMI mean that the aerosol height dependence is reduced in MODIS DeepBlue (Hsu et al., 2004). Similar to TOMS and OMI, the MODIS product is limited temporally, this means that only the dust in the atmosphere present at the time of a day-time overpass can be recorded. Ginoux et al. (2012) globally mapped dust source regions using MODIS Deep Blue and showed a similar seasonal shift

of dustiness from close to the Bodélé depression during the winter to over the Sahel and Sahara during the summer as shown in Schepanski et al. (2007) and Washington et al. (2003).

Schepanski et al. (2012) compared OMI, SEVIRI, and MODIS Deep Blue methods for the identification of regions of dust uplift in the Sahara. Their findings include that the different in techniques mean that there is likely to be transport of dust away from source regions causing an offset in source regions in OMI and MODIS Deep Blue. The signal in MODIS Deep Blue also showed high aerosol concentrations over the Sahel associated with biomass burning. The OMI and MODIS Deep Blue methods also failed to account for dust plume longevity. When dust stayed resident in the atmosphere for over a period of days the dust occurrence frequency is strongly influenced without the surface emitting any additional dust. Therefore, despite their utility in the past it is now recognised that sub-daily resolution data is required to improve the identification of Saharan dust sources from satellite.

There have been several attempts to use SEVIRI to produce an aerosol optical depth (AOD) both over the ocean (Bennouna et al., 2009; Thieuleux et al., 2005) and over land (Banks et al., 2013; Brindley and Ignatov, 2006; Carrer et al., 2010; Mei et al., 2013). Recently it has been shown that a SEVIRI dust AOD (Banks et al., 2013) is better able to retrieve dust loadings at optically thick events, while other products (including MODIS Deep Blue) are better at low dust loadings. Banks et al. (2013) also show that the SEVIRI AOD is sensitive to meteorological conditions, overestimating the AOD in moist conditions.

One issue not previously mentioned that is common to all satellite products discussed here, is the fact that clouds (even very thin ones) can block the surface and lower atmosphere. Under these circumstances very little to no information about dust uplift can be gleaned. This suggests that dust uplift mechanisms which are driven by meteorological processes linked to clouds are likely to be under represented compared to mechanisms which can (or preferentially) occur under clear sky conditions.

### 2.5.3 Seasonality

From the use of these satellite tools it has been recognised that the deflation of dust in different areas has a strong seasonality. The Bodélé Depression is a strong source

all year round but produces most dust at the beginning of the year (January–March) (Engelstaedter and Washington, 2007), with a smaller peak in October. This is because the Bodélé source is controlled by a northeasterly low-level jet that is accelerated as it passes between the Ennedi Plateau and the Tibesti Mountains (Figure 2.6). With stronger northeasterly flow during the winter the rate of sediment deflation is increased. In contrast to this, the large West African source becomes most active during the NH summer with peak intensity in June and July (Engelstaedter and Washington, 2007). It is thought that the activation of this region is driven by the production of convectively generated cold pools during the monsoon season. This is supported by Marsham et al. (2008) who show that there is a relationship between the asymmetry of seasonal dust cycle and the downdraught convective potential energy (DCAPE). There is both higher DCAPE and dust uplift during the onset of the monsoon than the retreat. This is in agreement with Engelstaedter and Washington (2007) who show peak intensity occurring before the monsoon flow reaches its northernmost point (Buckle, 2004)

## 2.6 Dust uplift processes

### 2.6.1 Haboobs

Haboobs, as mentioned in section 2.2.3, are a type of dust storm produced by the development of precipitating convective clouds over surfaces from which soil particles can be easily lifted. They take the form of imposing, churning walls of lifted sand and dust that move steadily forward in series of constantly developing lobes and clefts (Miller et al., 2008; Simpson, 1997). The winds produced by convective downdraughts and cold pools are often strong and gusty, and turbulence produced at the gust front of the flow is enough to provide significant levels of dust deflation. Haboobs are often associated with a drop in temperature and a spike in dewpoint temperature due to the fact that they are formed from thunderstorm outflows (Knippertz et al., 2007; Miller et al., 2008). As well as moisture, temperature and wind speed there is also usually an increase in the surface pressure due to enhanced density of the cold pool air.

Haboobs have been documented in the Sahel and Sahara (Emmel et al., 2010; Farquharson, 1937; Flamant et al., 2007; Freeman, 1952; Hamilton et al., 1945; Lawson, 1971; Reinfried

et al., 2009; Solomos et al., 2012; Sutton, 1925), the Arabian Peninsula (Membery, 1985; Miller et al., 2008), the southern USA (Brazel and Nickling, 1986; Chen and Fryrear, 2002; Idso et al., 1972), the Taklimakan and Gobi deserts in China (Mitsuta et al., 1995; Takemi, 1999), and their presence in Australia is mentioned in Strong et al. (2011).

The majority of work conducted on haboobs has focused on observations. These are either case studies or statistical analyses of a number of events at a single site. Such work was conducted by Sutton (1925), Freeman (1952) and Lawson (1971) in Sudan. Sutton (1925) was the first to clearly define the meteorological phenomena that should be described as a haboob and made several important links. Namely, the link between the frequency of haboobs and the season as well as the lack of consistent direction of approach and a connection to thunderstorms. Later work conducted by Freeman (1952) catalogued 82 haboobs taking meteorological measurements of their passage. His observations showed the features discussed earlier, but also highlighted the short-lived nature of these dust storms. On average their passage lasted less than an hour. Findings from Lawson (1971), a study of three haboobs in Khartoum, are similar, noting not only on the wind and temperature changes associated with the passage of the storms but also on the fact that of the three storms studied, two occurred during the night. This is not unusual with many other studies focusing on night time case studies (Knippertz et al., 2007; Knippertz et al., 2009b; Reinfried et al., 2009). This is consistent with Laing et al. (2008) who suggest that convective storms in West Africa most often occur during the afternoon and develop into the evening and night-time.

Although the relative importance of haboobs for dust uplift compared with other phenomena is not well known, recent work suggests that their activity during the WAM season maybe responsible for approximately 50% of deflation (Heinold et al., 2013; Marsham et al., 2008; Marsham et al., 2011; Marsham et al., 2013b). Observations have also shown that African haboobs are responsible for considerable low-level moisture fluxes into the Sahara (Knippertz et al., 2007; Marsham et al., 2013b). The lack of this effect in global models is a major source of bias in modelling the central Saharan heat low (Garcia-Carreras et al., 2013; Marsham et al., 2013b).

The mesoscale nature of the convective storms that are the source of haboobs means that usually they have front lengths on the order of tens to a hundred kilometres. However, in some circumstances they appear to be able to reach much larger sizes, with front lengths

of more than 1000 km and travelling similar distances (Miller et al., 2008). Chapter 4 discusses the occurrence of a long lived and very large haboob which occurred in West Africa in June 2010.

### 2.6.2 Other dust uplift processes

As well as haboobs other dust uplift processes in West Africa are nocturnal low-level jets (NLLJs), dust devils, dry convective plumes and winds associated with strong pressure gradients such as Sharav/Khamsin cyclones.

NLLJs are a feature of regions which have strong surface cooling over night. The often clear skies of the Sahara mean that long-wave radiative cooling of the surface produces a stable layer close to the surface. This stable nocturnal boundary layer (NBL) separates the air above it from surface friction due to the suppression atmospheric eddies. The atmospheric eddy viscosity of the air above the NBL is reduced allowing it to accelerate in response to a pre-existing pressure gradient (Blackadar, 1957). This forms a region of high speed air above the stable NBL. After dawn when the surface is heated, the NBL is eroded by the growth of the well mixed boundary layer and momentum from the NLLJ is transported to the surface. This mechanism produces dust uplift during mid- to late-morning. The mixing of the NLLJ during the morning has been shown to be linked with high winds at the surface and the deflation of mineral dust in the Sahel and Sahara (Bou Karam et al., 2010; Engelstaedter and Washington, 2007 Fiedler et al. 2013b; Knippertz and Todd, 2012; Todd et al., 2008; Washington and Todd, 2005). Dust can also be raised by the intermittent breakdown of the NBL during the night due to shear effects between the NBL and the NLLJ (Ohya et al., 2008).

Dust devils and dry convective plumes are dust uplift mechanisms that are associated with the dry convective circulations within the boundary layer. Dust devils are rotating columns of rising air that are entirely driven by surface heating and not the release of latent heat such as is seen in tornadoes (Balme and Greeley, 2006; Koch and Renno, 2005). In areas where there are loose surface sediments they can raise dust, making the vortex visible. Dry convective plumes, similarly are driven by surface heating, however they do not display the same rotation as dust devils. Dust devils seem to be preferentially generated on hot, flat, dry surfaces (Balme and Greeley, 2006; Koch and Renno, 2005)

where intense insolation causes the heating of the air just above the surface. It is thought that sensible heating of this air generates instability. This air rises as a result, stretching any pre-exisiting vorticity. Rotation of the air column is intensified due to the conservation of angular momentum and the vortex of the dust devil is formed.

North African depressions and cyclones that track across the region are another mechanism for dust uplift. Under these conditions pressure gradients are sufficiently strong to generate near-surface winds which exceed the local dust uplift threshold. It has been shown that depressions are relatively common and are associated with 55% of the dust emission amount annually (Fiedler et al., 2013a). A rarer subset of these events are known as Sharav or Khamsin cyclones, these are long-lived (over two days), occur predominantly during the spring and track across North Africa, often along the coast (Alpert and Ziv, 1989; Fiedler et al., 2013a).

As mentioned earlier the relative importance of all the dust lifting processes is largely undetermined, therefore further research into these processes is required to reduce uncertainty.

## 2.7 Conclusion to literature review

From this literature review we can see that the study of West African climate, meteorology and dust uplift processes are both important and interesting. The author has attempted to explain the important principles in sufficient detail such that the description of work in Chapters 4, 5 and 6 is comprehensible and that conclusions made fit into the framework of previous published work. This chapter should provide a good grounding in the physical and theoretical considerations, however, the practical use of observations and models has not been discussed. Therefore, the following chapter gives more detailed information on how observations are obtained, the methods used in modelling of the atmosphere, how both observations and modelling products have been used as well as the considerations for their use.

# Chapter 3

# Tools

In this section the tools that have been used to investigate the production of convective episodes near the intertropical discontinuity (ITD) are discussed. Simply, these can be broken down into observations and modelling products. Within these groups there are further distinctions. Observations are split into in-situ measurements and remote sensing measurements. Modelling products are split into coarse-grid global products and a high-resolution limited area model (the Weather Research and Forecasting (WRF) model). The methods used to collect or generate data are discussed as well as their utility for this study.

## 3.1 In-situ observations

### Surface observations

The use of the term, in-situ, is meant to convey that measurements are being taken at the same location for which they are valid. The two main types of in-situ data that have been used in this study are surface observations and upper air observations made using weather balloons (radiosondes).

In this study all surface observations have been obtained through the UK Met Office Integrated Data Archive System (MIDAS). The MIDAS record holds global surface observations from 1974–present. As shown in Figure 3.1, large areas of West Africa, particularly in the Sahara, have a very sparse surface observation network. It should also be noted that

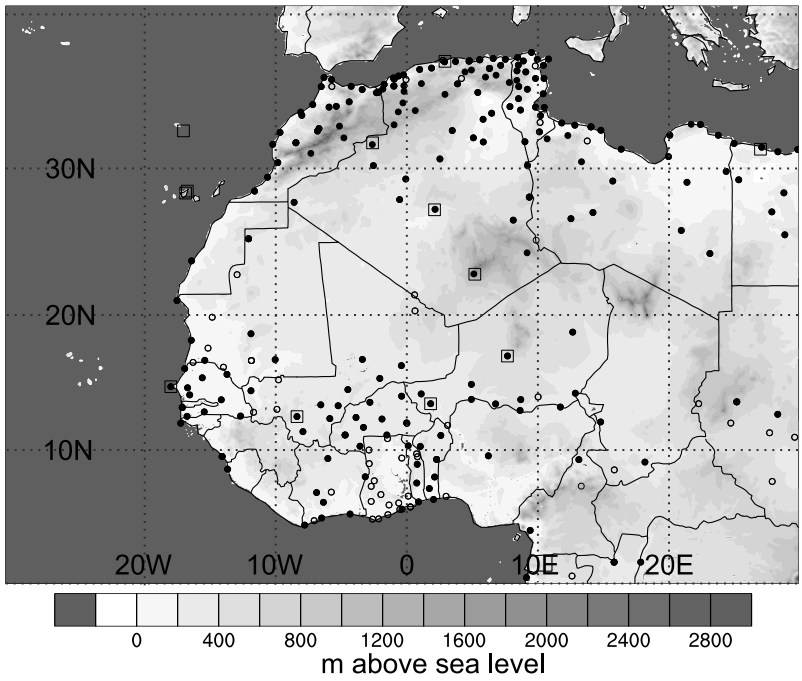


FIGURE 3.1: Geographical overview of West Africa. Also shown are squares which represent radiosonde stations that launched an average exceeding one sonde per day (based on the Integrated Global Radiosonde Archive) April–September, 2000–2010. The circles represent SYNOP stations, unfilled circles reported on at least 25% of the (re)analysis times and filled circles on at least 50% of the (re)analysis times being studied (based on MetOffice Integrated Data Archive System)

stations in this region can have a patchy observation record, having: long gaps where no observations are made, only a subset of the commonly variables recorded, or observations not made at particular times of day (mostly at night) (Cowie et al., 2014). Therefore, in this study the use of surface observations is limited to providing information about surface conditions in Chapter 4 and for additional information about the distribution of low-level water vapour in Chapter 5.

### Upper air observations

In-situ upper-air observations are made by radiosondes. These are instrument packages which measure a vertical profile of balloon location (and therefore winds), temperature, relative humidity and pressure. They are lifted through the atmosphere by weather balloons filled with a buoyant gas (helium or hydrogen) and are generally released close to 0000 and 1200 UTC. Radiosondes usually reach altitudes higher than the tropopause and

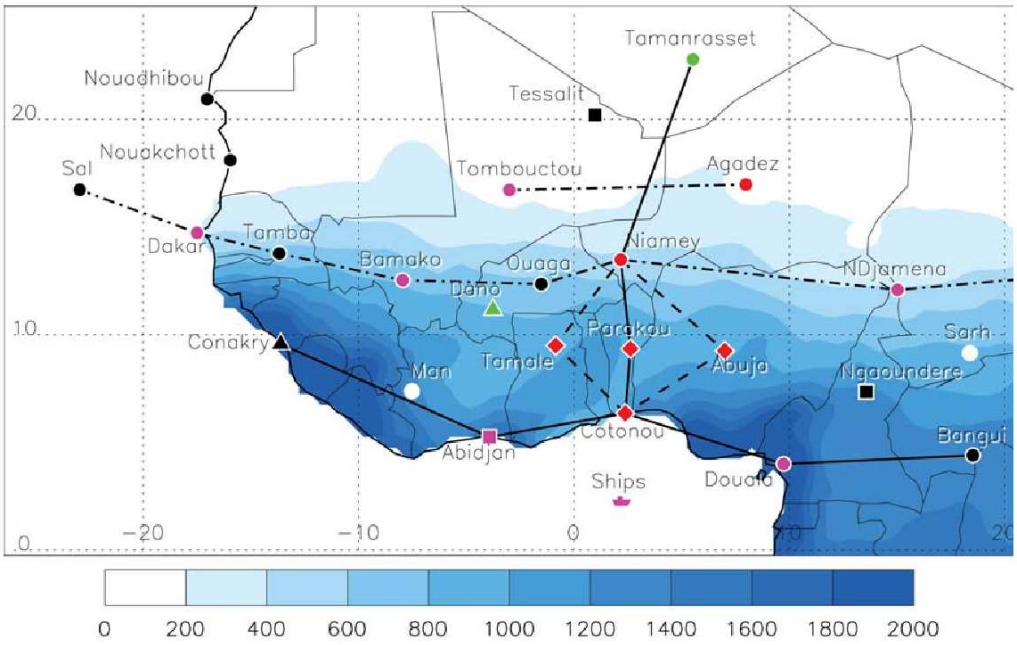


FIGURE 3.2: African monsoon multidisciplinary analysis AMMA radiosonde network from Parker et al. (2008). The station colours denote the frequency that radiosondes were launched during 2006: white represents 1 per day (no communication with the Global Telecommunication System; GTS), black represents 1 per day, magenta represents 2 per day, red represents 4 per day with 8 per day during special observing periods. Tamanrasset and Dano (green) launched 4 per day and a variable number respectively. Shapes denote the status of the stations: circles are established stations, diamonds are new AMMA stations, squares are disused, reactivated stations, and triangles were operationally temporarily during 2006. The blue colour denotes mean annual precipitation 1961–1990 (mm $yr^{-1}$). Lines represent important transects across the monsoon flow.

so supply data throughout the entire vertical extent of the atmosphere in which weather is produced. As they rise, data are transmitted back to the surface.

Upper air observations are also sparse in this part of the world (Figure 3.1). Augmentation of the upper air network in West Africa occurred during 2006 as part of the African Monsoon Multidisciplinary Analysis (AMMA) field campaign. Old, disused stations were reactivated and new stations were set up (Parker et al., 2008) (Figure 3.2).

Radiosonde data are typically plotted on a tephigram or skew-T logP diagram. These diagrams are produced and interpreted in very similar ways. Figure 3.3 shows a skew-T logP diagram produced by the University of Wyoming, Department of Atmospheric Science for a radiosonde ascent from Niamey, Niger at 1200 UTC on 07 June 2010.

In this example the different types of lines have been highlighted using colours to aid description. The black horizontal lines across the diagram represent atmospheric pressure,

these are labelled on the left hand side of the diagram. The grey diagonal lines sloping upward from left to right represent lines of constant temperature (isotherms), these are labelled in black along the bottom of the diagram. Blue lines represent lines of constant water vapour mixing ratio and are labelled in blue at the bottom of the diagram. The two types of green line which slope upward from right to left are both representative of lapse rates that a parcel would encounter as it rises through the atmosphere. The light green lines represent the dry adiabatic lapse rate, i.e. the rate at which a parcel would cool with height if no condensation occurred during its ascent and there was no exchange of heat between the parcel and its surroundings. The dark green lines represent the moist adiabatic lapse rate, the same as the dry adiabatic lapse rate except it includes the influence of latent heating as water is retained in the parcel but condenses to liquid form. Note the fact that below about -40°C the dry and moist adiabatic lapse rates are almost parallel. This is because at this temperature all liquid-water has frozen so there is no additional latent heating due to liquid water to ice phase changes (a small amount is available from deposition of vapour to ice).

The thick black lines represent the measurements taken during the radiosonde ascent. The line to the left gives information about the the moisture profile of the atmosphere whilst the line to the right represents the temperature profile. Simply the closer the two black lines are to one another the higher the relative humidity. When they are very close this indicates the presence of clouds (not shown in this example).

The dashed red lines represents the behaviour of a parcel of air lifted from near the surface through atmosphere without any mixing with the surrounding environmental air. By comparison of this parcel's behaviour with the vertical atmospheric profile, information can be gleaned about the stability of the atmosphere. The red dashed lines are known as a Normand's construction. As the parcel is forced away from the surface it initially cools at the dry adiabatic lapse rate. When the two lines meet this indicates that the parcel has reached its lifting condensation level (LCL) and latent heat starts to be released, from now on the parcel follows the moist adiabatic lapse rate. As mentioned in Chapter 2 latent heating means that often an ascending parcel will cool less rapidly than the environment with height. When the dashed line is to the left of the temperature profile line the parcel is negatively buoyant, when it crosses to the right hand side this represents the parcel's level of free convection (LFC) where it becomes positively buoyant. When

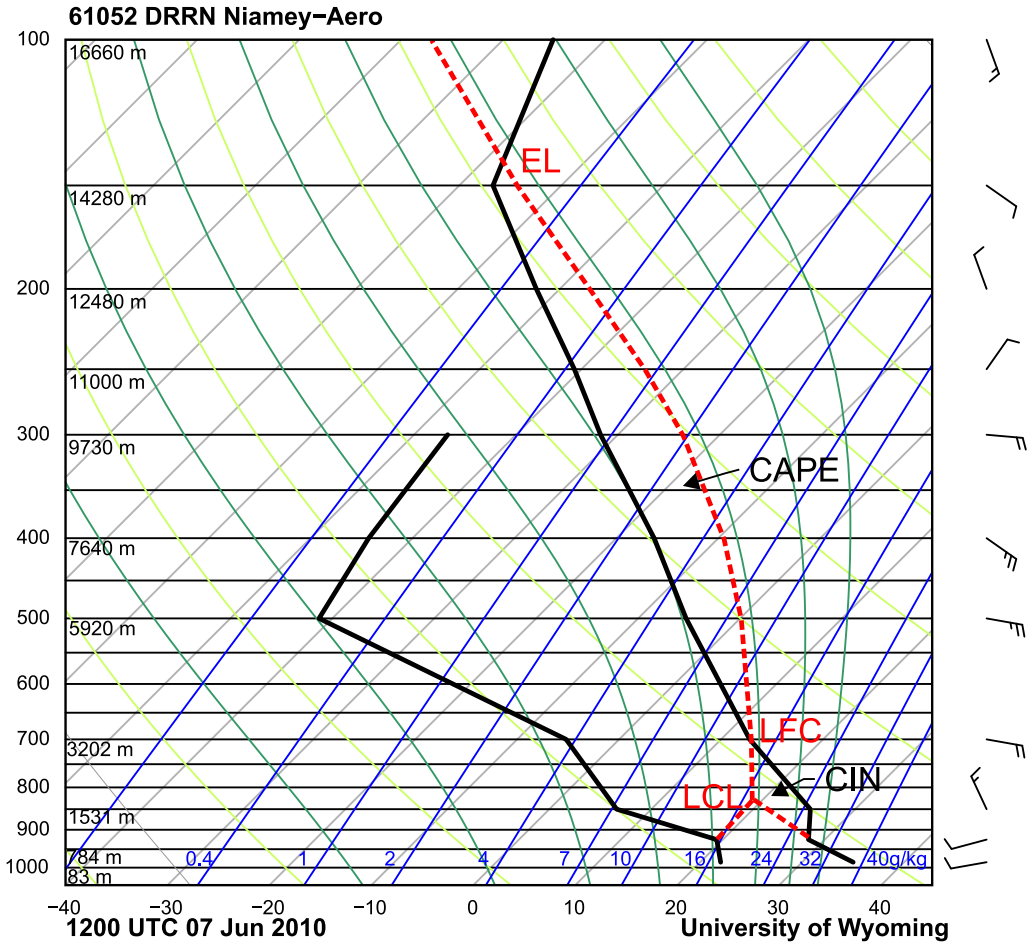


FIGURE 3.3: Skew-T logP diagram of a radiosonde sounding from Niamey in southern Niger made at 1200 UTC 7 June 2010. The horizontal lines on the plot represent lines of constant pressure, decreasing with height, grey diagonal lines represent lines of constant temperature, the numbers along the bottom of the plot relate these temperatures in °C, blue lines represent constant humidity mixing ratio and are labelled in blue at the bottom of the plot, light green lines represent the dry adiabatic lapse rate and dark green lines represent the moist adiabatic lapse rate. The bold black lines represent the atmospheric profile measured from the sonde. The line to the left represents the water vapour mixing ratio and to the right the temperature profile of the atmosphere. The dashed red line indicates the path of a surface parcel lifted through the atmosphere without any external mixing. Wind strength and direction is indicated by the wind barbs to the right.

using a tephigram, the size of the areas encompassed by the temperature profile and the Normand's construction is directly proportional to the convective inhibition (CIN) and convective available potential energy (CAPE). This is not strictly true when using a skew-T LogP diagram (such as Figure 3.3), however, the relative sizes of these regions does give information on the atmospheric stability profile.

Radiosonde data are used in this study for information on the temperature, moisture and wind profile of the atmosphere as well as the strength of CIN and CAPE. The stations used

are In Salah and Tamanrasset in Algeria, Agadez and Niamey in Niger, and Ougadougou in Burkina-Faso.

## 3.2 Remote sensing

The alternative to in-situ measurements is remote sensing. While this does not imply that instrumentation is satellite borne, all of the remote sensing tools used in this study are satellite products. These have been used to retrieve useful meteorological data including the spatial and temporal patterns of precipitation, and regions with lifted dust. The satellite products which have been used are: (1) the EUMETSAT (European organisation for the exploitation of meteorological satellites) Spinning Enhanced Visual and InfraRed Imager (SEVIRI) red-green-blue (RGB) dust imagery, (2) the Tropical Rainfall Measuring Mission (TRMM) 3B42 V7 precipitation product, (3) the North African Sand Storm Survey (NASCube) pseudo colour visual and infrared (IR) imagery and temperature anomaly identification product, (4) the Moderate Resolution Imaging Spectroradiometer (MODIS) Level 1B calibrated and geolocated radiances and (5) the MODIS Deep Blue 550 nm aerosol optical depth (AOD) product.

### SEVIRI

The geostationary Meteosat Second Generation (MSG) mounted SEVIRI instrument has a 15 minute temporal resolution and a field of view covering the whole of Africa. This means that it is an excellent tool for tracking the development of MCSs. To produce the dust images the atmospheric windows most sensitive to the presence of atmospheric dust but least influenced by water vapour, carbon dioxide and ozone are used (channels 7, 9, and 10 which are 8.7, 10.8 and 12.0 $\mu$m respectively). The images are constructed using standard RGB rendering with the different colours being described by combinations of brightness temperature (BT) and BT differences. Red is described by the BT difference between channels 10 and 9, green by the BT difference between 9 and 7 and blue by the channel 9 BT. As described in Brindley et al. (2012) in daytime clear sky conditions the blue channel will tend to reach saturation and the red and green channels will also be high, this produces a light blue to white colour to the daytime surface when no dust is

present. When dust is lifted SEVIRI channel 9 is suppressed faster than channels 7 and 10. All three colour saturation levels are reduced, however, the green channel has a stronger response to changing brightness temperatures due to cold atmospheric dust and so the SEVIRI dust image turns a magenta or pink. The resultant dust images produced provide valuable information on meteorology and lifted dust. An example SEVIRI dust image is shown in Figure 3.4a for the event that is discussed in Chapter 4. Deep convective clouds are shown in red, thick mid-level clouds in orange, thin mid-level clouds in green and thin high level clouds in black. Lifted dust is shown in magenta and when visible the ocean and land surface appear as purple or blue.

Recently, several limitations of the SEVIRI dust product have been identified (Brindley et al., 2012). These include a strong dependence on column water vapour, lower tropospheric lapse rate, and the altitude of lifted dust. Because of these limitations, images cannot be used quantitatively to describe the amount of dust lifted. However, SEVIRI has been particularly useful for this study due to: its high temporal resolution, an ability to distinguish convective clouds from lofted dust and a dependence on water vapour which produces a darker blue daytime surface in clear sky conditions when column water vapour is high. This final effect can prevent lifted dust from being detected, but also gives useful information about the distribution of atmospheric water vapour. Once again, the use of SEVIRI in way is subjective, preventing quantitative values of water vapour retrieval.

### NASCube

The NASCube thermal temperature anomaly product is derived from SEVIRI data. Therefore, it too, has a 15-minute temporal resolution making it useful for MCS and cold pool tracking. It uses two separate algorithms to generate the true colour and pseudo colour day- and night-time images (Figure 3.4b) making use of both visible and IR channels of SEVIRI. A cloud mask is generated using an artificial neural network, and thermal anomalies related to lifted dust are identified from a 10 day cloud free average of the same channels used to generate the SEVIRI dust product. This product helps to show where lifted dust is present and seems to show some regions of dust uplift which are not well represented in the SEVIRI dust image (Figure 3.4).

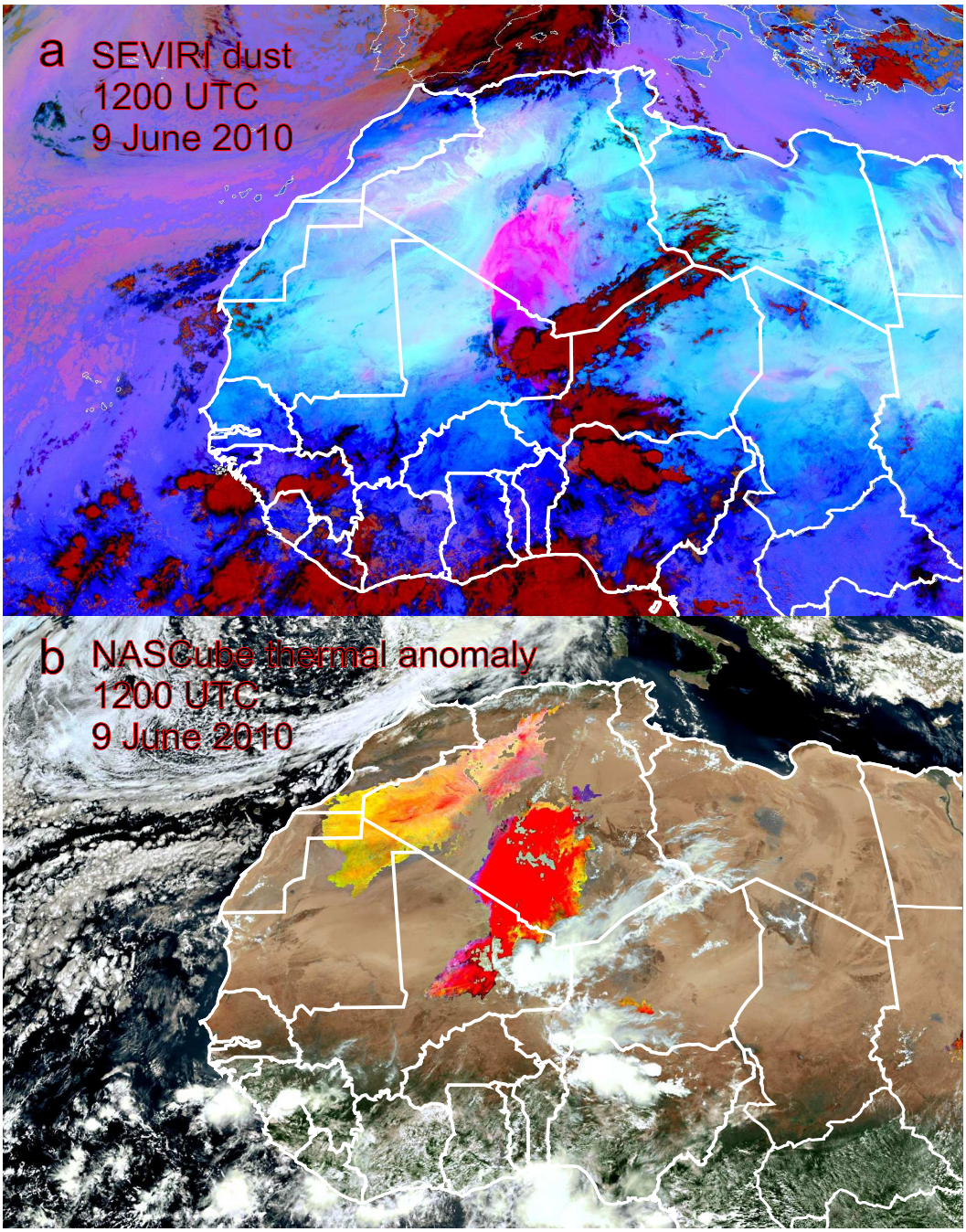


FIGURE 3.4: Examples of Spinning Enhanced InfraRed and Visual Imager (SEVIRI) and the North African Sand Storm Survey (NASCube) images from 09 June 2010 showing the large dust plume associated with the event being studied in Chapter 4. (a) shows a SEVIRI dust image in which the surface is blue, deep convective clouds are red and lifted dust is magenta, (b) shows a daytime NASCube true colour image with thermal anomalies associated with dust uplift overlaid.

However, there are some limitations to the usefulness of the NASCube product. As a relatively new product it has not been thoroughly tested. As yet there is no literature discussing any product biases. Also, there is only a small amount of information from the developers about the production and interpretation of the product. One clear limitation is the fact that it struggles to show the position of lifted dust at dawn and dusk. It is also incapable of detecting dust over the ocean meaning that dust transport out the Africa cannot be gauged.

### TRMM

The TRMM 3B42 V7 product uses a combination of space-borne data to create 3-hourly rainfall estimates at $0.25° \times 0.25°$ resolution (Huffman et al., 2007) (gauge data are used for calibration where available). Firstly TRMM Visible and InfraRed Scanner (VIRS) and TRMM Microwave Imager (TMI) as well as calibration parameters from the monthly TMI/TRMM Combined Instrument (TCI) are used to produce IR calibration parameters. Then, these parameters are used to produce a merged precipitation product from a variety of different satellite sources including radar, microwave sensors and IR radiance data, this includes a merged error.

Due to the fact that some of the satellite retrievals used to generate TRMM are mounted on polar orbiting satellites, the accuracy of the product varies both spatially and temporally. As well as this, the availability of satellite products over longer periods has varied (primarily due the introduction of new satellites), meaning that generally accuracy has increased with time. Included within the TRMM files is a high quality precipitation field, this only includes data from high quality sources and as such there can be large regions without data coverage in this field. This is especially true earlier in the life of TRMM. A typical high quality precipitation coverage from 1998 is 40%, however by 2011 the typical high quality data coverage is 88%. Despite these problems, TRMM rainfall retrievals are deemed to be sufficiently robust to detect the presence of the deep convective clouds which are the focus of this study. In large part, due to the spatial and temporal coverage of IR measurements from geostationary satellite products (such as the MSG SEVIRI). This means that even when there are no high quality data available there is still data available that has a strong correlation between the presence of deep clouds with cold cloud tops and therefore the production of precipitation.

It is also worth pointing out that in such instances there is no information about hydrometeors throughout the depth of the atmosphere. In the Sahara and Sahel where deep dry boundary layers are common there is likely to be a high rate of precipitation evaporation. This means that the quantity of precipitation that reaches the surface might be very different from estimated by TRMM 3B42 V7 product. However, with regards to the production of cold pools this is not a problem as the formation of downdraughts within MCSs is not dependent the on how much precipitation reaches the surface. Therefore in this study TRMM rainfall has been used as a method of identification of regions where precipitation is likely and specific values for surface rainfall are not integral to the analysis.

### MODIS and the Deep Blue algorithm

The MODIS instrument is aboard two NASA polar orbiting satellites (Terra and Aqua). MODIS data provide a number of different channels in both visible and IR wavelengths. MODIS imagery of Level 1B calibrated and geolocated radiances are used to identify cloud and dust features in Chapter 4. However, with maximum of 4 overpasses a day the use of MODIS is limited compared to products with a higher temporal resolution.

The daily MODIS Deep Blue aerosol optical depth (AOD) product is also used to identify periods when dust has been lifted and to establish a link to specific meteorological features. The Deep Blue algorithm is a measure of the radiation extinction due to scattering and absorption by atmospheric aerosols such as dust (Hsu et al., 2004). Deep Blue data is available from 2000 to 2007 from the Terra satellite and from 2002 to present for the Aqua satellite and is useful due to its ability to detect dust over bright surfaces (the MODIS dark target product which is applied over oceans and most other land surfaces is not able to detect dust over deserts). To generate Deep Blue AOD measurements a normalised radiance is calculated using the solar flux and the top of atmosphere radiance, the viewing and solar zeniths and the relative azimuth are also taken into account. From this the path radiance and transmission function are calculated using Lambertian reflectance and the spherical albedo of the atmosphere for illumination from below (Hsu et al., 2004). From these variables lookup tables are produced for different sun and sensor geometries to simulate received radiances from MODIS retrievals. Cloudy pixels are excluded, from the remaining non-cloudy pixels the 412, 490 and 670 nm reflectances are determined based on geolocation. These radiances are compared to those in the lookup tables mentioned above

and the most appropriate AOD and single scattering albedo values are matched to the radiances. This is advantageous compared to SEVIRI due to a more extensive catalogue of long term data and a quantitative measure related to lifted dust. However, the use of a visual (near UV) wavelength of light means that this product is only available for a single daily day-time overpass for each MODIS satellite (within the available years) making it temporally limited.

## 3.3 Global (re)analysis products

Operational analysis and reanalysis products are important modelling tools for studying the meteorology of West Africa. These products (collectively referred to as (re)analyses) aim to provide the best estimate of the state of the atmosphere. (Re)Analysis products are generated by running a short forecast from the previous analysis time and assimilating observations to correct the model's first guess. The advantage of this type of product is that it has complete global coverage at levels throughout the atmosphere corrected by observations in a way that is physically consistent. This global cover and the consistency of reanalyses over long periods, (assimilation systems and dynamical model of reanalysis products stays the same over time) means that they are useful in many different fields of science. Among other uses (re)analyses are used to initialise operational numerical weather prediction (NWP) simulations, drive chemistry transport models (e.g., Chipperfield (2006); Emmons et al. (2010); Huijnen et al. (2010)) and initialise high-resolution limited-area simulations for research (e.g., Knippertz et al., 2009b; Reinfried et al. (2009); Solomos et al. (2012)).

However, over large parts of West Africa there are very few in-situ observations, especially in the Sahel and Sahara (Figure 3.1). Therefore, (re)analysis products are poorly constrained and the paucity of the observational network means that evaluating which products are better able to represent reality is not trivial. In the Sahara, ground and upper air observations are particularly sparse due to both the inhospitable environment and politics of the region, making (re)analyses more reliant on satellite data. However, satellites have difficulties in retrieving near surface water vapour (Urban, 2013).

An example of the influence of upper-air observations on a coarse resolution model in a data poor region can be seen in Garcia-Carreras et al. (2013). Simulations using the operational Met Office Unified Model at 30 km grid-spacing show that the 925 hPa potential temperature around Bordj Badji Mokhtar in Algeria (21.4°N, 0.9°E) is strongly influenced by the assimilation of radiosonde soundings to an approximate diameter of 500 km. This work also highlights the importance of upper air observations over West Africa for robust (re)analyses. AMMA has shown that improvements in the upper air observation network are possible and can in some cases be relatively inexpensive (Parker et al., 2008), but sufficient funds and staff are required. The impact of a greater number of observations in this region is also shown in Augustí Panareda et al., (2010a) and Augustí Panareda et al., (2010b), who show significant improvements to the ECMWF reanalysis linked to the observations made as part of the AMMA campaign The shortage of radiosonde data makes the effective use of satellite data particularly important. One possible avenue for improvement in this way is by the assimilation of clouds into 3D/4D-Var systems. Storto and Tveter (2009) illustrate how a pseudo-observation assimilation scheme using CloudSat data has a clear benefit on a number of different fields in a 3D-Var assimilation scheme. They also suggest that the technique might be extended to be used for other sources of data including satellite-borne IR sensors. More recently Kostka et al. (2014) have presented work aimed at utilising both visible and near-IR data to increase the amount of information that can be assimilated about clouds.

In this study (re)analysis products have been used as a tool for studying the West African meteorology but their representation of the the WAM system has also been investigated (Chapter 5). In general their representation of the large-scale features of the atmosphere, such as upper level jets, is quite similar (particularly in regions with lots of observations; Hodges et al. 2003). The European Centre for Medium-Range Weather Forecasts (ECMWF) ERA-Interim reanalysis product has been used in Chapters 4 and 6. Its use is limited to the investigation of features that are likely to be well represented even in a poorly observed region such as West Africa. The magnitude of changes to particular features is also not integral to the conclusions drawn.

TABLE 3.1: Details of the seven (re)analysis products including: the name used in the text, the centre that produced the (re)analysis, the (re)analysis type, start and end years, and horizontal and vertical resolutions.

| *Name* | *Centre* | *Type* | *Start* | *End* | *Horizontal* | *Vertical* | *Model vintage* |
|---|---|---|---|---|---|---|---|
| NCEP-NCAR | NCEP | reanalysis | 1948 | Present | T62 ∼200 km | 28 levels | 1995 |
| NCEP-DOE | NCEP | reanalysis | 1979 | 2012 | T62 ∼200 km | 28 levels | 2001 |
| CFSR | NCEP | reanalysis | 1979 | 2010 | T382 ∼30 km | 64 levels | 2009 |
| MERRA | NASA | reanalysis | 1979 | Present | 1/2° lat ∼55 km<br>2/3° lon ∼75 km | 72 levels | 2009 |
| ERA-int | ECMWF | reanalysis | 1979 | Present | T255 ∼80 km | 60 levels | 2006 |
| ECMWF-op | ECMWF | operational analysis | NA | NA | Variable | Variable | NA |
| GFS | NCEP | operational analysis | NA | NA | Variable | Variable | NA |

In Chapter 5 the behaviour of the ITD in a collection of (re)analysis products is studied. These products are: (1) the National Center for Environmental Prediction (NCEP) National Center for Atmospheric Research (NCAR) Reanalysis 1 (NCEP-NCAR hereafter; Kalnay et al. 1996; Kistler et al. 2001), (2) the NCEP Department of Energy (DOE) Reanalysis 2 (NCEP-DOE hereafter; Kanamitsu et al. 2002), (3) the NCEP Climate Forecast System Reanalysis (CFSR; Saha et al. 2010), (4) the NASA Modern Era Retrospective-analysis for Research and Applications (MERRA; Rienecker et al. 2008; Rienecker et al. 2011), (5) the European Centre for Medium-Range Weather Forecasts (ECMWF) ERA-Interim reanalysis (ERA-int hereafter; Dee et al. 2011), (6) the ECMWF operational analysis (ECMWF-op hereafter), and (7) the NCEP FNL (final) operational Global Forecast System (GFS) analysis.

Further details of all these products can be found in Table 3.1. As the ECMWF-op and GFS products are operational analyses the models used to create them have been developed over time, changing considerably over the period being investigated in Chapter 5 (2000–2010). Further information on the development of ECMWF-op and GFS can be found at `http://www.ecmwf.int/products/data/technical/model_id/index.html` and
`http://www.emc.ncep.noaa.gov/gmb/STATS/html/model_changes.html`, respectively.

## 3.4 High resolution modelling

High resolution modelling provides another option to study the meteorology of West Africa. The smaller grid spacings used in these models mean that they are able to explicitly resolve some of the important processes that global models are incapable of representing. Convective processes in coarse grid models have to be parametrised. The inevitable simplifications of parametrisations means global products are poor at representing convective storms.

Convection permitting simulations have previously been used to study the triggering and growth of convective cells and the production of cold pools capable of lifting mineral dust both in Africa (Knippertz et al., 2009b; Reinfried et al., 2009; Solomos et al., 2012) and elsewhere (Takemi, 2005).

Recent studies have shown the direct impact of organised convection on the WAM and that global models struggle to capture these effects. As mentioned in Chapter 2, Cuesta et al. (2010), Flamant et al. (2007) and Flamant et al. (2009) show how a cold pool outflows from MCSs can influence the position of the ITD, even forming the leading edge of the monsoon. By comparing simulations with parameterised and explicit convection and observations, Marsham et al. (2013b) show that the representation of convection impacts on the entire WAM and its diurnal cycle. It has also been shown that cold pools contribute a substantial part of the monsoon flow in explicit simulations, but are essentially missing with in simulations using parameterised convection (Marsham et al., 2013b). This is consistent with recent observations from the central Sahara showing that cold pools contribute significantly to meridional water vapour transport and that their absence appears to be a major cause of global model bias (Garcia-Carreras et al., 2013; Marsham et al., 2013b). By studying convective storms (an important process in this region) using high resolution simulations, it is hoped that uncertainties can be reduced, leading to the development of parametrisations in coarse grid models to correct biases.

### 3.4.1 Weather Research and Forecasting (WRF) model

The WRF model is used to simulate a case of a large MCS and its associated cold pool (Chapter 4). The dynamics solver used is the advanced research WRF (ARW) version 3.3.1. The WRF ARW dynamical core is a Eulerian mass solver which calculates fluid motion based on fixed grid points development with time. WRF uses fully compressible, non-hydrostatic equations based on the description of atmospheric modelling in Ooyama (1990) and terrain following vertical co-ordinates. The flux-form Euler equations are based on variables with conservative properties, making many meteorologically useful outputs calculated prognostics.

The nonhydrostatic nature of the WRF ARW means that vertical momentum is treated explicitly rather than vertical motion being a result of perturbations from hydrostatic equilibrium. This allows for better representation of meteorological processes such as thunderstorms and squall lines that deviate from hydrostatic balance. Calculations are made for the partial differential flux equations for each time step, with the simulated atmosphere developing from one time step to another. A comprehensive description of the model architecture can be found in (Skamarock et al., 2008).

The vertical co-ordinate of the WRF model is a terrain following and is based on hydrostatic pressure. A user defined a number of levels are spread linearly between the model top pressure and the hydrostatic pressure at the surface. Variable terrain produces differences in the hydrostatic pressure at the surface therefore the the hydrostatic pressure at which the model levels are positioned also varies horizontally. The levels are closer together near the surface and spread further apart in the upper atmosphere due to the exponential nature of pressure change with height. Due the use of a single reference pressure for the top of the model (often 5 hPa) the model levels become smoother with height, only following the terrain near the surface.

The Eulerian method means that there are limitations on the time step that can be used. This is because the simulation must conform to the Courant-Friedrichs-Lewy (CFL) condition (Jacobson, 2005). This states that the time step used must be small enough for physical processes to progress through the spatial discretisation, i.e. if the user defined time step is too large, a feature propagating through the atmosphere will go beyond the adjoining grid point. This leads to numerical instabilities and can cause the model to crash. A rule of thumb advised by WRF developers is that the upper limit for time step choice in seconds is six times the horizontal resolution in kilometres. Therefore for a horizontal resolution of 3.33 km (used for the inner domain in Chapter 4) a time step of 20 s is recommended. Empirically for the simulation in Chapter 4, it was found that a 10 s time step was required to prevent numerical instabilities. It is thought that the high vertical velocities associated with updraughts and downdraughts meant that the vertical resolution was the limiting factor rather than the horizontal grid spacing.

The spatial discretisation of the WRF ARW is organised as an Arakawa C-grid. The structure of this can be seen in Figures 3.5a and 3.5b. The horizontal and vertical velocities are located on the edge of the grid cells and the other variables (pressure, mass, thermodynamic and scalar variables) are located in the grid centre. The vertical grid structure used in WRF is that of Lorenz grid (Arakawa and Konor, 1996), this is one of the two major methods of vertical grid staggering currently used, the other being the the Charney-Phillips grid. The Lorenz grid differs from the Charney-Phillips grid as it carries horizontal velocities at the same model levels as potential temperature whilst vertical fluxes are carried at the interface of the model levels (Arakawa and Konor, 1996). This has been shown to have the potential to introduce a computational mode which might reduce

accuracy (Arakawa and Konor, 1996). Despite this, it is still not universally accepted that the Charney-Phillips grid is superior for numerical weather prediction with different centres opting for different vertical staggering methods (UK MetOffice - Charney-Phillips, ECMWF - Lorenz)

Nesting of grids allows high resolution simulations to be performed within a number of coarser WRF grids simultaneously. All simulations in Chapter 4 have been conducted using two-way nested grids with a three to one grid size ratio for the internal to parent domain. Two-way nesting allows the internal domains to feed back onto the larger coarse grid parent domains. A visualisation of a nested grid can be seen in Figure 3.5c.

Runge Kutta time integration is used in the WRF ARW as it provides greater numerical stability. Instead of a single step forward in time (for each specified time step), trial steps of a third of a time step and a half of a time step are made. This is a third-order Runge Kutta method, however, it is only third order accurate for linear equations and second order accurate for non-linear equations (Skamarock et al., 2008). Once a full time step is complete the prognostic variables are calculated from the conservative variables that are used for calculations. Microphysics calculations occur outside of the Runge Kutta time integration loop (Skamarock et al., 2008). The WRF ARW allows for selection of between $2^{nd}$ and $6^{th}$ order horizontal and vertical advection schemes using a positive definite technique (negative masses are not permitted). In this study the advised advection schemes are used (Wang et al., 2011) with horizontal advection being treated with a $5^{th}$ order scheme and vertical advection being treated ith a $3^{rd}$ order scheme.

The WRF ARW system can be split into several components. The dynamical solver described above combined with a number of individual physics schemes including: microphysics, cumulus parametrisations, surface layer physics, land-surface model and planetary boundary-layer model.

To initialise WRF, data must first be unpacked and re-interpolated using the WRF preprocessing system (WPS) and vertical interpolation performed. The WPS consists of: (1) *geogrid* which describes the grid being used, including the map projection, surface data and grid positioning and spacing, (2) *ungrib* which decodes meteorological data (usually in gridded binary format; GRIB) into the binary format used by WRF and (3) *metgid* which horizontally interpolates meteorological data onto the grid described by *geogrid*.

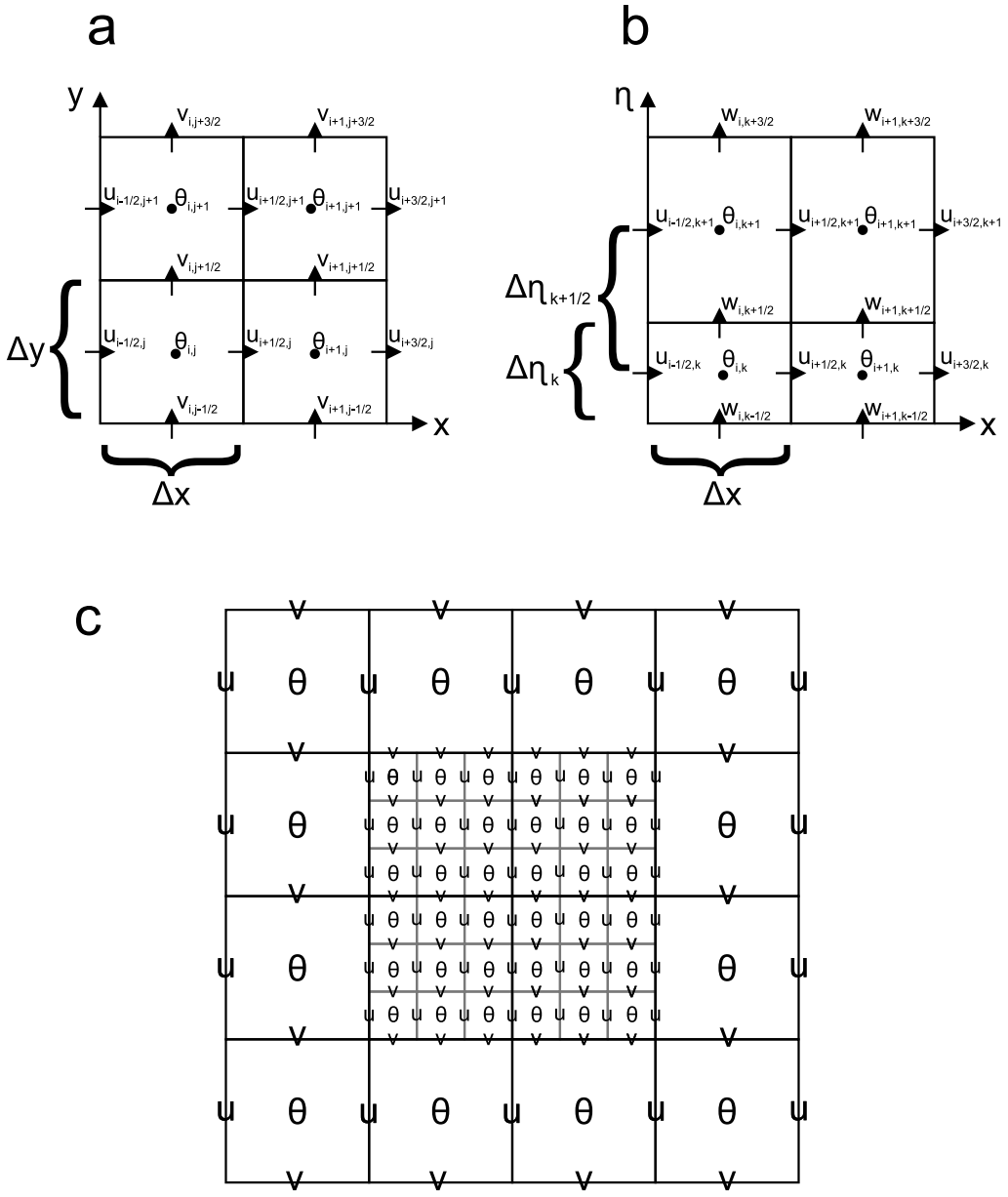


FIGURE 3.5: Schematics showing the spatial discretisation and nesting method used in the Weather Research and Forecasting (WRF), advanced research WRF (ARW) model (redrawn from Skamarock et al. (2008)). (a) shows the horizontal Arakawa C-Grid structure with horizontal winds being positioned on the grid cell boundaries, mass, thermodynamic and scalar variables are located in the centre of the grid cell ($\theta$). (b) shows the vertical Arakawa C-Grid structure, similar to (a) but showing x and w winds instead of x and y, note that the vertical co-ordinate ($\eta$) is based on hydrostatic pressure and so vertical grid spacing is variable. WRF employs a Lorenz method of vertical discretisation whereby the pressure and calculated prognostic variables are stored on the vertical mass points (Arakawa and Konor, 1996; Skamarock et al., 2008). (c) shows a 3:1 grid ratio nest structure, the larger grid cells represent the parent domain in which a smaller higher resolution domain is embedded

Output from the WPS is then vertically interpolated by the program *real*, giving the initial conditions and lateral boundary conditions used by the WRF system. Within the external domain and each nested grid there is a "relaxation zone" of 5 grid cells which are dominated by the lateral boundary conditions (Wang et al., 2011). Therefore, the WRF output shown in Chapter 4, is shown without these regions.

The details of the WRF setup used are described in Chapter 4, including: domain and nest positions, grid spacing, vertical resolution, time step choice, and physics schemes.

# Chapter 4

# Case Study of a Large Summertime Saharan Dust Plume

## 4.1 Introduction to case study

As discussed in Chapter 2 haboobs are dust storms produced by the spreading of evaporatively cooled air from thunderstorms over dusty surfaces and are a major dust uplift process in the Sahara. In this Chapter observations, reanalysis, and a high resolution simulation using the Weather Research and Forecasting (WRF) model are used to analyse the multi-scale dynamics which produced a long-lived Saharan mesoscale convective system (MCS) and an unusually large haboob in June 2010.

The mesoscale nature of convective storms mean that generally haboobs are limited in their extent. However, in some circumstances, including this case, they appear to be able to reach much larger sizes, traversing large areas of desert and producing very large dust plumes. The case being studied occurred between 08-10 June 2010 and was initiated over the Hoggar and Aïr Mountains in southern Algeria and northern Niger, respectively. The dust plume covered parts of Algeria, Mali and Mauritania and was later deformed by the background flow and transported over the Mediterranean Sea (Figure 4.1).

This Chapter: (1) identifies the meteorological processes responsible for the production of the MCS, (2) tests whether the Weather Research and Forecasting (WRF) model is capable of simulating the case despite the data sparse nature of the region, and, (3) examines the

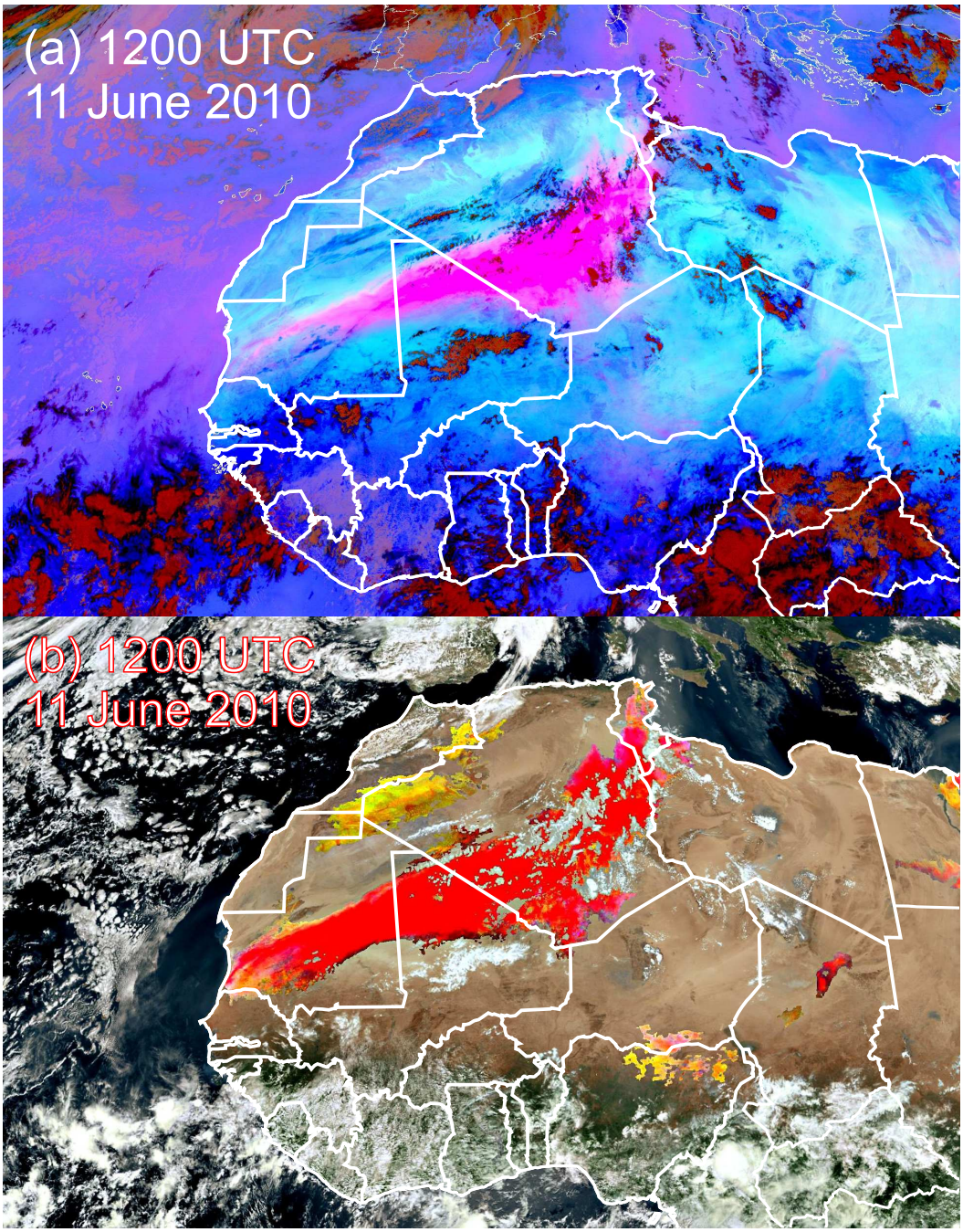


FIGURE 4.1: Deformation of dust plume at 1200 UTC 11 June 2010 in Spinning Enhanced Visual and InfraRed Imager (SEVIRI) dust and North African Sand Storm Survey (NASCube) image. The plume has been stretched both north and west with dust transported over the Atlantic and the Mediterranean.

mesoscale dynamics to identify the processes important for dust deflation. To the best of the author's knowledge there have been no published modelling studies that have looked into the production of haboobs in the central Sahara and none that focus on the generation of very large haboobs apart from Roberts and Knippertz (2014), on which this chapter is

based.

Section 4.2 of this chapter describes the WRF model setup including some preliminary findings which are subsequently developed in Chapter 5. Section 4.3 focuses on results from observational and reanalysis data, section 4.4 compares these findings with the WRF simulation of the case, and section 4.5 identifies potential dust uplift mechanisms from the simulation. Section 4.6 contains a summary of the findings and outlines the conclusions from this chapter.

## 4.2 WRF model setup

The WRF dynamics solver used is the advanced research WRF (ARW) version 3.3.1. incorporating: fully compressible non-hydrostatic equations, terrain following vertical co-ordinates, Arakawa C-grid, $3^{rd}$ to $2^{nd}$ order Runge-Kutta time integration, and both one and two way nesting options.

Despite this being the first time that a very large Saharan haboob has been modelled recent studies have simulated haboobs using high resolution models. Takemi (2005) used a 3-D non-hydrostatic cloud resolving model and initialised an idealised simulation using observations from an event in the Chinese Gobi desert. This model included a dust scheme meaning that information about both dust uplift and transport could be gleaned. Knippertz et al. (2009a), Reinfried et al. (2009), and Solomos et al. (2012) all modelled the production of cold pools in the northwestern Sahara close to the Atlas Mountains. Both Takemi (2005) and Solomos et al. (2012) conclude that haboobs are an efficient mechanism for lifting dust and that they have the capability to transport dust away from the surface and into the air above the cold pool. Reinfried et al. (2009) found that cold pool production was strongly dependent on convective parameterisations with the most realistic simulations explicitly resolving convective processes. Knippertz et al. (2009a) found that microphysics had a moderate impact on cold pool evolution but that the length scale for turbulent vertical mixing had a stronger influence.

More recently Heinold et al. (2013) and Marsham et al. (2013b) have discussed the role of deep convection for both dust uplift processes and within the broader West African

Monsoon (WAM). Both were conducted within the framework of the high resolution simulations of the *Cascade* project. These are UK MetOffice Unified Model simulations over West Africa over a 40 day period during the 2006 monsoon season, the external domain was run at 40 km grid spacing, there were two 12 km intermediate domains (one with parameterised convection, one with explicit convection) and a 4 km internal domain with explicit convection. The use of these simulations is the ability to compare between different grid spacings, and see the impact of convective parameterisations on grids of equal spacing. As the simulations cover a large time period there is also enough data for statistics to be produced based on a number of convection events. One of the findings from Heinold et al. (2013) is that parameterised convection reduced the occurrence of cold pools and therefore substantiates the findings of Reinfried et al. (2009). Marsham et al. (2013b) found that the representation of convection has a strong impact on the behaviour of the WAM. The 12 km grid spaced simulations (both convection permitting and parameterised) were compared. The simulation with explicit convection produced greater latent and radiative heating further north with greater latent heating later in the day. This has the impact of weakening the pressure gradient between the Sahel and Sahara, changing the behaviour of the monsoon, boundary layer convection and the diurnal cycle.

With these results in mind, it was decided that to simulate a cold pool capable of generating such strong surface winds, a grid spacing that allows for the explicit representation of convection should be used. A three-tiered, two-way nested structure was created. The external domain has a grid spacing of 30 km, the intermediate domain has 10 km grid spacing and the internal domain a 3.33 km grid (Figure 4.2). The external domain covers a large part of the African continent, the intermediate domain covers most of West Africa and the internal domain covers the mountainous regions over which the convective cells are triggered and the region into which the MCS travels. All domains have 50 vertical levels, with a higher concentration of levels in the lower atmosphere. The simulation is initialised at 0000 UTC on 07 June 2010 giving adequate spin up time before the initiation of small convective cells during the afternoon of 07 June 2010.

The two outer domains rely on the Kain-Fritsch cumulus parameterisation scheme, whilst the high resolution inner domain simulates convection explicitly. This allows for better representation of convection in the inner domain and the formation of mesoscale structures such as cold pools (Reinfried et al., 2009). The microphysics scheme used is the updated

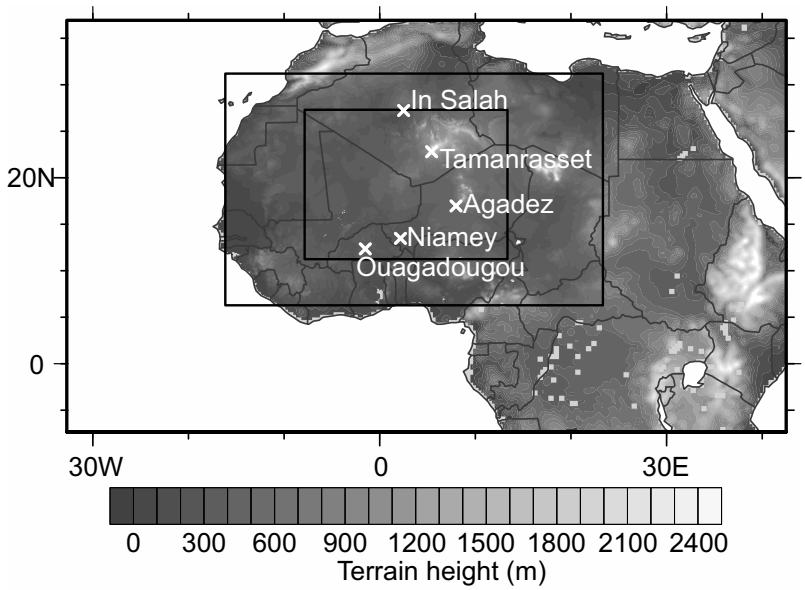


FIGURE 4.2: Weather Research and Forecasting (WRF) model domains used for the simulation of the MCS and associated cold pool. The outer domain is at 30 km grid spacing, the intermediate domain at 10 km grid spacing and the internal domain at 3.33 km grid spacing. Radiosonde stations used in this chapter and terrain height are also shown.

Thompson scheme containing six hydrometeor classes (Thompson et al., 2008). These are (1) water vapour, (2) cloud water , (3) cloud ice, (4) rain, (5) snow and (6) graupel, there are also number concentrations for cloud ice and rain.

Initially an attempt was made to initiate the simulation using Global Forecast System (GFS) analysis data. This is one of the standard input datasets for WRF simulations (Wang et al., 2011) and is chosen due to its ease of use with the WRF-ARW. However, from analysis of the output from this simulation it is clear that a convective storm of a similar scale to the observed MCS is not present. In fact only very small convective cells were initiated, and very quickly dissipated.

It was decided that different initialisation data should be used to see if there was a significant difference in outcome. The first alternative is the European Centre for Medium-Range Weather Forecasts (ECMWF) ERA-Interim reanalysis (ERA-Int) data. This is at $1° \times 1°$ resolution and has global coverage from 1979 to present. The simulation using ERA-int data also shows convective cells on a much smaller scale than that observed and does not produce the large MCS and the associated cold pool being studied. Following this, ECMWF operational analysis (ECMWF-op) data at $0.5° \times 0.5°$ resolution is used to

initialise the simulation. During this simulation a MCS similar to that seen in observations is produced, therefore, it was decided that the case study should be initialised using ECMWF-op data. The fact that using different initialisation data produces such different outcomes suggests significant differences between the analysis and reanalysis products mentioned above. In this case the distribution of low-level water vapour seems to be an important factor limiting the production of convective cells. This does not represent a problem with the WRF model as a tool, as different conditions in the real atmosphere would also be likely to produce very different conditions over time due to the chaotic development of weather systems with time. Similar behaviour relating to differences in initial conditions can be seen in Birch et al. (2013) and Schepanski et al. (2014). The differences between operational analyses and reanalyses are explored in detail in Chapter 5.

Using ECMWF-op data for initialisation, a number of sensitivity simulations are run with different combinations of planetary boundary layer (PBL) scheme, land surface scheme, and surface layer scheme. The PBL and surface layer schemes in WRF are linked and so only certain combinations can be used. The PBL and surface layers schemes used are: (1) the Yonsei University (YSU) PBL scheme which uses a counter gradient flux for heat and moisture in unstable conditions, enhanced vertical flux coefficients in the PBL and a PBL top defined by a Richardson number of zero. With the YSU PBL scheme the fifth generation Pennsylvania State University - National Center for Atmospheric Research (NCAR) mesoscale model (MM5) similarity surface layer scheme is used which uses stability functions to determine surface fluxes of momentum, heat and moisture (Wang et al., 2011). (2) the Mellor-Yamada-Janic (MYJ) PBL scheme, based on the Mellor-Yamada Level 2.5 turbulence disclosure model (Mellor and Yamada, 1982). An upper limit is imposed on the length scales used which depends on the turbulent kinetic energy (TKE), buoyancy and shear. With the MYJ PBL scheme the Eta surface layer scheme is used which uses a viscous sub layer to determine surface fluxes (Wang et al., 2011).

The two land surface models used are: (1) the 5-layer thermal diffusion scheme based on the the MM5 soil temperature model. It has a fixed deep soil temperature as well as four 16 cm thick soil layers Moisture content is not considered and latent heat fluxes are calculated based on land use, season and soil temperature. There are also no explicit vegetation effects (Wang et al., 2011), (2) the Noah land surface model developed by the National Center

TABLE 4.1: Details of the four combinations of Weather Research and Forecasting (WRF) model planetery boundary layer (PBL), surface layer and land surface schemes used for basic sensitivity study.

| *Simulation number* | *PBL scheme* | *Surface layer scheme* | *Land surface model* |
|---|---|---|---|
| 1 | YSU | MM5 surface similarity | 5-layer thermal diffusion |
| 2 | YSU | MM5 surface similarity | 4-layer Noah |
| 3 | MYJ | Eta surface similarity | 5-layer thermal diffusion |
| 4 | MYJ | Eta surface similarity | 4-layer Noah |

for Environmental Prediction (NCEP) and NCAR. It is much more sophisticated than the 5-layer thermal diffusion scheme as it has 4 soil levels and a considers both moisture and vegetative effects.

A total of four simulations are run with the combinations of PBL, surface layer and land surface schemes discussed above. It should be noted that the these simulations are numbered from one to four (Table 4.1) and are referred to by their number.

For the first 24 hours of the simulations there is relatively little difference between them, however, beyond this time they begin to diverge into two groups. This appears to be linked to the choice of land surface model. From the simulations it is clear that the land surface scheme has a strong influence on the triggering and development of convective events, whilst the combined choice of PBL and surface layer scheme has a relatively small impact. Simulations 2 and 4 produce organised deep convective clouds faster and more readily than simulations 1 and 3 which use the five-layer thermal diffusion scheme. This means that the initiation time for the MCS in simulations 2 and 4 is closer to that observed in satellite imagery. However, the subsequent behaviour of the MCS is much more closely matched by the simulations using the simpler 5-layer thermal diffusion scheme.

As mentioned above the different combined PBL and surface land surface schemes only slightly influenced the behaviour of the convective systems in the simulation. However, between 64 and 65 hours into its run, simulation 3 becomes numerically unstable and crashes. This is possibly caused by an exceedance of the Courant-Friedrichs-Lewy (CFL) condition. Because of this it was decided that the 5-layer thermal diffusion land surface scheme combined with the YSU PBL scheme and the MM5 surface layer scheme, would be used for further analysis of the case.

Other physics options used include the rapid radiative transfer model for long-wave radiation and the Goddard two-stream multi-band scheme for short-wave radiation. These settings closely resemble those used by the NCAR for hurricane forecasting (Wang et al., 2011), suggesting their applicability to mesoscale convectively driven systems. This WRF simulation does not contain dust and so conclusions about dust uplift are drawn from identifying meteorological processes capable of lifting dust from the surface, this is similar to the approach used by Burton et al. (2013) and Marsham et al. (2011).

It is noteworthy that the largest impact on the simulations discussed here is produced by varying the initialisation data rather than changes to the model physics. This represents a significant problem for the high-resolution, limited area modelling community in data sparse regions. It confirms that there can be significant differences between products, which are ostensibly providing the best estimate of the atmosphere from the same (or very similar) observational data (Birch et al., 2013; Marsham et al., 2011). The differences between the distribution of low-level moisture over West Africa in a number of operational analysis and reanalysis products are investigated in Chapter 5 and show significant differences between products at the time of initialisation of WRF. As low-level moisture is such an important prerequisite for the development of MCSs, variations in its distribution are likely to lead to large impacts when performing high resolution limited areas modelling studies in this region. It also highlights that as moisture is a potential limiting factor in the development of strong convective systems (which can have a chaotic effect on deterministic forecasts) it is very important to try to have the best input water vapour fields available for simulation initialisation.

## 4.3 Observational re-analysis

### 4.3.1 Synoptic-scale meteorology prior to MCS initiation

Figure 4.3 shows the evolution of the synoptic-scale meteorology prior to the formation of the MCS being studied. It includes 200 hPa geopotential and wind speed, mean sea level pressure and the position of the inter-tropical discontinuity (ITD; 14° dewpoint temperature) from ERA-int. Also shown is the accumulated Tropical Rainfall Measuring Mission (TRMM) 3B42 V7 rainfall estimate for the 24 hours proceeding the time indicated on

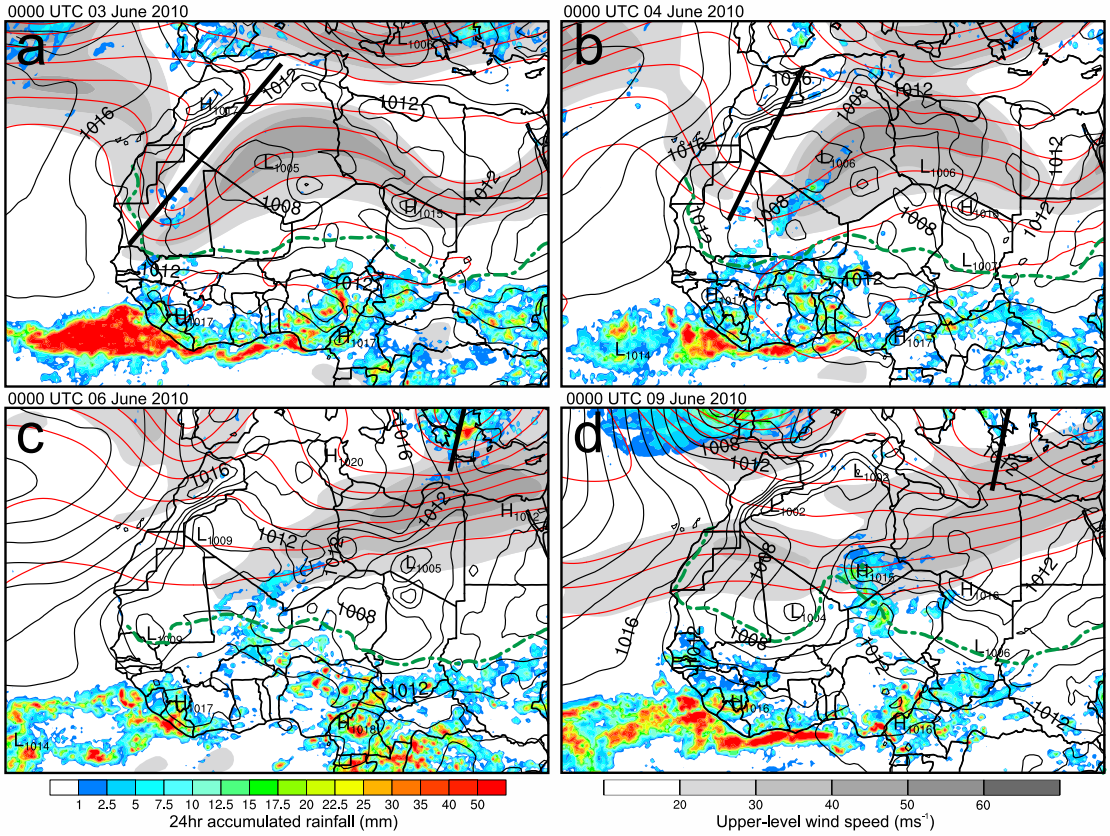


FIGURE 4.3: Synoptic-scale evolution before the initiation of the haboob producing MCS. Shown is the ERA Interim (ERA-int) reanalysis 200 hPa geopotential (red lines), 200 hPa wind speed (grey shading), mean sea level pressure in hPa (black isobars), 14 °C 2 m dewpoint temperature over land showing the ITD (dashed green line) and the estimated 24 hr accumulated rainfall from Tropical Rainfall Measuring Mission (TRMM) 3B42 V7 (colour shading) at (a) 0000 UTC 03 June, (b) 0000 UTC 04 June, (c) 0000 UTC 06, and (d) 0000 UTC 09 June 2010. The thick black lines highlight the axes of troughs discussed in the text.

each panel. On 03 June 2010, a week before the formation of the dust plume shown in Figure 4.1, a deep upper-level trough is present with a southwest-northeast orientation from Senegal to northern Algeria. The position of this trough is marked on Figure 4.3a. At this time the Saharan heat low (SHL) can be seen as a 1005 hPa minimum in mean sea-level pressure positioned over central Algeria. The ITD is predominantly zonal and is close to its climatological position. Another important feature is the presence of light TRMM precipitation over the southern part of the trough in the proceeding 24 hours (Figure 4.3a).

The wave on the subtropical jet propagates east and by 04 June the southerly limb begins to weaken, producing a southwesterly subtropical jet streak over Mali and Algeria (Figure 4.3b). The SHL and ITD position remain largely unchanged at this time but rainfall is

produced over a more widespread area with TRMM 3B42 V7 precipitation estimates over 2.5 mm over Mauritania, Mali, and Algeria. This rainfall is coincident with the southern part of the jet streak and the synoptic-scale dynamics are similar to that of a tropical plume (Fröhlich et al., 2013; Knippertz and Martin, 2005). This suggests that near surface or mid-level tropical air is advected north due to low-level convergence associated with the upper level flow. The additional moisture in the lower and mid atmosphere then allows for the formation of precipitating clouds.

By 06 June (Figure 4.3c) the upper level trough starts to decay and the jet straightens becoming westerly. This change to the upper-level atmospheric structure seems to weaken the tropical plume. Despite this, the cloudy/rainy conditions persist for four days from 04 to 07 June 2010. It is hypothesised that the strong modification of the SHL, which is split into two distinct regions (isobars on Figure 4.3c) is caused by the combination of reduced surface short-wave radiation (cloud shading) and the production of a meso-high associated with evaporating precipitation. Between 03 and 06 June (6 to 3 days before cold pool production) the ERA-int ITD position remains largely zonal with only slight northward movement. Another important feature at this time is the development of a second trough over the eastern Mediterranean (marked on the top right of Figure 4.3c). The straightening of the subtropical jet and the positioning of this trough produces conditions similar to those examined by Vizy and Cook (2009). Under this regime it was found that high surface pressure often develops over Libya and produces a Mediterranean cold air surge into the Sahara. The ERA-int mean sea-level pressure develops a high which builds over the Mediterranean Sea and Tunisia and is later positioned over eastern Algeria and Libya (Figure 4.3d).

Figure 4.3d shows the synoptic situation approximately 12 hours after the initiation of the MCS. At this time the trough over the eastern Mediterranean is still present and the sub-tropical jet is largely westerly. The decay of the tropical plume after 06 June is followed by a re-establishment of the SHL over central Mali. This can bee seen in Figure 4.3d with a minimum sea-level pressure of 1004 hPa. The position of the ITD in Figure 4.3d highlights the northward flow of low-level moist air from the tropics into southern Algeria and northern Niger. Convective triggers in the form of the Hoggar and Aïr Mountain ranges are also present, and the rainfall from the early stages of the MCS can be seen in the TRMM rainfall estimate in Figure 4.3d.

### 4.3.2 Mesoscale processes

#### Early Convective Events

On 07 June a number of smaller convective systems were triggered and collapsed one day prior to the initiation of the haboob-producing system. These developed into storms which produced strong downdraughts and cold pools during the night of 07 and early morning of 08 June (Figure 4.4a). Rope clouds forming along the leading edges indicate that they spread north and west, crossing the Niger-Algeria and Niger-Mali borders (Figure 4.4a). This, combined with the northward bulge in the ITD (Figure 4.3d) is likely to have further advected moist air toward the Hoggar and Aïr Mountain ranges, encouraging convective activity on 08 June.

#### Initiation and Development of MCS

On 08 June the first convective cells are initiated at approximately 1200 UTC in the vicinity of the Aïr Mountains and over the Algeria-Niger border. These cells grow and by 1500 UTC more cells start to develop over the southwestern edge of the Hoggar Mountains in what remains of the tropical plume cloud streak. This creates a line of convection with a northwest-southeast orientation (Figure 4.4b). Simultaneously a number of smaller cells initiate southwest of the main axis of systems over the Adrar des Iforas, on the Malian side of the Mali-Algeria border (Figure 4.4b). The northern cells (N in Figure 4.4b) appear to move northwest with little or no cloud formation along the western edge of the cold pool (marked with a dashed line in Figure 4.4c). In contrast, the southern cells (S in Figure 4.4b) produce a more well developed cloud shield and the resultant cold pool has a strong rope cloud and cumulonimbus cells are triggered along its leading edge. This indicates strong updraughts at the leading edge of the cold pool and higher moisture levels in the surrounding environment. If conditions are preferable, updraughts along the leading edge of a cold pool can trigger further convective storms. In this case, new convective cells are triggered intermittently along the southern edge of the cold pool from S. Convective triggering along the cold pool edge of N appears to require a stronger forcing.

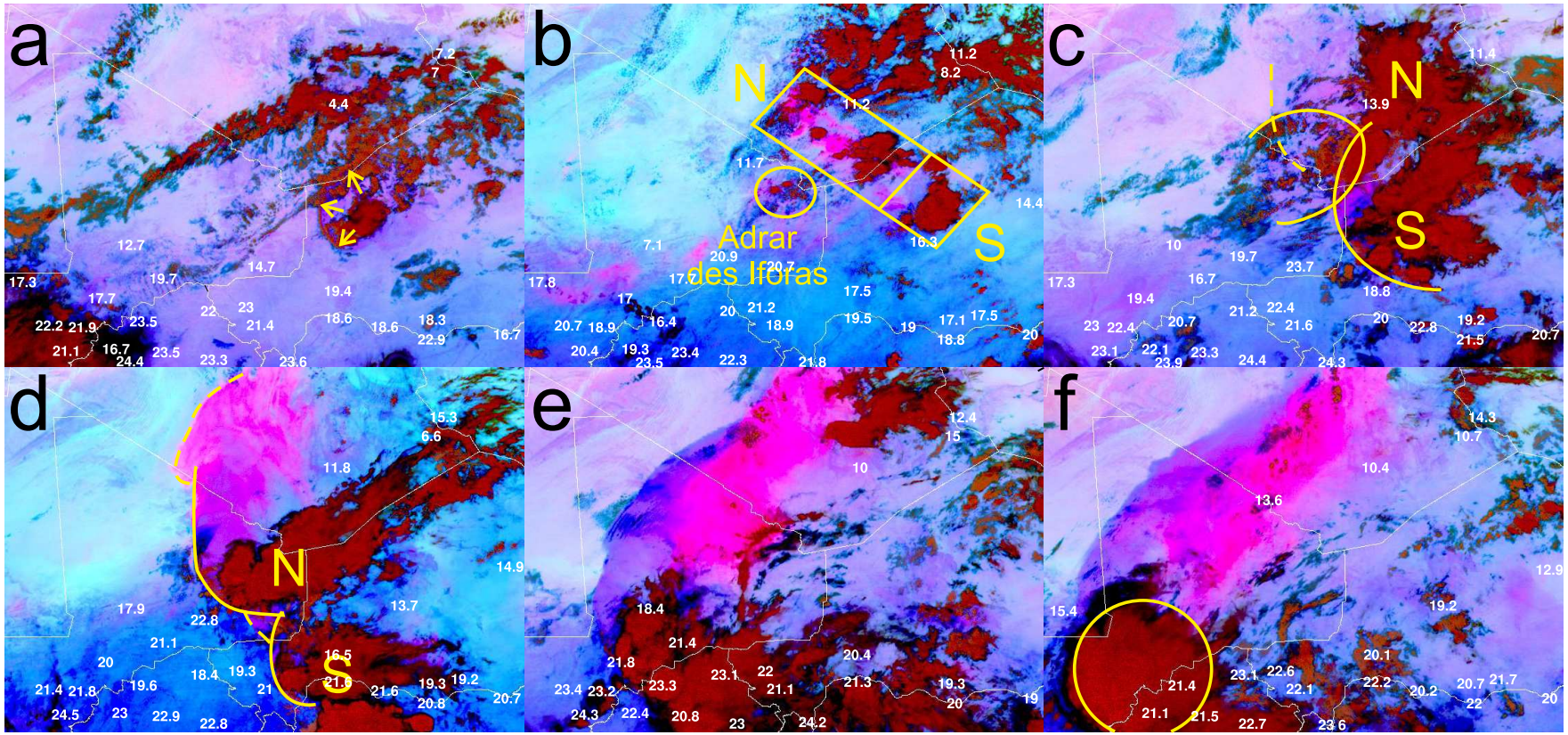


FIGURE 4.4: Spinning Enhanced Visual and InfraRed Imager (SEVIRI) dust images and surface observations of dewpoint temperature (°C; white numbers) at (a) 0000 UTC 08 June, (b) 1500 UTC 08 June, (c) 0000 UTC 09 June, (d) 1200 UTC 09 June, (e) 0000 UTC 10 June, and (f) 0600 UTC 10 June 2010 over the region simulated using Weather Research and Forecasting (WRF) model. Marked in yellow are (a) the cold pool flow from the early convective events, (b) three key regions of convective initiation during early development of the main MCS, (c) and (d) cold pool fronts with older cold pool edges being dashed, and (f) the circular cloud shield formed when the MCS develops into a mesoscale convective complex (MCC) type system. Note that the northern part of the dust plume shown in (d) is associated with the aged cold pool marked in (c).

At approximately 2200 UTC the collision of cold pool from the Adrar des Iforas cells and the S cold pool generates even stronger initial updraughts and is responsible for the generation of a group of new convective cells in the northern part of the system. At 0000 UTC 09 June we can see a restrengthening of deep convective clouds on the SW side of N (Figure 4.4c). These develop rapidly, strengthening cold pool production from N. This cold pool can be seen flowing west and north into the desert producing the southern half of the dust plume shown in Figure 4.4d, the northern part of which is associated with the aged cold pool marked with a dashed line in Figure 4.4c and 4.4d.

The initiation of new cells in different parts of the system at different times produces distinct lobes along the leading edge of the cold pool (Figure 4.4d). The cold air spreading away from more than one convective centre along a single gust front produces conditions similar to the collision of two separate gravity currents. It is in these regions where new cells are preferentially generated. Other factors such as topographical lifting and localised convergence are also likely to play a role. The need for a combination of uplift mechanisms (especially true of N) before further convective initiation is achieved is likely a result of limited boundary layer moisture. This can be seen in the distribution of moisture from surface stations in the region (Figure 4.4). In the south where dew point temperatures are higher new cells are triggered along the southwestern edge without the need for cold pool collisions.

By 0000 UTC 10 June (Figure 4.4e) N and S have merged and later at 0600 UTC (Figure 4.4f) a well defined round cloud shield has formed, suggesting the system's development into a system that could be described as a mesoscale convective complex (MCC). Radiosonde launches show that there is a strong change in the direction of deep layer shear (0-8 km; from the surface to approximately 350 hPa) between the stations in the north and south (see Figure 4.2 for station positions). The deep layer shear for 1200 UTC on 08 and 09 June at: (1) In Salah is 19-23 $ms^{-1}$ in westerly and northwesterly directions (Figure 4.5a), (2) Tamanrasset is 19-26 $ms^{-1}$ in a predominantly westerly direction (Figure 4.5b), (3) Agadez is 8-10 $ms^{-1}$ in an easterly and southeasterly directions (Figure 4.5c), (4) Niamey 8-15 $ms^{-1}$ in predominantly easterly direction (Figure 4.5d), and (5) Ouagadougou (only 1200 UTC 09 June available) 12.8 $ms^{-1}$ in a northeasterly direction (Figure 4.5e). All soundings shown in Figure 4.5 are valid for 1200 UTC 09 June 2010.

It has been shown that deep layer shear has a strong influence on MCS organisation, speed and intensity (Cohen et al., 2007; Coniglio et al., 2006). This suggests that after the system moves into the influence of the African easterly jet (AEJ) and deep layer shear is increased and easterly, the MCS develops into a more organised MCC like system (Figures 4.4d–f). The soundings in Figure 4.5 also illustrate the strong moisture gradient from north to south with PBL water vapour mixing ratios decreasing from 14 $gkg^{-1}$ at Ouagadougou (12.4 N) to between 5 and 7 $gkg^{-1}$ at In Salah (27.2 N).

### 4.3.3 Synoptic-scale flow responsible for dust transport

Figure 4.6 shows the same synoptic fields from ERA-int and TRMM rainfall estimates as in Figure 4.3 valid for 0000 UTC 10 June, but it also shows southern Europe. By this time a large amount of dust has been lifted by successive cold pools and a large dust plume covers parts of Algeria, Mali and Mauritania (Figure 4.4e). The 200 hPa winds, 200 hPa geopotential, mean sea-level pressure and TRMM rainfall show the presence of a mid-latitude cyclone and trough over the Iberian Peninsula. The subtropical jet over West Africa is predominantly zonal, the northward bulge in the ITD is still present and the rainfall associated with the MCS can be seen over Algeria, Niger, Mali, and Burkina Faso. The Iberian mid-latitude cyclone produces a secondary low south of the Atlas Mountains through lee cyclogenesis.

Lee cyclogenesis is process where a mountain range interacts with a synoptic-scale cyclonic system. The normal cyclonic advection of low-level air is disrupted by the presence of the mountain barrier, in this case the Atlas Mountains (Schultz and Doswell, 2000; Steenburgh and Mass, 1994). This deflection of the flow forces it out of quasi-geostrophic balance (where pressure gradient and Coriolis forces dominate fluid movement). Modification of the local pressure and wind fields occurs (including the development of cyclonic flow in the mountain lee) to return the flow to equilibrium. Coupling of this low-level cyclonic disturbance with the upper level trough generates further cyclonic rotation and deepens the low on the lee side of the mountain barrier.

The presence of this lee cyclone deforms the SHL, creating southwesterly flow over Algeria and northern Mali. This flow provides a mechanism for dust transport out of the Sahara toward the Mediterranean. SEVIRI dust and NASCube thermal temperature anomaly

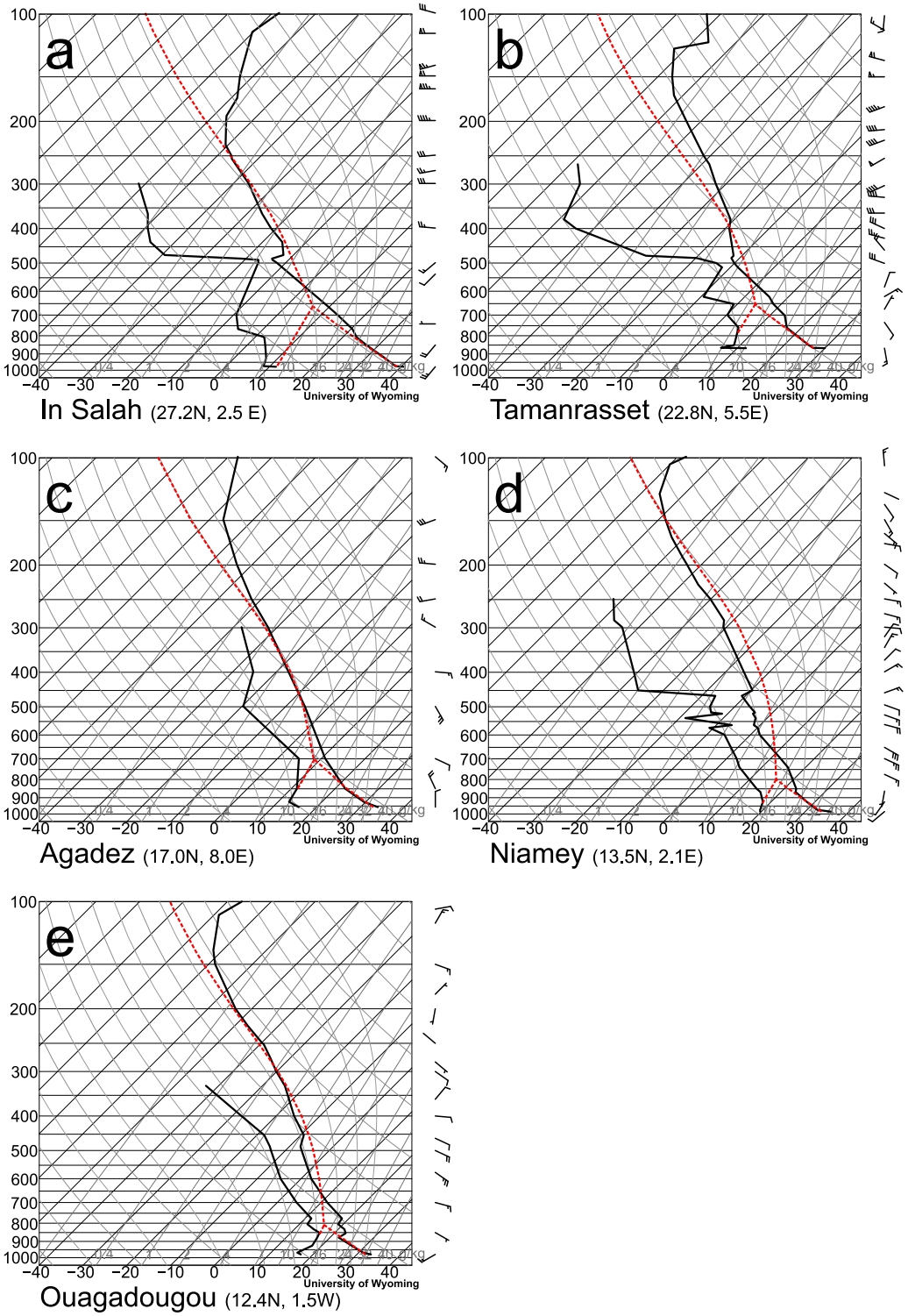


FIGURE 4.5: Skew-T LogP diagrams for (a) In Salah (27.2°N 2.5°E), (b) Tamanrasset (22.8°N 5.5°E), (c) Agadez (17.0°N 8.0°E), (d) Niamey (13.5°N 2.1°E) and (e) Ouagadougou (12.4°N 1.5°W). From the stations in the north to the stations in the south the direction and strength of easterly deep layer shear becomes preferable for the formation of well organised convective systems. There is also greater conditional instability over Niamey than any of the other stations at this time. Original plots from the University of Wyoming, Department of Atmospheric Science.

images show the stretching of the dust plume and northward transport of dust at 1200 UTC 10 June (Figure 4.1), this continues throughout 10 and 11 June.

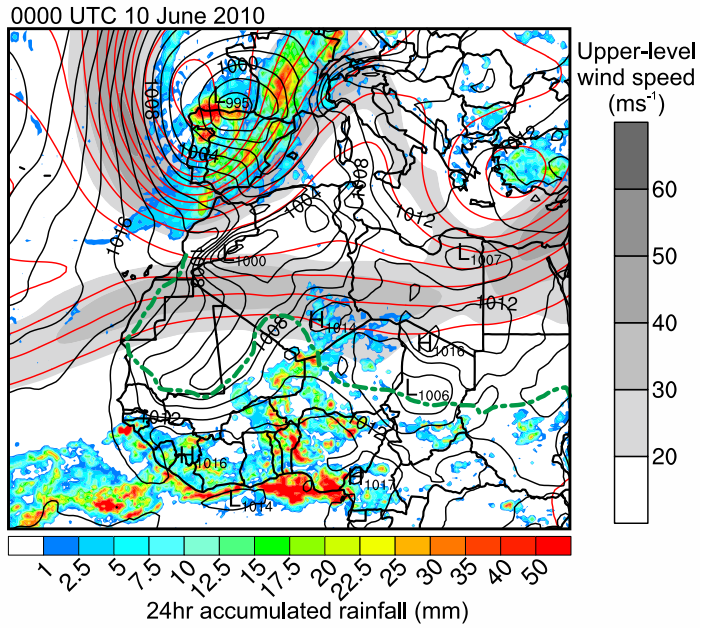


FIGURE 4.6: Same as Figure 4.3 but at 0000 UTC 10 June and including fields over southern Europe.

## 4.4 Model analysis

### 4.4.1 Effect of early convection events on boundary layer moisture

As mentioned in section 4.3.2 convective cells initiated over the Aïr Mountains on the afternoon of 07 June created convective cold pools thought to favour convective triggering on 08 June. In the WRF simulation there is only very weak convective activity in the region of the Aïr at this time. However, there is widespread initiation over the Hoggar Mountain range in the simulation. This is likely due to the orographic forcing of the mountains combined with a region of high moisture convergence associated with the Mediterranean cold surge and the restrengthening of the SHL (Figure 4.7). In the simulation this region of moisture convergence is strongest near the Hoggar Mountains, perhaps explaining the lack of convective development over the Aïr Mountains. These convective cells over the Hoggar Mountains produce a cold pool that spreads as far south as the northern Aïr Mountains. The simulated 1200 UTC boundary layer specific humidity over the the grid point closest to Tamanrasset increases by 2.0 $gkg^{-1}$ (5.1 $gkg^{-1}$ to 7.1 $gkg^{-1}$) between 07 and 08 June.

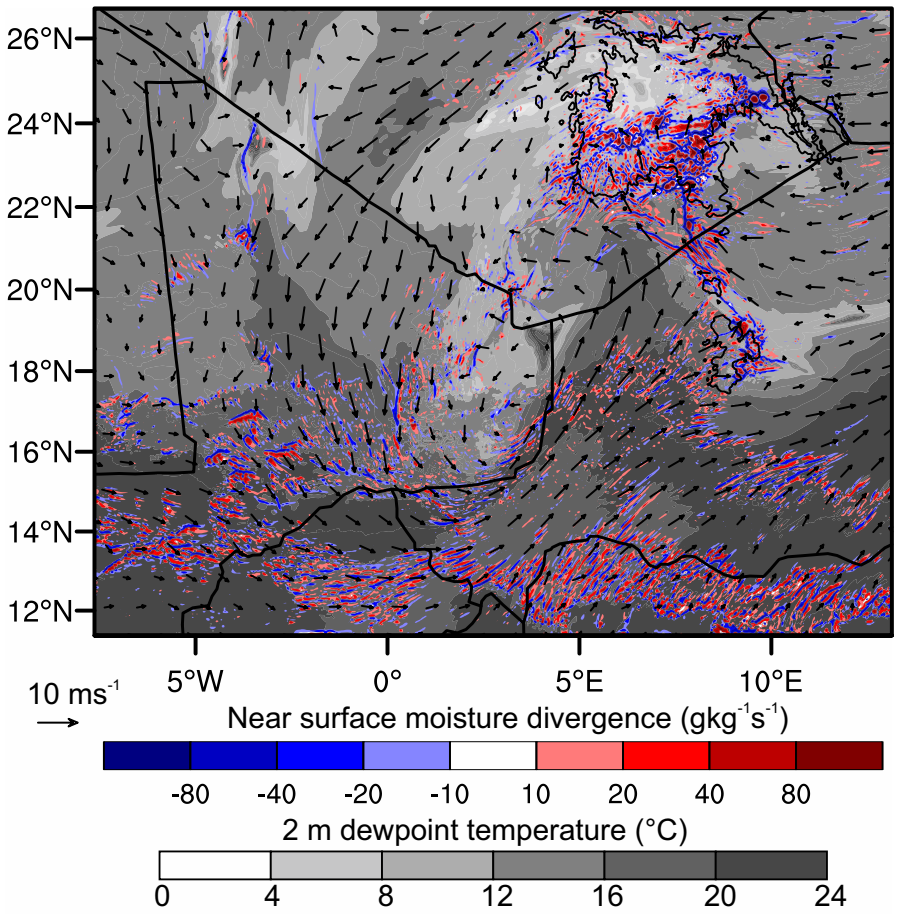


FIGURE 4.7: Moisture divergence calculated using 10 m winds and 2 m specific humidity (red and blue shading, each point plotted represents a model grid point), 2 m dewpoint temperature (grey shading), and 10 m winds (vectors) from WRF simulation at 1200 UTC 07 June 2010 (approximate time of initiation of convective cells over the Hoggar Mountains). Note that over the Hoggar mountains there are bands of moisture convergence and divergence as well as divergent cells surrounded by convergence lines. These cells indicate the early stages of cold pool formation as downdrafts are produced which reach the surface and spread. Also circulations associated with the Libyan high and the heat low positioned over the Algeria/Mali/Niger border triple point these produce the regions of moisture convergence and the tongue of moist air advected toward the Hoggar Mountains west of the Aïr Mountains.

Over the same period there was an increase of only 0.3 $gkg^{-1}$ (12.8 $gkg^{-1}$ to 13.1 $gkg^{-1}$) over the grid point closest to Agadez in the southern Aïr Mountains. Similarly the 1200 UTC radiosonde launches from Tamanrasset show that the water vapour mixing ratio of the well mixed boundary layer increase from 4.9 $gkg^{-1}$ on 07 June to 6.4 $gkg^{-1}$ on 08 June, an increase of 1.5 $gkg^{-1}$ over more than 3 km of the lower atmosphere (Figure 4.8). The 0900 UTC and 1200 UTC radiosonde launches from Agadez on 07 and 08 June, respectively, show little change to boundary layer moisture (about 12 $gkg^{-1}$). This, and the surface dew point temperatures at the two sites (Tamanrasset $< 14°C$, Agadez $> 14°C$) suggests that

convection on 07 June is an important factor for boundary layer moistening north of the ITD, whilst south of the edge of the monsoonal flow it had little impact.

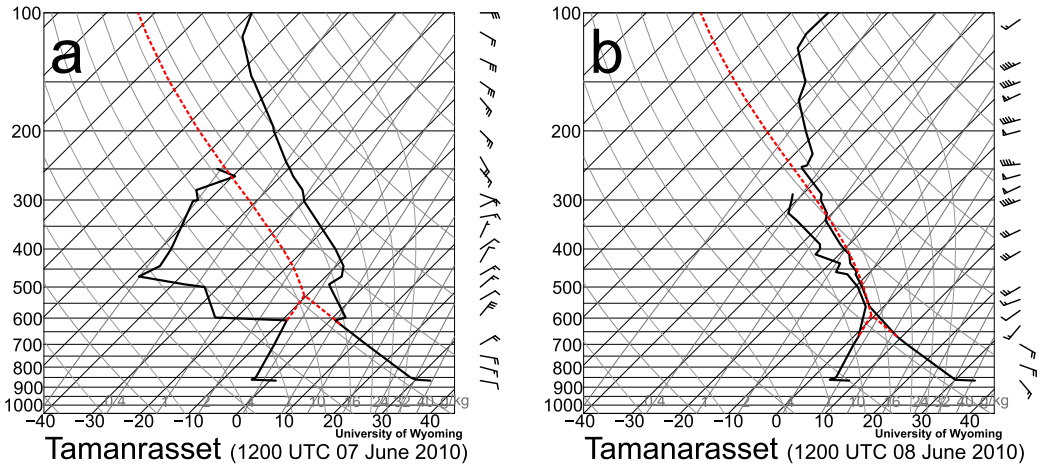


FIGURE 4.8: Skew-T LogP diagrams for Tamanrasset at (a) 1200 UTC on 07 June 2010 and (b) 1200 UTC on 08 June 2010. Note the increase in boundary layer moisture from approximately 3 gkg$^{-1}$ to 6 gkg$^{-1}$ over the entire well mixed boundary layer (approximately 3 km) in a 24 hour period. Original plots from the University of Wyoming, Department of Atmospheric Science.

### 4.4.2 Initiation of convection and organisation

The triggering of convective cells over the Hoggar/Aïr region on 08 June occurs in the WRF simulation at approximately 1200 UTC. This agrees well with the initiation time seen in SEVIRI imagery (Figure 4.4b shows developed cells at 1500 UTC). Figure 4.9 shows the 2205 UTC 8.4-8.7 $\mu$m BT from Moderate Resolution Imaging Spectrometer (MODIS) and the 2200 UTC on 08 June estimated BT using WRF outgoing longwave radiation and an emissivity of 1. The regions where convection has been produced in the simulation spatially differ to those seen in satellite imagery. There are two distinct regions of cold cloud tops (Figure 4.9b) rather than a number of cells oriented along a northwest-southeast axis (Figure 4.9a). In the simulation, active regions are over and west of the Aïr Mountains, and over the Hoggar Mountains. The simulated system does not become organised as observed in satellite imagery. Instead, both groups of convective cells decay by 0000 UTC 09 June. It is likely that the spatial differences between the simulated and observed convective initiation regions plays a role in the lack of convective organisation due to the lack of favourable shear over the Hoggar mountains compared to further south (Section 4.3.2). The convective activity in the simulation is then re-initiated

at 0600 UTC in the Niger-Mali-Algeria border region by the arrival of the cold pool (visible approximately 200 km northeast of the re-initiation region and spreading away from the Hoggar system in Figure 4.9b) This creates an approximate 6 hour lag between the observed and simulated systems.

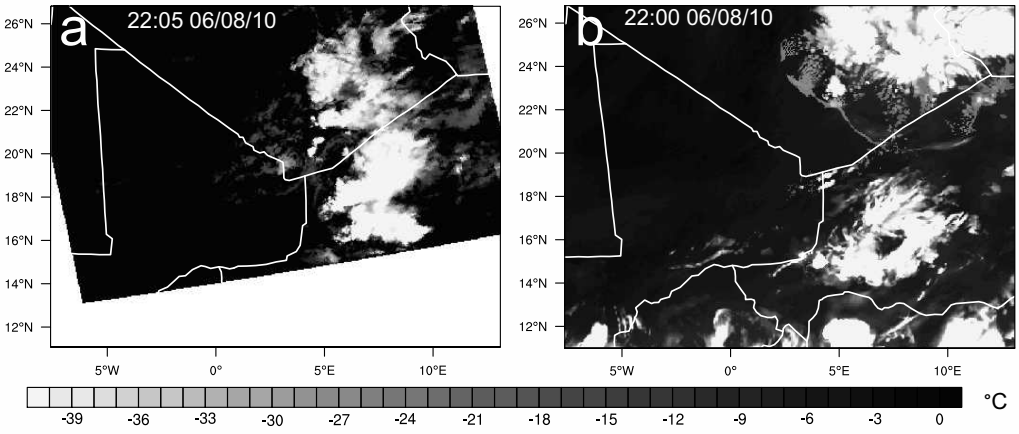


FIGURE 4.9: Comparison of position of deep cloud from (a) Moderate Resolution Imaging Spectrometer (MODIS) and (b) Weather Research and Forecasting (WRF) model simulation using 8.4-8.7 micrometre brightness temperature from MODIS and an estimated cloud top temperature found by using the WRF outgoing longwave radiation (OLR) and the Stefan Boltzman Law.

Despite this lag, the subsequent development of the system in the simulation compares well with the observed MCS (as mentioned in Section 4.2) Once triggered, the system rapidly becomes organised along a northwest-southeast axis and moves southwest (the model rainfall from the organised but still relatively small system can be seen in Figure 4.10a). The behaviour displayed after the re-initiation (section 4.4.3) is consistent with that observed in satellite imagery (Figures 4.4 and 4.10) despite the temporal delay between the simulated and observed systems.

### 4.4.3 Behaviour of the mature MCS

Figure 4.10 shows the development of the simulated MCS. Shown are: vectors representing 10 m wind speed and direction, hourly accumulated rainfall, 7 $ms^{-1}$ isotach at 10 m, updraughts exceeding 3 $ms^{-1}$ at 700 hPa, the position of the ITD derived from boundary layer dewpoint temperature, and the dust uplift potential (DUP) as described in Marsham et al. (2011). The DUP is based on the parameterisation of dust uplift by Marticorena

and Bergametti (1995).

$$DUP = \nu U^3(1 + U_t/U)(1 - U_t^2/U^2) \tag{4.1}$$

Where $\nu$ is bare soil fraction, $U_t$ is a threshold wind speed (7 $ms^{-1}$ used in this study based on the values in Chomette et al. (1999) and Marticorena et al. (1997)), and $U$ is the WRF 10 m winds. Its cubic nature means that it is highly sensitive to high winds. DUP is an idealised metric which isolates the role of meteorology in dust uplift from the land surface. Cakmur et al. (2004) observed that almost all areas of bare soil in this region lead to some dust uplift and Heinold et al. (2013) showed that the reduction in uplift due to washout and soil moisture was 20% at most. Therefore, DUP is used here to identify the meteorological processes capable of lifting dust rather than providing a quantitative measure of dust uplift.

By 1200 UTC 09 June (Figure 4.10a) the convection has been re-triggered by the cold pool mentioned in section 4.4.2 and has become organised, producing new cells on its southwestern edge. A line of systems can be seen on a southeast-northwest orientation across the Mali-Niger border. At this time the cells are still relatively small and have not yet merged into a single organised system. They are positioned within the monsoon flow shown by the direction of the 10 m winds and the position of the ITD. Other convective cells appear to have been triggered over the Hoggar and Aïr Mountains (labelled on Figure 4.10) at this time. Rainfall rates are high (exceeding 5 mm $hr^{-1}$) and high DUP values are produced within the radially spreading cold pools.

6 hours later at 1800 UTC 09 June (Figure 4.10b) the individual groups of cells have merged into a single organised system and continue to travel southwest. The cold pools spread away from the initial downdraught regions and still display high DUP values. There is more rainfall production in the southern half of the system and updraught regions (black dots) are mostly along the leading edge of the cold pool. However, some updraughts and the regions of highest rainfall are set back from the leading edge. The cold pools from the studied MCS and the system over the Aïr Mountains spread into the desert and push the ITD north (as seen in Flamant et al. 2007). A region of high DUP is also present in the northwestern corner of the domain. This is thought to be linked to strong pressure gradients from the lee cyclone south of the Atlas Mountains. Such high DUP values suggest

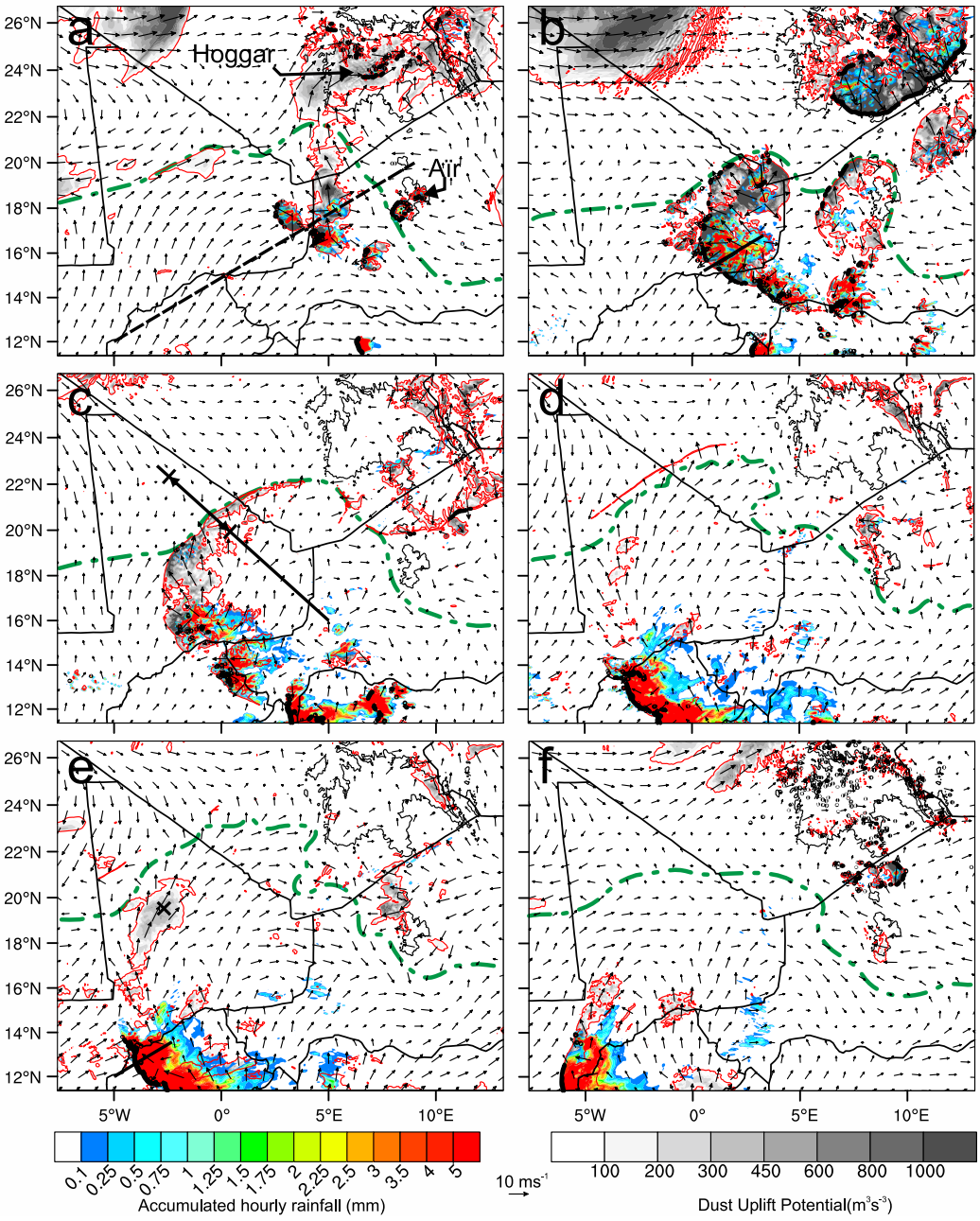


FIGURE 4.10: Temporal evolution of mesoscale convective system (MCS) and cold pool on 09-10 June 2010 as simulated by WRF. Shown is the 1 hr accumulated rainfall (colour shading), 10 m wind vectors, 7 $ms^{-1}$ 10 m isotach (red contour), dust uplift potential described in section 4.4.3 (grey shading), 700 hPa vertical velocities exceeding 3 $ms^{-1}$ (black dots, most easily seen along leading edge of MCS in (d) and (e)), and ITD position ascertained from boundary layer dew point temperature (dashed green contour) at (a) 1200 UTC 09 June, (b) 1800 UTC 09 June, (c) 0000 UTC 10 June, (d) 0600 UTC 10 June, (e) 0800 UTC 10 June, and (f) 1200 UTC 10 June 2010. The thick black dashed line shown in (a) is the common track along which the simulated MCS and the satellite observations were compared (Figure 4.11). The thick black lines in (b),and (e) represent cross sections shown in Figures 4.12a and 4.12b and the line in (c) represents the cross section used in Figure 4.15 with the region marked by arrows marking the part of the cross section used in Figure 4.18. The cross marked on (e) represents the point chosen to represent nocturnal LLJ formation (Figure 4.17).

significant dust uplift. SEVIRI dust images (Figure 4.1) show some dust is raised by these winds and NASCube dust imagery also highlights this region as having a dust related thermal anomaly.

By 0000 UTC 10 June (Figure 4.10c) the cold pools have forced the position of the ITD as far north as 22 °N and the MCS has continued to travel southwest. The DUP within the cold pool has weakened and regions exceeding the 7 $ms^{-1}$ threshold are positioned close to the leading edge of the cold pool and near precipitating parts of the system. The cold pool flow starts to change, with winds becoming less radial and beginning to turn to the right due to Coriolis effects (Section 2.3; Figure 2.10). Rainfall is focused in small intense regions well behind the leading edge of the cold pool edge and updraughts in excess of 3 $ms^{-1}$ at 700 hPa are similarly positioned.

At 0600 UTC 10 June (Figure 4.10d) the MCS has travelled further southwest, rainfall along its northern edge has stopped, and rainfall in the southern half of the system becomes much stronger. Strong updraughts and heavy rainfall now occur along the entire leading edge of the system and heavy rainfall is no longer centred in small intense regions suggesting a change in convective behaviour. A region of weaker stratiform rain has also developed behind the main heavily precipitating region. By this stage the cold pool has aged and is not forcing moist air further into the desert. The flow within the aged cold pool is weaker with very few regions above 7 $ms^{-1}$ and has become almost parallel to the edge of the cold pool. A region of interest is the narrow band of winds exceeding the dust uplift threshold beyond the edge of the aged cold pool and ITD. This feature is over 600 km long but less than 20 km wide and has DUP values in excess of 600 $m^3s^{-3}$. It is discussed further in section 4.5.3.

In Figures 4.10e and 4.10f (0800 and 1200 UTC 10 June, respectively) the MCS continues to travel southwest and rainfall rates, rainfall distribution, and updraughts are similar to Figure 4.10d. The wind direction within the aged cold pool continues to veer and by 1200 UTC, mixing due to solar heating of the surface, has begun to reduce the dewpoint temperature perturbation and force the ITD position south. At 0800 UTC there is a large region of moderate DUP values inside the aged cold pool, the processes responsible for this will be discussed in section 4.5.2

Also shown is a common track between the simulated and observed system (dashed line on Figure 4.10a). This is used to analyse the behaviour of the MCS in both the simulation and in satellite imagery. The leading edge of the system is found by manually identifying the boundary of lifted dust and rope clouds in satellite imagery, and strong updraughts and equivalent and virtual potential temperature ($\theta_e$ and $\theta_v$, respectively) gradients in the WRF simulation. These variables were chosen as $\theta_e$ is an adiabatically conserved quantity often used for air mass identification, while $\theta_v$ is a proxy for atmospheric density in adiabatic conditions and is useful for identifying density driven flows.

Figure 4.11 shows the front speed of the leading edge plotted against the distance away from the northeastern end of the track. This plotting method compensates for the temporal differences between the observed and simulated systems and accounts for topographic influences on convective initiation. The velocities of the real and simulated fronts closely resemble each other. However, the first increase in front speed (at 800 km along the common track) is produced by different processes in the observed and simulated systems. From satellite imagery it is identified as the result of the rapid generation of convective cells to the north of the track. The cold pool surge associated with this development moves south, rapidly shifting the position of the cold pool boundary along the track. In the WRF simulation the leading edge is accelerated by the development of a number of cells ahead of the main system producing a region of uplift and cold pool air that becomes indistinguishable from the original front.

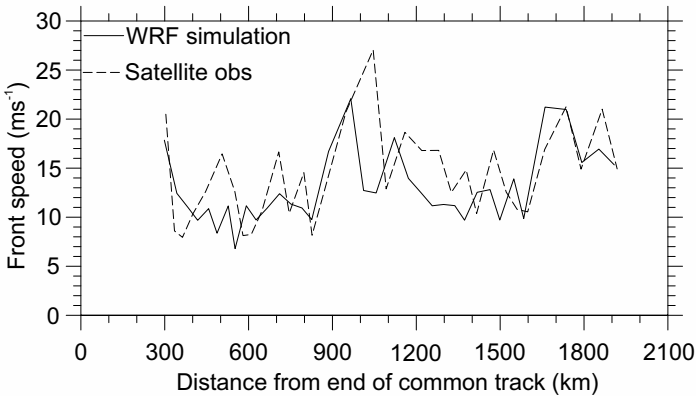


FIGURE 4.11: Comparison of front speed of simulated and observed mesoscale convective system (MCS) plotted against the distance from the northeast end of the common track (black dashed line in Figure 4.10a).

As discussed earlier the MCS undergoes a change of convective mode with patterns of updraughts, rainfall intensity and rainfall distribution changing as the system develops.

Solid black lines on Figures 4.10b and 4.10e show the time and position of cross sections shown in Figure 4.12. These show wind, $\theta_e$, $\theta_v$, cloud, and updraughts exceeding 2 $ms^{-1}$. Figure 4.12a shows that on 09 June the main cloud column is far behind the gust front (∼30km), convective updraughts are weak, and the cloud base is at approximately 2.5 km above the surface. In contrast on 10 June (Figure 4.12b) the system fits the conceptual model of a MCS proposed by Houze et al. (1989), much more closely (Figure 2.5). There is a region of strong updraughts produced along the gust front, a system relative rear inflow jet (jet winds parallel to the common track are 5 $ms^{-1}$ faster than the propagation speed of the simulated system's leading edge), and the cloud base is below 1 km. In the simulation there is only a small change in the low-level moisture ahead of the storm between these times (approximately 1 $gkg^{-1}$) and a reduction in the convective available potential energy (CAPE; approximately 2500 $Jkg^{-1}$ to 1500 $Jkg^{-1}$). The convective inhibition (CIN) also remains low (below 150 $Jkg^{-1}$). This suggests that the change in behaviour is controlled by other factors.

One candidate for the change in MCS behaviour is the shear profile. Shallow shear (over the depth of the cold pool) has been shown to have a strong influence on the behaviour of the cold pool leading edge. However, in this case the shallow layer shear (0-2 km) is almost parallel to the gust front at the leading edge of the system and does not change much between 1800 UTC 09 June and 0800 UTC 10 June. As described in section 4.3.2, MCS behaviour is also strongly linked to deep layer shear. The deep vertical wind shear (0-8 km depths) ahead of the simulated system changes from values of 4-8 $ms^{-1}$ for the earlier convective regime to over 20 $ms^{-1}$ for the regime with greater organisation. The simulated pattern of both shear strength and direction agrees well with that seen from radiosonde data (Figure 4.5). Deep shear is generally westerly at latitudes to the north of 20 °N with shear direction changing to easterly south of 15 °N strengthening toward the southern edge of the WRF domain (approximately 12 °N). Therefore, it is thought that increased deep vertical shear associated with the presence of the AEJ largely governs the behaviour of this MCS with the increasing depth of the monsoon layer also encouraging the development of convective cells.

The agreement of the simulation and observations with respect to: (1) the timing of convective initiation before the early decay, (2) the direction and speed of propagation once an organised system is generated, (3) the influence of deep layer shear on the behaviour of

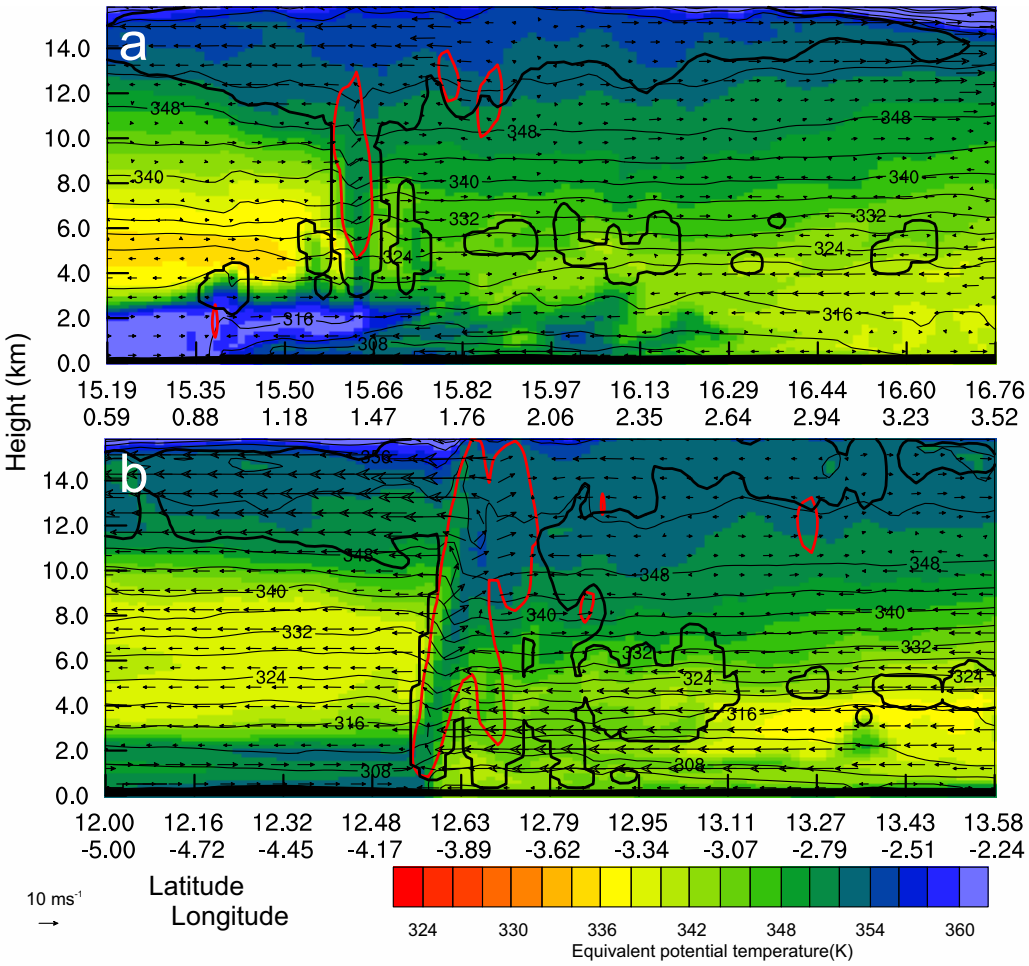


FIGURE 4.12: Cross sections through leading edge of mesoscale convective system (MCS) showing equivalent potential temperature (colour shading), virtual potential temperature (thin black contours), outline of cloud including liquid and ice (thick black contour) and updraughts exceeding 2ms$^{-1}$ (thick red contours) at (a) 1800 UTC 09 June and (b) 0800 UTC 10 June 2010. The positions of the cross sections are shown in Figure 4.10b and 4.10e.

the MCS, (4) the production of a very large cold pool and (5) the agreement between the DUP metric and the regions observed to emit dust suggests that WRF has successfully modelled the dynamical features important to the production of the very large haboob observed.

### 4.4.4 Processes responsible for large cold pool size

The scale of the cold pool in both observations and in the simulation is very large. The front is seen to propagate approximately 800 km and the front length is in excess of 1000

km. As density driven flows on this scale are likely to be strongly influenced by rotational forces it is might at first be surprising that the the cold pool seems to reach such a size.

The influence of rotational effect can be seen in the simulated cold pool. As mentioned in section 4.4.3 its flow veers from a radial flow until it is almost parallel to the edge of the cold pool. This behaviour is also suggested in the observed dust plume by the formation of structures consistent with horizontal shear instability (Figure 4.13; Kawashima 2010).

The maximum radius (assuming the flow is solely driven by density differences) is estimated using equations from Hallworth et al. (2001) and found to be from 415 km to 535 km. The observed and simulated cold pools seem to be in excess of these values (∼800 km). This suggests that other factors play an important role in the behaviour of the cold pool. The similarity between the WRF simulation and satellite imagery suggests that whatever dynamical processes are responsible for this are successfully represented by using WRF.

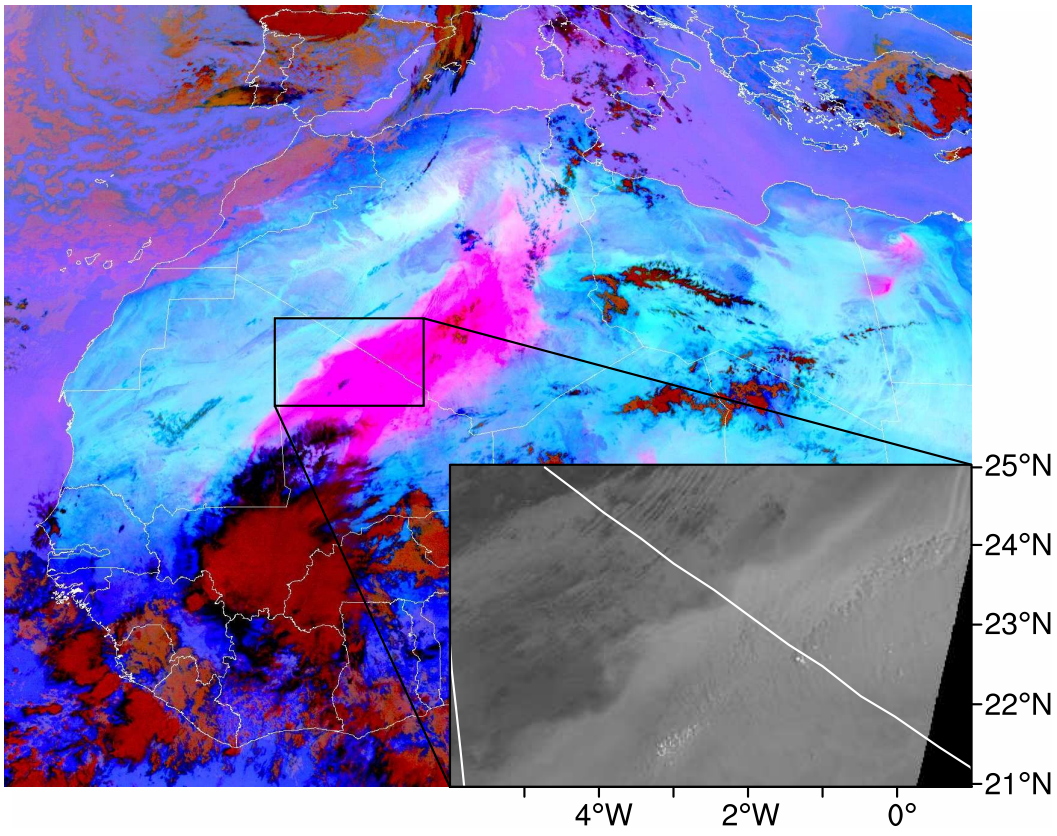


FIGURE 4.13: Spinning Enhanced Visual and InfraRed Imager (SEVIRI) dust image showing the extent of the large dust plume and the mesoscale convective system (MCS) that produced it at 1030 UTC 10 June 2010. Inset is the MODIS band 4 (545-565 nm) visible radiance showing the production of horizontal shear instability along the edge of the old cold pool.

### MCS behaviour

The simplest explanation of how the cold pool seen in satellite imagery is so large is the behaviour of the convective systems that produce it. As mentioned in Section 4.3.2 the northern part of the dust plume is generated by an earlier cold pool which was initiated over the Hoggar mountains. Subsequent generation of another large cold pool which spreads into the already dusty region makes the separate events difficult to distinguish. Despite this the size of the later cold pool is still very large. This seems to be a product of the movement of the MCS which is generating the cold air. As such, the behaviour is different to a single release gravity current explaining the extreme front length of the cold pool seen in satellite imagery. Less obvious, is the factors that allow for the front of this cold pool to travel so far into the desert. These are discussed below.

### Synoptic-scale pressure gradient

The large-scale pressure gradient is a potential source of additional northward motion. At 0000 UTC 10 June the pressure field (Figure 4.6) is in broad agreement with that of the WRF simulation (not shown). The main difference between the WRF simulation and ERA-int pressure fields at this time is the presence of a mesoscale high in WRF of approximately 2 hPa associated with the cold pool. Generally this is likely to be absent in ERA-int, due to the convective parameterisations used in the model first guess and the impact this has on representing the effects of convective storms on surface pressure. The paucity of observations means that the first guess cannot be sufficently corrected. The development of the lee-cyclone discussed in section 4.3.3 southeast of the Atlas Mountains in Morocco produces an elongated SHL along a northeast-southwest axis, just south of the Atlas Mountains. This not only enhances the relative depth of the heat low, but also displaces its centre much further north than usually seen. This creates a northwestward pressure gradient force over a much greater latitudinal extent of the Sahara. A mean sea-level pressure difference of 10 hPa is present between the leading edge of the cold pool and the low pressure centre of the lee cyclone. Despite the uncertainty associated with ERA-int mean sea-level pressure, changes in the SHL shape are thought to be sensible. This additional forcing might help to explain the propagation of the cold pool deep into the desert.

Features that look very similar to large convectively generated haboobs from satellite imagery can occur without the downdraughts associated with MCSs (Figure 4.14). These dust lifting cold fronts are also found in other part of the world such as Australia (Strong et al., 2011) and China (Aoki et al., 2005) and are driven entirely by the synoptic-scale meteorology. This suggests how an existing convectively generated cold pool might behave in the presence of an similar synoptic scale pressure gradient.

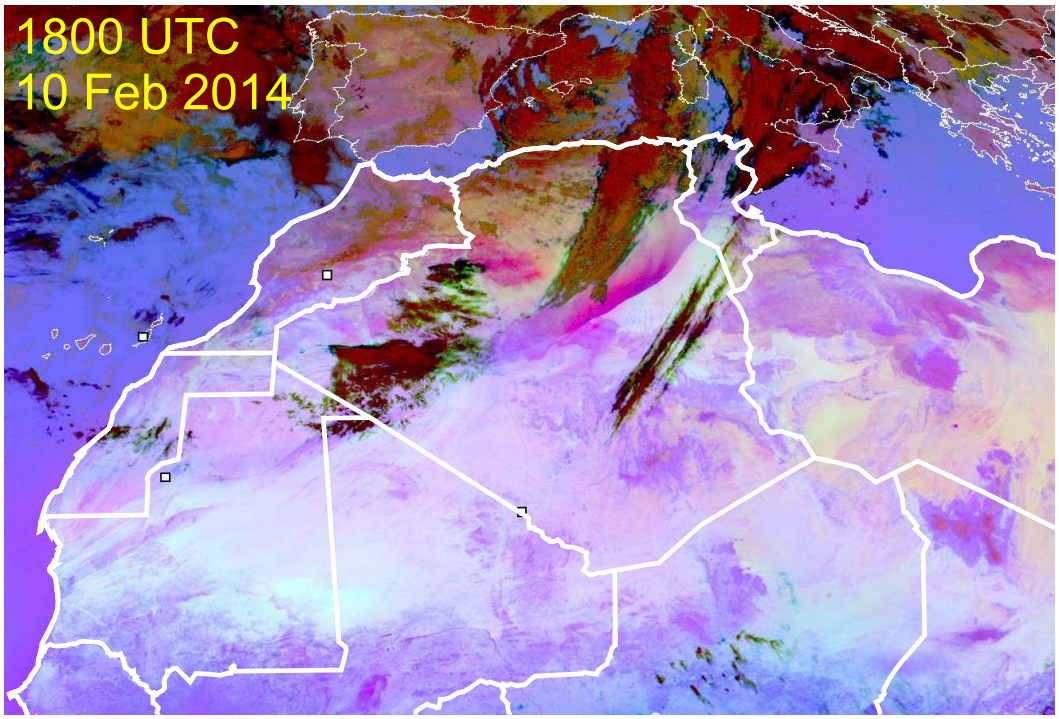


FIGURE 4.14: Spinning Enhanced Visual and InfraRed Imager (SEVIRI) dust image showing the a lifted dust event over northern Algeria at 1800 UTC 10 February 2014. The dust in the image has a sharp leading edge and from satellite imagery looks very similar to a convectively generated haboob, however, it is not associated with a mesoscale convective system (MCS) and the mid-level clouds behind the dust plume suggest that evaporative cooling plays a less important role than in a convectively generated cold pool.

### Shallow convection on Saharan edge of cold pool

Another factor that might explain the extent of the cold pool ingress into the desert is the generation of additional convective cells along the leading edge of the cold pool. When considering the movement of a MCS, the limitations on the distance travelled are not related to a theoretical maximum outflow distance of the initial cold pool. If new convective cells are triggered along a section of the leading edge travelling into the desert, the cold air in the head of the flow is refreshed by new downdraughts. Figure 4.15 is

a cross-section through the head of the cold pool positioned roughly perpendicular to its direction of travel (solid black line marked on Figure 4.10c). Contours of $\theta_e$ and $\theta_v$ show the position of different air masses, vectors show winds parallel to the cross section, and thick black and blue contours outline regions of cloud and precipitation, respectively. Shallow convective cells near the edge of the cold pool (between 3.5 and 7 km above the surface and 20 to 30 km across) produce precipitation that evaporates in the boundary layer. Cells producing precipitation which reaches the surface can also be seen close to the northern edge of the cold pool in Figure 4.10c. These have the potential to alter the expected behaviour of a density current by refreshing the cooled air in the cold pool.

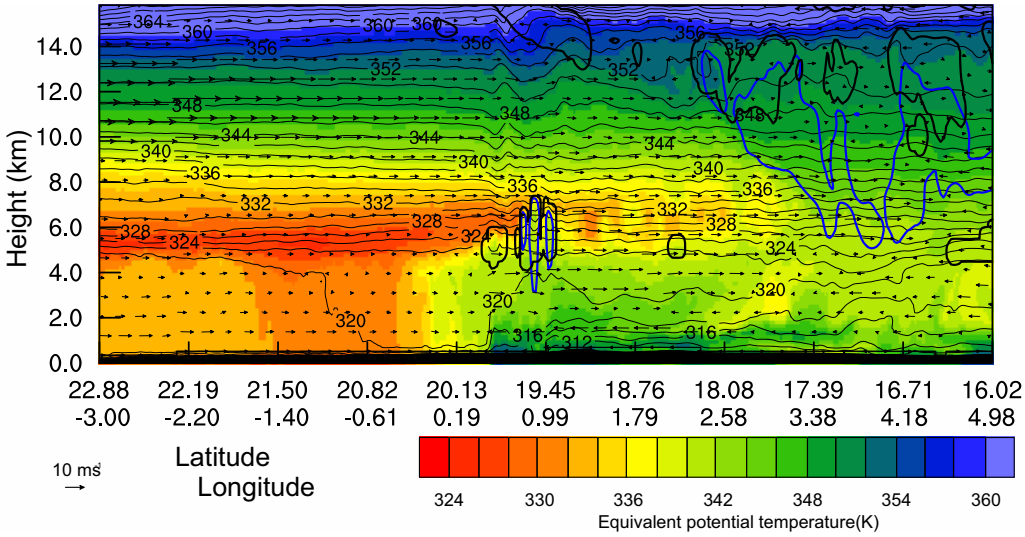


FIGURE 4.15: Cross section through cold pool travelling into the Sahara desert showing equivalent potential temperature (colour shading), virtual potential temperature (thin black contours), outline of cloud including liquid and ice (thick black contour) and outline of precipitation (thick blue contours) at 2100 UTC 09 June. The position of the cross section is shown in figure 4.10.

It is possible that clouds similar to those shown in Figure 4.15 could be overlooked in satellite imagery as they are shallow and their tops do not significantly differ in temperature to the lofted dust below (Figure 4.16). The clouds shown in Figure 4.16 have a limited horizontal extent (approximately 3km), this means that they are very difficult to see in 3 km pixel geostationary satellite imagery (Figure 4.16a and 4.16b). These clouds are evident in Figure 4.16c in the 250 m resolution MODIS true colour imagery whilst they are difficult to see in either the NASCube thermal anomaly or SEVIRI dust imagery due to limitations associated with their dependence on BT and BT differences and the similar temperature of cloud and lofted dust.

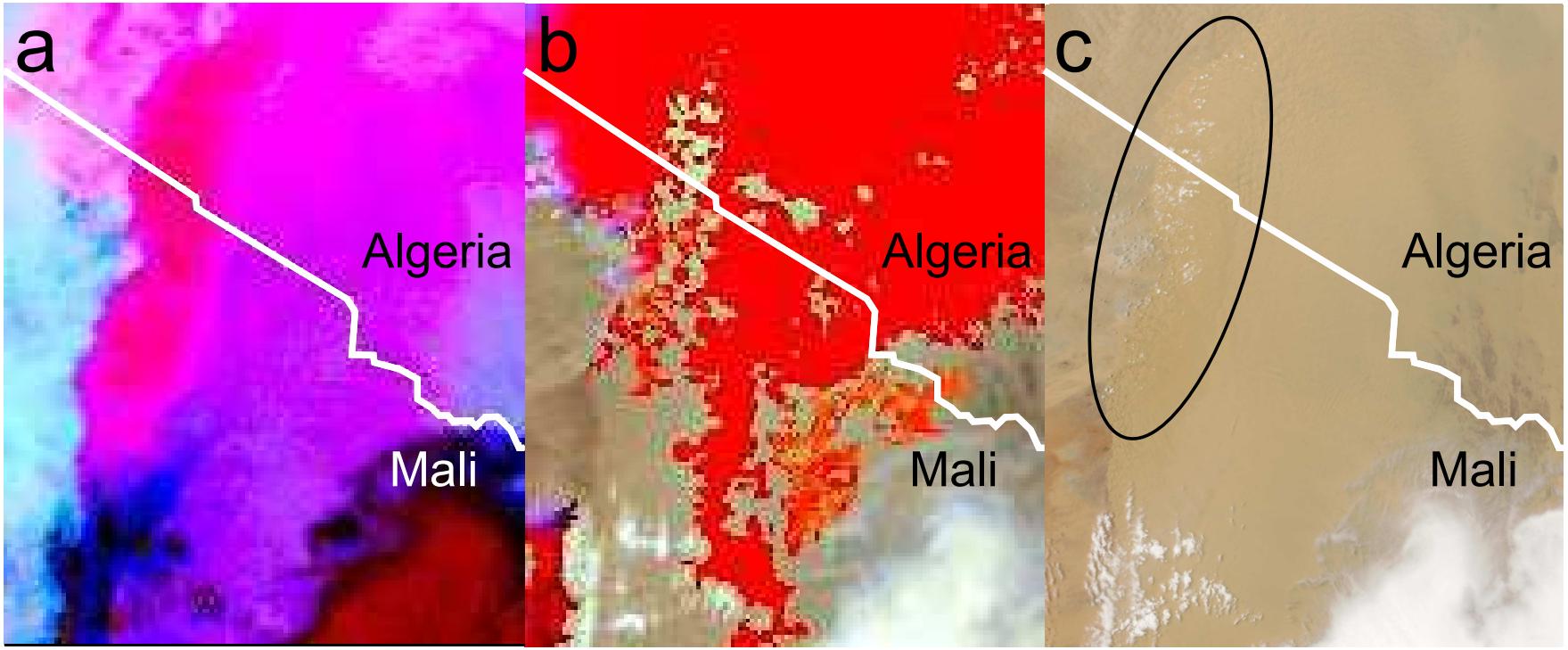


FIGURE 4.16: Comparison of (a) Spinning Enhanced Visual and InfraRed Imager (SEVIRI) dust imagery, (b) North African Sand Storm Survey (NASCube) visible and temperature anomaly and (c) Moderate Resolution Imaging Spectrometer (MODIS) visual satellite products at 1330 UTC 09 June 2010 showing the difference in representation of shallow cumulus clouds formed over a region of raised dust. The area highlighted shows the position of small clouds visible in MODIS imagery.

The grid spacing of the WRF simulation is too coarse to model the horizontal scale of clouds seen in Figure 4.16c, however, it is thought that the production of shallow, hydrometeor-producing convective cells is a realistic process and could help to to force cold pool air into the desert.

## 4.5 Dust uplift processes

To identify important dynamical processes for dust deflation the meteorological mechanisms which produce high DUP values have been identified. Three dust uplift processes are identified in the simulation, these are: (1) high winds associated with the leading edge of the cold pool, (2) an enhanced nocturnal low-level jet (NLLJ) mixed to the surface in the morning, and (3) the production of an internal bore on the nocturnal boundary layer (NBL).

### 4.5.1 Turbulence along cold pool leading edge

Despite the fact that observed and simulated cold pools cannot be considered simple single release density currents (Section 4.4.4), here we assume that the mesoscale dynamics of the head of the observed cold pool behave similarly to two-dimensional laboratory experiments discussed in Simpson (1997) (Section 2.3). The turbulent leading edge creates intense gusts which can be sufficiently strong to deflate dust in arid regions. As a dust uplift mechanism turbulence in the head of a convective cold pool is well documented (Chen and Fryrear, 2002) and is the most commonly attributed dust uplift mechanism ascribed to cold pools (Section 2.6.1). The grid spacing in the simulation is not sufficient to resolve the small-scale turbulent eddies, therefore high surface winds in the simulation are largely produced by the model's reaction to the mesoscale pressure gradient with an additional turbulent component from the PBL scheme.

In Figure 4.10a and 4.10b large areas of strong surface winds are found behind the northward travelling edge of the simulated cold pool. Over time the region of high DUP gets narrower and more closely associated with the leading edge. This is caused by the weakening of winds within the cold pool as downdraught production ceases and the speed of the flow decreases. By 0600 UTC (Figure 4.10d) only a very small section of the cold pool

front still has wind speeds exceeding 7 $ms^{-1}$ suggesting that little dust uplift is produced by the leading edge of the cold pool at this time. DUP values are also likely to be reduced close to downdraught producing regions as the system travels south into vegetated regions, reducing the bare soil fraction.

### 4.5.2 Enhancement of NLLJ

As mentioned in section 4.4.3 an area within the aged cold pool produces winds above the dust uplift threshold from 0700 to 1100 UTC 10 June (Figure 4.10e). This is linked to the production of a NLLJ (Section 2.6.2). Momentum from this NLLJ is then mixed to the surface by the growth of the boundary layer the following morning. As mentioned in Section 2.6.2 NLLJs are an important dust uplift mechanism in the Sahara. They are not normally associated with cold pools, however recent work by Heinold et al. (2013) and Marsham et al. (2013b) has highlighted a connection between the two. The effect seen in the WRF simulation is very similar to that identified in high resolution MetOffice Unified Model runs discussed therein. DUP values over a large area within the aged cold pool in Figure 4.10e are 300-600 $m^3s^{-3}$, suggesting a link between the presence of the cold pool and an enhancement of the processes forming the nocturnal LLJ.

Figure 4.17 shows wind speed and $\theta_v$ for the boundary layer during the cold pool passage for the point marked on Figure 4.10e. The profile shows the increasing depth of the stable layer prior to the arrival of the cold pool just before 0100 UTC and the production of a NLLJ reaching 8 $ms^{-1}$. The passage of the leading edge of the cold pool at 0100 UTC produces strong winds, decreased $\theta_v$, and higher levels of water vapour (not shown) in the lowest 1.5 km of the atmosphere. After the leading edge of the flow has passed, the strongest winds are between 200 m and 600 m above the surface, reaching 17 $ms^{-1}$. Between 0100 and 0500 UTC the wind speeds at this elevation reduce slightly to between 14 $ms^{-1}$ and 16 $ms^{-1}$, most likely associated with weaker flow to the rear of the leading edge. The highest wind speeds are found at the interface between the cold pool and the residual mixed/monsoon air above. This marks the most stable layer of the lower atmosphere. The near surface winds are still relatively strong (>5 $ms^{-1}$) but not as high as the 7 $ms^{-1}$ threshold velocity chosen for dust uplift. From 0500 to 0700 UTC there is a further acceleration of the jet to as high as 18 $ms^{-1}$. This may at least be partly due to an inertial oscillation (Blackadar, 1957; Fiedler et al., 2013b; Van de Wiel et al., 2010),

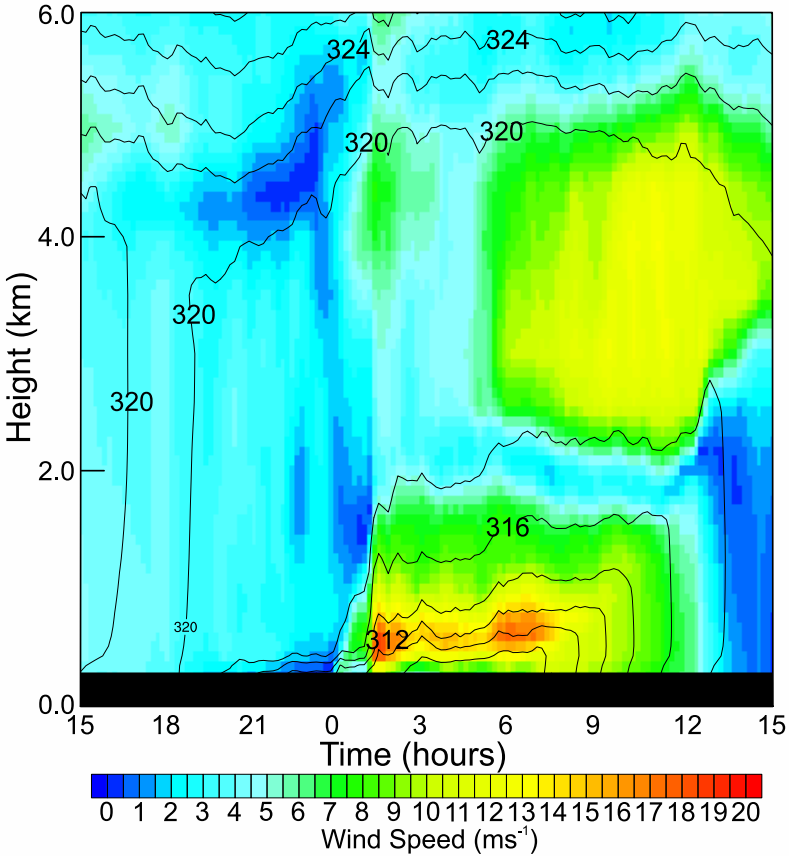


FIGURE 4.17: Time series of wind speed and stability in the boundary layer from 1500 UTC 09 June to 1500 UTC 10 June 2010. Wind speed is represented by the colour shading and stability is represented through contours of virtual potential temperature (black contours).

where supergeostrophic winds can be achieved due to the effects of Coriolis acceleration. Also at this time the synoptic-scale pressure gradient force and the direction of the now anticyclonic cold pool flow are perpendicular. This suggests that the superposition of cold pool flow larger-scale background flow driven by the pressure gradient force is a factor in the production of this strong NLLJ. At 0700 UTC the increase in near-surface values of $\theta_v$ indicate that the low-level inversion is being eroded by surface heating. Higher winds at the surface at this time indicate that NLLJ momentum has started to be mixed throughout the growing boundary layer. This process continues throughout the morning producing surface wind speeds in excess of 7 $ms^{-1}$ for over 4 hours.

Identifying if a process such as this was important for dust uplift for the real world case is difficult. The temporal lag between the production of the observed and simulated cold pool means that the simulated cold pool is subject different stability conditions compared

to the observed. Also, even if this process is present, it would be very difficult to observe additional lifted dust in satellite imagery within an aged dusty cold pool.

### 4.5.3 Interaction between cold pool and developing nocturnal boundary layer (NBL)

The narrow region of high DUP values ahead of the aged cold pool mentioned in section 4.4.3 (Figure 4.10d) is produced by the formation of an internal bore on the NBL. A cold pool moving through the growing NBL is considered here to be dynamically similar to a density current flowing in a stratified environment (Section 2.3). After sunset at approximately 1800 UTC 09 June the NBL begins to form and grows in depth. At approximately 2300 UTC 09 June the NBL reaches a depth approximately 1/4 the height of the density current, the depth at which a gravity current begins to be influenced by a shallow stable layer (Simpson, 1997). As expected, at this time the behaviour of the cold pool head begins to change. At 2300 UTC the cold pool, shown by the region of elevated water vapour, still seems unimpeded by the presence of the NBL (Figure 4.18a). The head of the flow becomes depressed and the NBL air is forced over the flow by 0000 UTC June, similar to the smooth hump that envelops a density current head described in Simpson (1997) (Figure 4.18b). An internal bore formed by the cold pool then propagates ahead of the the edge of the flow at approximately 0500 UTC (Figure 4.18c). During this time the overall behaviour of the cold pool flow has changed with it becoming increasingly parallel to the cold pool edge due to Coriolis effects. There is also rapid deceleration of the cold pool front between 0500 and 0700 UTC which is consistent with a density driven flow reaching its Rossby radius of deformation. The deceleration of the cold pool allows the bore produced at its front to propagate into the desert.

The type of bore formed is known to be controlled by the ratio of bore height to stable layer height ($h_0/\ h_1$; Simpson 1997). A value between 1 and 2 produces a smooth undular bore, a value between 2 and 4 produces a bore with some turbulent mixing, and a value higher than 4 is dynamically very similar to a gravity current. Before solar heating of the surface begins to erode the NBL, the amplitude of the simulated bore is large compared to the depth of the NBL. Therefore it is likely that a significant amount of turbulence would be created at the rear of such a bore. It is proposed here, that a turbulent bore has the potential to raise dust from the surface as the simulated DUP along much of the bore is in

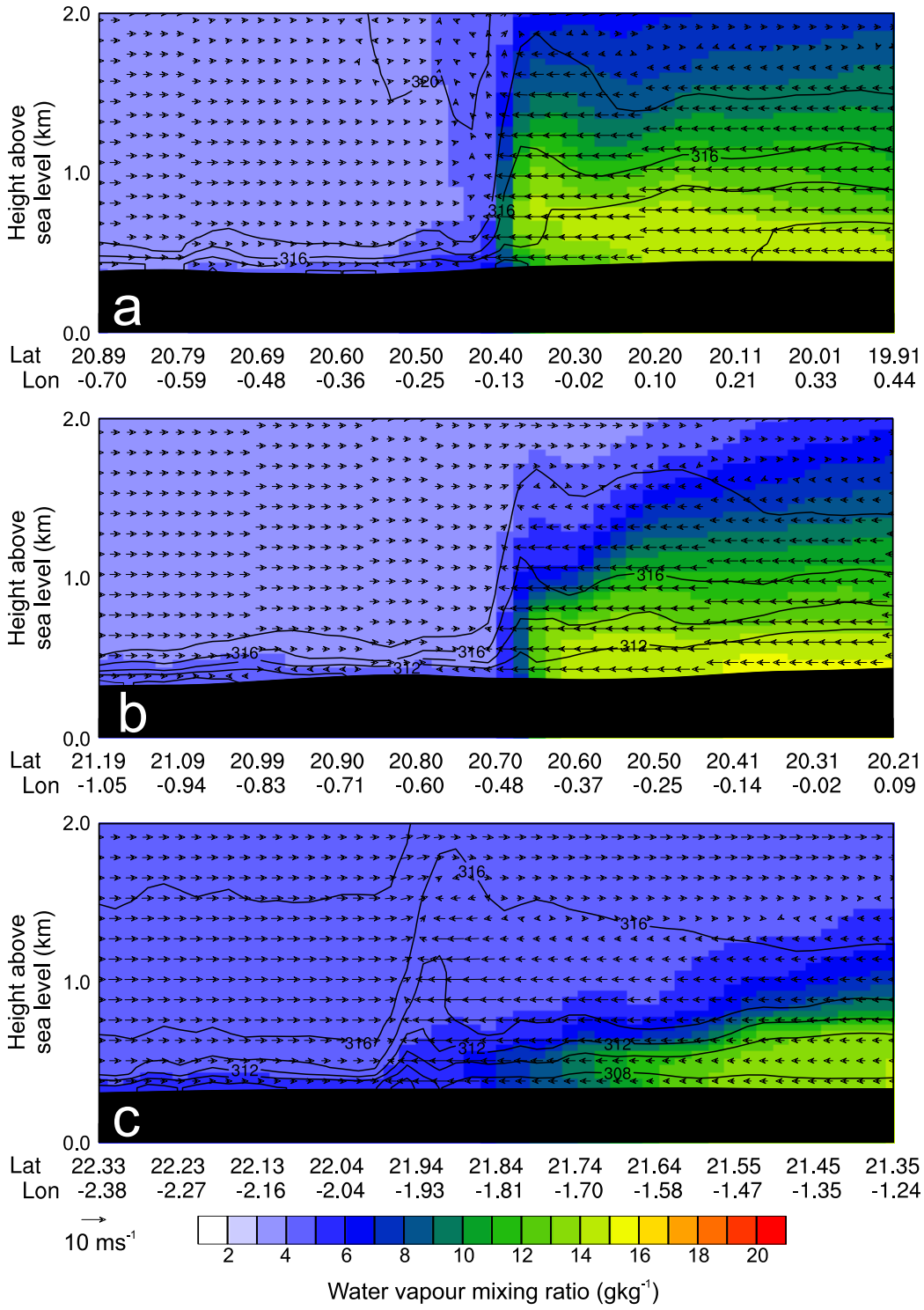


FIGURE 4.18: Cross sections through the head of the simulated cold pool showing water vapour mixing ratio (colours), virtual potential temperature as a proxy for density (black lines) and wind vectors parallel to the cross section at (a) 2300 UTC 09 June 2010, (b) 0000 UTC 10 June 2010 and (c) 0500 10 June 2010. The cross sections shown here are all taken along the line shown on Figure 4.10c from the section marked by arrows.

excess of 600 $m^3s^{-3}$. This mechanism appears to be similar to a case in southwest Algeria (17 and 18 June 2011) as part of the Fennec field campaign (Hobby et al., 2013), where winds associated with the bore were in excess of 7 $ms^{-1}$ and dust was observed in SEVIRI dust.

Once again the difference in stability profile between the simulated and observed systems caused by the temporal offset means that the deceleration of the cold pool front occurs too early for a NBL to have developed. Also, if this process is present more commonly the temporal resolution of most surface observations (3 hourly) is insufficient to identify them as a dust uplift process. The limited spatial extent and time period at which this process can occur further limit the amount of dust that internal bores are likely able to lift. Despite the fact that this feature is unlikely to lift a large amount of dust, it does represent a process which extends the distance from a MCS that dust can be raised.

## 4.6 Summary and conclusions

This study simulates the dynamical conditions of a MCS triggered over the Aïr and Hoggar Mountain ranges on 08 June 2010 and the very large cold pool it creates. This includes analysis of how these conditions are likely to impact Saharan dust emission. Despite temporal discrepancies in the development of the MCS between the simulation and observations, it is argued that the two are sufficiently similar that useful conclusions can be drawn about this case and similar systems. Figure 4.19 is a schematic showing the main processes responsible for the production of the dust plume in this case study.

**The synoptic-scale environment plays an important role in creating the conditions for the production of the MCS and for the transport of dust.** An upper-level trough and wave on the subtropical jet are responsible for the production of conditions dynamically similar to a tropical plume (Figure 4.19a). The persistent and precipitating clouds created, lead to the disruption of the SHL, splitting it in two, as well as moistening the desert air. Subsequent straightening of the subtropical jet and the development of an upper-level trough over the eastern Mediterranean are linked to the development of a high over Libya (Figure 4.19b). In the simulation, flows associated with the restrengthening SHL and Libyan high produce a convergence zone over the Hoggar and Aïr Mountains. Convergence, large-scale moisture advection, and high terrain create favourable conditions

for convective triggering. Later, the dust plume produced by the MCS is deformed by the background flow produced by the deformation of the SHL by lee cyclogenesis. This deformation is present from 09 to 11 June, and the large-scale circulation induced is able to transport dust over hundreds of km.

**Mesoscale dynamics are also important for the development of the observed and simulated MCSs** On 07 June smaller convective systems are triggered, producing cold pools that spread over the Hoggar/Aïr regions and extend the area of moist southerlies. These cold pools increase levels of moisture in the boundary layer and encourage the production of further convective cells. At 1200 UTC on 08 June the first cells of the MCS are triggered (Figure 4.19c). Cells produced further south along the northwest-southeast axis of the system develop more rapidly and produce more new cells than those in the north. The marginal nature of new cell triggering early in the system's development is likely due to low boundary layer moisture and unfavourable shear. The initiation of new cells at this stage seems reliant on a number of factors, making the generation of new cells more intermittent.

**The system's behaviour changes radically when it moves into a region of strong easterly deep layer shear and increasing boundary layer moisture.** The shear (provided by the AEJ (Figure 4.19c)) produces a convective system which closely resembles a conceptual MCS with: well organised updraughts, continuous convective initiation along the cold pool edge, a large area of stratiform rain behind the region of heavy precipitation and a rear inflow jet.

**The observed and simulated cold pools are both very large (fronts travel >800 km), several likely driving factors are identified.** Comparison between the simulated and observed cold pools and theoretical density currents has shown that the analogy of a simple single release gravity current is not appropriate. Factors which are likely to make this case behave differently to the simple model are: (1) the southwestward movement of the MCS while it continues to generate convective downdraughts, (2) the presence of a strong northward pressure gradient over almost the entire latitudinal extent of the Sahara, generated by lee cyclogenesis south of the Atlas Mountains, and (3) shallow, precipitating, convective cells along the northern edge of the cold pool, repeatedly refreshing the evaporatively cooled air in the flow.

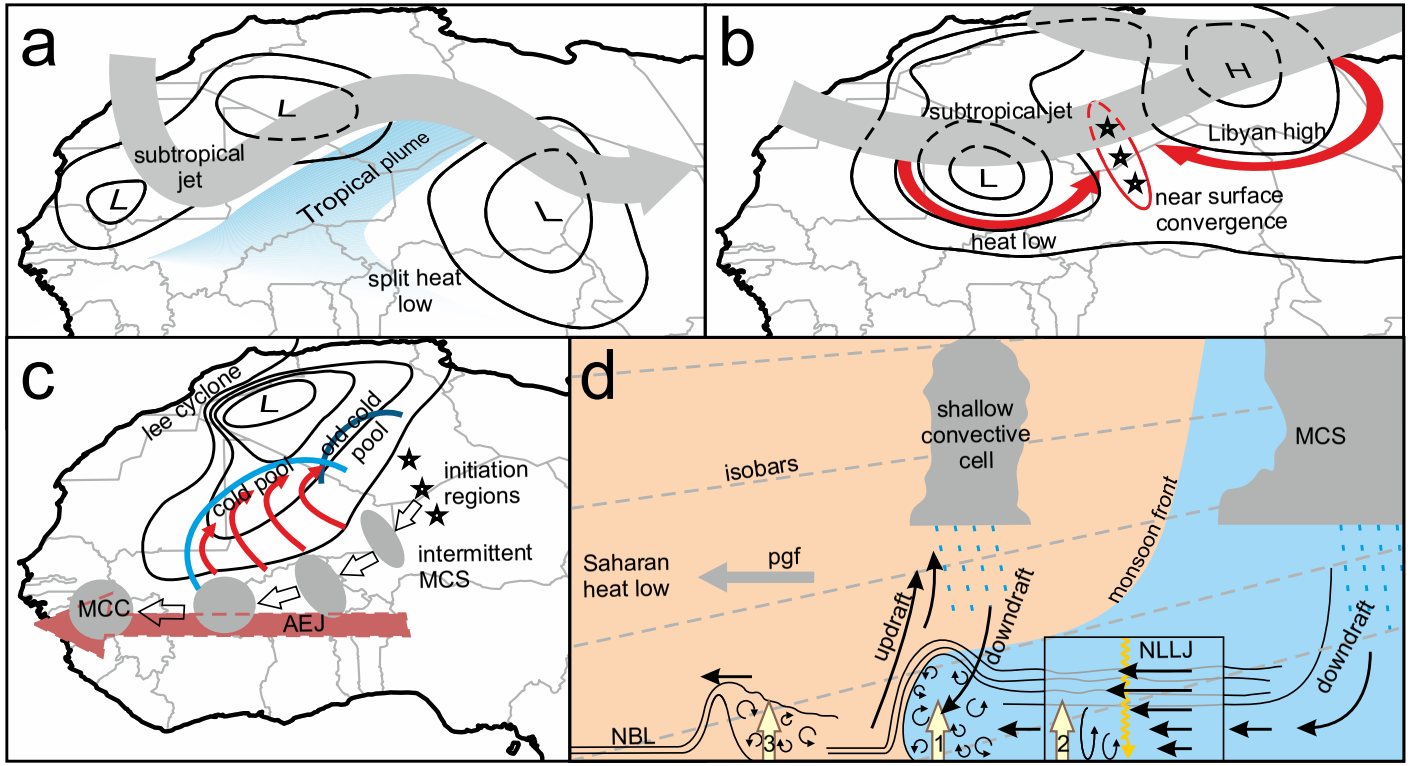


FIGURE 4.19: Schematic detailing both the synoptic- and mesoscale processes that led to the production of the large mesoscale convective system (MCS) and dust plume on 10 June 2010. (a) Formation of a tropical plume and the effect on the Saharan heat low (SHL) (Section 4.3). (b) Restrengthening of the SHL and generation of a high over Libya creating low-level convergence (Section 4.3). (c) Initiation and development of the MCS, its production of cold pools and the influence of the lee cyclone and the African easterly jet (AEJ) (Sections 4.3.2, 4.4.2, and 4.4.3). (d) The mesoscale features that lead to dust uplift. Shown in (a), (b), and (c) is: mean sea-level pressure features (black isobars), subtropical jet (large grey arrows), tropical plume (blue shading), low-level winds (red arrows), cold pool edges (blue lines), convective initiation regions (black stars), the African easterly jet (large light red arrow) and the position of the MCS (grey ellipses). Shown in (d) is the production of a convective cold pool spreading into the desert including the pressure gradient force (pgf) produced by the lee cyclone, shallow convective cells, the monsoon front, and the three dust uplift processes identified. These are (1) strong winds at the leading edge of the cold pool flow, (2) nocturnal LLJ within the aged cold pool, and (3) formation of an internal bore on the NBL. See section 4.6 for a more detailed discussion.

**Several meteorological features capable of lifting dust have been identified in the simulation of this case.** To identify dust uplift processes a measure of the meteorological impact on dust uplift (DUP) was used, as it separates the meteorological influences of dust deflation from the land surface. Three main processes were identified from the WRF simulation (Figure 4.19d): (1) high winds at the leading edge of the cold pool, (2) the mixing of high momentum air to the surface from an enhanced NLLJ within the aged cold pool once solar heating begins to erode the nocturnal stable layer, this process is not extensively documented in literature but is dynamically similar to that proposed in Heinold et al. (2013), (3) the generation of an internal bore on the NBL, by the cold pool, which then propagates into the desert with the stable layer acting as a wave guide. As the amplitude of the bore is large compared to the depth of the NBL, the bore is thought to be turbulent and in the simulation produces high values of DUP. This represents a little considered mechanism for dust uplift. It generates much lower total DUP than the cold pool, but does represent a mechanism which increases the distance from a MCS that dust uplift can occur.

The results presented here address the specific mechanisms that produced this unusual dust plume. Chapter 6 identifies the synoptic-scale conditions common for other convective, dusty episodes. Another area that has been investigated (Chapter 5) is the difference in low-level moisture between a number of operational analysis and reanalysis products. As in Section 4.2 of different initialisation data has been found to have a large impact on the outcome of this high resolution simulation.

Important findings from this work include:

- A precipitating tropical cloud plume causes disruption of the Saharan heat low (SHL) and moistening of the central Sahara.
- Later, restrengthening of the SHL and a Mediterranean cold surge produce convergence over the Hoggar and Aïr Mountains.
- Emerging from this region a mesoscale convective system (MCS) is produced with intermittent triggering of new cells.
- Later, favourable deep layer shear produces a much stronger and regular triggering of new cells.
- A very large cold pool is produced that lifts dust.
- The longevity and vigor of the MCS, an enhanced pressure gradient due to lee cyclogenesis near the Atlas Mountains, and shallow precipitating clouds along the northern edge of the cold pool help the cold pool spread deep into the Sahara.
- Dust uplift processes identified are: (1) strong winds near the cold pool front, (2) enhanced nocturnal low-level jet within the aged cold pool, and (3) a bore formed by the cold pool on the nocturnal boundary layer.

# Chapter 5

# Disagreement between Low-level Moisture Distribution in (Re)analysis Products

In Chapter 4 it is described how different initialisation data for a high resolution simulation of a large mesoscale convective system (MCS) had a much greater impact on the outcome of the simulation than changes made to the model physics. This is in agreement with the findings of Birch et al. (2013) and Schepanski et al. (2014), both of which highlight the sensitivity of high-resolution simulations over West Africa to differing initial conditions. Also important is the fact that there can be significant disagreement in mean sea-level pressure between operational analysis and reanalysis products (collectively referred to as (re)analysis products) in the Saharan heat low (SHL) region (Marsham et al., 2011). In this chapter low-level moisture is used to identify differences between (re)analysis products due to the importance of the representation of the West African Monsoon (WAM) both for operational and research activities (Section 2.1). This is of specific importance for this study due to the connection between the position of the intertropical discontinuity (ITD) and the production of mesoscale convective systems (MCSs) which provide the majority of rainfall for West Africa and are mechanism for dust uplift. Further discussion of the importance of these processes is discussed in Section 2.1

Studies discussed in Chapter 2 have shown the direct impact of organised convection on the position of the intertropical discontinuity (ITD) (Cuesta et al., 2010; Flamant et al., 2007, 2009) and that global models struggle to capture these effects (Garcia-Carreras et al., 2013; Marsham et al., 2013b). Comparing simulations with parameterised and explicit convection and observations, Marsham et al. (2013b) show that the representation of convection impacts on the entire WAM and its diurnal cycle. Cold pools contribute a substantial part of the monsoon flow in explicit simulations, but are essentially missing when using parameterised convection. This is consistent with recent observations from the central Sahara showing that cold pools contribute significantly to meridional water vapour transport and that their absence appears to be a major cause of global model bias (Garcia-Carreras et al., 2013; Marsham et al., 2013b). The complex and mesoscale nature of these processes mean that they are difficult to represent in highly parameterised coarse grid models. When combined with poor observations it is not surprising that, under certain meteorological conditions, (re)analysis products disagree with one another.

In this chapter the position of the intertropical discontinuity (ITD) is estimated in 7 (re)analysis products (Table 3.1 in Chapter 3) during 11 monsoon seasons (April–September, 2000–2010). The ITD is used as it gives information about the large-scale distribution of moisture over west Africa as well as providing information about the representation of the WAM. This chapter aims to answer the following questions: (1) how big are the differences between products? (2) Where and when is the disagreement in ITD position greatest? (3) Under what meteorological conditions do episodes of high disagreement occur? And (4) are periods of disagreement linked with increased likelihood of dust uplift over the Sahara.

Section 5.1 of this chapter describes the methods that have been used to identify disagreement of the low-level moisture fields and the verification of those methods. Section 5.2 focuses on the characteristics of the periods of disagreement, including the magnitude and location of disagreement, product biases as well as seasonal and interannual variations of disagreement. Section 5.3 contains analysis of periods of extreme disagreement including the role of rainfall and the lifting of dust. Section 5.4 is a summary of the findings and an outline of the conclusions from this chapter.

It is important to note that agreement between products does not imply that they are correct. Disagreement on the other hand, points to differences in model first guesses or in the ability to assimilate the available data. It is assumed here that these periods of

disagreement are associated with meteorological conditions that make it particularly hard to produce a consistent ensemble of (re)analyses. By characterising these conditions it is hoped that decisions regarding the use of (re)analyses will be informed by greater knowledge of the conditions associated with disagreement. Special caution should be used employing any product in isolation at such times. Investigating periods of disagreement and the weather associated with them gives clues as to the process errors leading to (re)analysis ensemble deviation. This motivates future work into improving the representation of these processes and research to identify which products perform better at such times.

## 5.1 Methods

As mentioned in Chapter 2, the ITD is the interface between the moist southwesterly monsoonal flow and the dry northerly Saharan wind. It is defined as the confluence of surface winds and also has strong near-surface moisture and temperature gradients. In practice the ITD is more usually recognised as the point at which the near-surface dew point temperature is equal to 14°C. The ITD moves north over the northern hemisphere (NH) summer and then retreats during and after September (Sultan and Janicot, 2000, 2003). As well as the seasonal cycle, the position of the ITD also has a strong diurnal dependence (Parker et al., 2005; Pospichal et al., 2010; Sultan et al., 2007) and is influenced by synoptic- and mesoscale meteorology. Increased boundary-layer moisture south of the ITD in regions where the monsoon flow is deep, allows for the production of MCSs. The ITD is also an important feature for dust uplift due the production of haboobs by MCSs, nocturnal low-level jets (NLLJs) and dust uplift along the monsoon front itself (Bou Karam et al., 2008; Burton et al., 2013; Marsham et al., 2008).

The (re)analysis products used in this study are: (1) the National Center for Environmental Prediction (NCEP) National Center for Atmospheric Research (NCAR) Reanalysis 1 (NCEP-NCAR hereafter), (2) the NCEP Department of Energy (DOE) Reanalysis 2 (NCEP-DOE hereafter), (3) the NCEP Climate Forecast System Reanalysis (CFSR), (4) the NASA Modern Era Retrospective-analysis for Research and Applications (MERRA), (5) the European Centre for Medium-Range Weather Forecasts (ECMWF) ERA-Interim reanalysis (ERA-int hereafter), (6) the ECMWF operational analysis (ECMWF-op hereafter), and (7) the NCEP FNL (final) operational Global Forecast System (GFS) analysis.

These products are discussed in greater detail in Section 3.3.

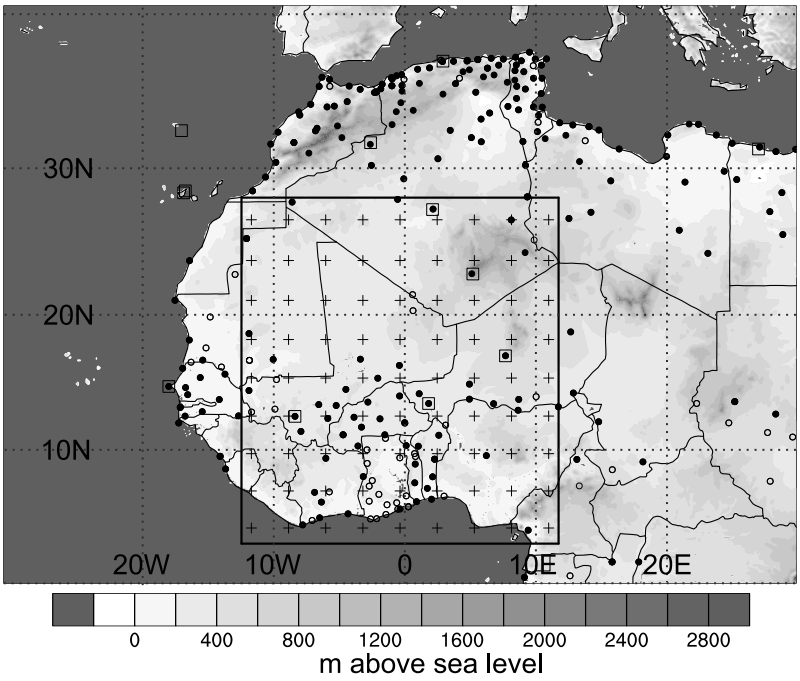


FIGURE 5.1: Geographical overview of West Africa. Also shown is the box bounding the area being studied (3°–28°N and 12°W to 12°E) with crosses to show the points onto which (re)analysis data has been re-gridded. Squares represent radiosonde stations that launched an average exceeding one sonde per day (based on the Integrated Global Radiosonde Archive) April–September, 2000–2010. The circles represent surafce observation stations, unfilled circles reported on at least 25% of the (re)analysis times and filled circles on at least 50% of the (re)analysis times being studied (based on MetOffice Integrated Data Archive System; MIDAS).

The box marked on Figure 5.1 shows the region being studied (3–28°N, 12°W–12°E). This box covers the latitudinal range of the monsoon flow including the Gulf of Guinea coast, the Sahel, and the southern to central Sahara. All (re)analysis products are re-gridded to approximately 2.5° × 2.5° to match the coarsest resolution products (NCEP-NCAR and NCEP-DOE), producing the 9 × 9 grid shown on Figure 5.1. For each product and time, the zonal-mean position of the ITD is estimated by estimating the location of the 10gkg$^{-1}$ isoline of the 925-hPa specific humidity ($q_{925}$) by interpolation. As mentioned above, the ITD is more usually defined by confluence of low-level winds, a strong gradient in moisture, or a surface dewpoint temperature of 14°C. The 10 gkg$^{-1}$ method used here for large-scale ITD identification gives similar results to the ITD found from the maximum gradient in $q_{925}$ and the maximum gradient in total column water vapour. However, the confluence of near surface winds is much more variable and so does not agree as strongly as the methods based on the distribution of atmospheric moisture. This is not seen as a problem for this

study as the distribution of low-level water vapour is deemed to be the more important feature due to its role in the production of convective storms. This suggests that despite being based on a threshold value (which is typically a little drier than a surface dewpoint of 14°C) this metric is a good indicator of the large-scale latitude that the moist monsoon flow reaches. Therefore, the single latitude value generated for each product at each time is a good measure of the approximate ITD position across the zonal range of the box this is referred to as ITDΦ hereafter.

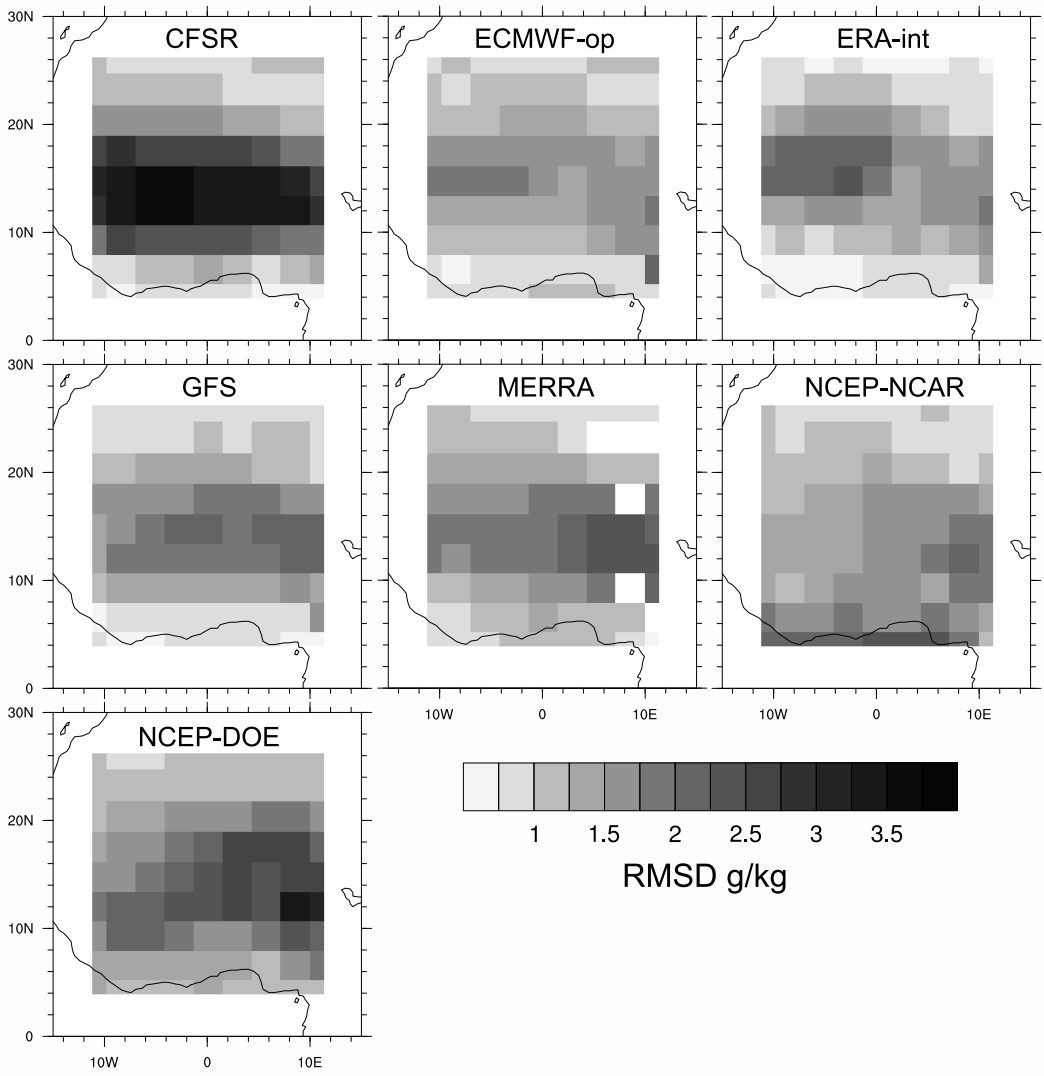


FIGURE 5.2: Root Mean Square Difference (RMSD) of 925 hPa specific humidity ($q_{925}$) relative to the mean $q_{925}$ of all products averaged over the monsoon season April–September, 2000–2010. For abbreviation of product names see Table 3.1 in Section 3.3.

To check whether differences between ITDΦs across (re)analysis products are controlled by their individual representation of the WAM or by large-scale moisture biases, the root mean square difference (RMSD) of $q_{925}$ is calculated. Thereby, each product is compared

to the mean $q_{925}$ field calculated from all seven products, indicating the difference between a product and the ensemble mean. Figure 5.2 shows the RMSD for each product averaged over all the times in the study. There is a clear pattern in the distribution of high values with the majority occurring between 10°N and 20°N. This coincides with the climatological position of the ITD over the monsoon season (Buckle, 2004; Sultan and Janicot, 2003). CFSR has the highest RMSD values, suggesting that its $q_{925}$ deviates from the ensemble mean by a larger amount and/or more frequently than the other products over this latitude range. The low RMSD values to the north and south, present in most products, show that these regions are far less likely to produce disagreement between the products. The high RMSD values over the Gulf of Guinea in NCEP-NCAR show that this product has a moisture bias not associated with the monsoon front. This is in agreement with (Trenberth and Guillemot, 1995), who identified large and significant moisture biases in NCEP-NCAR over the tropics.

It has been shown that the ITDΦ is an adequate measure of the large-scale low-level moisture distribution over West Africa. It has also been shown that the largest/most frequent disagreements occur in the region of the ITD. Therefore, it has been decided that differences of ITDΦ between (re)analysis products can be used to identify periods when there is disagreement in the representation of the monsoon flow.

In order to identify periods of ITDΦ disagreement, the standard deviation ($\sigma$) in ITDΦ across (re)analyses is calculated using ITDΦ values at each 6-hourly (re)analysis time. The top 5% of $\sigma$ values across all eleven monsoon seasons are then used to detect the periods of strongest disagreement. By identifying when these events occur and by investigating the meteorology at these times the specific conditions that produce disagreement can be identified. Figure 5.3 shows an example time series of ITDΦ from each product (coloured lines) and $\sigma$ (black dashed line) for the 2010 monsoon season. The grey areas indicate periods where the $\sigma$ threshold (1.34° latitude) is exceeded and so is in the top 5% of $\sigma$ values across all 11 years. Figure 5.3 shows the northward progression and then southward retreat of the ITDΦ through the season. It can be seen by eye that large disagreements tend to occur during more rapid northward shifts and retreats in the ITDΦ, which last between 1 and 8 days. More systematic analysis of this is made in Section 5.3.

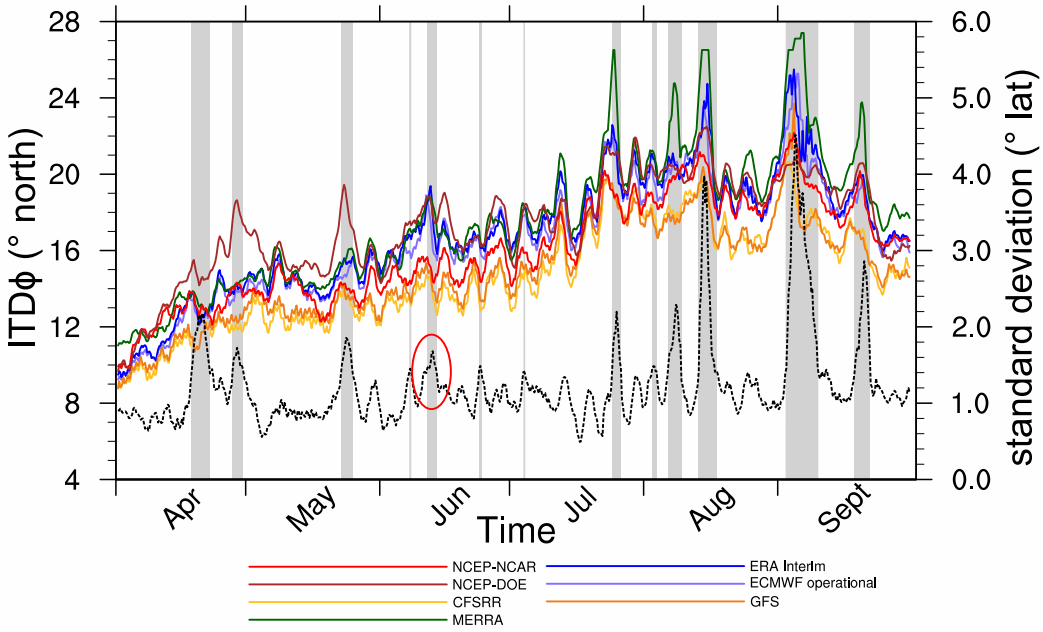


FIGURE 5.3: Behaviour in 2010 of the zonal-mean intertropical discontinuity position (ITDΦ) for all seven (re)analysis products (coloured lines), standard deviation calculated from ITDΦs (excluding CFSR, dashed black line) and periods when the standard deviation exceeds the threshold and is in the top 5% of standard deviation values across all eleven years (grey shading). The circled disagreement event is the event discussed in Chapter 4.

## 5.2 Characteristics of the disagreement between (re)analysis products

### 5.2.1 Magnitude and distribution

As an example, Figure 5.4 shows a difference plots between three (re)analyses at 0000 UTC 07 June 2010 (the initialisation time used for the high-resolution limited area simulation in Chapter 4). This time is part of an extreme disagreement event that is highlighted in Figure 5.3.

Shown in Figures 5.4b–d are the differences in $q_{925}$ between ECMWF-op and ERA-int, MERRA and ERA-int, and MERRA and CFSR (all regridded to a 2.5° × 2.5° grid). The estimated position of the ITD in each product is also displayed (based on a $q_{925}$ 10 gkg$^{-1}$ isopleth) as well as the perturbation of the monsoon front away from its zonal, climatological configuration. Stippled areas on Figures 5.4b–d show where the difference between the products is greater than 50% of the mean value of the two products. For better interpretation, an image from the Meteosat Second Generation (MSG) Spinning Enhanced

Visual and InfraRed Imager (SEVIRI) channel 7 (8.7 $\mu$m thermal infrared) is also shown for the same time (Figure 5.4a). The production of this northward bulge is associated with anomalous low-level winds linked to the tropical plume like event, discussed in detail in Chapter 4. The deformation of the monsoon flow can be seen in all four products by the 10 gkg$^{-1}$ isopleths (Figures 5.4b–d).

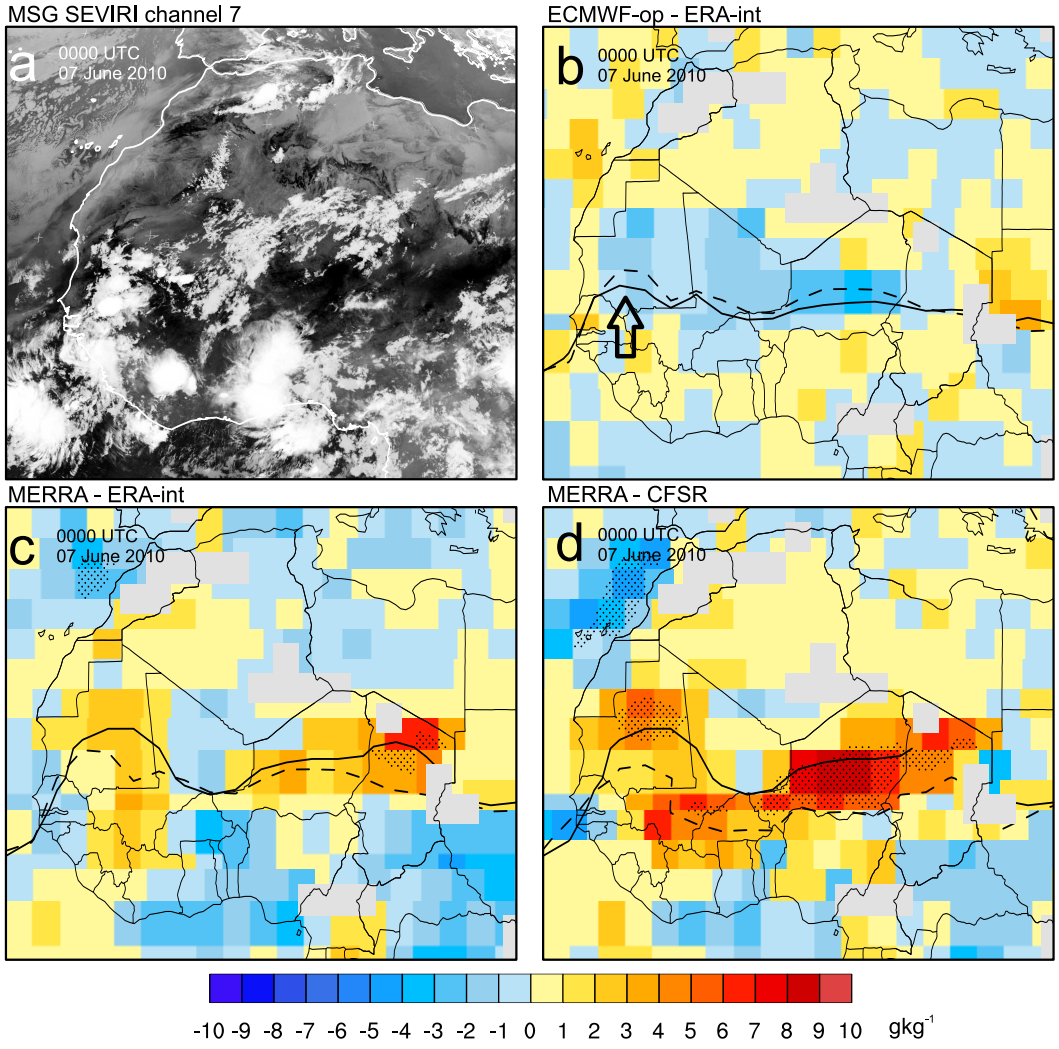


FIGURE 5.4: Magnitude and distribution of disagreement at 0000 UTC 07 June 2010. (a) shows a Spinning Enhanced Visual and InfraRed Imager (SEVIRI) channel 7 (8.3 9.10 $\mu$m thermal infrared) image. (b), (c), and (d) show difference plots of 925 hPa specific humidity ($q_{925}$) for (a) ECMWF-op and ERAint, (b) MERRA and ERA-int, and (c) MERRA and CFSR. Black lines represent the $q_{925}$ 10 gkg$^{-1}$ isopleth in both products shown in each panel (solid line for the first product in plot label, dashed for the second). Grey areas indicate where the 925 hPa pressure surface in either product intersects with the ground (this is very similar across all products), whilst stippled regions indicate where the difference between products is greater than 50% of the mean value.

Figure 5.4b shows the difference between the ECMWF-op and ERA-int. Both are produced by ECMWF, as such, they have similar model physics and data assimilation methods.

There are relatively small differences between these products. As expected from Figure 5.2, $q_{925}$ differences are largest close to the edge of the monsoonal flow. In particular, ERA-int has over 3 gkg$^{-1}$ higher $q_{925}$ compared to ECMWF-op in central Niger. Figures 5.4c and 5.4d show the difference between MERRA and ERA-int and MERRA and CFSR, respectively. The comparison between MERRA and ERA-int (Figure 5.4c) shows a greater range of $q_{925}$ differences compared to Figure 5.4b. ERA-int has values over 3 gkg$^{-1}$ higher than MERRA in the northward perturbation of the monsoon flow. Similarly to Figure 5.4b, the position of the two 10 gkg$^{-1}$ isopleths in Figure 5.4c are quite close together. However, over Mauritania and eastern Niger and Chad the ITD in MERRA is further north than in ERA-int by as much as 300 km.

The comparison between MERRA and CFSR shows very large differences in $q_{925}$ (Figure 5.4d). The differences associated with the northward perturbation of the monsoon flow are large, MERRA has values over 6 gkg$^{-1}$ higher than CFSR in this region. There are also large differences in the region between the two ITD positions over much of the longitudinal extent of West Africa. MERRA positions the ITD approximately 200–300 km further north than the CFSR, producing $q_{925}$ differences of over 8 gkg$^{-1}$, with differences of over 6 gkg$^{-1}$ covering very large areas of central and southern Niger. The magnitude of these differences represent a large fraction of the typical values for the Sahel (between 5 and 25 gkg$^{-1}$) as shown by the widespread stippled regions on Figure 5.4d.

Recently the suitability of CSFR, ERA-int, and MERRA data for climate trend analysis and long-term water budget studies has been questioned by Lorenz and Kunstmann (2012). This is due to differences when they were compared with observations of the hydrological cycle.

It should also be noted that there are differences in $q_{925}$ close to the Moroccan and Western Saharan coasts. These are present in Figures 5.4b–d, but do not appear to be linked to the behaviour of the monsoon flow. Instead the flow in this region is controlled by the Azores high and the Atlantic inflow to the Saharan heat low (e.g., Grams et al. (2010)).

### 5.2.2 Biases

Figures 5.5a–g show the ITDΦs for each product plotted against the mean ITDΦs calculated from all other products, with each point representing a single (re)analysis time

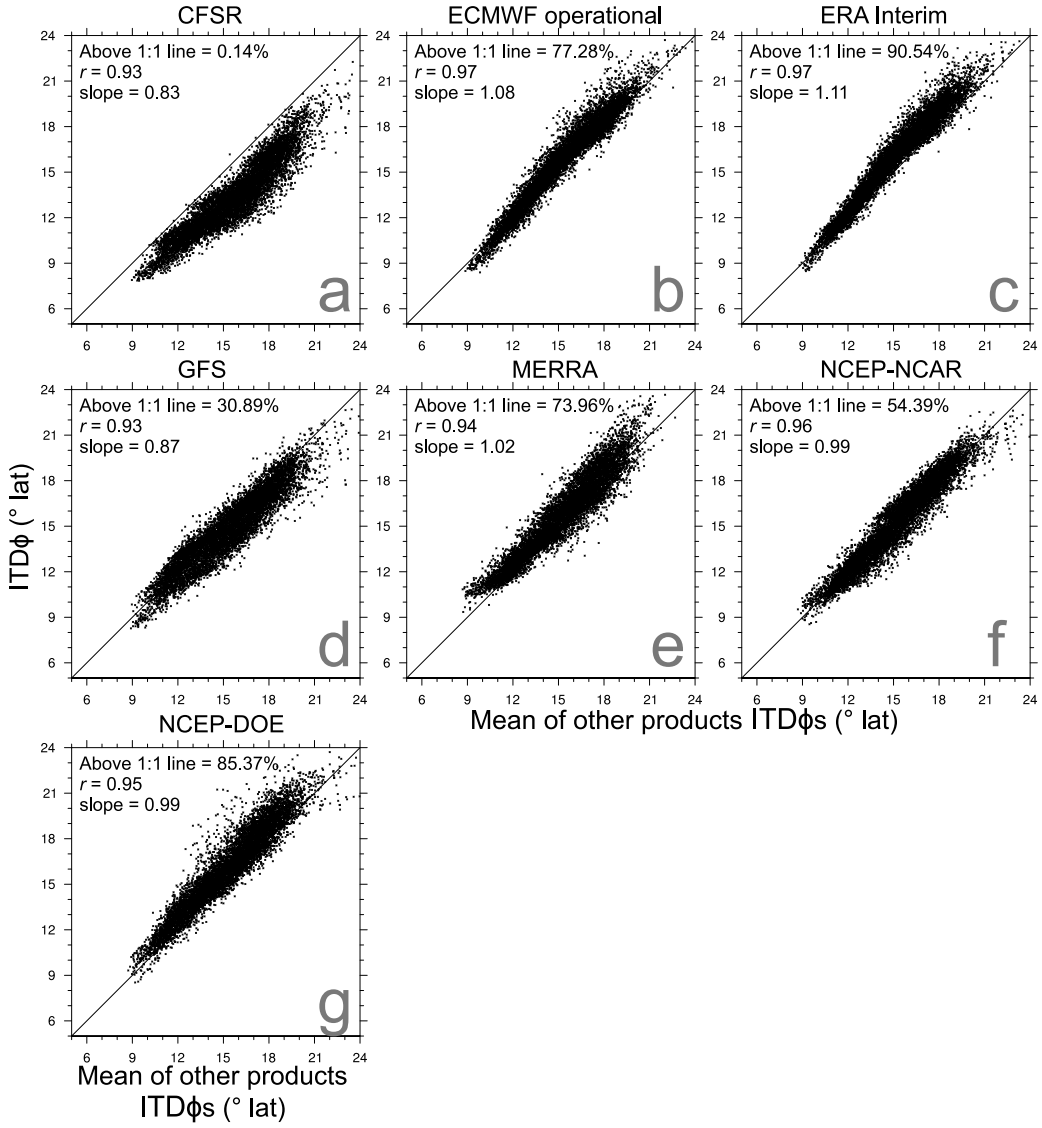


FIGURE 5.5: Scatter plots showing zonal-mean intertropical discontinuity position (ITDΦ) from each product plotted against the mean ITDΦ calculated from all other products. Shown is (a) CFSR, (b) ECMWF-op, (c) ERA-int, (d) GFS, (e) MERRA, (f) NCEP-NCAR, and (g) NCEP-DOE. Shown on each plot is a diagonal line indicating where perfect agreement between the products' and the mean ITDΦ would lie, a percentage of the points that lie above the diagonal line, a Pearson's correlation coefficient ($r$), and a slope of the least squares linear trend.

over the eleven monsoon seasons. Shown on each plot is a diagonal that represents perfect agreement between each product and the mean of the other products, the percentage of points above the diagonal, a Pearson correlation coefficient ($r$), and the slope of the least squares linear trend. All products display high $r$ values (over 0.93), showing that there is very good agreement with respect to the dominating seasonal behaviour of the ITD. ECMWF-op and ERA-int both score particularly highly (0.97). The slopes too, are

all close to 1, this suggests that the direction and magnitude of the dominating seasonal movement is similar in all products. CFSR and GFS produce the lowest slope values, 0.83 and 0.87, respectively. This, and the position of their points with respect to the diagonal suggest that their ITDΦs are likely to be further south compared to other products, when the monsoon flow reaches especially far north. CFSR has all but 0.14% of the points below the diagonal showing that its ITDΦ values are systematically further south compared to the mean ITDΦ values of the other products (between 100 to 200 km). This feature can also be seen in Figure 5.6a, which shows the mean difference between each product's ITDΦ and the mean of all the other products for all eleven monsoon seasons. In Figure 5.6a the CFSR ITDΦ is clearly positioned much further south than most of the other products in all years, however, it shows a slight reduction in this difference over time (possibly driven by the introduction of new satellite data assimilated into the product). Another striking feature in Figure 5.6a is the variation in GFS behaviour, showing a southward displacement of ITDΦ in 2000 and 2007–2010. Given that it is an operational product, possible reasons for this behaviour are changes to the GFS model or data assimilation technique or different meteorological conditions from year to year. In Figure 5.5d we can see that 31% of GFS points are above the diagonal. This is relatively low when we consider the influence that CFSR has on the mean ITDΦ. Figure 5.5g shows that NCEP-DOE's ITDΦ is sometimes much further north than the other products. While the magnitude of this difference can be hundreds of km, the occurrence of such behaviour is rare.

### 5.2.3 Interannual variations

In order to ascertain whether certain years produced higher or lower levels of disagreement, two measures are used. Figure 5.6b shows the mean $\sigma$ (black line) and the proportion of times $\sigma$ is in the top 5% (grey line, see section 5.2) for each of the eleven monsoon seasons. Both measures have been calculated without using CFSR due to the systematic bias discussed in section 5.2.2. Figure 5.6b shows that the lowest scoring year in both metrics is 2006. Its mean $\sigma$ across the entire monsoon season is approximately 0.5° latitude and contains less than 2% of the highest-ranking disagreement events. This is much smaller than 1/11 of the events (9.1%) if the extreme events were distributed evenly across the monsoon seasons. Other years that stand out are 2000 and 2010 with much higher scores in both metrics. By comparison of 6-hourly time series of ITDΦ and $\sigma$, such as those

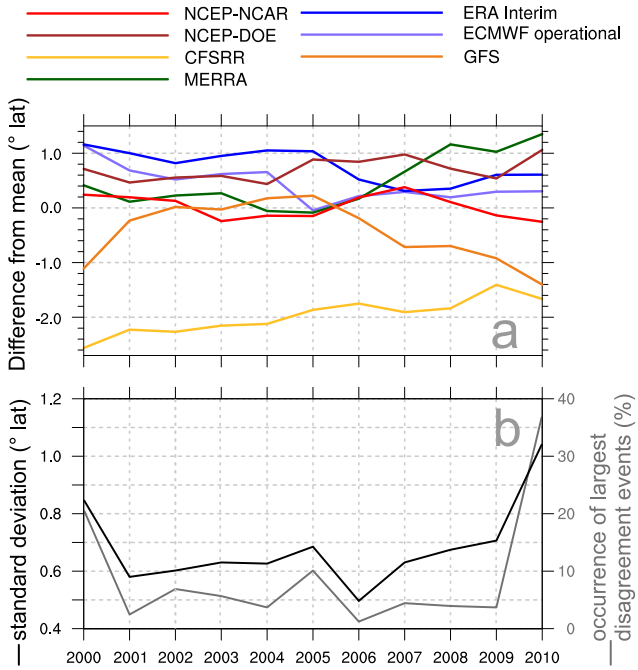


FIGURE 5.6: Interannual behaviour where (a) shows the mean displacement of the zonal-mean Intertropical Discontinuity position (ITDΦ) from the mean ITDΦ of the other products, (b) shows the standard deviation ($\sigma$) averaged over the monsoon season (black lines) and the percentage of times that it exceed the extreme disagreement threshold for each year (grey line). Both measures in (b) have been calculated without CFSR due to the systematic bias it displays.

shown in Figure 5.3 for 2010 (see Appendix A), it appears that the high $\sigma$ values in 2000 are primarily the result of the GFS ITDΦ being south of the other products, with its behaviour resembling that of the CFSR for extended periods. This raises the mean $\sigma$ value over the season to approximately 0.85° latitude compared to the values seen in most other years (between 0.6° and 0.7° latitude). It also means that when other products display disagreement with one another in 2000 $\sigma$ is more likely to be within the top 5% of values across the 11 years. Over 20% of highest-ranking disagreement times occur in 2000.

As mentioned in Section 5.2.2, from 2007 to 2010 GFS behaves similarly to 2000, being further south than other products (Figure 5.6a). However, it is only in 2010 that $\sigma$ and the proportion of top disagreement times is significantly increased. The high values for these measures in 2010 appear to be driven by a number of single events. These are responsible for large differences between the products' ITDΦs, and therefore, produce spikes in $\sigma$ over several days (Figure 5.3). The impact this has is to raise the mean monsoon season $\sigma$ to over 1° latitude and the number of highest ranking disagreement times to over 35%.

The events that produce these large spikes in disagreement in 2010 and other years are predominantly associated with northward surges and retreat of the monsoon front, this behaviour is discussed in detail in 5.3.

### 5.2.4 Seasonal variations

Figure 5.7a shows the seasonal cycle of disagreement between (re)analysis products for 18 decads across the monsoon season. There seems to be a relationship between the position of the ITDΦ and the level of disagreement between products. This can be seen through the increase in $\sigma$ (Figure 5.7a, black line) over the period from April to August, and a reduction during September, which matches the climatological northward progression and retreat of the monsoon front (Sultan and Janicot, 2003). A more rapid increase in $\sigma$ occurs at the end of May/start of June with a smaller increase in early August. The distribution of the extreme disagreement times across the season (grey line) shows that there is a peak in early June and another in August. It is thought that the May/June feature is linked to the monsoon pre-onset where the monsoon flow jumps further inland prior to the start of the monsoon rains (Sultan and Janicot, 2003). This is also a time of year associated with an increased occurrence of dry squall lines and regions of large downdraught convective available potential energy (DCAPE; Marsham et al. (2008)). The features in August are likely linked to the position of the ITD, in the poorly observed interior of West Africa (Figure 5.1; with the ITDΦ at 15° to 25°N at this time of year), and the higher frequency of MCSs producing cold pools (Guy and Rutledge, 2012).

Figure 5.7b shows the same mean $\sigma$ as in Figure 5.7a (black line), but also $\sigma$ calculated including CFSR (single dot dashed line) and $\sigma$ for 2006 only (double dot dashed line). By removing CFSR the mean $\sigma$ is reduced by approximately a third (Figure 5.7b) but the pattern of disagreement stays the same. When only considering 2006, $\sigma$ across almost the entire monsoon season is significantly reduced. It is likely this result is due to the heavy augmentation of the upper air observation network that formed part of the African Monsoon Multidisciplinary Analysis (AMMA) field campaign(Augustí Panareda et al., 2010b; Parker et al., 2008).

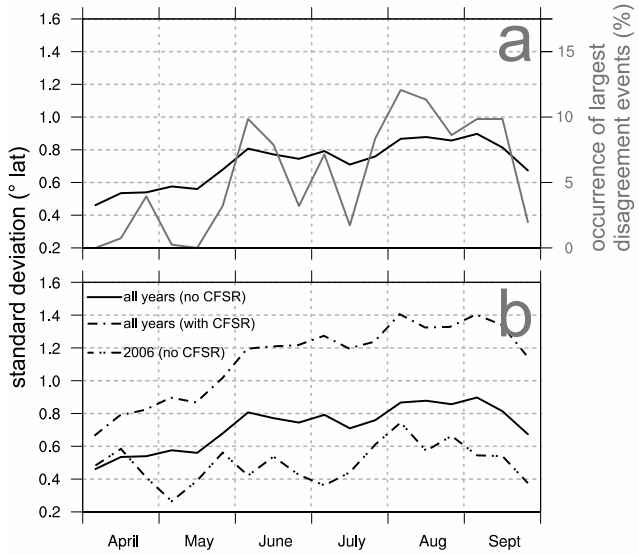


FIGURE 5.7: Seasonal behaviour of zonal-mean intertropical discontinuity (ITDΦ) disagreement. (a) shows the mean standard deviation ($\sigma$) for 18 decads across the monsoon season (black line) and the percentage of times that it exceeded the extreme disagreement threshold for each of the 18 decads (grey line). (b) shows the same mean $\sigma$ as in (a) (black line), but also the mean $\sigma$ calculated including CFSR (single dot dashed line) and the $\sigma$ for 2006 only (double dot dashed line).

## 5.3 Meteorology of extreme ITD disagreement events

As described in section 5.2, any period which exceeds the $\sigma$ threshold (1.34° latitude) to place it in the top 5% of events is classified as an extreme disagreement event (calculated without CFSR). This technique identifies 34 individual events. For each of these, the peak disagreement time was identified (referred to as DAY=0, all other times are relative to the time of peak disagreement). At least one event occurs in each monsoon season (Figure 5.6b). In 2010, 13 extreme events occur, which is far higher than any other year. The next highest are 2000 and 2005 with four events each, this suggests a higher frequency of the meteorological conditions which lead to strong disagreement between products in these years. This is also suggested by the fact that the peaks in $\sigma$ are coincident with large perturbations in the ITDΦ values. This behaviour can be seen in all 11 years studied in this Chapter.

### 5.3.1 An example ITD disagreement event

Figure 5.8 shows the meteorological conditions leading up to a peak in disagreement. This event occurred toward the end of July in 2010 and can clearly be seen in Figure 5.3 as a

northward surge of the ITD$\Phi$ and a peak in $\sigma$. SEVIRI dust imagery and Tropical Rainfall Measuring Mission (TRMM) rainfall retrievals allow for the identification of important meteorological features. The SEVIRI dust imagery is used to diagnose northward surges in the monsoon flow, the production of convective cloud and the presence of convective cold pools. As mentioned in Chapter 3 the detection of changes in the position of the monsoon flow is possible due to a dependence on column water vapour that makes the clear sky daytime surface appear a darker shade of blue when there is more moisture in the atmosphere.

Figure 5.8a shows that at 0000 UTC 20 July 2010 (DAY-4.75) there is a zonally positioned band of MCSs producing heavy precipitation between approximately 5° and 15°N. One day later (DAY-3.75) a large MCS has developed and is positioned over eastern Mali and western Niger (Figure 5.8b). This MCS propagates west and by DAY-3 initiates further convective cells to the north over mountainous regions in southern Algeria and eastern Mali (Figure 5.8c). These new cells grow and form a large MCS (see Figure 5.8d), which propagates southwestward producing heavy rain over Mali and Burkina Faso by DAY-2.25. At this stage SEVRI imagery shows that there is a large northward surge of moist air behind the MCS (dark blue showing elevated humidity and magenta regions indicating dust lifted by a cold pool). This region of anomalously moist air remains over parts of Mali, Mauritania, and Algeria and by DAY-1 a group of convective cells are produced as far as 25° north (Figure 5.8e). This is much further north than is normally expected based on studies of West African convective systems (e.g. Laing et al. 2008; Mathon et al. 2002). These cells later form a MCS (Figure 5.8f; DAY-0.5), which travels west over Mali and Mauritania. After this the northward surge in the ITD drifts west and become less clearly defined through mixing (Figure 5.8g; DAY+0.75), before returning to a more zonal configuration.

The behaviour presented in this example indicates that there is a strong possibility that at least some of the disagreement events are associated with the presence of convective cells. The generation of new cells on the edge or in the wake of an earlier MCS is likely to make the situation more difficult for (re)analyses to represent. In other words, there is little chance that this series of events will be successfully modelled due to the limitations of coarse grids and parameterisations of moist convection. This specific case is also likely

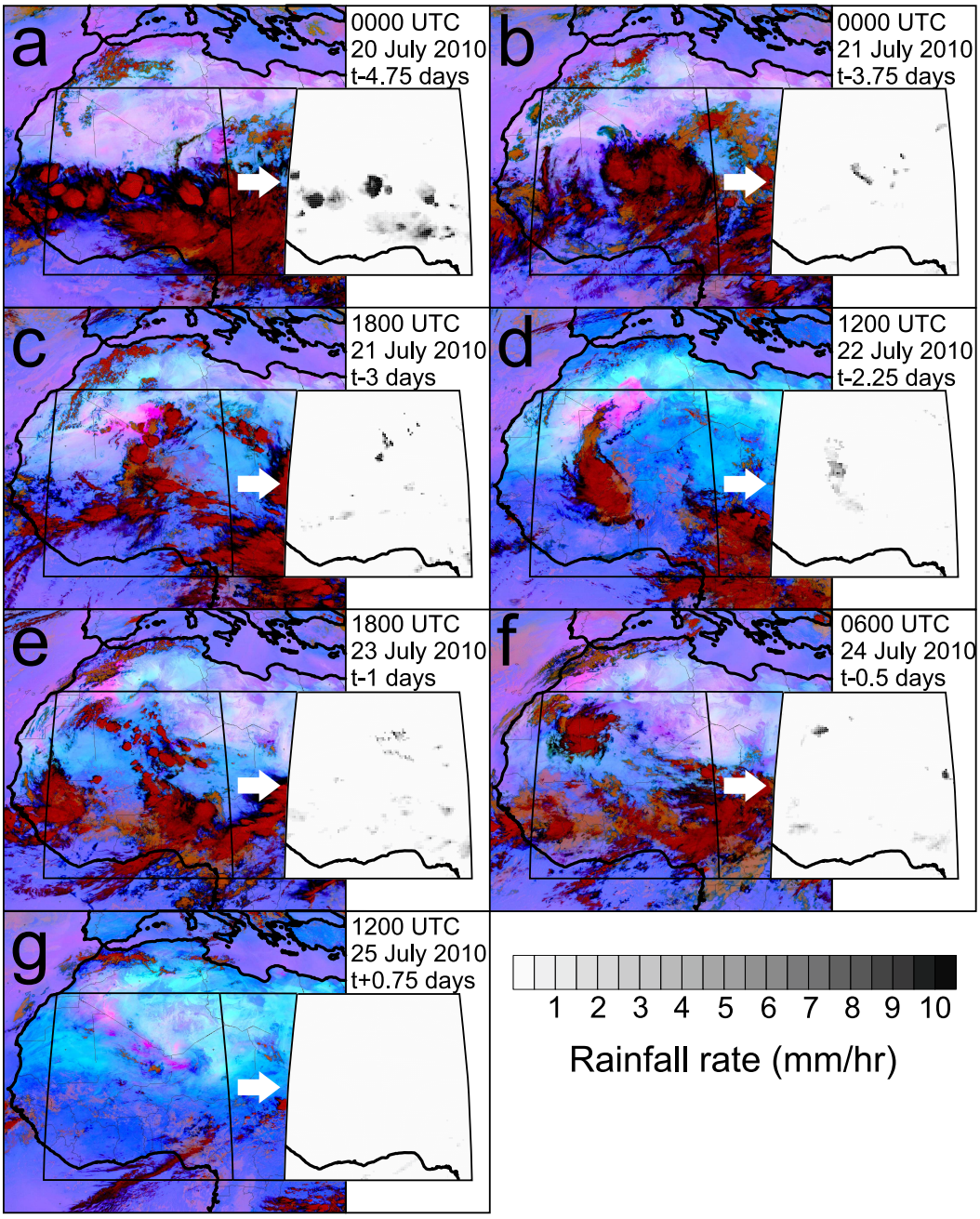


FIGURE 5.8: Development and passage of a northward surge of the monsoon flow, including the repeated production of numerous convective cells within the surge. Shown are Spinning Enhanced Visual and InfraRed Imager (SEVIRI) dust images and Tropical Rainfall Measuring Mission (TRMM) 3B42 rainfall retrievals for (a) 0000 UTC 20 July 2010, (b) 0000 UTC 21 July 2010, (c) 1800 UTC 21 July 2010, (d) 1200 UTC 22 July 2010, (e) 1800 UTC 23 July 2010, (f) 0600 UTC 24 July 2010, and (g) 1200 UTC 25 July 2010. The box shown on the SEVIRI images and bounding the TRMM retrievals is the region being studied in this Chapter and is the same box as shown on Figure 5.1.

to be more difficult to represent as later convective cells are initiated in very data sparse regions (Figure 3.1; Chapter 3).

### 5.3.2 Composites of ITD disagreements

#### Behaviour of the zonal-mean ITD (ITDΦ)

Figure 5.9a is a composite plot of 7 days preceding and 5 days following the peak disagreement time (DAY=0) of the 34 disagreement events identified. The grey-scale shading represents a time-latitude Hovmöller plot of TRMM 3B42 rainfall for the area within the box shown in Figure 5.1 at 3-hourly intervals. The latitudinal position of rainfall is plotted relative to an ITDΦ value averaged across all products and over the 12-day period. This 12-day ensemble mean varies between 13.6° and 21.9°N over the 34 events and has a mean value of 17.8°N. This is similar to the expected range and position of the ITD during the monsoon season. The coloured lines show the position of the ITDΦ for each product plotted relative to the same 12-day ensemble mean. These lines give a good idea of the relative position of each of the products when compared to one another and how they compare to the position and strength of TRMM rainfall. The dashed black line represents the mean $\sigma$ (calculated without CFSR) across all 34 events.

Figure 5.9a shows that the ITDΦ in CFSR is likely to be positioned approximately 3° south of most of the other products. This offset is in agreement with that shown in Figure 5.5a. Also, as expected from Figures 5.5d and 5.6a, the GFS ITDΦ is approximately 1.5° further south than most other products. Unexpectedly, however, there is also an offset in the NCEP-NCAR ITDΦ of approximately 0.75° south of the main group of products during these events. In order to illustrate the range and timing of movement of the ITDΦ in different products rather than their absolute position, they have also been plotted relative to their own 12-day mean ITDΦ rather than the 12-day ensemble mean (Figure 5.9b). The dashed black line showing $\sigma$ remains the same as in Figure 5.9a. In all seven products the composite ITDΦ moves north prior to DAY=0. In CFSR and GFS this northward movement is gradual over the period from DAY-7 to DAY-2. However, in the rest of the products, the ITDΦ maintains its position until approximately DAY-4 at which point a northward surge of the monsoon flow commences. This agrees well with the example shown in Figure 5.8. From DAY-7 to DAY-2, $\sigma$ is relatively stable at around 1° latitude (larger than the long-term mean; see Figures 5.6 and 5.7). This includes the first two days of the northward surge of the ITDΦs seen in most of the (re)analyses. However, between DAY-2 and DAY=0, $\sigma$ increases rapidly during the northward surge and the start of the

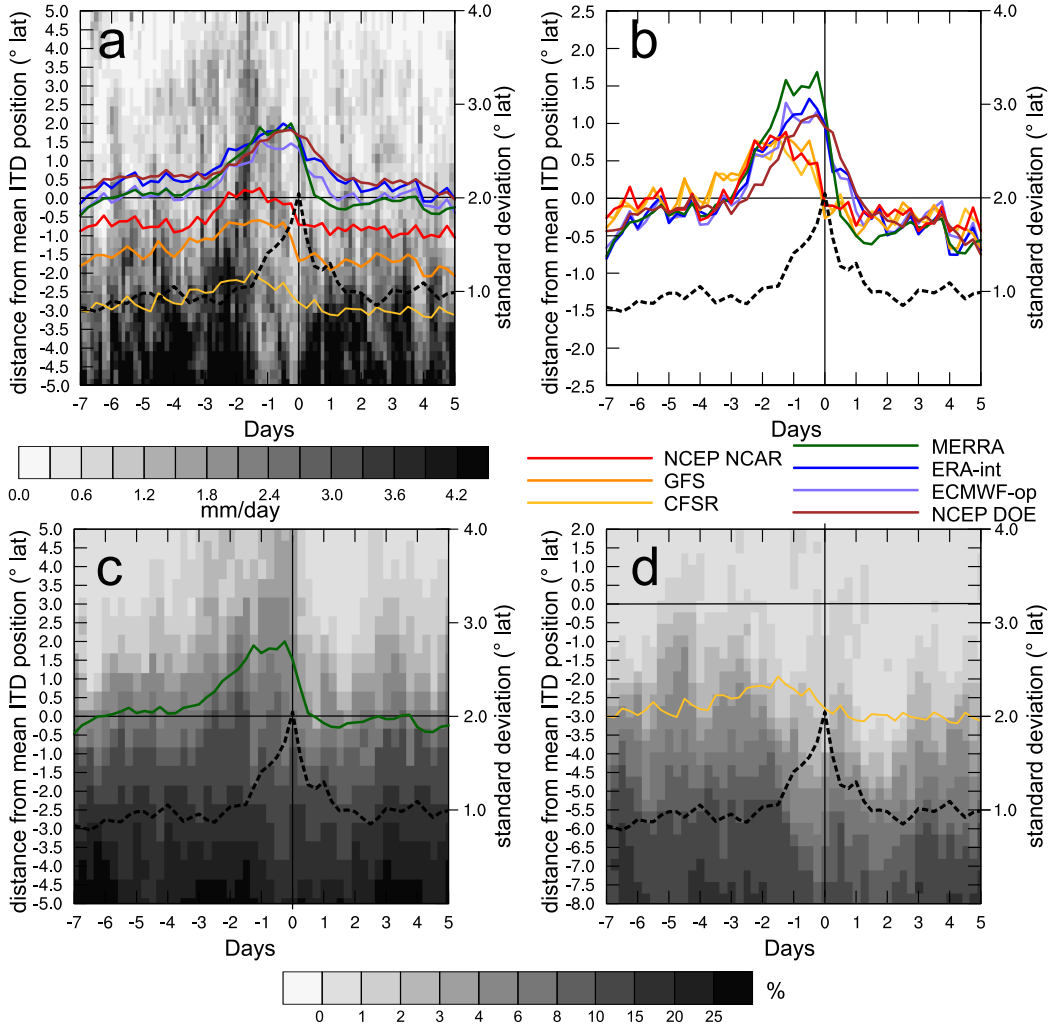


FIGURE 5.9: Composite plots of the 34 events that exceed the standard deviation ($\sigma$) threshold. All panels show seven days preceding and five days following the time of peak disagreement. (a) shows the composite position of each of the products' zonal-mean intertropical discontinuity position (ITDΦ) during extreme disagreement events relative to a 12-day ensemble mean ITDΦ (coloured lines), also shown is a time-latitude Hovmöller plot of Tropical Rainfall Measuring Mission (TRMM) 3B42 V7 rainfall retrievals for the area shown in the box on Figure. 5.1 at 3 hourly intervals (grey shading). (b) shows the ITDΦs for each product plotted relative to their own 12-day mean values, therefore showing the behaviour of the ITDΦs rather than absolute position. (c) and (d) show Hovmöllers of the frequency of cold clouds below −40°C in MERRA and CFSR respectively. The coloured lines on (c) and (d) are the same as plotted in (a) and the dashed black lines on all plots show the same composite standard deviation over the twelve day period.

retreat of the ITDΦs. In Figure 5.9b ERA-int, NCEP-DOE, and MERRA all show the ITDΦ continue to move north reaching a maxima at DAY-0.25. The ECMWF-op ITDΦ behaves similarly but peaks at DAY-1.25 and maintains its position until the start of the rapid retreat at the same time as the ITDΦ in ERA-int, NCEP-DOE, and MERRA. The ITDΦs in NCEP-NCAR and GFS plateau at DAY-2.25 and then start to retreat at the

same time as the products already discussed. The ITDΦ in CFSR starts to retreat at DAY-2 without having moved very far north compared to other products.

The fact that $\sigma$ remains relatively low (still higher than mean value for any part of the season; Figure 5.7) during the initial stage of the northward motion of the ITDΦ could be due to one of three reasons: (1) the important processes are synoptic-scale in nature and therefore are satisfactorily resolved, even with the coarse grids used in the (re)analyses, (2) the assimilation of observations is sufficient to constrain the products despite possible differences between their short-term forecasts or (3) that none of the products represent the situation well due to similar problems representing dynamics, but they converge on a single incorrect answer, there are also insufficient observations to correct the first guesses.

**Rainfall**

TRMM rainfall shown on Figure 5.9a shows the production of heavy rainfall south of the ITDΦ between DAY-6 to DAY-1.5, suggesting the presence of MCSs. This agrees well with the example discussed in section 5.3.1 (Figure 5.8). As seen in Flamant et al. (2007), Marsham et al. (2008) and the case shown in Chapter 4, large MCSs produced close to the ITD are able to significantly advance the position of the monsoon flow by the generation of large evaporatively generated cold pools. However, it is also the case that meteorological features that favour the development of MCSs can be responsible for similar northward surges of the monsoon flow. In particular the passage of African easterly waves (AEWs) across West Africa (Berry and Thorncroft, 2005; Cuesta et al., 2010) or the formation of tropical plumes due to interactions with the subtropical jet stream are known to produce enhanced southerly flow (as shown in Chapter 4).

The composite TRMM rainfall also shows that rain occurs further north than all the products' ITDΦs. The presence of MCSs to the south of the ITDΦs, followed by an increased likelihood of heavy rainfall in the north, points toward incursions of moist air into the northern Sahel and southern Sahara. This might allow for convective triggering in areas that are usually too dry, as is shown in the example in Figure 5.8. Despite the fact that heaviest rain north of the ITDΦs occurs between DAY-3 and DAY-1 there is also some indication of heavy rainfall occurring on DAY-6. $\sigma$ rapidly increases after the northern rainfall on DAY-2 due to the different ITDΦ behaviours described above. This suggests a

link between the unusual rainfall observed in TRMM and the large disagreement produced by the differing behaviours visible in Figure 5.9b.

Two of the most extreme examples are MERRA and CFSR. MERRA shows a wide range of ITDΦ movement (approximately 2.5° latitude), behaves similarly to 3 other products (ERA-interim, ECMWF-op, and NCEP-DOE), and has an ITDΦ that continues to move north after the production of rain north of its ITDΦ. CFSR has a small range of ITDΦ movement (approximately 1° latitude), behaves similarly to GFS and NCEP-NCAR (despite the differences in absolute ITDΦ position, see Figure 5.9b), and shows a southward retreat in ITDΦ after the production of rain in the north. Figures 5.9c and 5.9d show the ITDΦs for MERRA and CFSR (coloured lines) whilst the grey-scale shading shows a time-latitude Hovmöller diagram of the frequency of model outgoing longwave radiation (OLR) that equate to cloud top temperatures of -40°C or colder (assuming an emissivity of 1). These are both plotted relative to the same 12-day ensemble mean ITDΦ used in Figure 5.9a and so can be directly compared to the TRMM rainfall Hovmöller plot shown in Figure 5.9a (note that the window for Figure 5.9d has been shifted to centre on the CFSR ITDΦ). This method has been employed rather than (re)analysis rainfall due to the dependence of TRMM rainfall retrievals on cloud-top temperature. As well as the fact that the deep dry boundary layer in the Sahel and Sahara has a strong potential to limit the amount of lighter parameterised convective rainfall that reaches the surface in the (re)analysis products.

Rainfall produced by MCSs in the TRMM retrievals (Figure 5.9a) south of all the ITDΦs between DAY-6 to DAY-1.5, should correspond to regions of cold cloud in Figures 5.9c and 5.9d. In fact, the shading in Figure 5.9c suggests that MERRA does represent these MCSs. A similar pattern can also be seen in Figure 5.9d for CFSR but less well defined. Also, due to the offset in the position of the ITDΦ the cold cloud occurs significantly further south than seen in observations. Another similarity between MERRA and TRMM Hovmöller plots is the increased frequency of rainfall/cold cloud close to and even north of the ITDΦ. There are, however, some differences in the distributions. Notably TRMM rainfall suggests that relatively heavy rain is likely north of all the ITDΦs between DAY-3.5 and DAY-1. In contrast, the increased frequency of cold cloud at these latitudes is weaker in MERRA (an equivalent period of cold cloud is not present in CFSR). Another difference between TRMM and MERRA is that cold cloud north of the ITDΦ persists until DAY=0, while

there is very little TRMM rainfall in this region after DAY-1. This suggests that the rapid growth and collapse of convective cells, likely responsible for this rainfall (Figure 5.9a), is not well represented by the convective parameterisations in MERRA.

In the TRMM Hovmöller (Figure 5.9a) there is a large reduction of the amount of rainfall over almost the entire 10° latitude range and a much weaker north–south gradient between DAY-1.5 and DAY+0.5. During the same period MERRA and CFSR still display strong north-south gradients of cold cloud frequency and a much less pronounced reduction in cold cloud in the south. The overall greater success of MERRA over CFSR in reproducing the evolution of cold cloud compared to TRMM rainfall, in particular the production of cloud north of the ITDΦ at DAY-1 suggests that the greater northward shift in the ITD in MERRA compared with CFSR is perhaps more realistic, although further research would be needed to confirm this.

### 5.3.3 Increased dustiness

The same days used to produce composites of ITDΦ, TRMM 3B42 V7 rainfall and product OLR (Figure 5.9) have been used to identify whether the meteorology associated with (re)analysis disagreement is linked to the lifting of dust. It is hypothesised that there is a connection due to the increased frequency of heavy rainfall north of the ITDΦs (Figure 5.9a) leading to the production of cold pools over what is likely to be a dry dusty surface.

To investigate this, composites of the 34 events identified are produced using Moderate Resolution Imaging Spectrometer (MODIS) Deep Blue aerosol optical depth (AOD), AOD anomaly and daily mean TRMM 3B42 V7 rainfall. As these are daily averages the plots are generated for 13 days to cover the 12 day period used in Figure 5.9 (these discrete sections of time are referred to as *day* rather than DAY for differentiation from the continuous scale used in Figure 5.9). *day*0 represents the day on which peak disagreement occurred and the daily MODIS Deep Blue and TRMM plots shown in Figure 5.10 are relative to this day. Figure 5.10 shows MODIS Deep Blue 550 nm daily AOD at the top of each panel, and the daily AOD anomaly compared to a MODIS Deep Blue climatology on the bottom of each panel (both AOD measures are plotted in colour), inset is the grey-scale daily TRMM rainfall. Also shown, is the composite ERA-int mean sea-level pressure, position of the composite 10 $gkg^{-1}$ isopleth and a box highlighting the region being studied. The panels

in Figure 5.10 are valid for *day*-6, *day*-4, *day*-2 and *day*+1. Anomalies are calculated with respect to an 11 year climatology of MODIS Deep Blue using a 31 day triangular window filter to produce a smoothed climatology of dustiness. Composites of anomalies are then calculated.

Figure 5.10a indicates that at *day*-6 even before the shift in ITDΦ position discussed in Section 5.3.2 there is a large region with elevated AOD and a strong positive AOD anomaly over large parts of Algeria, northern Mali and northern Niger. The positio and shape of the composite SHL suggest that the anomalously strong AODs are generated by the lifting of dust by low-level jets over Algeria (eg. Birch et al., 2013). The composite TRMMrainfall for *day*-6 indicates a strong north south gradient (more rain in the south) and the 10 $gkg^{-1}$ isopleth is relatively zonal further indicating processes other than convective rainfall being responsible for dust uplift at this time.

By *day*-4 (Figure 5.10b) strength of the AOD has reduced and the AOD anomaly shows that the dust levels present are not far away from climatological values. During *day*-4, which shows weakening and deformation of the SHL and is associated with the start of the northward surge of the ITDΦ in the majority of the (re)analysis products, there is a slight increase in rainfall in the north. This seems to be strongest near the Algeria-Mali border. It is thought that this is likely to be the result of systems such as that shown in Figure 5.8b, that further enhance the northward motion of the ITD. 2 days later at *day*-2 (Figure 5.10c) the composite SHL has weakened and is centred further north and west and there has been a large increase in the amount of rain produced in the northwest of the box being studied. There is only a small change to the AOD and AOD anomaly at this time which is coincident with the rainfall over Mauritania and northern Mali.

As shown in Figure 5.9a the rainfall in the far north persists from DAY-3.5 to DAY-0.5, therefore the day after peak disagreement (*day*+1) there is much less rainfall in the north of 20° north (Figure 5.10d). However, there is a strong increase in the AOD and the AOD anomaly over Mauritania and northern Mali. This region displays a strong positive anomaly compared to the AOD climatology. Although not shown here, the AOD (and AOD anomaly) over Mauritania and western Mali increases steadily over the course of *day*-2 to *day*+1, this is spatially coincident and occurs during and after the strongest rainfall over this region. This suggests that the rainfall has led to the lifting of dust through the generation of convective cold pools. It is possible that once raised in this way

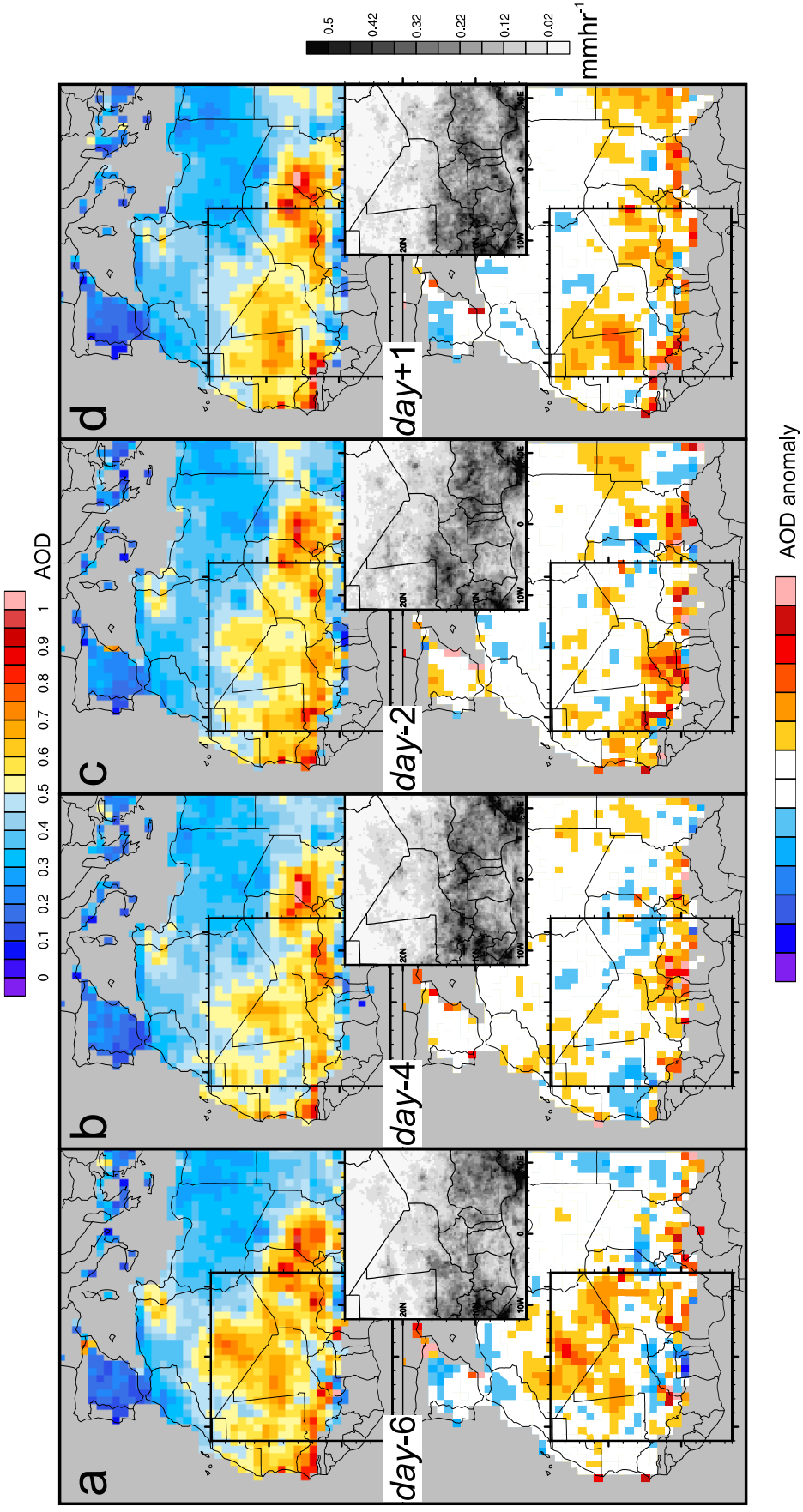


FIGURE 5.10: Composites showing the relationship between rainfall and dust uplift during extreme disagreement events (for definition see Section 5.1). The top of each panel shows the Moderate Resolution Imaging Spectrometer (MODIS) Deep Blue 550 nm aerosol optical depth (AOD), the bottom of each panel shows the AOD anomaly calculated from the MODIS Deep Blue AOD and an AOD climatology calculated over a 31 day triangular window over 11 years (2000–2010). Inset in each panel is the Tropical Rainfall Measuring Mission (TRMM) 3B42 V7 composite rainfall. These are shown for (a) day-6, (b) day-4, (c) day-2 and (d) day+1.

dust could be transported over the Atlantic or north towards the Mediterranean. However, by using a product such as MODIS Deep Blue with a poor temporal resolution, there are limitations on what can be gleaned about the fate of this dust once it is lifted. It is also likely that the dustiness, associated with rainy conditions is underestimated. This is due to the fact that the detection of dust is strongly impaired by the presence of clouds, which in these cases are highly likely to be present. Also, convective cells are likely to reach maturity and produce their strongest downdraughts during the evening and night. The daytime retrieval of dust by MODIS Deep Blue means that dust can be transported far away from the source or could even be deposited before detection can be achieved.

## 5.4 Summary and conclusions

This chapter investigates the differences in low-level moisture distribution over West Africa in seven different reanalysis and operational analysis products (see Section 3.3) during 11 consecutive monsoon seasons (April–September, 2000–2010). These products are routinely used as the best estimates of the atmospheric state for a range of operational and research purposes. However, in parts of West Africa the paucity of the observation network means that the coarse-grid models' first guesses are poorly constrained, leading to product disagreement. The work conducted for this Chapter: (1) identifies periods of the largest disagreement, (2) discusses the interannual and seasonal patterns of disagreement, (3) analyses the meteorology of the episodes that display the strongest disagreement and (4) establishes a link between the the same meteorological processes and anomalously dusty conditions.

**The largest differences in low-level humidity over summertime West Africa tend to be near the ITD and differences between products tends to be large.** Variation in the representation of the West African Monsoon, specifically the latitudinal position of the intertopical discontinuity (ITD), lead to differences in low-level water vapour which represent a large fraction of expected values for the Sahara and Sahel. These differences are shown to be smaller in products that have similar model physics and data assimilation methods, e.g., products from the same centres.

**The position of the zonal mean ITD (ITD$\Phi$) has been used to investigate biases and interannual and seasonal patterns of disagreement between (re)analyses.**

CFSR has a systematic bias, which positions the ITDΦ 100–200 km further south compared to other products during the monsoon season. This southerly offset reduces slightly over the 11 year period studied. GFS shows variable behaviour over the same period, displaying a similar bias to CFSR in the years 2000 and 2007–2010. NCEP-DOE ITDΦ is characterised by rare, but markedly northern outliers.

2006 stands out as a year with very low disagreement between the (re)analyses, most likely due to enhanced upper-air observations during the AMMA field campaign. The two years with the highest levels of disagreement are 2000 and 2010, likely associated with the bias present in GFS and the occurrence of a larger number of extreme events compared to other years respectively.

Seasonally disagreement increases from April to August with particularly large disagreement occurring in late May/early June and in August. The May/June feature is coincident with the monsoon pre-onset, associated with an increased occurrence of dry squall lines and high DCAPE values. The August feature is likely produced by the occurrence of a greater number of MCSs in the poorly observed interior of West Africa.

**The position of the ITDΦ across (re)analyses and retrieved rainfall from TRMM have been investigated and a connection between product disagreement and rainfall north of the ITDΦs has been identified.** 34 extreme events identified are linked to northward surges of the ITDΦ with peak disagreement usually coinciding with the southward return of the ITDΦ. Two groups of (re)analyses are identified, NCEP-DOE, MERRA, ERA-int and ECMWF-op have similar ITDΦ behaviour and values throughout extreme events. CFSR, GFS and NCEP-NCAR have southward offsets of their composite ITDΦ positions of 3°, 1.5° and 0.75° respectively. In all products apart from CFSR the ITDΦ starts to retreat at almost the same time (just before DAY=0). In CFSR the retreat southward begins at DAY-2.

Relatively low disagreement during the first few days of the surge is likely due to either: (1) processes at this time being synoptic-scale and satisfactorily resolved in (re)analyses, (2) assimilation of observations being sufficient to constrain the products or (3) all products fail to represent reality but are still convergent on a single incorrect representation of the atmosphere, before diverging over the following days.

**A link between disagreement events and the occurrence of rainfall is shown, suggesting a role for convective processes in producing (re)analysis disagreement.** TRMM shows the production of rainfall north of the ITDΦs days before peak disagreement possibly linked to secondary triggering of convective cells within the northward perturbation of the ITD. Extreme examples of composite ITDΦ behaviour are examined (MERRA and CFSR; which produce the largest and smallest ranges in ITDΦ movement respectively and the have northerly and southerly position compared to one another). MERRA contains clouds which match the latitude and timing of rainfall retrievals from TRMM prior to peak disagreement. This feature is present but less well defined and offset to the south in CFSR.. Both cold cloud distribution in MERRA and TRMM rainfall composites have an increased frequency north of the ITDΦ, whereas this is absent in CFSR. A reduction in TRMM rainfall over the latitudinal range of the composite at the time of peak disagreement is not reflected in MERRA or CFSR cold cloud which retain a strong north-south gradient. This suggests that they are not capturing all the relevant processes for the evolution of northward surges of the ITD and might explain some of the product disagreement.

**A link has been found between disagreement events and the occurrence of anomalously high aerosol optical depths (AODs) over Mauritania and northern Mali.** High levels of dust are present before the northward surge of the ITDΦ (*day*-6) in the studied products, likely associated with low-level jets forced by a well defined Saharan heat low (SHL). The production of rainfall to the north of the ITDΦs, mostly on *day*-2 and *day*-1, produce an area of anomalously high AOD which persists until *day*+1. This is thought to be driven by the production of convective cold pools and the formation of haboobs as it is spatially and temporally coincident with the composite TRMM rainfall. It is also possible that daytime overpasses of the MODIS product and the connection between the dust uplift and cloud presence leads to MODIS Deep Blue retrievals underestimating the AOD.

Case studies (e.g., Bou Karam et al. (2008); Flamant et al. (2007); Marsham et al. (2008); Chapter 4) show how monsoon surges are commonly associated with MCSs and cold pools. These provide moisture and convergence to trigger further storms. It is difficult to disentangle whether this convective activity produces northward surges through the generation

of cold pools, or is as a result of synoptic-scale features that encourage both convective triggering and northward surges of the monsoon flow (e.g., AEWs, subtropical disturbances). In reality, both probably contribute through the life-cycle of the surges. (Re)analysis models rely on parameterised convection. These parameterisations struggle to produce MCSs and the extensive cold pool outflows. It is known that explicitly resolving convection changes the entire monsoon, with cold-pools forming a major part of the monsoon flow (Marsham et al., 2013b), meaning that their absence is a major cause of bias in global models. Therefore, the results summarised here are consistent with the known errors in modelled moist convection, known to be relevant to the strength of monsoon surges and the position of ITD. The shortage of data in West Africa mean that these model errors cannot be corrected by the data assimilation. Monsoon surges are a major mechanism for dust mobilisation and this work highlights the connection between surges of the monsoon flow, rainfall north of where it is climatologically expected and the lifting of dust. It also underlines the difficulty of using (re)analyses to model dust uplift due to their limitations in representing these processes.

Important findings in this Chapter are:

- Different models, assimilation techniques and assimilated datasets lead to differences between (re)analysis products.
- Deviations on the order of 50% of the mean value of $q_{925}$ over areas spanning hundreds of kilometres are not uncommon
- When disagreement events occur, with respect to low-level moisture, they are often coincident with multi-day northward excursions of the ITDΦs and unusually heavy and northerly rainfall in the Sahel and Sahara.
- The largest disagreement occurs during the southward retreat of the ITDΦs.
- Known errors in the representation of moist convection and cold pools may contribute to the identified disagreements.
- A large reduction in disagreement occurs in 2006, when upper air observations were enhanced during the AMMA campaign, suggesting a greater observational constraint of the (re)analyses than in other years.
- A link has been found between extreme disagreement events and the occurrence of anomalously dusty conditions over Mali and Mauritania.

# Chapter 6

# Anomalously heavy rainfall and dust in the arid Sahara and northern Sahel

It has been shown in Chapter 4 that large mesoscale convective systems (MCSs) are capable of generating very large dust plumes through the production of convective cold pools. Intuitively, it seems that the chance of a MCS lifting dust is increased if it is triggered further north than might usually be expected. This is in part due to the reduced vegetative cover, but also the lack of soil moisture, making surface sediments easier to lift. Therefore, this chapter investigates the occurrence of unusual heavy rainfall events in the Sahara and northern Sahel. In Chapter 5 it was shown that periods when operational analysis and reanalysis products (collectively referred to as (re)analysis products) were in disagreement with regards to the edge of the monsoon flow, were also associated with rainfall north of the zonal-mean intertropical discontinuity (ITD$\Phi$). It was also shown that these events were associated with anomalously dusty conditions coincident with the regions with increased rainfall.

This chapter aims to connect the occurrence of anomalous summertime rainfall in the northern Sahel and Sahara with the lifting of dust. As well as identifying the large-scale meteorological conditions that lead to the production of rainy episodes in the Sahara. This Chapter also suggests a technique for the forecasting of such anomalous rainfall events.

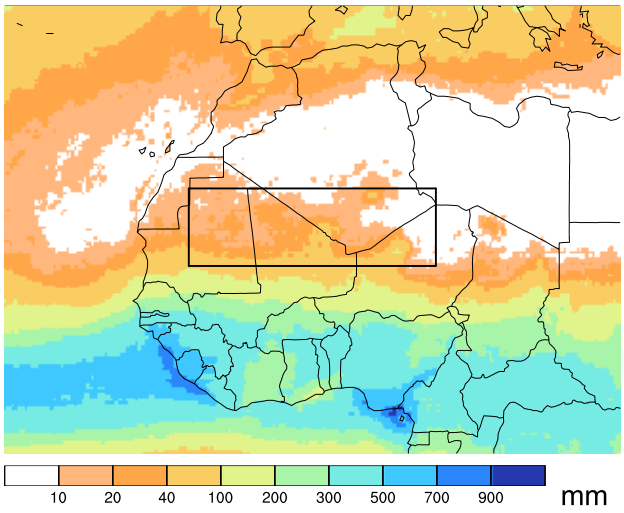


FIGURE 6.1: Mean monsoon season accumulated rainfall. This is calculated using Tropical Rainfall Measuring Mission (TRMM) 3B42 V7 rainfall retrievals from April–September, 1998–2011. The box shown indicates the area being studied in this chapter and is from 12° W to 12° E and 18° N to 25° N.

Section 6.1 details the method used to identify sustained, anomalously rainy periods that include particularly widespread heavy rainfall events. Section 6.2 explores the hypothesis linking anomalously rainy periods to dust uplift and Section 6.3 investigates the synoptic-scale meteorology present before and during anomalously rainy periods. The scale of meteorological anomalies is also shown and statistical comparisons are made with randomly selected days from the 14 monsoon seasons being studied (April–September, 1998–2011). Section 6.4 discusses the preliminary stages of work toward a method of predicting similar periods of anomalously high rainfall in the Sahara and how this compares to observed and forecast rainfall. Section 6.5 provides a summary and conclusions.

## 6.1 Method for rainy period identification

A method has been devised to identify periods that are characterised by prolonged or repeated production of anomalous rainfall in the Sahara and northern Sahel. Firstly a region to be studied is selected, this is shown by the box on Figure 6.1. This region (12° W to 12° E and 18° N to 25° N) covers the dry northern Sahel and a large region of the Sahara desert. Figure 6.1 also shows the mean accumulated Tropical Rainfall Measuring Mission (TRMM) 3B42 V7 rainfall for the monsoon season, calculated using the 14 monsoon seasons studied in this chapter. The daily climatology for the mean rainfall accumulation

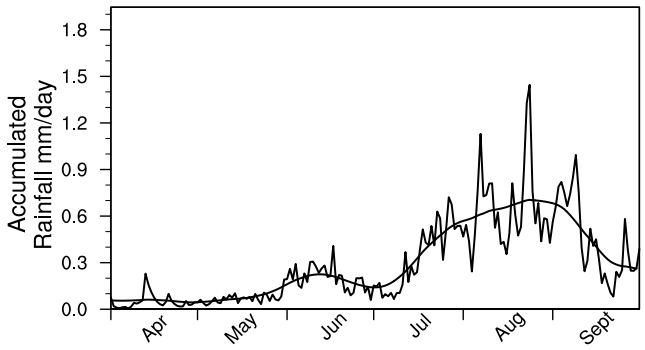


FIGURE 6.2: Climatology of rainfall in the Sahara and northern Sahel calculated using the Tropical Rainfall Measuring Mission (TRMM) 3B42 V7 rainfall retrievals within the box shown on Figure 6.1. The highly variable line indicates the behaviour of the daily means over all 14 years and the smoothed line is calculated from the daily means using a 31 day triangular window filter.

within the box is calculated and shown as the highly variable line on Figure 6.2. Due to this behaviour it is unsuitable to attempt to diagnose anomalous rainfall in given years, therefore, a 31 point triangular-window filter is applied to produce a smoothed climatology, (Figure 6.2). It should be noted that the rainfall within the box is clearly associated with the seasonal variation of the West African Monsoon (WAM). Of note are, the increase in daily rainfall at the end of May/start of June which coincides with the WAM pre-onset (Sultan and Janicot, 2003), a rainfall minima in late June/early July that coincides with the onset of the main monsoon season and an increase in rainfall during July, peaking in August. Also, the monsoon rains recede over the course of September which can also be seen with the rainfall within the box. This pattern also closely matches the seasonal pattern of disagreement with respect to low-level moisture between (re)analysis products (Chapter 5), further suggesting a connection between anomalously rainfall in the Sahara and disagreement between (re)analysis products.

In order to identify periods of anomalous rainfall, a time series of mean rainfall within the box for each of the monsoon seasons is compared to the climatology shown in Figure 6.2. Figure 6.3 is an example showing the anomalies of mean rainfall within the box (black line), and the percentage of the box with rainfall over 5 mm day$^{-1}$ (red line) for the 2010 monsoon season. It is clear from this plot (and those for other years; Appendix B) that the rainfall in this box is heavily dependent on how much of the region is covered by rainfall over the 5 mm day$^{-1}$ threshold. This is not surprising as heavy rainfall is likely to produce a larger, daily, mean rainfall rate. It is also expected that the majority of rainfall in this region is associated with the presence of convective cells which have a

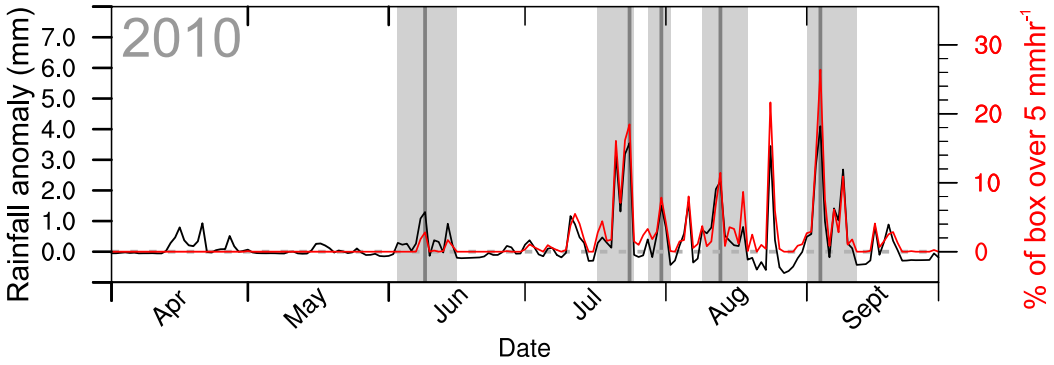


FIGURE 6.3: Seasonal variation in daily rainfall anomaly (black line) and the proportion of the box being studied with an accumulated daily rainfall in excess of 5 mm (red line) for the 2010 monsoon season. Also shown are the 5 anomalous rainy episodes identified (light grey shaded regions) and the day within each of these events with the largest proportion of the box exceeding the 5 mm threshold (dark grey lines).

high rate of rainfall. The dashed, grey, horizontal line indicates zero for both the mean rainfall anomaly and the area covered by heavy rainfall. It should be noted that rainfall detected by TRMM in this region might not accurately represent rainfall reaching the surface, this is due to evaporation in the deep, dry Saharan boundary layer and limited high quality precipitation data in some years (Section 3.2). However, in terms of identifying periods when convective cells are present and might lead to dust uplift, TRMM is sufficient to highlight the most important periods. The grey shaded regions shown in Figure 6.3 indicate periods where there is a positive rainfall anomaly within the box and at least one day with rainfall exceeding 5 mm day$^{-1}$ over a region greater than 3.5% of the box. This equates to approximately 70,000 km$^2$, and, given the total rainfall amounts over an entire monsoon season (Figure 6.1) 5 mm day$^{-1}$ represents a high rate of rainfall. In addition to this, anomalously rainy episodes must be 5 days in length or longer. If these criteria are fulfilled for shorter periods separated by a single day, adjacent episodes are combined and treated as a single event. The dark grey, vertical lines indicate the day within an anomalously rainy episode which has the largest area covered by heavy rain. In further analysis in Sections 6.2 and 6.3 these extreme days within more prolonged rainy episodes are used as reference time ($day0$), other days are referenced relative to this reference day.

This method of episode identification has found 36 separate events over the 14 year period. The shortest episodes are 5 days in length while the longest is 24 days. The distribution of events across the 14 year period is not even. 2006 and 2010 have 6 and 5 events respectively,

while the conditions in 2001 do not qualify at all due to the lack of any prolonged anomalous rainy periods. The lack of anomalously rainy episodes in 2001 might serve to explain why in Chapter 5 it is second only to 2006 in having the lowest disagreement (both measures shown in Figure 5.6). However, the occurrence of six episodes of anomalous rainfall in 2006, contrasts strongly with the very low levels of product disagreement. This further suggests the positive impact of enhanced upper-air observations as part of the African Monsoon Multidisciplinary Analysis (AMMA) field campaign. 48% of anomalous rainfall events appear to be linked to periods of extreme (re)analysis disagreement (Chapter 5). While 41% of the identified periods of extreme disagreement between (re)analyses are temporally coincident with anomalous rainy episodes. By removing 2006 from the calculation of these percentages due to the likely impact of AMMA observations the percentage of rainy episodes temporally coincident with disagreement events increases to 57% while the percentage of disagreement events temporally coincident with anomalous rainy episodes reduces slightly to 39%. This suggests that in 2006 the link between heavy rainfall in the Sahel and Sahara and the production of disagreement of (re)analyses was weakened, this is consistent with the problems with (re)analyses discussed in Section 5.3.2 in Chapter 5.

## 6.2 Dust uplift associated with anomalous rainy episodes

It is hypothesised that anomalously rainy episodes in the Sahara and northern Sahel are linked to the lifting of dust from the surface. This is thought to be due to the production of evaporatively generated cold pools, however, it is also true that the northward surges of the monsoon flow that encourage the initiation of convective cells are known to be associated with the lifting of dust (Bou Karam et al., 2008; Burton et al., 2013; Marsham et al., 2008). To test this hypothesis, the rainy episodes and extreme rainfall days identified above have been used to produce composites of the MODIS Deep Blue aerosol optical depth (AOD) in a similar manner to the shown in Chapter 5 (Figure 5.10). As MODIS Deep Blue data is only available from 2000 to present only 31 of the 36 identified episodes are included in the AOD composites. A detailed description of the MODIS Deep Blue AOD product can be found in Section 3.2. Figure 6.4 shows the composite AOD and AOD anomaly for days before and after *day*0. A climatology for each grid point of the MODIS Deep Blue AOD is calculated and subtracted from the daily values of AOD in the

same manner as discussed for the box average TRMM rainfall in Section 6.1. The black lines and labels shown on the AOD map at the top of each panel indicate the percentage of the possible MODIS overpasses that were used to generate the composite AOD. As MODIS Deep Blue only works over bright surfaces the percentage is zero over heavily vegetated and oceanic regions. Variations in this percentage over the Sahara are produced by gaps between satellite swaths as well as the rejection of cells due to the presence of clouds. The cells unavailable due to gaps in the swaths are likely to be relatively evenly distributed, therefore a lower value shown on the composites here indicates an increased chance of cloudiness.

Figure 6.4a shows that on four days before the peak raininess (*day*-4) the AOD within the box is already high, having absolute AOD values in excess of 0.6 (0.4 represents very hazy conditions). From the AOD anomaly we can see that in most regions this level of airborne mineral dust is not unusual as the AOD anomalies are relatively low (most parts of the box have AOD anomalies smaller than $\pm 0.04$). However, there are stronger positive anomalies located over central and southern Algeria and northern and western Niger.

Two days later at *day*-2 (Figure 6.4b) the AOD within the box has risen, especially in the west. There is a strengthening of the AOD over Mauritania, Mali and Algeria, and what was a small region of high AOD on the northern edge of the box on *day*-4 has spread over much of the western and central parts of the box. In the AOD anomaly there is a trend of increasingly positive anomaly suggesting that the meteorological conditions present are responsible for greater than normal dust uplift. North of the studied region there is a positive anomaly that stretches from western Algeria to Tunisia. The eastern part of this anomaly seems to be linked to the Basin of Chotts paeloelake in the Algeria-Tunisia border region (Figure 2.12). It is thought that the western part of the same feature is linked to dust lifted, both from the Basin of Chotts, but also dust transported north from the western Sahara dust hot spot (Schepanski et al., 2007; Washington et al., 2003). The maximum anomalies in the studied region in Figure 6.4b are $\pm 0.12$.

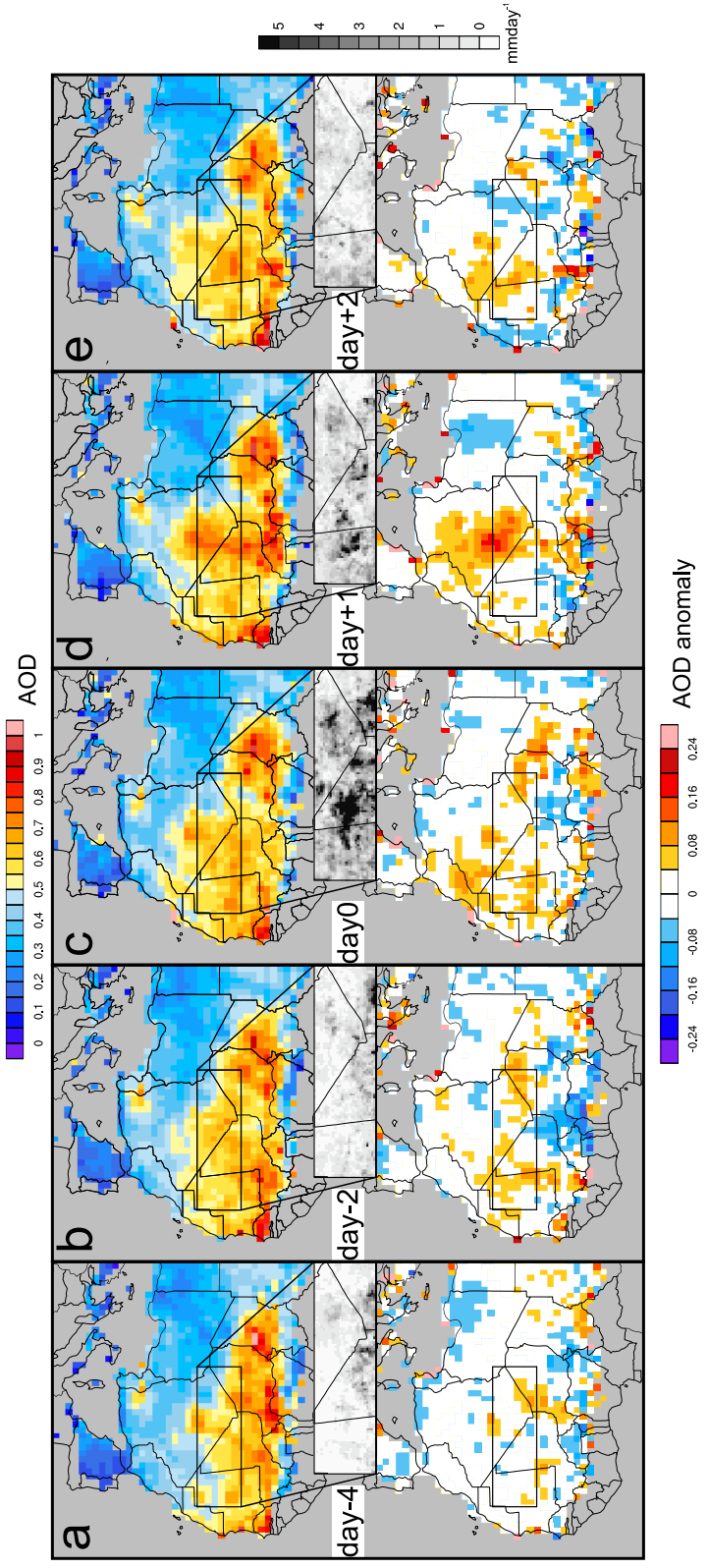


FIGURE 6.4: Composite Moderate Resolution Imaging Spectrometer (MODIS) Deep Blue 550 nm aerosol optical depth (AOD) (top of each panel) and AOD anomaly (bottom of each panel) and composite Tropical Rainfall Measuring Mission (TRMM) 3B42 V7 rainfall (grey shaded panels) for 36 anomalous rainy episodes. The box shown is from 12° W to 12° E and 18° N to 25° N. The days shown are (a) *day*-4, (b) *day*-2, (c) *day*0, (d) *day*+1 and (e) *day*+2.

On *day*0 the AOD values increase slightly from *day*-2 and have maximum values in excess of 0.7 (Figure 6.4c). The high AOD values in the northwest cover all of Mauritania and Mali, and a large part of southern and western Algeria. In southeastern Algeria there is a reduction in the AOD with values falling below 0.5. The high AOD region over Mauritania, Mali and Algeria is positioned further north again compared to *day*-2. By looking at the AOD anomaly for this day, it can be seen that within the studied box the region of strong positive anomaly has weakened in the east. However, the positive anomaly has strengthened in the west.

The following day (*day*+1; Figure 6.4d) there are very high AOD values present in the central longitudinal section of the box. AODs in excess of 0.8 are also present within the box, as well as north and south of it. These very high AOD values suggest that the anomalously heavy rainfall within the box is linked to strong dust uplift. The AOD anomaly strength is greatest at this time, with values in excess of 0.20 over central Algeria. It is likely that the AOD is highest one day after the heaviest rainfall for three reasons, these are: (1) the overpasses of MODIS satellites that are used to generate the Deep Blue AOD occur during the day. When we consider that the peak strength of MCSs are generally during the evening and night, we can see that much dust uplift by haboobs will occur after the *day*0 MODIS overpasses, (2) as shown in Chapter 4, Heinold et al. (2013) and Marsham et al. (2013b), there is a connection between the production of nocturnal low-level jets (NLLJs) and aged cold pools. Once again this dust uplift is likely to occur the morning after the generation of a cold pool and will therefore peak on *day*+1 and (3) despite improving on Total Ozone Mass Spectrometer (TOMS) and the Ozone Monitoring Instrument (OMI) in terms of reducing the height bias, Hsu et al. (2004) and Shi et al. (2012) indicate that aerosol height might have an influence on MODIS Deep Blue AOD. Therefore, it is possible that the mixing of dust throughout the deep Saharan boundary layer the day after it is lifted produces higher AOD retrievals. Another consideration is that the MODIS Deep Blue product (among others) is less capable of retrieving very high AOD values compared to the SEVIRI AOD (Banks et al., 2013). As the events being studied are likely to produce very high atmospheric loadings of dust there is a chance that the AODs shown here are underestimated.

Considering that the events have been selected due to the occurrence of heavy rainfall it was suspected that the composite AOD retrievals might be depressed by the occurrence

of clouds. However, the percentage of possible overpasses used to generate composites (not shown) suggests that the cloudiest conditions occur on *day*+1 and coincide with the highest AOD values both temporally and spatially.

By *day*+2 (Figure 6.4e) the retrieved AOD values are still high and the region of high AOD seems to have moved west slightly. This is possibly due to the transport of the dust lifted the previous two days by the African Easterly Jet (AEJ). The AOD anomaly has weakened with a negative anomaly in the east of the box and a positive anomaly in the west. The maximum anomaly values are in excess of ±0.08, much weaker than only one day earlier suggesting that there has been significant mixing or deposition over this time.

## 6.3 Synoptic-scale meteorological analysis

### 6.3.1 Composites of meteorological fields

It has been shown that the anomalously rainy periods (focussing on periods of most widespread intense rain) are linked to anomalously strong values of AOD. Therefore, it has been decided to investigate the meteorological conditions present to glean information about the synoptic-scale conditions which lead to anomalously rainy and dusty episodes.

Figure 6.5 shows daily mean composite plots over the 36 heavy rainfall events of a number of useful meteorological fields. Included on each panel is: (1) 200 hPa geopotential ($geo_{200}$; red lines), geopotential can be used in a similar way to pressure at a given height and information about the direction and speed of the flow can be gleaned, (2) 925 hPa streamlines based on 925 hPa u and v winds ($stream_{925}$; blue arrows), this gives information about the low-level circulation of air, as well as regions of low-level convergence and divergence, (3) mean sea level pressure ($mslp$; black lines and high and low labels) this is used for indicating the position of the composite Saharan heat low (SHL), (4) 10 gkg$^{-1}$ isopleth for the composite 925 hPa specific humidity ($q_{925}$; thick dashed green line) indicating the large-scale position of tropical moisture associated with the monsoon flow and (5) the frequency of cloud cover (grey shading), giving further information about the availability of moisture and the potential regions where clouds (including convective cells) might be produced.

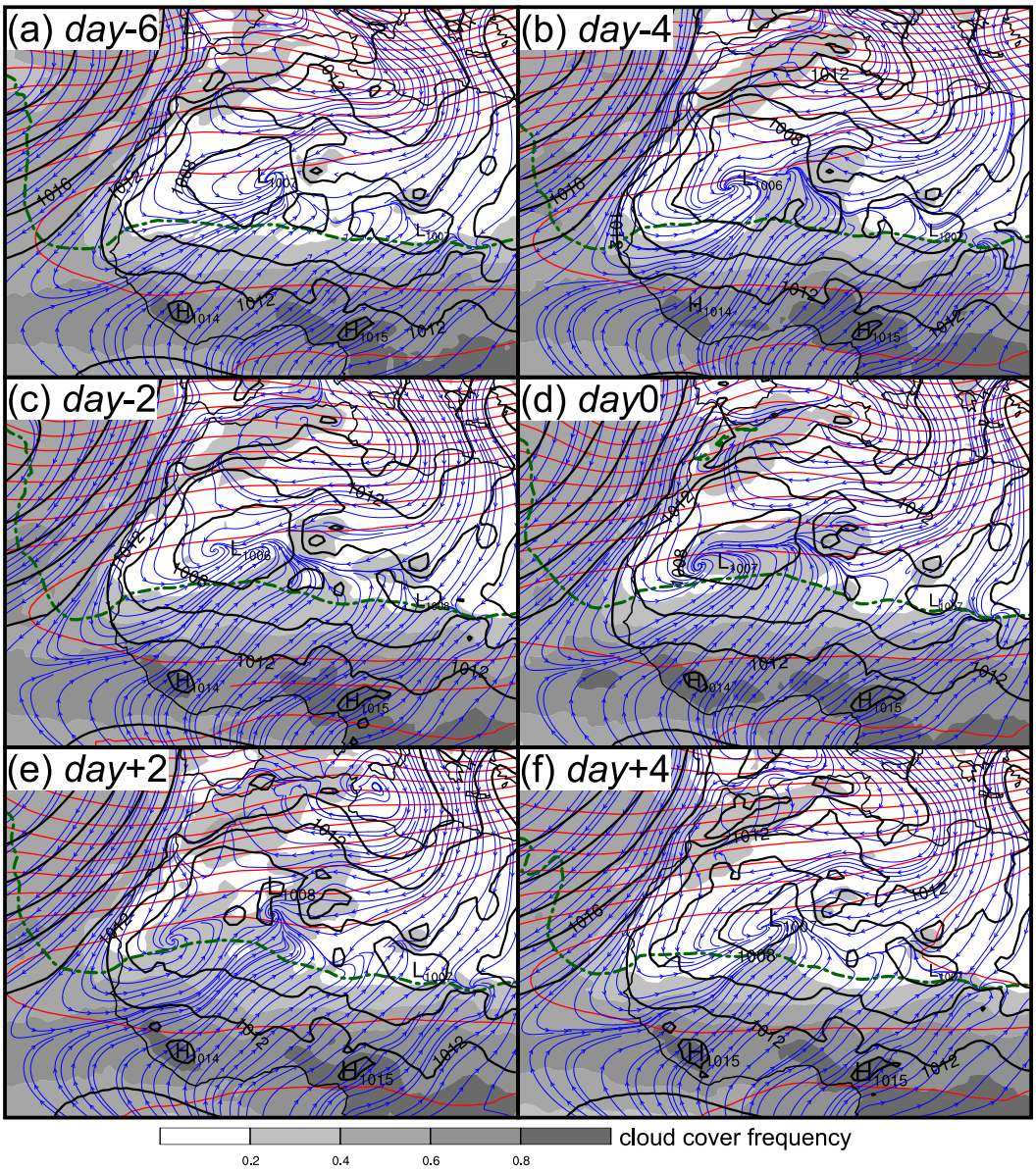


FIGURE 6.5: Composites of meteorological fields during anomalously rainy episodes using European Centre for Medium-Range Weather Forecasts (ECMWF) ERA Interim (ERA-int) reanalysis data. Shown are: frequency of cloud cover across the 36 events identified (grey shading), the position of the 10 gkg$^{-1}$ specific humidity isopleth on the 925 hPa pressure level ($q_{925}$; bold, green, dashed line), streamlines of 925 hPa winds calculated from u and v winds ($stream_{925}$; blue arrows), mean sea level pressure and high and low pressure labels ($mslp$; black lines) and 200 hPa geopotential ($geo_{200}$; red lines separated by 400 m$^2$s$^{-2}$). These are shown for (a) *day*-6, (b) *day*-4, (c) *day*-2, (d) *day*0, (e) *day*+2 and (f) *day*+4.

All fields are taken from European Centre for Medium-Range Weather Forecasts (ECMWF) ERA interim reanalysis (ERA-int). It is assumed that synoptic-scale features at upper-levels are sufficiently well reproduced within reanalyses, therefore features in the $geo_{200}$ should be well represented. Also, despite issues with reanalysis products highlighted in

Chapter 5 the behaviour of near surface fields such as $stream_{925}$, and those heavily dependent on water vapour distribution ($q_{925}$) are also used here. The interpretation of these fields takes into account the issues of reanalyses over poorly observed regions by focusing on changes in features with time and how these are likely to influence the large-scale behaviour of the atmosphere. Inferences about mesoscale processes, or any assumptions that they will be represented are avoided. It is assumed that the changes over time will at least partly represent the evolution of the real cases, and that the magnitude of changes might not be representative. The *mslp* is used solely to indicate the changing position of the SHL, this is further informed by the circulations indicated by the $stream_{925}$. The days used for description on the Figure labels are the same as those discussed in Section 6.2.

Figure 6.5a shows the daily mean composite of meteorological fields for *day*-6. The 10 $gkg^{-1}$ isopleth of $q_{925}$ is positioned zonally across the continent at approximately 18° north. The SHL is centred over southwest Algeria and the $stream_{925}$ show the low-level circulation of winds toward and around the SHL. The $stream_{925}$ also show the monsoon flow from the southwest, the anticyclonic circulation of air over northern Algeria, Tunisia and Libya and northerly flow over the Atlantic associated with the Azores high. The shaded cloud frequency indicates that there is a high chance of cloud cover over the tropics, likely associated with the frequency of MCSs, there is also a chance of cloud between 0.4 and 0.6 over much of the Atlantic. Cloud cover frequency over the Sahara is almost uniformly below 0.2 at this time with the exception of over the Hoggar and Tibesti mountain ranges. The $geo_{200}$ suggests that the subtropical jet is most likely to be positioned across North Africa and southern Europe. Some waviness is present including a weak trough positioned over the eastern Mediterranean.

Two days later on *day*-4 (Figure 6.5b, same as that shown in Figure 6.4a) the 10 $gkg^{-1}$ isopleth of $q_{925}$ is still largely zonal and has not moved very far north or south. The centre of the SHL has moved to the west and is located just west of the Algeria-Mali border. The $stream_{925}$ circulation associated with the SHL is centred even further to the west close to the Mali-Mauritania border. Another feature shown by the $stream_{925}$ is the formation of a weaker, secondary circulation in southwestern Algeria, and southerly winds into the Sahara across a broader longitudinal range. Despite the fact that the $q_{925}$, 10 $gkg^{-1}$ isopleth has not moved significantly, the increased frequency of clouds in the Sahara in the form of a tongue of cloud from the tropical cloud band suggests that there

is an increase in column water vapour. The frequency of this region of clouds is between 0.2 and 0.4. The pattern of $geo_{200}$ has not changed significantly from *day*-6.

By *day*-2 (Figure 6.5c) the 10 gkg$^{-1}$ isopleth of $q_{925}$ indicates that the monsoon flow is reaching further inland that previously seen. Especially so, over Mali and Mauritania, where it reaches approximately 19° north. Similar to *day*-4, the centre of the SHL indicated by the *mslp* is positioned just to the west of the Mali-Algeria border, whilst the $stream_{925}$ circulation is further west. The $stream_{925}$ also show that there is still a broad longitudinal region with southerly flow into the Sahara. The pattern of cloud frequency is also similar to *day*-4 with a tongue of increased cloud frequency from the tropics and over the Hoggar mountains.

On the day when the most widespread, heavy rainfall occurs (*day*0; Figure 6.5d) the 10 gkg$^{-1}$ isopleth of $q_{925}$ has moved further north. The composite northward surge of the monsoon flow is still strongest over Mali and Mauritania, reaching approximately 20° north in central Mali. The *mslp* shows that SHL has moved further west and is positioned over the Mali-Mauritania border, the $stream_{925}$ circulation associated with the SHL is much further west, positioned over eastern Mauritania. The southerly flow reaches particularily far into the Sahara and along with the SHL circulation seems to be strongly linked to the change in structure of the cloud cover frequency. The tongue of increased cloud frequency mentioned earlier has extended west and there is a large part of the Sahara with a frequency of cloud between 0.2 and 0.4. This illustrates that tropical water vapour has reached further north and west than seen in earlier composite days. The $geo_{200}$ shows a trough positioned over the eastern Atlantic. If this feature is connected to conditions such as a mid-latitude low pressure system it might further influence the meteorology of the region. This can include the strong deformation of the SHL as seen in Chapter 4 and help to produce convective storms.

Two days after *day*0 (Figure 6.5e) the 10 gkg$^{-1}$ isopleth of $q_{925}$ is positioned even further north. This northward bulge is still centred over Mali and Mauritania and reaches approximately 22° north. However, the southerly winds which appear to have driven this transport of moisture have become more southwesterly and the main circulation is around the SHL positioned in southwest Algeria. These changes appear to suggest a return to conditions similar to those seen prior to the formation of the increased cloud frequency feature (*day*-6). The apparent lag in response for atmospheric moisture and clouds (which

are still present over large parts of the Sahara at this time) is similar to the behaviour seen in Chapter 4, where the large MCS was only triggered after the formation of a tropical plume like event and several smaller systems days earlier. The upper level trough seen in $geo_{200}$ on *day*0 is still present but appears to have weakened by *day*+2.

By *day*+4 (Figure 6.5f) the monsoon flow is returning south and has become more zonal. There is no descernable secondary SHL in either the *mslp* or the $stream_{925}$ circulation and the centre of the SHL is positioned further east over the Algeria-Mali border. The region of increased cloud frequency has been reduced to a small northward extension from the tropical cloud mass and a small isolated area of increased cloud frequencey over the Hoggar mountains.

### 6.3.2 Composites of geopotential anomalies

A key feature in terms of generating convection in the usually arid Sahara and northern Sahel is the availability of atmospheric water vapour. The composites shown in Section 6.3.1 illustrate how changes to the low level flow field (possibly associated with deformation of the SHL) produce a more southerly (rather than southwesterly) flow over a broad longitudinal range of the the region. Therefore, it seems likely that this flow is responsible for tropical air reaching further north than usual and helping to trigger convective events. In this section composite plots of geopotential anomaly have been created to help identify the regions which are important for the forcing of moist tropical air into this region. It is thought that such northward excursions of the monsoon flow then lead to triggering of convective storms accounting for the anomalously high levels of rainfall and dust uplift.

Figure 6.6 shows the geopotential anomaly (colour contours) on the 925 hPa and 200 hPa pressure levels ($geo'_{925}$ and $geo'200$; note the separate scales used) and the composite geopotential isopleths separated by 100 $m^2s^{-2}$ and 200 $m^2s^{-2}$ respectively (black lines). As mentioned in Section 6.3.1 geopotential on pressure levels has a strong connection to the pressure field, it is used here to diagnose anomalous features which are able to influence the large-scale flow. Figure 6.6 shows composites for *day*-4, *day*-2, *day*0 and *day*+2, these are the same days plotted in parts of Figures 6.4 and 6.5 and so can be compared directly with the appropriate panels.

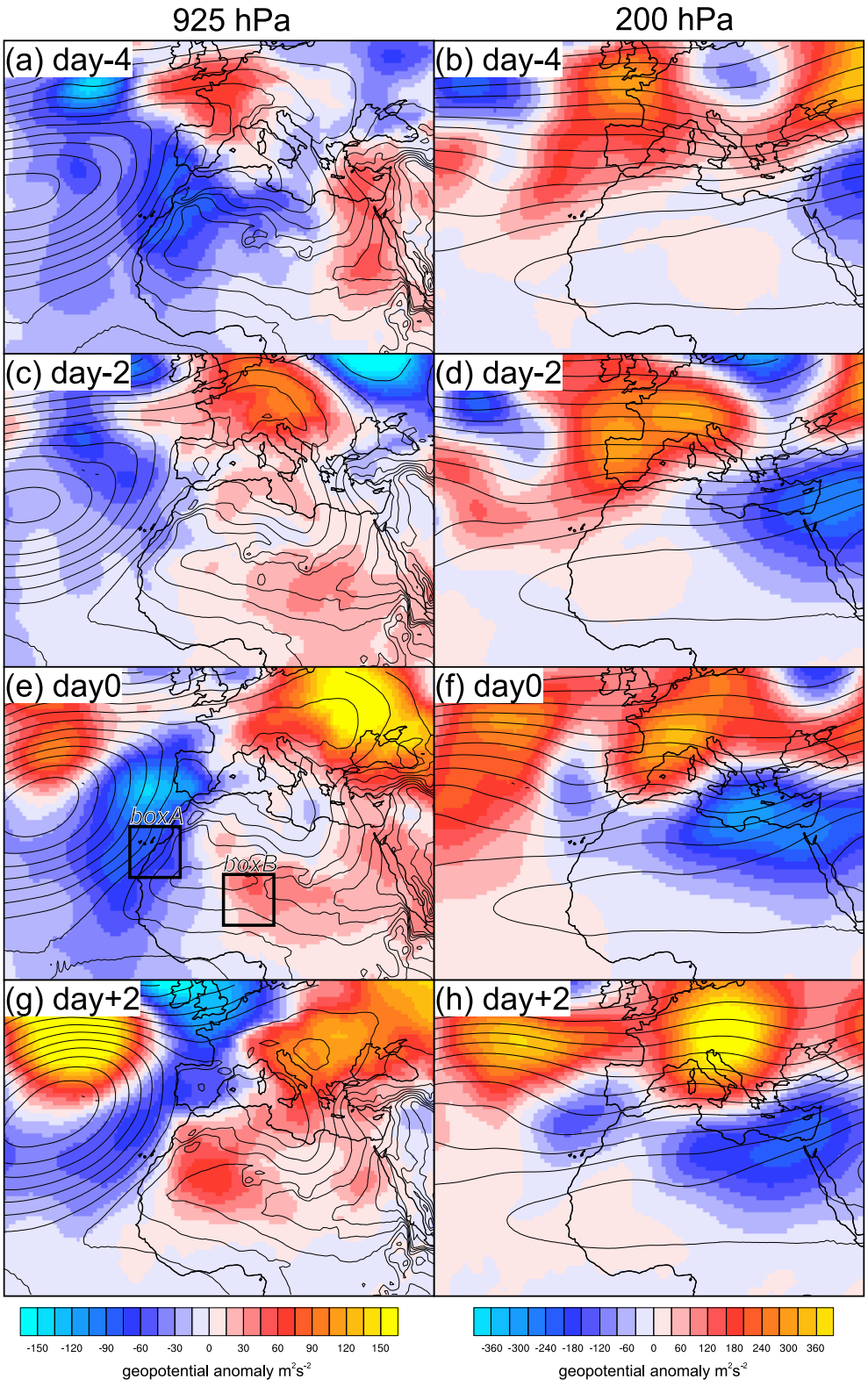


FIGURE 6.6: Composites of geopotential (black lines) and geopotential anomaly (colour shading) at 925 hPa (left-hand side panels) and at 200 hPa (right-hand side panels). These are shown for (a) and (b) *day*-4, (c) and (d) *day*-2, (e) and (f) *day*0 and (g) and (h) *day*+2. *box*$A$ and *box*$B$ shown on (e) indicate regions used for further analysis of 925 hPa geopotential. *box*$A$ covers 20° to 30° N and 20° to 10° W and *box*$B$ covers 10° to 20° N and 0° to 10° E.

Figure 6.6a and 6.6b show the composite geopotential anomaly and composite geopotential for the 36 events on *day*-4 at 925 hPa and 200 hPa respectively. Figure 6.6a hows that there is a large region of anomalously low $geo'_{925}$ positioned over Morocco, Western Sahara, Algeria, Mauritania and parts of Mali, Libya and out over the Atlantic Ocean. At the same time there are very weak anomalies over most of West Africa in the $geo'200$ field (Figure 6.6b). However, there is evidence of a wave train on the subtropical jet with strong positive anomalies over the UK, France and the Iberian Peninsula as well as Eastern Europe.

On *day*-2, a day previously shown to be linked to have increased dustiness and displacement of the SHL, the region of negative $geo'_{925}$ has reduced in size and over much of west Africa the $geo'_{925}$ field is close to climatological values (Figure 6.6c). There is still a region of negative $geo'_{925}$ over the Atlantic Ocean the movement of this negative anomaly suggests the possible presence of a mid-latitude cyclone. There is also a strengthening region of positive $geo'_{925}$ over Chad and Sudan. On the same day the $geo'200$ field displays the strengthening of the positive anomaly over Western Europe and a strong negative anomaly over the eastern Mediterranean and eastern North Africa (Figure 6.6d).

$geo'_{925}$ and $geo'_{200}$ for *day*0, the day thought to be responsible for strong dust uplift and westward displacement of the SHL, are shown in Figures 6.6e and 6.6f respectively. The $geo'_{925}$ field indicates that there is, once again, a large region of negative $geo'_{925}$. The strengthening of this negative anomaly positioned over the eastern North Atlantic appears to be linked to the upper-level negative anomaly which is propagating southeast. The positive anomaly shown in Figure 6.6c has also strengthened and is now centred further west over northwest Niger. It is thought that the $geo'_{925}$ dipole is likely to be a major factor in helping to drive tropical moisture north toward the Sahel and Sahara. On the same day we can see that waves on the subtropical jet in the east of the domain have become stationary and the positive and negative $geo'_{200}$ are positioned with one north of the other. This suggests that the jet curves back on itself and potentially indicates Rossby wave breaking which then has the ability to influence the low-level geopotential field. The weaker negative anomaly in the west is spatially coincident with the low $geo'_{925}$ shown in Figure 6.6e, there is also an negative anomaly at mid-levels (not shown). This suggest the presence of a vertically coherent feature such as a mid-latitude cyclone. As shown in Chapter 4, mid-latitude cyclones close to the Atlas Mountains can deform the SHL through lee cyclogenesis. Although not a necessary feature for modifying the Saharan

low-level pressure field it is thought that in some of the cases identified, interactions with mid-latitude storms is likely to help drive moisture north into the desert.

On *day*+2 the negative $geo'_{925}$ feature over the coast has reduced in size and the positive $geo'_{925}$ feature has increased in size and strength (Figure 6.6g). The centre of the positive $geo'_{925}$ has also moved west and is positioned over northern Mali on this day. Figure 6.6h shows that the anomalous features associated with the ridges and troughs have moved further east.

Some of these findings are consistent with those of Lavaysse et al. (2010) who highlight pulsations of the strength of the SHL on both a 10- to 30-day time scale and a sub 10-day time scale. An example shown in Lavaysse et al. (2010) from the 2006 monsoon season indicates that there is a collapse of the SHL with it being displaced to the west, this is then followed by the production of the largest Saharan convection event that summer. Lavaysse et al. (2010) also show the westward movement of the SHL, a northerly shift in the ITD position and anomalous southerly low-level wind in composites of ECMWF ERA-40 reanalysis data, focussing on the sub 10-day period pulsations.

### 6.3.3 Individual events

From analysis of individual events (not shown) the deformation or westerly displacement of the SHL seen in the composite plots (Figure 6.5) is present in 93% of the cases. This suggests that the modification of the SHL and its associated circulation is likely to have a strong impact on the flow of moist air into the Sahara, and therefore, the triggering of convective storms with the studied region. However, the upper level trough and low-level geopeotential features consistent with a small mid-latitude cyclone shown in Figure 6.5d and Figure 6.6f are only present in approximately 30 % the events. The fact that they are not present for more cases suggests that they are only one of the possible features which can help to drive this near-surface deformation of the geopotential field and therefore anomalous rainfall. Despite being unable to identify the meteorology driving all these events it is clear that the low-level geopotential field is likely to represent the greatest effect of forcing moist tropical air into the Sahara. This allows for the formation of clouds and precipitation over relatively large areas of what is a very arid region.

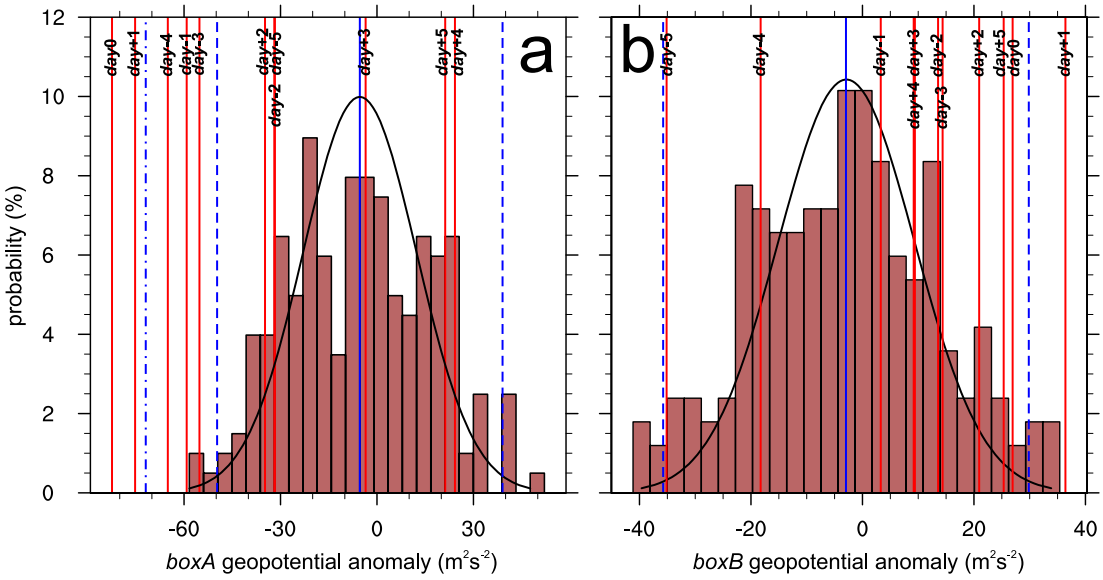


FIGURE 6.7: Distribution of composite mean 925 hPa geopotential anomalies ($geo'_{925}$) from *boxA* and *boxB* (as shown in Figure 6.6e) from 200 groups of 36 randomly selected days. Shown is the distribution of the box mean anomalies (dark red bars), a normal curve based on the mean and standard deviation ($\sigma$) of the distribution (black line), vertical lines representing the mean (solid blue line), the $\pm 2\sigma$ from the mean range (dashed blue lines) and the $\pm 3\sigma$ from the mean range (dot dashed blue lines), also shown are values of the mean $geo'_{925}$ with each box the days linked to the anomalously rainy periods found using Tropical Rainfall Measuring Mission (TRMM) 3B42 V7 rainfall retrievals. These are shown for (a) *boxA* covering 20° to 30° north and 20° to 10° west and (b) *boxB* covering 10° to 20° north and 0° to 10° east.

### 6.3.4 Significance of composite anomalies

The nature of using composite plots means that unless a certain result is caused by only a single meteorological process it is difficult to show the particular mechanisms which produce the events being studied. However, a strength of this method is the ability to identify common aspects of the conditions across the majority of the events being studied. In this case, it appears that the modification of the low-level geopotential field (by a number of different unidentified meteorological conditions) produces a change in the behaviour of the monsoon flow which allows for the triggering of rainfall in normally arid regions. By looking at both the positions of the positive and negative anomalies (especially close to *day*0), as well considering which regions of anomalous geopotential are likely to drive moist tropical air toward the Sahara, two boxes have been chosen to estimate how unusual these conditions are. These boxes are shown on Figure 6.6e are referred as *boxA* and *boxB* hereafter.

In order to test whether the anomalies in *boxA* and *boxB* are significant, 200 groups of 36 randomly selected days from the same period are chosen (April–September, 1998–2011). Composites of geopotential anomaly at 925 hPa are calculated in the same way as for the rainy episodes and a mean anomaly value within both *boxA* and *boxB* is taken. Figure 6.7 shows the probability distributions for these means within *boxA* and *boxB* for the 200 groups of randomly selected days (dark red bars; both are plotted on the same vertical scale but the horizontal scales differ). Also shown are: (1) normal curves for both *boxA* and *boxB*, generated using the means and standard deviations ($\sigma$) found from the 200 composites (black lines), (2) vertical lines representing the means of the *boxA* and *boxB*s mean $geo'_{925}$ values from all 200 composites (solid blue lines), (3) vertical lines representing $\pm 2\sigma$ from the mean (dashed blue lines), (4) where possible vertical lines representing $\pm 3\sigma$ from the mean (dot-dashed blue lines) and (5) vertical lines indicating the *boxA* and *boxB* mean $geo'_{925}$ values from *day*0 and the 5 days preceding and following *day*0 (red lines, labelled at top of Figure 6.7).

It can be seen from the distributions that they are similar to the normal curves shown in Figure 6.7. Therefore the distance the difference between the mean $geo'_{925}$ values from the rainy episodes and the mean calculated from the groups of randomly selected days gives a good idea of how unusual the anomalies shown in Figure 6.6 are. Also, the number of standard deviations from the mean allows for the significance levels to be ascertained.

Figure 6.7a shows the probability distribution for the mean $geo'_{925}$ in *boxA* from the 200 random groups of days. Also shown is the *boxA* mean $geo'_{925}$ values from the 11 days associated with the the rainy episodes. At *day*-5 the *boxA* mean $geo'_{925}$ is approximately -32 $m^2s^{-2}$, this is within the $\pm 2\sigma$ of the mean and is clearly not significantly anomalous compared to the distribution. However, *day*-4 and *day*-3 both have stronger negative anomalies falling outside the $\pm 2\sigma$ of the mean range. *day*-2 has a mean $geo'_{925}$ value very similar to *day*-5 but is again followed by a stronger negative anomaly on *day*-1. *day*0 and *day*+1 have the strongest negative anomalies, with values of -83 $m^2s^{-2}$ and -75 $m^2s^{-2}$ respectively, both of which are outside the $\pm 3\sigma$ of the mean range. After this there is a weakening of the negative anomaly and *day*+2 to *day*+5 all lie within the $\pm 2\sigma$ range. The fact that the *boxA* mean $geo'_{925}$ values for *day*0 and *day*+1 are outside the $\pm 3\sigma$ range, suggests that the null hypothesis that the *boxA* mean $geo'_{925}$ values calculated for these days, is statistically no different from the that calculated from random days can be

rejected. The similarity to the normal distribution suggests that the significance level at which the hypothesis is rejected is close to the 99.7%.

Figure 6.7b shows the same as Figure 6.7a but for *boxB*. Immediately noticeable is that all days apart from *day*+1 are within $\pm 2\sigma$ of the mean. This suggests that the anomalies seen in *boxB* are less unusual than those seen in *boxA* (Figure 6.7a). At *day*-5 the *boxB* mean $geo'_{925}$ is -35 $m^2s^{-2}$, whilst this is within the $\pm 2\sigma$ of the mean range it still appear to a relatively strong negative anomaly. Between *day*-5 and *day*0 the *boxB* mean $geo'_{925}$ gets less negative and becomes positive, by *day*0 the *boxB* mean $geo'_{925}$ is 27 $m^2s^{-2}$ which is close to the edge of the $\pm 2\sigma$ of the mean range. The *boxB* mean $geo'_{925}$ value on *day*+1 is 37 $m^2s^{-2}$ (more than $2\sigma$ from the mean), but after this the positive anomaly weakens to within $2\sigma$ of the mean. This suggests that the anomalies present in *boxB* are less unusual. However, it is thought that the change in direction of the anomaly and the strong (if not statistically significant) positive anomaly on *day*0 is likely to influence the behaviour of the large-scale flow. The timing of this change when coupled with the timing of the extreme values in *boxA* suggest that it is the difference between these two regions that is likely to be a very important feature in terms of forcing moist, tropical air into the desert.

To test this hypothesis a similar plot to Figure 6.7 has been created which shows the distribution of differences between *boxA* and *boxB* mean composite $geo_{925}$ (absolute values, not anomalies). It is thought that the anomalously low $geo_{925}$ values over *boxA* and anomalously high $geo_{925}$ values over *boxB* create a weaker gradient between the two boxes. The modification of the $geo_{925}$ field changes the flow structure and is linked to the production of anomalously rainy periods over the Sahara and northern Sahel.

Figure 6.8 shows the probability distribution for the difference between mean *boxA* and *boxB* composite $geo_{925}$ values from the 200 groups of 36 random monsoon days. The features of the Figure are the same as that described for Figure 6.7. From this we can see that the mean $geo_{925}$ difference between the boxes is similar to the normal distribution generated from the mean and $\sigma$ values from the 200 groups. On *day*-5 the $geo_{925}$ *boxA*-*boxB* value is within the $\pm 2\sigma$ of the mean range, however after this, the values from *day*-4 to *day*+2 are all positioned outside $\pm 3\sigma$ of the mean. *day*0 and *day*+1 have particularly small differences in composite $geo_{925}$ between *boxA* and *boxB*. Both have values outside $\pm 5\sigma$ of the mean. This suggests that for *day*-4 to *day*+2 the null hypothesis that

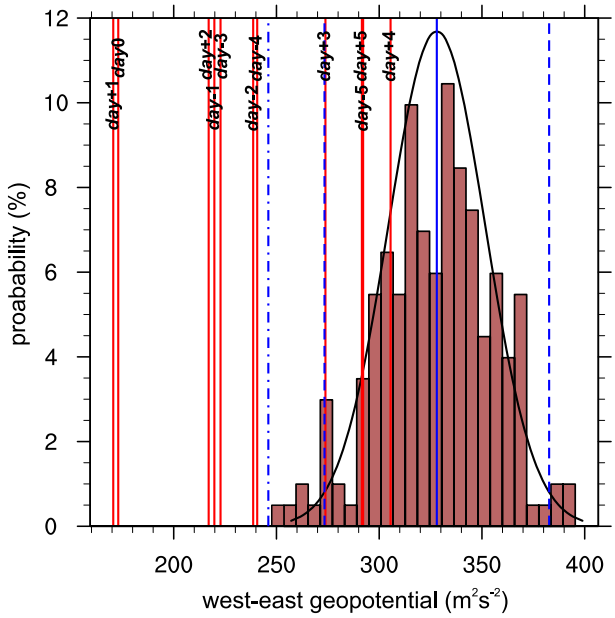


FIGURE 6.8: Distribution of difference between composite mean 925 hPa geopotential ($geo925$) from $boxA$ and $boxB$ (as shown in Figure 6.6e) from 200 groups of 36 randomly selected days. Shown is the distribution of the differences between the box mean values of $geo925$ (dark red bars), a normal curve based on the mean and standard deviation ($\sigma$) of the distribution (black line), vertical lines representing the mean (solid blue line), the $\pm 2\sigma$ from the mean range (dashed blue lines) and the $\pm 3\sigma$ from the mean range (dot dashed blue lines), also shown are values of the mean $geo'_{925}$ with each box the days linked to the anomalously rainy periods found using tropical rainfall measuring mission (TRMM) 3B42 V7 rainfall retrievals.

these composites are statistically no different than the composites created from randomly selected days can be rejected to at least a 99.7% significance level.

## 6.4 Toward an anomalous rainfall in the Sahara index

The fact that the composite difference in $geo_{925}$ between $boxA$ and $boxB$ is statistically significant for a number of days surrounding the day with the most widespread, heavy rainfall suggests that a simple index can be created for the identification of potentially anomalous heavy rain periods in the Sahara and northern Sahel. This would be a very useful tool as it would rely on a variable common to all global forecast models (geopotential or geopotential height), does not rely on simulations being convection permitting, and therefore computationally expensive and also does not rely on atmospheric moisture within a model to be accurate (as seen in Chapter 5, this is a problem in operational analysis even when forecasts have observations for correction). It is unlikely that a simple index such

as this would be better able to forecast rainy episodes than forecast models, especially as the index is reliant on geoptential values from the forecast. However, it is possible that it might give insight into the factors within forecast models which do produce Saharan rainfall and identify the meteorological features which drive it.

In order to perform some preliminary tests using this $geo_{925}$ difference method ECMWF operational forecasts (ECMWF-op) and the National Center for Environmental Prediction (NCEP) Global Forecast System (GFS) forecasts have been used to generate an anomalous rainfall in the Sahara (ARS) index for the 2012 monsoon season. This is compared to TRMM 3B42 V7 rainfall and operational forecast rainfall from GFS and ECMWF-op.

In order to calculate the ARS index a mean value is calculated for $geo_{925}$ within $boxA$ and $boxB$ shown on Figure 6.6e. The mean value from $boxB$ is subtracted from the mean value from $boxA$, this is then smoothed using a 10 day linear filter. This filter calculates a smoothed line with the most recent values having the greatest weighting (10 times larger than 9 days earlier), and only uses data from days earlier than that being calculated. For both ECMWF-op and GFS three ARS index lines have been plotted, these represent forecasts of different lead times. The one day forecast uses the 0000 UTC analysis and the 6, 12 and 18 hour forecasts for the corresponding times of day. Similarly the two day forecast uses the 24, 30 ,36 and 42 hour forecasts for the 0000, 0600, 1200 and 1800 UTC times of day and the three day forecast uses the 48, 54, 60 and 66 hour forecasts. This method aims to replicate the generation of the ARS index in a real world situation. As such it would be calculated a number of days in advance using similar forecast lead times.

Figure 6.9 shows the ARS index (top of panel) for both ECMWF-op (red lines) and GFS (blue lines) for the three different forecast lead times (denoted by dash pattern) for the entire 2012 monsoon season. Also shown is the percent of the box shown in Figure 6.1 covered by rainfall in excess of 5 mm day$^{-1}$ (bottom of panel) from ECMWF-op forecast (red lines), GFS forecast (blue lines) and TRMM 3B42 V7 (black line). This measure is based on the area of the box over a threshold and uses a relatively low threshold for convective rain (5 mm day$^{-1}$). As such the effects of evaporation before model rainfall reaches the surface, as well as the influence of convective parameterisations generally producing lighter rainfall than real systems is reduced. Therefore this method indicates how widespread heavy rain is and allows for a comparison with the ARS index with model forecasts and observations. From Figure 6.9a it can be seen that there is generally very

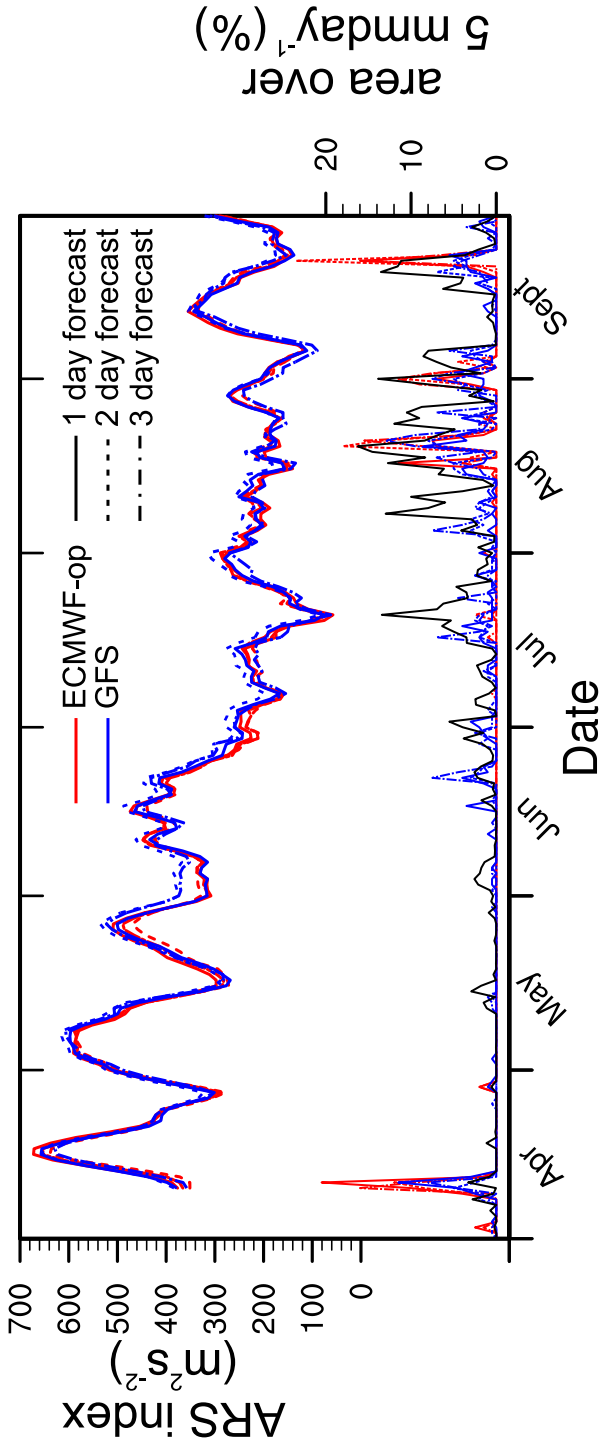


FIGURE 6.9: Time series of 2012 monsoon season (April–September) showing anomalous rainfall in Sahara (ARS) index calculated from the box mean 925 hPa geopotential ($geo_{925}$) values from the European Centre for Medium-Range Weather Forecasts (ECMWF) operational forecast (solid, coloured lines) and the National Center for Environmental Prediction (NCEP) Global Forecast System (GFS) operational forecast (dashed, coloured lines). These are plotted for different forecast lead times of: 1 day, using 00, 06, 12 and 18 hour forecast times, 2 day, using 24, 30, 36 and 42 hour forecast times and 3 day, using 48, 54, 60 and 66 hour forecasts. Also shown is the daily rainfall anomaly in the Sahara and northern Sahel from Tropical Rainfall Measuring Mission (TRMM; black line) calculated as a box mean for the box shown in Figure 6.1.

good agreement for the ARS index not only between the different forecast models, but also the differing lead times used to generate the index. When compared with the percent of the region covered by forecast rain in excess of 5 mm day$^{-1}$ we can see that this is much more variable with different lead times of forecast having a significant impact on the coverage of heavy rain.

Particular periods of note are the rainfall peaks in mid July, early August and late September. In the July and August cases, the percentage of the box covered by heavy rainfall in the forecasts, even at a short lead times, is much lower than observed from TRMM. The time of most widespread heavy rain is also missed. The August event does not seem to have a strong link to a feature in the ARS index while the event in July is clearly strongly connected. This suggests that despite the forecasts being capable of producing a low-level geopotential feature which is linked to the production of widespread heavy rainfall in this region, the moisture distribution and cumulus parameterisations do not produce rainfall at the correct time or over a large enough area. The event in September is also linked to a minima in the ARS index in both models. However, the TRMM rainfall coverage maxima is earlier than the forecast rainfall, this suggests that in this case there were other important meteorological factors or that the large scale forecast was incorrect. Another feature the ARS index displays is a seasonal change with higher values throughout April, May and June and generally lower values throughout July, August and September.

The development of an index such as this requires further work and is beyond the remit of this study. However, this preliminary work has shown promise due to the clear link between anomalous rainfall and the geopotential gradient from $boxA$ to $boxB$ and the coherence between ARS values produced from different forecast models and different forecast lead times. Also, the difference in the representation of particular events using observed and forecast rainfall and the ARS index indicates its utility for the investigation of numerical weather prediction models and their representation of Saharan rainfall events. Further development of this method is likely to include investigation into other years, the production of a climatology and the identification of a method to more closely link ARS with the occurrence of anomalous rainfall episodes in the Sahara.

## 6.5 Summary and conclusions

This chapter investigates the occurrence of anomalously rainy episodes in the Sahara and northern Sahel and during 14 consecutive monsoon seasons (April–September, 1998–2011). Episodes are identified using Tropical Rainfall Measuring Mission (TRMM) 3B42 V7 daily rainfall retrievals. Dust uplift is explored using the Moderate Resolution Imaging Spectrometer (MODIS) Deep Blue 550 nm aerosol optical depth (AOD) and meteorology is studied using composites of ECMWF ERA Interim reanalysis (ERA-int). The strength of anomalies is judged through comparisons with composites produced from 200 groups of 36 random days.

**The pattern of rainfall in the studied region is largely controlled by the position of the monsoon flow and there is a connection between the seasonality of rainfall and disagreement between (re)analysis products.** Within the studied box there is a small rainfall peak in June followed by a minima in late June/early July and a large peak in August. Rainfall reduces during September coinciding with the retreat of the monsoon flow. Weak and strong low-level moisture disagreement in (re)analyses in 2001 and 2010 respectively (Chapter 5), a lack of anomalous rainfall events during 2001 and the large number of episodes during 2010, suggest a connection between the production of convective clouds in the Sahara and (re)analysis disagreement. The increased agreement between (re)analyses despite a large number of rainfall events in 2006 also suggests that increased observations as part of the AMMA field campaign positively impacted on the (re)analysis ensemble.

**AOD retrievals and anomalies indicate the presence of high levels of atmospheric dust during rainy episodes.** Both AOD values and anomalies are strongest the day following the strongest rainfall within the box. This is likely associated with: (1) the day time overpass of MODIS satellites, meaning dust lifted by MCSs is detected the following day, (2) the connection between aged cold pools and enhanced NLLJ formation (Section 4.5.2, Chapter 4), meaning that more dust is likely to be lifted and detected the day after heavy rainfall and (3) biases in the MODIS Deep Blue algorithm mean that retrieved AOD is affected by the height of dust and column water vapour. It has also been shown that the MODIS Deep Blue is not best suited to the retrieval of high AOD values (Banks et al., 2013).

**Specific meteorological features have been shown to be linked to the occurrence of anomalous rainfall in the Sahara and northern Sahel.** These include: (1) the displacement of the composite Saharan heat low (SHL) to the west, (2) modification of the monsoon flow linked to the change in position of the SHL, (3) encouragement of moist tropical air north toward the Sahara creating a tongue of cloud from the tropics and (4) a composite upper level trough off the west coast of the Iberian peninsula suggesting the presence of mid-latitude cyclones in a number of cases.

925 hPa geopotential anomalies show the growth of a strong negative anomaly over the western coast of West and North Africa, as well as a westward moving positive anomaly. At upper-levels there is a Rossby wave train present and possible wave breaking. Blocking of subsequent waves by this potentially influences the low-level geopotential field. The day with the most widespread heavy rainfall ($day0$) is characterised by strong dipole in the low-level geopotential anomaly. The magnitude of the anomalies in two key regions are assessed. The region to the west ($boxA$) is shown to have a significant negative anomaly on $day$-4, $day$-3, $day$-1, $day0$ and $day$+1. The region to the east ($boxB$) has only one day with a significant positive anomaly ($day$+1), however there is a strong change from negative anomaly to significant positive anomaly from $day$-5 to $day$+1. The difference between $boxA$ and $boxB$ 925 hPa geopotential shows a particularly weak gradient during anomalously rainy episodes.

**A simple measure is devised which measures the difference in 925 hPa geopotential between *boxA* and *boxB*, this metric is referred to as the anomalous rainfall in the Sahara (ARS) index.** The hypothesis being, that when the value of the index is small there a greater chance of a northward surge of the monsoon flow and therefore the generation of anomalous rainfall in the Sahara and northern Sahel. Preliminary work on the 2012 monsoon season suggests a link between low ARS index values and rainfall in the box shown in Figure 6.1. Further study is required beyond what has been shown in this chapter to develop this index but it is hoped that it might prove useful for forecasting of anomalous rainfall episodes and developing understanding of numerical weather prediction models.

Important findings in this chapter are:

- The climatology of rainfall in the region is strongly associated with the monsoon flow, but also is very similar to the seasonal disagreement investigated in Chapter 5.
- Periods with widespread heavy rain are associated with high values of AOD, this is strongest one day after the most widespread heavy rain.
- Most episodes appear to be linked to certain meteorological conditions, these include: deformation/shifting of the Saharan heat low, strengthened southerly component of the monsoon flow across a broad longitudinal region, formation of a tongue of cloud and an upper level trough over the Atlantic.
- The channelling of moist tropical air is linked to the production of an anomaly dipole with anomalously low 925 hPa geopotential along the west coast of West Africa and anomalously high 925 hPa geopotential in the interior. The difference in composite geopotential between these regions has been shown to be significant compared to composites produced from random days.
- The same measure used on operational data for 2012 has been shown to be linked to the occurrence of widespread heavy rainfall and should be developed to improve the understanding of rainfall production in West Africa in operational models.

# Chapter 7

# Conclusions and recommendations for future work

In this chapter the conclusions presented in Chapters 4–6 are summarised. As well as this, recommendations for future work are made. These recommendations are based on both the gaps in the literature highlighted in Chapter 2 as well as scientific results from Chapters 4 to 6.

## 7.1 Summary of conclusions

The aim of this study was to investigate the formation and behaviour of mesoscale convective systems (MCS) produced in the summertime, close to the edge of the West African Monsoon (WAM), the implications that these storms have on dust uplift and their representation within both global and high-resolution, limited-area models. This has been done through the investigation of a case study of a large Saharan MCS that was triggered in June 2010. Also investigated is the representation of the low-level moisture fields in a number of operational analysis and reanalysis products (collectively referred to as (re)analysis products) and the synoptic-scale meteorological conditions which are common to anomalously rainy episodes in the Sahara and northern Sahel.

### Chapter 4

MCSs have important impacts on the WAM, rainfall in the Sahel and Sahara and the lifting of dust. Through these effects they influence the lives of millions of people both in the region and globally. By studying them it is hoped a greater understanding can be reached about their formation and behaviour as well as reduce uncertainty linked to the WAM system and the climate impacts of Saharan dust.

Chapter 4 details the observed and modelled meteorology associated with a MCS triggered over the Hoggar and Aïr Mountains and the cold pool it produced in June 2010. Important synoptic-scale features for the development of the case study MCS are: (1) an upper-level trough on the subtropical jet produces tropical plume-like conditions over West Africa up to a week before the initiation of the MCS, (2) this is linked to disruption of the Saharan heat low (SHL) which is split into two distinct regions, (3) subsequent movement of the subtropical jet trough leads to the development of high surface pressure over Libya consistent with a Mediterranean cold air surge (Vizy and Cook, 2009) and (4) re-strengthening of the SHL combined with the circulation around the Libyan high produce low-level convergence close to the Hoggar and Aïr Mountains. These conditions prove favourable for the triggering of convective cells over the mountainous terrain and the development of a large MCS.

One day before the triggering of the large MCS small convective cells are triggered, generating cold pools which spread over the Hoggar and Aïr regions. These cold pools increase low-level moisture and extend the region of moist southerlies into the initiation region for the large MCS. This is similar to cases in Cuesta et al. (2010), Flamant et al. (2007) and Flamant et al. (2009). The first cells that later for the large MCS being studied are orientated on a northeast-southwest axis, the cells in the south develop preferentially, likely due to higher levels of atmospheric moisture. The behaviour of the observed system changes dramatically as it travels into conditions of favourable deep layer shear (associated with the presence of the African easterly jet; AEJ), becoming faster, triggering more new cells and producing a round cloud shield. This behaviour is consistent with previously published work by Cohen et al. (2007) and Coniglio et al. (2006).

Another important synoptic-scale process is the deformation of the heat low after the triggering of the MCS by the formation of a lee cyclone south of the Atlas Mountains. This

produces a northestward pressure gradient over the region which encourages northward motion of the cold pool air into the Sahara as well as the transport of the dust plume toward the Mediterranean .

The WRF simulation of the case produces convective cells at the correct time, however, these cells are not positioned in the same northwest-southeast orientation and a single large organised system does not initially develop. Instead the two separate regions of moist convection produced decay. Convective activity is then re-initiated in the simulation approximately six hours later, after which the system develops similarly to observed. Early in its development the initiation of new cells is intermittent, with weak updraughts and the heaviest rainfall positioned far behind the leading edge of the cold pool. However, in favourable deep layer shear conditions the simulated system travels faster, produces stronger updraughts along the leading edge of the cold pool, heavier rainfall including a region of stratiform rain and a system relative rear inflow jet. Both observed and simulated systems are seen to produce a very large cold pool which spreads in to the Sahara desert. Despite the difference between the observed and simulated systems their agreement with regards to: (1) the timing of initial convection, (2) the direction and speed of propagation after re-initiation, (3) the influence of deep layer shear and (4) the production of a very large cold pool suggest that the simulation has successfully modelled the important processes for this study.

The behaviour of the cold pool has also been investigated. It is found that the most important factors for producing such the large dust plume are: (1) a number of separate convective events and the movement of an organised system with time whilst producing convective downdraughts, (2) a strong northwestward pressure gradient due to the deformation of the heat low and (3) shallow precipitating clouds along the northern edge of the MCS cold pool.

Three dust uplift processes are identified and are highlighted through the application of the dust uplift potential (DUP; Section 4.4.3). These are: (1) high winds along the leading edge of the cold pool, (2) the production of an enhanced nocturnal low-level jet (NLLJ) within the aged cold pool and (3) the formation of an internal bore along the interface of the residual boundary layer and the stable nocturnal boundary layer (NBL) by the cold pool. The identification of a bore on the nocturnal boundary layer represents a recently

recognised dust uplift mechanism, potentially similar to an observed event discussed in Hobby et al. (2013).

The simulation of the case initially proved problematic as initialisation using Global Forecast System (GFS) analysis data and European Centre for Medium-Range Weather Forecasts (ECMWF) ERA Interim reanalysis (ERA-int) data produced simulations that failed to form a MCS similar to that observed. ECMWF operational analysis (ECMWF-op) was used and a system similar to that observed was produced. The different outcomes for these simulations suggests significant differences between (re)analysis products. The differences between such products in this region is indicated in Marsham et al. (2011) which highlights differences in the strength of the SHL. Also, Birch et al. (2013) and Schepanski et al. (2014) both indicate the sensitivity of high-resolution, limited-area models to initialisation data. This study (Chapter 4) is in agreement with these publications and further illustrates the difficulties faced by the modelling community when performing simulations in data sparse regions. This provides the motivation for Chapter 5 which explores disagreement between the positioning of the edge of the monsoon flow in seven commonly used (re)analysis products.

### Chapter 5

With the differences between simulations initialised using GFS, ERA-int and ECMWF-op in Chapter 4 in mind, Chapter 5 investigates the differences in low-level moisture distribution over West Africa in seven (re)analysis products over 11 consecutive monsoon seasons (April–September, 2000-2010). The use of low-level moisture as a measure was chosen due to the information this provides about the behaviour of the WAM because it is an important prerequisite for the triggering and development of MCSs.

The largest differences in summertime low-level moisture over West Africa are found to be close to the edge of the monsoon flow suggesting variable representation of the WAM in different (re)analyses. This is troubling as the WAM is important to millions of people and (re)analyses are the most frequently relied upon tools for studying the climate and weather of West Africa. The magnitude of differences can be surprisingly large often in excess of 50% of the mean of two products. Products from the same national centres (such as ECMWF operational analysis and reanalysis) are more similar, likely as a result of similar

model physics and data assimilation methods. This raises questions about the verification of forecasts as the skill of forecasts is determined by comparison with a (re)analyses. Over West Africa there are very few observations to constrain the (re)analyses, making verification of this kind more akin to a comparison of two forecasts. Periods of disagreement within the ensemble of (re)analyses mean that verification of a forecast in this way is even more unreliable as it is difficult to know which products are outperforming the others.

By comparing the zonal-mean ITDs (ITDΦ) of each product it is shown that the Climate Forecast System Reanalysis (CFSR) contains a systematic bias, positioning its ITDΦ between 100 and 200 km further south than the mean ITDΦ from the other products. This offset reduces slightly over the course of the 11 consecutive monsoon seasons. The GFS ITDΦ shows much more interannual variation, being positioned further south than other products (excluding CFSR) in 2000 and 2007–2010. The National Center for Environmental Prediction (NCEP) department of energy (DOE) reanalysis (NCEP-DOE) has rare but markedly northern outliers in ITDΦ position.

Interannually there are variations in the level of disagreement seen between (re)analysis products. 2006 has the lowest disagreement, most likely as a result of enhanced upper-air observations as part of the African Monsoon Multidisciplinary Analysis (AMMA) field campaign. 2000 and 2010 have higher disagreement, in 2000 this is thought to be connected to the behaviour of GFS, however in 2010 there is a higher number of extreme events driven by northward surges and retreat of the monsoon flow. The impact of additional upper-air observations in 2006 suggests need to improve the radiosonde network. However, the lack of political will or the capability of nations in the region to implement this type of upgrade makes this an unlikely prospect. Therefore, it is likely that novel techniques for the assimilation of satellite data are required to improve the representation of the regions meteorology in (re)analyses.

Seasonally, disagreement increases from April to August with a small peak in late May/early June and a large peak in August. The earlier peak is likely associated with the monsoon pre-onset and the occurrence of dry squall lines and high downdraught convective available potential energy (DCAPE). The August peak is likely due to a greater number of convective events occurring in the poorly observed interior of West Africa. This seasonality raises questions about the predictability of the WAM, as disagreement between products

which are able to assimilate observations, suggest that similarly coarse resolution forecasts will be less able to predict features such as monsoon onset and retreat.

34 extreme disagreement events are identified and are usually connected to northward surges of the ITDΦ in all (re)analysis products, peak disagreement occurs during the retreat. Two groups of (re)analyses have been identified, NCEP-DOE, MERRA, ERA-int and ECMWF-op have siilar composite ITDΦ values throughout extreme events. CFSR, GFS and NCEP-NCAR have southward ITDΦ offsets of approximately 3°, 1.5° and 0.75° respectively. There is relatively low disagreement between products during the first few days of the composite surge. This is likely due to: (1) the important processes being synoptic in scale and therefore, are resolved in the (re)analyses, (2) that the assimilation of observations (however sparse) is sufficient to constrain the products or (3) that all products are failing to represent reality but are still convergent on similar incorrect representation of the atmosphere.

A link is shown between periods of disagreement and the presence of convective cells further north than would usually be expected. This convective activity is thought to be linked to secondary triggering within anomalous northward surges of the monsoon flow and are focussed over Mauritania and northern Mali. Moderate Resolution Imaging Spectrometer (MODIS) Deep Blue AOD retrievals show high AOD and AOD anomalies the next day, suggesting that the same processes implicated in causing (re)analysis disagreement are also connected to dust uplift in the same region.

From the findings of Chapter 5 it is difficult to disentangle what the causal processes that produce northward surges associated with disagreement. This is because processes which are known to produce northward surges of the monsoon flow are also known to be linked to favourable conditions for the initiation and development of MCSs. In reality, both synoptic- and mesoscale features probably contribute to the life cycle of the northward surges. Also, it is thought that convective storms are likely to be important due to the fact that their explicit inclusion in models is known to significantly modify the behaviour of the monsoon flow (Marsham et al., 2013b).

Chapter 4 has shown that large MCSs are capable of generating very large dust plumes when they are triggered and develop in the Sahara, and Chapter 5 has shown a link between periods of disagreement and rainfall further north than would be expected from

climatology. The role of MCSs for dust uplift, rainfall and (re)analysis disagreement in West Africa means that investigating the meteorological conditions under which they occur in the Sahara and northern Sahel is very important. This provides the motivation for Chapter 6, which focusses on anomalously rainy episodes and the large-scale features responsible for their production.

### Chapter 6

Chapter 6 investigates periods of anomalous rainfall in the Sahara and northern Sahel including links to anomalous AOD retrievals and the meteorology driving moist monsoon air into the Sahara. 36 anomalously rainy episodes in the summertime Sahara are identified from 14 consecutive monsoon season (April–September, 1998–2011) using Tropical Rainfall Measuring Mission (TRMM) 3B42 V7 rainfall retrievals.

The temporal rainfall pattern largely matches the seasonality of the monsoon flow and also seems to be connected to the seasonal pattern of (re)analysis product disagreement. This further connects the occurrence of disagreement in (re)analysis products with the production of anomalously heavy rain in the Sahara and northern Sahel.

The MODIS Deep Blue AOD and AOD anomaly peak the day after the most widespread heavy rainfall in the studied region. This is most likely caused by: (1) the first MODIS overpass likely occurring the day after dust is lifted by haboobs , (2) additional uplift of dust by enhanced NLLJs within aged cold pools the morning after cold pool production and (3) height biases in MODIS Deep Blue making dust easier to detect when it is lifted higher into the atmosphere, which occurs as dust is mixed throughout the growing boundary layer the day after uplift.

The days with most widespread rainfall within a rainy episode are linked to: (1) weakening and displacement of the SHL west, (2) changes to the low-level circulation producing southerly winds into the Sahara, (3) an increased chance of cloudiness over the Sahara and (4) approximately 30% of anomalous rainfall events are linked to the presence of a trough on the upper-level jet and a mid-latitude surface low over the Atlantic or Iberian Peninsula. These features are consistent with those linked to pulsations (including the collapse) of the SHL discussed in Lavaysse et al. (2010) which lead to the production of rainfall north of 20° north. Channelling of moist, tropical, low-level air is connected to

the presence of a dipole in the 925 hPa geopotential anomaly. A high anomaly tracks westward over West Africa and strengthens with time and the low anomaly is positioned over the Atlantic coast.

The measure of difference between the mean geopotential value in the west and east regions has been called the anomalous rainfall in Sahara (ARS) index and is applied to 2012 using geopotential values from different forecast products and different lead times. There is good agreement between the GFS and ECMWF-op ARS indices for forecast lead times of one, two and three days. There is a link between the occurrence of low ARS index values and the occurrence of widespread rain over the 5 mm day$^{-1}$ threshold. The ARS index has the potential to be a useful tool for model development. It is based on both statistically significant differences and a physically sensible process driving moisture into the Sahara, the production some rainfall events in models can be attributed to the representation of this specific synoptic-scale feature. However, disagreement between ARS index, forecast and observed rain provides an starting point for the identification of meteorological processes which are poorly represented in forecasts.

## 7.2 Recommendations

This study has indicated a number of difficulties faced when studying the meteorology of West Africa and the subject of dust uplift and transport. This section discusses some key areas in which further research is needed in these fields generally as well as avenues of research which have been particularly highlighted through the work discussed in Chapters 4, 5 and 6.

Firstly the quantification of dust uplift that is attributable to different processes is needed and better understanding of their dynamics. Satellite observations of AOD or dustiness are likely to underestimate dust raised by haboobs due to the connection between their formation and the rejection of cloudy pixels as well as a reliance on daytime observations. Also, the study of winds capable of lifting dust over a period spanning multiple years is restricted to coarse grid global products which are unable to suitably represent the formation of dust uplift processes that rely on convective scales (eg. haboobs). The work conducted as part of the *Cascade* project (Heinold et al., 2013; Marsham et al., 2013b) has started to tackle this issue and needs to be built on to develop a greater

statistical understanding of the mechanisms of dust uplift. To further investigate specific mechanisms of dust uplift simulations of cases similar to that presented in Chapter 4 with higher horizontal and vertical resolutions are needed. This would allow for a greater degree of insight into the dust uplift processes, especially the behaviour of the leading edge of convective cold pools and the effects of stable boundary layers.

There is a need for a more in depth understanding of the behaviour of density driven flows. Their behaviour is generally understood, however it is felt that additional laboratory and idealised numerical modelling would be valuable to help understand the behaviour of gravity currents travelling through stably stratified fluids, the turbulent flow structures within the head of the current and the modelling of flows which are approaching their Rossby radii of deformation. Additional work in understanding their link to dust uplift is also needed. Including further investigation of very large convectively generated haboobs and the synoptic-scale features which raise dust that are almost indistinguishable from them in satellite imagery.

Further work should also be undertaken on the connections between the relatively well understood and represented meteorology of the extratropics and its influence on the meteorology of tropical, Sahelian and Saharan West Africa. As seen in Chapters 4 and 6 there are occasions when the conditions further north have a strong influence on the meteorology of West Africa including the generation of spectacular and high impact events. In order to understand these processes work should be conducted on these connections and the influence they have, specific examples include the generation of tropical plume like events and lee cyclogenesis forced by the Atlas mountains and how these features interact with the SHL.

Chapter 5 highlights some major problems with the representation of the WAM in (re)analysis products, as such there are several key areas which require further investigation. The fact that the year with the lowest disagreement coincides with the enhancement of the upper-air network it is suggested that a significant reduction in (re)analysis disagreement could be achieved through the improvement of the observation network across West Africa. More data to constrain products would improve their representation of the atmosphere without a improved representation of sub-grid scale processes. However, it is recognised that this would require significant monetary investment and the political will of the local governments, this does not seem likely. Therefore it is recognised that the most useful course of

action to improve (re)analyses is to find ways to assimilate more information from satellite borne instruments. This includes the introduction of new and more advanced satellites but it is recommended that should be focussed on the development of novel techniques to assimilate existing datasets. As previously mentioned such assimilation of clouds has been discussed in Kostka et al. (2014) and Storto and Tveter (2009) with encouraging results. A major change to data assimilation techniques is required to be better able to assimilate discontinuous data. Most fields currently assimilated are continuous and so smoothing between known points can be applied, however, smoothing of fields such the presence or absence of clouds or even elevated levels of atmospheric dust associated with a sharp edged cold pool is inappropriate.

A question raised by the findings of Chapter 5 is which of the (re)analyses are outperforming the others? This is not a trivial question to answer as verification of these products is hampered by the assimilation of much of the available data. The first option is to compare observations with fields which are not assimilated by (re)analyses but are prognostic outputs. This technique means that comparisons are likely to be limited due to the paucity of observations across the region and the large quantity of data that are assimilated (such as that from radiosondes and satellite radiances). This could be supported by further examination of 2006 possibly through the application of data denial experiments similar to that conducted as part of Augustí Panareda et al. (2010a). Another avenue of research into this topic are the investigation of the changes between the first guess forecast and the final (re)analysis and the rates of rejection of data through the quality control process. This might highlight which products have models that produce worse short term forecasts and in turn influence the quality of the final (re)analysis.

A method to reduce disagreement between (re)analyses is to improve the representation of processes that lead to a spread in the (re)analysis ensemble. Chapter 5 highlights the connection between disagreement and northward surges of the monsoon flow and rainfall further north than the ITD$\Phi$. It is difficult to identify the meteorological cause of the northward surges of the monsoon flow, however, it is likely that there is both synoptic-scale and convective components driving them. Within this is, it is difficult to ascertain which of these features is likely to be the cause of disagreement between the (re)analyses. Further work into the attribution of disagreement to meteorological processes is needed, but it is hypothesised here that the disagreement is a result of the poorly represented

convective storms. The impact of cold pools are already known to influence the behaviour of the WAM as discussed in Marsham et al. (2013b). Therefore, the development of improved parameterisations which allow for MCSs that travel and include impacts of cold pools is likely to improve the more general representation of the WAM in models. On a similar note, it would also be useful to have a cold pool parameterisation with coarse grid models to improve the representation of winds able to lift dust.

Chapter 6 indicated that there are specific features which are present during the majority of anomalous rainfall events in the Sahara, the most obvious being the weak 925 hPa geopotential gradient between the Western Sahara coast and the Niger Sahel/Sahara region. An obvious area for future work is to investigate the meteorological features which produce this low-level geopotential dipole. This includes more detailed analysis of the individual events identified and the identification of the processes responsible for the displacement/collapse of the SHL. Work by Lavaysse et al. (2010) indicates that there are two particular frequencies ranges important for the pulsation of the SHL strength but do not identify the cause. It is possible that there are links to African Easterly waves (AEWs), waves on the subtropical jet and periodic interactions with the extratropics.

Another avenue for future work is the use of the SEVIRI AOD product (Banks et al., 2013) to investigate the lifting of dust during and after heavy rainfall events. As mentioned in Chapter 6 MODIS Deep Blue has temporal limitations preventing the identification of dust uplift on a sub-daily scale, as well as a limitation for detecting very high AODs. In comparison the SEVIRI AOD has a better temporal resolution, potentially allowing for the attribution of airborne dust to specific processes which occur at particular times of day (haboobs generally occur at night and high momentum air from NLLJs lift dust in the morning). However, one problem of using SEVIRI data is that it has been active for fewer years than the MODIS satellites reducing the number of events it would be possible to study.

Further development of the ARS index should include investigation of into a number of other years and the production of a climatology. It is thought that there is likely to be an improved method for generating the index which produces a closer link between the index and the production of anomalous rainfall in the Sahara. It is also suggested that the climatology of the index should be compiled for all seasons allowing for the seasonal cycle to be studied. As this index is linked to anomalously northerly flow into the Sahara

it is suspected that there might be a signal associated with the onset and retreat monsoon season. If so this could help to improve the understanding of the WAM as a system and therefore lead to better representation of it within models.

# References


Agustí-Panareda, A., Beljaars, A., Ahlgrimm, M., Balsamo, G., Bock, O., Forbes, R., Ghelli, A., Guichard, F., Köhler, M., Meynadier, R. and Morcrette, J.-J. (2010b), "The ECMWF re-analysis for the AMMA observational campaign", *Quarterly Journal of the Royal Meteorological Society* , Vol. 136, John Wiley & Sons, Ltd., pp. 1457–1472.

Agustí-Panareda, A., Beljaars, A., Cardinali, C., Genkova, I. and Thorncroft, C. (2010a), "Impacts of assimilating AMMA soundings on ECMWF analyses and forecasts", *Wea. Forecasting* , Vol. 25, American Meteorological Society, pp. 1142–1160.

Alessandrini, E. R., Stafoggia, M., Faustini, A., Gobbi, G. P. and Forastiere, F. (2013), "Saharan dust and the association between particulate matter and daily hospitalisations in Rome, Italy", *Occupational and Environmental Medicine* , Vol. 70, pp. 432–434.

Alpert, P. and Ziv, B. (1989), "The Sharav cyclone: Observations and some theoretical considerations", *Journal of Geophysical Research: Atmospheres* , Vol. 94, pp. 18495–18514.

Ansmann, A., Petzold, A., Kandler, K., Tegen, I., Wendisch, M., Müller, D., Weinzierl, B., Müller, T. and Heintzenberg, J. (2011), "Saharan mineral dust experiments SAMUM-1 and SAMUM-2: what have we learned?", *Tellus B* , Vol. 63, pp. 403–429.

Ansmann, A., Tesche, M., Knippertz, P., Bierwirth, E., Althausen, D., Müller, D. and Schulz, O. (2009), "Vertical profiling of convective dust plumes in southern Morocco during SAMUM", *Tellus* , Vol. 61B, pp. 340–353.

Aoki, I., Kurosaki, Y., Osada, R., Sato, T. and Kimura, F. (2005), "Dust storms generated by mesoscale cold fronts in the Tarim Basin, northwest China", *Geophysical Research Letters* , Vol. 32, p. L06807.

Arakawa, A. and Konor, C. S. (1996), "Vertical differencing of the primitive equations based on the Charney Phillips grid in hybrid sigma-p vertical coordinates", *Mon. Wea. Rev.* , Vol. 124, American Meteorological Society, pp. 511–528.
**URL:** *http://dx.doi.org/10.1175/1520-0493(1996)124¡0511:VDOTPE¿2.0.CO;2*

Atlas, D. and Williams, C. R. (2003), "The anatomy of a continental tropical convective storm", *J. Atmos. Sci.* , Vol. 60, American Meteorological Society, pp. 3–15.

Ballantine, J.-A. C., Okin, G. S., Prentiss, D. E. and Roberts, D. A. (2005), "Mapping North African landforms using continental scale unmixing of MODIS imagery", *Remote Sensing of Environment* , Vol. 97, pp. 470–483.

Balme, M. and Greeley, R. (2006), "Dust devils on Earth and Mars", *Rev. Geophys.* , Vol. 44, p. RG3003.

Banks, J., Brindley, H., Flamant, C., Garay, M., Hsu, N., Kalashnikova, O., Klüser, L. and Sayer, A. (2013), "Intercomparison of satellite dust retrieval products over the West African Sahara during the Fennec campaign in June 2011", *Remote Sensing of Environment* , Vol. 136, pp. 99–116.

Benjamin, T. (1968), "Gravity currents and related phenomena", *Journal of Fluid Mechanics* , Vol. 31, pp. 209–248.

Bennouna, Y. S., de Leeuw, G., Piazzola, J. and Kusmierczyk-Michulec, J. (2009), "Aerosol remote sensing over the ocean using MSG-SEVIRI visible images", *Journal of Geophysical Research: Atmospheres* , Vol. 114, p. D23203.

Berry, G. and Thorncroft, C. D. (2005), "Case study of an intense African easterly wave.", *Monthly Weather Review* , Vol. 133, pp. 752–766.

Birch, C. E., Parker, D. J., O'Leary, A., Marsham, J. H., Taylor, C. M., Harris, P. P. and Lister, G. M. S. (2013), "Impact of soil moisture and convectively generated waves on the initiation of a West African mesoscale convective system", *Q.J.R. Meteorol. Soc.* , Vol. 139, pp. 1712–1730.

Blackadar, A. (1957), "Boundary layer wind maxima and their significance for the growth of nocturnal inversions", *Bull. Amer. Meteor. Soc.* , Vol. 38, pp. 283–290.

Bou Karam, D., Flamant, C., Cuesta, J., Pelon, J. and Williams, E. (2010), "Dust emission and transport associated with a Saharan depression: February 2007 case", *Journal of Geophysical Research-Atmospheres* , Vol. 115, p. D00H27.

Bou Karam, D., Flamant, C., Knippertz, P., Reitebuch, O., Pelon, J., Chong, M. and Dabas, A. (2008), "Dust emissions over the Sahel associated with the West African monsoon intertropical discontinuity region: A representative case-study", *Quarterly Journal of the Royal Meteorological Society* , Vol. 134, pp. 621–634.

Brazel, A. J. and Nickling, W. G. (1986), "The relationship of weather types to dust storm generation in Arizona (1965–1980)", *J. Climatol.* , Vol. 6, pp. 255–275.

Breed, C. S., McCauley, J. F., Whitney, M. I., Tchakarian, V. P. and Laity, J. E. (1997), Wind erosion in drylands., *in* D. S. Thomas, ed., 'Arid Zone Geomorphology', 2nd edn, Wiley.

Brindley, H. and Ignatov, A. (2006), "Retrieval of mineral aerosol optical depth and size information from meteosat second generation SEVIRI solar reflectance bands", *Remote Sensing of Environment* , Vol. 102, pp. 344–363.

Brindley, H., Knippertz, P., Ryder, C. and Ashpole, I. (2012), "A critical evaluation of the ability of the spinning enhanced visible and infrared imager (SEVIRI) thermal infrared red-green-blue rendering to identify dust events: Theoretical analysis", *J. Geophys. Res.* , Vol. 117, p. D07201.

Bristow, C. S., Drake, N. and Armitage, S. (2009), "Deflation in the dustiest place on earth: The Bodélé Depression, Chad", *Geomorphology* , Vol. 105, pp. 50–58.

Bristow, C. S., Hudson-Edwards, K. A. and Chappell, A. (2010), "Fertilizing the Amazon and equatorial Atlantic with West African dust", *Geophys. Res. Lett.* , Vol. 37, p. L14807.

Britter, R. and Simpson, J. (1978), "Experiments on the dynamics of a gravity current head", *Journal of Fluid Mechanics.* , Vol. 88, pp. 223–240.

Buckle, C. (2004), *Weather and Climate in Africa*, Longman, Michigan, USA.

Burton, R. R., Devine, G. M., Parker, D. J., Chazette, P., Dixon, N., Flamant, C. and Haywood, J. M. (2013), "The Harmattan over West Africa: nocturnal structure and

frontogenesis", *Q.J.R. Meteorol. Soc.* , Vol. 139, John Wiley & Sons, Ltd., pp. 1364–1373.

Byers, H. R. (1949), "Structure and dynamics of the thunderstorm", *Science* , Vol. 110, pp. 291–294.

Cakmur, R., Miller, R. and Torres, O. (2004), "Incorporating the effect of small-scale circulations upon dust emission in an atmospheric general circulation model", *Journal of Geophysical Research* , Vol. 109, p. D07201.

Carrer, D., Roujean, J.-L., Hautecoeur, O. and Elias, T. (2010), "Daily estimates of aerosol optical thickness over land surface based on a directional and temporal analysis of SEVIRI MSG visible observations", *Journal of Geophysical Research: Atmospheres* , Vol. 115, p. D10208.

Chen, W. and Fryrear, D. W. (2002), "Sedimentary characteristics of a haboob dust storm", *Atmospheric Research* , Vol. 61, pp. 75–85.

Chipperfield, M. P. (2006), "New version of the TOMCAT/SLIMCAT off-line chemical transport model: Intercomparison of stratospheric tracer experiments", *Q.J.R. Meteorol. Soc.* , Vol. 132, pp. 1179–1203.

Chomette, O., Legrand, M. and Marticorena, B. (1999), "Determination of the wind speed threshold for the emission of desert dust using satellite remote sensing in the thermal infrared", *Journal of Geophysical Research-Atmospheres* , Vol. 104, pp. 31207–31215.

Cohen, A. E., Coniglio, M. C., Corfidi, S. F. and Corfidi, S. J. (2007), "Discrimination of mesoscale convective system environments using sounding observations", *Wea. Forecasting* , Vol. 22, American Meteorological Society, pp. 1045–1062.

Coniglio, M. C., Stensrud, D. J. and Wicker, L. J. (2006), "Effects of upper-level shear on the structure and maintenance of strong quasi-linear mesoscale convective systems", *J. Atmos. Sci.* , Vol. 63, American Meteorological Society, pp. 1231–1252.

Cowie, S. M., Knippertz, P. and Marsham, J. M. (2014), "A climatology of dust emission events from northern Africa using long-term surface observations", *Atmos. Chem. Phys. Discuss.* , Vol. 14, pp. 7425–7468.

Coz, E., Gómez-Moreno, F. J., Pujadas, M., Casuccio, G. S., Lersch, T. L. and Artíñano, B. n. (2009), "Individual particle characteristics of North African dust under different long-range transport scenarios", *Atmospheric Environment* , Vol. 43, pp. 1850–1863.

Cuesta, J., Lavaysse, C., Flamant, C., Mimouni, M. and Knippertz, P. (2010), "Northward bursts of the West African monsoon leading to rainfall over the Hoggar Massif, Algeria", *Quarterly Journal of the Royal Meteorological Society* , Vol. 136, pp. 174–189.

D'Alessio, S. J. D., Bryant Moodie, T., Pascal, J. P. and Swaters, G. E. (1996), "Gravity currents produced by sudden release of a fixed volume of heavy fluid", *Studies in Applied Mathematics* , Vol. 96, pp. 359–385.

Dee, D. P., Uppala, S. M., Simmons, A. J., Berrisford, P., Poli, P., Kobayashi, S., Andrae, U., Balmaseda, M. A., Balsamo, G., Bauer, P., Bechtold, P., Beljaars, A. C. M., van de Berg, L., Bidlot, J., Bormann, N., Delsol, C., Dragani, R., Fuentes, M., Geer, A. J., Haimberger, L., Healy, S. B., Hersbach, H., Hólm, E. V., Isaksen, L., Kållberg, P., Köhler, M., Matricardi, M., McNally, A. P., Monge-Sanz, B. M., Morcrette, J.-J., Park, B.-K., Peubey, C., de Rosnay, P., Tavolato, C., Thépaut, J.-N. and Vitart, F. (2011), "The ERA-Interim reanalysis: configuration and performance of the data assimilation system", *Q.J.R. Meteorol. Soc.* , Vol. 137, John Wiley & Sons, Ltd., pp. 553–597.

Denman, K., Brasseur, G., Chidthaisong, A., Ciais, P., Cox, P., Dickinson, R., Hauglustaine, D., Heinze, C., Holland, E., Jacob, D., Lohmann, U., Ramachandran, S., da Silva Dias, P., Wofsy, S. and Zhang, X. (2007), Couplings between changes in the climate system and biogeochemistry., *in* S. Solomon, D. Qin, M. Manning, Z. Chen, M. Marquis, K. Averyt, M. Tignor and H. Miller, eds, 'Climate Change 2007: The Physical Science Basis. Contribution of Working Group I to the Fourth Assessment Report of the Intergovernmental Panel on Climate Change', Cambridge University Press, Cambridge, United Kingdom and New York, NY, USA.

Derbyshire, E. (2007), "Natural minerogenic dust and human health", *AMBIO: A Journal of the Human Environment* , Vol. 36, pp. 73–77.

Doswell III, C. A. (2001), Severe convective storms- An overview, *in* C. A. Doswell, ed., 'Severe Convective Storms.', American Meteorological Society., chapter 1, pp. 1–26.

Drake, N. and Bristow, C. (2006), "Shorelines in the Sahara: Geomorphological evidence for an enhanced monsoon from palaeolake Megachad", *The Holocene* , Vol. 16, pp. 901–911.

Emmel, C., Knippertz, P. and Schulz, O. (2010), "Climatology of convective density currents in the southern foothills of the Atlas Mountains", *Journal of Geophysical Research* , Vol. 115, p. D11115.

Emmons, L. K., Walters, S., Hess, P. G., Lamarque, J.-F., Pfister, G. G., Fillmore, D., Granier, C., Guenther, A., Kinnison, D., Laepple, T., Orlando, J., Tie, X., Tyndall, G., Wiedinmyer, C., Baughcum, S. L. and Kloster, S. (2010), "Description and evaluation of the model for ozone and related chemical tracers, version 4 (MOZART-4)", *Geosci. Model Dev.* , Vol. 3, pp. 43–67.

Engelstaedter, S. and Washington, R. (2007), "Atmospheric controls on the annual cycle of North African dust", *J. Geophys. Res.* , Vol. 112, p. D03103.

Escudero, M., Stein, A., Draxler, R., Querol, X., Alastuey, A., Castillo, S. and Avila, A. (2011), "Source apportionment for African dust outbreaks over the western Mediterranean using the HYSPLIT model", *Atmospheric Research* , Vol. 99, pp. 518–527.

Farquharson, M. (1937), "Haboobs and instability in the Sudan", *Quarterly Journal of the Royal Meteorological Society* , Vol. 63, pp. 393–414.

Fiedler, S., Schepanski, K., Heinold, B., Knippertz, P. and Tegen, I. (2013b), "Climatology of nocturnal low-level jets over North Africa and implications for modeling mineral dust emission", *J. Geophys. Res. Atmos.* , Vol. 118, pp. 6100–6121.

Fiedler, S., Schepanski, K., Knippertz, P., Heinold, B. and Tegen, I. (2013a), "How important are cyclones for emitting mineral dust aerosol in North Africa?", *Atmos. Chem. Phys. Discuss.* , Vol. 13, Copernicus Publications, pp. 32483–32528.

Flamant, C., Chaboureau, J.-P., Parker, D., Taylor, C., Cammas, J.-P., Bock, O., Timouk, F. and Pelon, J. (2007), "Airborne observations of the impact of a convective system on the planetary boundary layer thermodynamics and aerosol distribution in the intertropical discontinuity region of the West African Monsoon", *Quarterly Journal of the Royal Meteorological Society* , Vol. 133, pp. 1175–1189.

Flamant, C., Knippertz, P., Parker, D. J., Chaboureau, J.-P., Lavaysse, C., Agusti-Panareda, A. and Kergoat, L. (2009), "The impact of a mesoscale convective system cold pool on the northward propagation of the intertropical discontinuity over West Africa", *Q.J.R. Meteorol. Soc.* , Vol. 135, pp. 139–159.

Formenti, P., Schütz, L., Balkanski, Y., Desboeufs, K., Ebert, M., Kandler, K., Petzold, A., Scheuvens, D., Weinbruch, S. and Zhang, D. (2011), "Recent progress in understanding physical and chemical properties of African and Asian mineral dust", *Atmos. Chem. Phys.* , Vol. 11, pp. 8231–8256.

Freeman, M. (1952), "Duststorms over the Anglo-Egyptian Sudan.", *Met Office Meteorological Reports* , Vol. 535, pp. 1–22.

Fritsch, J. and Forbes, G. (2001), Mesoscale convective systems., *in* C. A. Doswell III, ed., 'Severe Convective Storms', American Meteorological Society., chapter 9. Mesoscale Convective Systems., pp. 323–358.

Fröhlich, L., Knippertz, P., Fink, A. H. and Hohberger, E. (2013), "An objective climatology of tropical plumes", *J. Climate* , Vol. 26, American Meteorological Society, pp. 5044–5060.

Fujita, T. T. and Byers, H. R. (1977), "Spearhead echo and downburst in the crash of an airliner", *Mon. Wea. Rev.* , Vol. 105, pp. 129–146.

Garcia-Carreras, L., Marsham, J. H., Parker, D. J., Bain, C. L., Milton, S., Saci, A., Salah-Ferroudj, M., Ouchene, B. and Washington, R. (2013), "The impact of convective cold pool outflows on model biases in the Sahara", *Geophys. Res. Lett.* , Vol. 40, pp. 1647–1652.

Ginoux, P., Prospero, J. M., Gill, T. E., Hsu, N. C. and Zhao, M. (2012), "Global-scale attribution of anthropogenic and natural dust sources and their emission rates based on MODIS Deep Blue aerosol products", *Reviews of Geophysics* , Vol. 50, p. RG3005.

Goudie, A. S. (2009), "Dust storms: Recent developments", *Journal of Environmental Management* , Vol. 90, pp. 89–94.

Goudie, A. S. and Middleton, N. J. (2001), "Saharan dust storms: Nature and consequences", *Earth-Science Reviews* , Vol. 56, pp. 179–204.

Grams, C. M., Jones, S. C., Marsham, J. H., Parker, D. J., Haywood, J. M. and Heuveline, V. (2010), "The Atlantic inflow to the Saharan heat low: observations and modelling", *Q.J.R. Meteorol. Soc.* , Vol. 136, John Wiley & Sons, Ltd., pp. 125–140.

Guy, N. and Rutledge, S. A. (2012), "Regional comparison of West African convective characteristics: a TRMM-based climatology", *Quarterly Journal of the Royal Meteorological Society* , Vol. 138, John Wiley & Sons, Ltd., pp. 1179–1195.

Hallworth, M. A., Huppert, H. E. and Ungarish, M. (2001), "Axisymmetric gravity currents in a rotating system: Experimental and numerical investigations", *Journal of Fluid Mechanics* , Vol. 447, pp. 1–29.

Hamilton, R. A., Archbold, J. W. and Douglas, C. K. M. (1945), "Meteorology of Nigeria and adjacent territory", *Q.J.R. Meteorol. Soc.* , Vol. 71, pp. 231–264.

Heinold, B., Knippertz, P., Marsham, J. H., Fiedler, S., Dixon, N. S., Schepanski, K., Laurent, B. and Tegen, I. (2013), "The role of deep convection and nocturnal low-level jets for dust emission in summertime West Africa: Estimates from convection-permitting simulations", *J. Geophys. Res. Atmos.* , Vol. 118, pp. 4385–4400.

Herrmann, L., Stahr, K. and Jahn, R. (1999), "The importance of source region identification and their properties for soil-derived dust : The case of Harmattan dust sources for eastern West Africa", *Contributions to Atmospheric Physics* , Vol. 72, pp. 141–150.

Hobby, M., Gascoyne, M., Marsham, J. H., Bart, M., Allen, C., Engelstaedter, S., Fadel, D. M., Gandega, A., Lane, R., McQuaid, J. B., Ouchene, B., Ouladichir, A., Parker, D. J., Rosenberg, P., Ferroudj, M. S., Saci, A., Seddik, F., Todd, M., Walker, D. and Washington, R. (2013), "The Fennec automatic weather station (AWS) network: Monitoring the Saharan climate system", *J. Atmos. Oceanic Technol.* , Vol. 30, pp. 709–724.

Hodges, K. I., Hoskins, B. J., Boyle, J. and Thorncroft, C. (2003), "A comparison of recent reanalysis datasets using objective feature tracking: storm tracking and tropical easterly waves", *Monthly Weather Review* , Vol. 131, pp. 2012–2037.

Holyer, J. and Huppert, H. (1983), "Gravity currents entering a two-layer fluid.", *Journal of Fluid Mechanics.* , Vol. 100, pp. 739–767.

Houze, R. (2004), *Cloud Dynamics*, Academic Press.

Houze, R. A., Biggerstaff, M. I., Rutledge, S. A. and Smull, B. F. (1989), "Interpretation of doppler weather radar displays of midlatitude mesoscale convective systems", *Bull. Amer. Meteor. Soc.* , Vol. 70, pp. 608–619.

Hsu, N. C., Herman, J. R., Torres, O., Holben, B. N., Tanre, D., Eck, T. F., Smirnov, A., Chatenet, B. and Lavenu, F. (1999), "Comparisons of the TOMS aerosol index with sun-photometer aerosol optical thickness: Results and applications", *Journal of Geophysical Research: Atmospheres* , Vol. 104, pp. 6269–6279.
**URL:** *http://dx.doi.org/10.1029/1998JD200086*

Hsu, N., Tsay, S.-C., King, M. and Herman, J. (2004), "Aerosol properties over bright-reflecting source regions", *Geoscience and Remote Sensing, IEEE Transactions on* , Vol. 42, pp. 557–569.

Huffman, G. J., Bolvin, D. T., Nelkin, E. J., Wolff, D. B., Adler, R. F., Gu, G., Hong, Y., Bowman, K. P. and Stocker, E. F. (2007), "The TRMM multisatellite precipitation analysis (TMPA): Quasi-global, multiyear, combined-sensor precipitation estimates at fine scales", *J. Hydrometeor* , Vol. 8, American Meteorological Society, pp. 38–55.

Huijnen, V., Williams, J. E., van Weele, M., van Noije, T. P. C., Krol, M. C., Dentener, F., Segers, A., Houweling, S., Peters, W., de Laat, A. T. J., Boersma, K. F., Bergamaschi, P., van Velthoven, P. F. J., Le Sager, P., Eskes, H. J., Alkemade, F., Scheele, M. P., Nédélec, P. and Pãtz, H.-W. (2010), "The global chemistry transport model TM5: description and evaluation of the tropospheric chemistry version 3.0", *Geosci. Model Dev. Discuss.* , Vol. 3, pp. 1009–1087.

Huppert, H. and Simpson, J. (1980), "The slumping of gravity currents.", *Journal of Fluid Mechanics.* , Vol. 99, pp. 785–799.

Idso, S. B., Ingram, R. S. and Pritchard, J. M. (1972), "An American haboob", *Bull. Amer. Meteor. Soc.* , Vol. 53, pp. 930–935.

Jacobson, M. (2005), Numerical solutions to partial differential equations, *in* 'Fundamentals of Atmospheric Modeling', Cambridge University Press, Cambridge, United Kingdom and New York, NY, USA., chapter 6, pp. 169–203.

Johnson, R. H. and Mapes, B. E. (2001), Mesoscale processes and severe convective weather., *in* C. A. Doswell, ed., 'Severe Convective Storms', American Meteorological Society., chapter 3, pp. 71–122.

Jonas, P. (1991), "Growth of droplets in cloud edge downdraughts", *Q.J.R. Meteorol. Soc.* , Vol. 117, pp. 243–255.

Kalnay, E., Kanamitsu, M., Kistler, R., Collins, W., Deaven, D., Gandin, L., Iredell, M., Saha, S., White, G., Woollen, J., Zhu, Y., Leetmaa, A., Reynolds, R., Chelliah, M., Ebisuzaki, W., Higgins, W., Janowiak, J., Mo, K. C., Ropelewski, C., Wang, J., Jenne, R. and Joseph, D. (1996), "The NCEP/NCAR 40-year reanalysis project", *Bull. Amer. Meteor. Soc.* , Vol. 77, American Meteorological Society, pp. 437–471.

Kamburova, P. and Ludlam, F. (1966), "Rainfall evaporation in thunderstorm downdraughts", *Quarterly Journal of the Royal Meteorological Society* , Vol. 92, pp. 510–518.

Kanamitsu, M., Ebisuzaki, W., Woollen, J., Yang, S.-K., Hnilo, J. J., Fiorino, M. and Potter, G. L. (2002), "NCEP-DOE AMIP-ii reanalysis (R-2)", *Bull. Amer. Meteor. Soc.* , Vol. 83, American Meteorological Society, pp. 1631–1643.

Kawashima, M. (2010), "Numerical study of horizontal shear instability waves along narrow cold frontal rainbands", *J. Atmos. Sci.* , Vol. 68, American Meteorological Society, pp. 878–903.

Kistler, R., Collins, W., Saha, S., White, G., Woollen, J., Kalnay, E., Chelliah, M., Ebisuzaki, W., Kanamitsu, M., Kousky, V., van den Dool, H., Jenne, R. and Fiorino, M. (2001), "The NCEP-NCAR 50-year reanalysis: Monthly means CD-ROM and documentation", *Bull. Amer. Meteor. Soc.* , Vol. 82, American Meteorological Society, pp. 247–267.

Knippertz, P. (2008), "Dust emissions in the West African heat trough - the role of the diurnal cycle and of extratropical disturbances", *Meteorologische Zeitschrift* , Vol. 17, pp. 553–563.

Knippertz, P., Ansmann, A., Althausen, D., Müller, D., Tesche, M., Bierwirth, E., Dinter, T., Müller, T., Von Hoyningen Huene, W., Schepanski, K., Wendisch, M., Heinold, B., Kandler, K., Petzold, A., Schütz, L. and Tegen, I. (2009a), "Dust mobilization

and transport in the northern Sahara during SAMUM 2006 a meteorological overview", *Tellus B* , Vol. 61, Blackwell Publishing Ltd, pp. 12–31.

Knippertz, P., Deutscher, C., Kandler, K., Müller, T., Schulz, O. and Schütz, L. (2007), "Dust mobilization due to density currents in the Atlas region: Observations from the SAMUM 2006 field campaign", *Journal of Geophysical Research* , Vol. 112, p. D21109.

Knippertz, P. and Martin, J. E. (2005), "Tropical plumes and extreme precipitation in subtropical and tropical West Africa", *Q.J.R. Meteorol. Soc.* , Vol. 131, pp. 2337–2365.

Knippertz, P. and Todd, M. C. (2010), "The central west Saharan dust hot spot and its relation to African easterly waves and extratropical disturbances", *Journal of Geophysical Research* , Vol. 115, p. D12117.

Knippertz, P. and Todd, M. C. (2012), "Mineral dust aerosols over the Sahara: Meteorological controls on emission and transport and implications for modeling", *Rev. Geophys.* , Vol. 50, p. RG1007.

Knippertz, P., Trentmann, J. and Seifert, A. (2009b), "High-resolution simulations of convective cold pools over the northwestern Sahara", *Journal of Geophysical Research-Atmospheres* , Vol. 114, p. D08110.

Knupp, K. and Cotton, W. (1985), "Convective cloud downdraft structure: An interpretative survey", *Reviews of Geophysics* , Vol. 23, pp. 183–215.

Koch, J. and Renno, N. O. (2005), "The role of convective plumes and vortices on the global aerosol budget", *Geophys. Res. Lett.* , Vol. 32, p. L18806.

Kostka, P., Weissmann, M., Buras, R., Mayer, B. and Stiller, O. (2014), "Observation operator for visible and near-infrared satellite reflectances", *J. Atmos. Oceanic Technol.* , Vol. 31, pp. 1216–1233.

Kröpelin, S., Verschuren, D., Lézine, A.-M., Eggermont, H., Cocquyt, C., Francus, P., Cazet, J.-P., Fagot, M., Rumes, B., Russell, J. M., Darius, F., Conley, D. J., Schuster, M., von Suchodoletz, H. and Engstrom, D. R. (2008), "Climate-driven ecosystem succession in the Sahara: The past 6000 years", *Science* , Vol. 320, pp. 765–768.

Lafore, J.-P., Flamant, C., Guichard, F., Parker, D. J., Bouniol, D., Fink, A. H., Giraud, V., Gosset, M., Hall, N., Höller, H., Jones, S. C., Protat, A., Roca, R., Roux, F., Saïd,

F. and Thorncroft, C. (2011), "Progress in understanding of weather systems in West Africa", *Atmosph. Sci. Lett.* , Vol. 12, pp. 7–12.

Laing, A. and Fritsch, J. (2000), "The large-scale environments of the global populations of mesoscale convective complexes.", *Monthly Weather Review* , Vol. 128, pp. 2756–2776.

Laing, A. G., Carbone, R., Levizzani, V. and Tuttle, J. (2008), "The propagation and diurnal cycles of deep convection in northern tropical Africa", *Quarterly Journal of the Royal Meteorological Society* , Vol. 134, pp. 93–109.

Lavaysse, C., Flamant, C., Janicot, S. and Knippertz, P. (2010), "Links between African easterly waves, midlatitude circulation and intraseasonal pulsations of the West African heat low", *Quarterly Journal of the Royal Meteorological Society* , Vol. 136, John Wiley & Sons, Ltd., pp. 141–158.

Lawson, T. (1971), "Haboob structure in Khartoum", *Weather* , Vol. 26, pp. 105–112.

Lebel, T., Parker, D. J., Flamant, C., Bourlès, B., Marticorena, B., Mougin, E., Peugeot, C., Diedhiou, A., Haywood, J. M., Ngamini, J. B., Polcher, J., Redelsperger, J.-L. and Thorncroft, C. D. (2010), "The AMMA field campaigns: multiscale and multidisciplinary observations in the West African region", *Q.J.R. Meteorol. Soc.* , Vol. 136, pp. 8–33.

Liu, C. and Moncrieff, M. W. (1996), "A numerical study of the effects of ambient flow and shear on density currents", *Mon. Wea. Rev.* , Vol. 124, pp. 2282–2303.

Lorenz, C. and Kunstmann, H. (2012), "The hydrological cycle in three state-of-the-art reanalyses: Intercomparison and performance analysis", *J. Hydrometeor* , Vol. 13, American Meteorological Society, pp. 1397–1420.

Maddox, R. A. (1980), "Meoscale convective complexes", *Bull. Amer. Meteor. Soc.* , Vol. 61, pp. 1374–1387.

Mahowald, N. M., Bryant, R. G., del Corral, J. and Steinberger, L. (2003), "Ephemeral lakes and desert dust sources", *Geophys. Res. Lett.* , Vol. 30, p. 1074.

Mapes, B. E. (1993), "Gregarious tropical convection", *J. Atmos. Sci.* , Vol. 50, pp. 2026–2037.

Mari, C. H., Reeves, C. E., Law, K. S., Ancellet, G., Andrés-Hernández, M. D., Barret, B., Bechara, J., Borbon, A., Bouarar, I., Cairo, F., Commane, R., Delon, C., Evans, M. J., Fierli, F., Floquet, C., Galy-Lacaux, C., Heard, D. E., Homan, C. D., Ingham, T., Larsen, N., Lewis, A. C., Liousse, C., Murphy, J. G., Orlandi, E., Oram, D. E., Saunois, M., Serça, D., Stewart, D. J., Stone, D., Thouret, V., van Velthoven, P. and Williams, J. E. (2011), "Atmospheric composition of West Africa: Highlights from the AMMA international program", *Atmosph. Sci. Lett.* , Vol. 12, pp. 13–18.

Marsham, J. H., Dixon, N. S., Garcia-Carreras, L., Lister, G. M. S., Parker, D. J., Knippertz, P. and Birch, C. E. (2013b), "The role of moist convection in the West African monsoon system: Insights from continental-scale convection-permitting simulations", *Geophys. Res. Lett.* , Vol. 40, pp. 1843–1849.

Marsham, J. H., Hobby, M., Allen, C. J. T., Banks, J. R., Bart, M., Brooks, B. J., Cavazos-Guerra, C., Engelstaedter, S., Gascoyne, M., Lima, A. R., Martins, J. V., McQuaid, J. B., OLeary, A., Ouchene, B., Ouladichir, A., Parker, D. J., Saci, A., Salah-Ferroudj, M., Todd, M. C. and Washington, R. (2013a), "Meteorology and dust in the central Sahara: Observations from Fennec supersite-1 during the june 2011 intensive observation period", *Journal of Geophysical Research: Atmospheres* , Vol. 118, pp. 4069–4089.

Marsham, J. H., Knippertz, P., Dixon, N. S., Parker, D. J. and Lister, G. M. S. (2011), "The importance of the representation of deep convection for modeled dust-generating winds over West Africa during summer", *Geophysical Research Letters* , Vol. 38, p. L16803.

Marsham, J. H., Parker, D. J., Grams, C. M., Taylor, C. M. and Haywood, J. M. (2008), "Uplift of Saharan dust south of the intertropical discontinuity", *J. Geophys. Res.* , Vol. 113, p. D21102.

Marticorena, B. and Bergametti, G. (1995), "Modeling the atmospheric dust cycle: 1. design of a soil-derived dust emission scheme", *J. Geophys. Res.* , Vol. 100, pp. 16415–16430.

Marticorena, B., Bergametti, G., Aumont, B., Callot, Y., N'Doumé, C. and Legrand, M. (1997), "Modeling the atmospheric dust cycle: 2. simulation of Saharan dust sources", *J. Geophys. Res.* , Vol. 102, pp. 4387–4404.

Mathon, V., Laurent, H. and Lebel, T. (2002), "Mesoscale convective system rainfall in the Sahel", *J. Appl. Meteor.* , Vol. 41, American Meteorological Society, pp. 1081–1092.

Maxworthy, T., Leilich, J., Simpson, J. E. and Meiburg, E. H. (2002), "The propagation of a gravity current into a linearly stratified fluid", *Journal of Fluid Mechanics* , Vol. 453, pp. 371–394.

Mei, L., Xue, Y., Kokhanovsky, A. A., von Hoyningen-Huene, W., de Leeuw, G. and Burrows, J. P. (2013), "Retrieval of aerosol optical depth over land surfaces from AVHRR data", *Atmospheric Measurement Techniques Discussions* , Vol. 6, pp. 2227–2251.

Mellor, G. L. and Yamada, T. (1982), "Development of a turbulence closure model for geophysical fluid problems", *Reviews of Geophysics* , Vol. 20, pp. 851–875.

Membery, D. (1985), "A gravity-wave haboob?", *Weather* , Vol. 40, pp. 214–221.

Middleton, N. J. and Goudie, A. S. (2001), "Saharan dust: sources and trajectories", *Transactions of the Institute of British Geographers* , Vol. 26, pp. 165–181.

Miller, S. D., Kuciauskas, A. P., Liu, M., Ji, Q., Reid, J. S., Breed, D. W., Walker, A. L. and Mandoos, A. A. (2008), "Haboob dust storms of the southern Arabian peninsula", *J. Geophys. Res.* , Vol. 113, p. D01202.

Mitsuta, Y., Hayashi, T., Takemi, T., Hu, Y., Wang, J. and Chen, M. (1995), "Two severe local storms as observed in the arid area of northwest China : HEIFE", *Journal of the Meteorological Society of Japan* , Vol. 73, pp. 1269–1284.

Mohr, K. I., Famiglietti, J. S. and Zipser, E. J. (1999), "The contribution to tropical rainfall with respect to convective system type, size, and intensity estimated from the 85-GHz ice-scattering signature", *J. Appl. Meteor.* , Vol. 38, pp. 596–606.

Moncrieff, M. W. and Liu, C. (1999), "Convection initiation by density currents: Role of convergence, shear, and dynamical organization", *Mon. Wea. Rev.* , Vol. 127, pp. 2455–2464.

Nofal, F. H., Saeed, A. A. W. and Anokute, C. C. (1996), "Aetiological factors contributing to road traffic accidents in Riyadh City, Saudi Arabia", *The Journal of the Royal Society for the Promotion of Health* , Vol. 116, pp. 304–311.

Ohya, Y., Nakamura, R. and Uchida, T. (2008), "Intermittent bursting of turbulence in a stable boundary layer with low-level jet", *Boundary layer meteorology* , Vol. 126, pp. 349–363.

Ooyama, K. V. (1990), "A thermodynamic foundation for modeling the moist atmosphere", *J. Atmos. Sci.* , Vol. 47, American Meteorological Society, pp. 2580–2593.

Parker, D. J., Burton, R. R., Diongue-Niang, A., Ellis, R. J., Felton, M., Taylor, C. M., Thorncroft, C. D., Bessemoulin, P. and Tompkins, A. M. (2005), "The diurnal cycle of the West African monsoon circulation", *Q.J.R. Meteorol. Soc.* , Vol. 131, John Wiley & Sons, Ltd., pp. 2839–2860.

Parker, D. J., Fink, A., Janicot, S., Ngamini, J.-B., Douglas, M., Afiesimama, E., Agusti-Panareda, A., Beljaars, A., Dide, F., Diedhiou, A., Lebel, T., Polcher, J., Redelsperger, J.-L., Thorncroft, C. and Ato Wilson, G. (2008), "The AMMA radiosonde program and its implications for the future of atmospheric monitoring over Africa", *Bulletin of the American Meteorological Society* , Vol. 89, p. 1015.

Parker, D., Lebel, T. and Bourles, B. (2007), "Overview of the AMMA observing campaigns", *Clivar Exchanges* , Vol. 41, pp. 4–6.

Petzold, A., Rasp, K., Weinzierl, B., Esselborn, M., Hamburger, T., Dörnbrack, A., Kandler, K., Schütz, L., Knippertz, P., Fiebig, M. and Virkkula, A. (2009), "Saharan dust absorption and refractive index from aircraft-based observations during SAMUM 2006", *Tellus B* , Vol. 61, pp. 118–130.

Phillips, V. T. J., Donner, L. J. and Garner, S. T. (2007), "Nucleation processes in deep convection simulated by a cloud-system-resolving model with double-moment bulk microphysics", *J. Atmos. Sci.* , Vol. 64, pp. 738–761.

Polcher, J., Parker, D. J. and Gaye, A. T. (2011), "African monsoon multidisciplinary analysis: an integrated project for understanding of the West African climate system and its human dimension", *Atmosph. Sci. Lett.* , Vol. 12, p. 1.

Pospichal, B., Karam, D., Crewell, S., Flamant, C., Hünerbein, A., Bock, O. and Saïd, F. (2010), "Diurnal cycle of the intertropical discontinuity over West Africa analysed by remote sensing and mesoscale modelling", *Quarterly Journal of the Royal Meteorological Society* , Vol. 136, pp. 92–106.

Prospero, J. M., Landing, W. M. and Schulz, M. (2010), "African dust deposition to Florida: Temporal and spatial variability and comparisons to models", *J. Geophys. Res.* , Vol. 115, p. D13304.

Rangno, A. L. and Hobbs, P. V. (2005), "Microstructures and precipitation development in cumulus and small cumulonimbus clouds over the warm pool of the tropical Pacific Ocean", *Q.J.R. Meteorol. Soc.* , Vol. 131, pp. 639–673.

Reinfried, F., Tegen, I., Heinold, B., Hellmuth, O., Schepanski, K., Cubasch, U., Huebener, H. and Knippertz, P. (2009), "Simulations of convectively driven density currents in the Atlas region using a regional model: Impacts on dust emission and sensitivity to horizontal resolution and convection schemes", *Journal of Geophysical Research* , Vol. 114, p. D08127.

Rienecker, M. M., Suarez, M. J., Gelaro, R., Todling, R., Bacmeister, J., Liu, E., Bosilovich, M. G., Schubert, S. D., Takacs, L., Kim, G.-K., Bloom, S., Chen, J., Collins, D., Conaty, A., da Silva, A., Gu, W., Joiner, J., Koster, R. D., Lucchesi, R., Molod, A., Owens, T., Pawson, S., Pegion, P., Redder, C. R., Reichle, R., Robertson, F. R., Ruddick, A. G., Sienkiewicz, M. and Woollen, J. (2011), "MERRA: NASA's modern-era retrospective analysis for research and applications", *J. Climate* , Vol. 24, American Meteorological Society, pp. 3624–3648.

Rienecker, M., Suarez, M., Todling, R., Bacmeister, J., Takacs, L., Liu, H.-C., Gu, W., Sienkiewicz, M., Koster, R., Gelaro, R., Stajner, I. and Nielsen, J. (2008), The GEOS-5 data assimilation system - documentation of versions 5.0.1, 5.1.0, and 5.2.0, Technical report, NASA.

Roberts, A. J. and Knippertz, P. (2014), "The formation of a large summertime Saharan dust plume: Convective and synoptic-scale analysis", *Journal of Geophysical Research: Atmospheres* , Vol. 119, pp. 1766–1785.

Roberts, A. and Knippertz, P. (2012), "Haboobs: convectively generated dust storms in West Africa", *Weather* , Vol. 67, pp. 311–316.

Rottman, J. and Simpson, J. (1983), "Gravity currents produced by instantaneous releases of a heavy fluid in a rectangular channel.", *Journal of Fluid Mechanics.* , Vol. 135, pp. 95–110.

Rotunno, R., Klemp, J. B. and Weisman, M. L. (1988), "A theory for strong, long-lived squall lines", *J. Atmos. Sci.* , Vol. 45, pp. 463–485.

Saha, S., Moorthi, S., Pan, H.-L., Wu, X., Wang, J., Nadiga, S., Tripp, P., Kistler, R., Woollen, J., Behringer, D., Liu, H., Stokes, D., Grumbine, R., Gayno, G., Wang, J., Hou, Y.-T., Chuang, H.-Y., Juang, H.-M. H., Sela, J., Iredell, M., Treadon, R., Kleist, D., Van Delst, P., Keyser, D., Derber, J., Ek, M., Meng, J., Wei, H., Yang, R., Lord, S., Van Den Dool, H., Kumar, A., Wang, W., Long, C., Chelliah, M., Xue, Y., Huang, B., Schemm, J.-K., Ebisuzaki, W., Lin, R., Xie, P., Chen, M., Zhou, S., Higgins, W., Zou, C.-Z., Liu, Q., Chen, Y., Han, Y., Cucurull, L., Reynolds, R. W., Rutledge, G. and Goldberg, M. (2010), "The NCEP climate forecast system reanalysis", *Bull. Amer. Meteor. Soc.* , Vol. 91, American Meteorological Society, pp. 1015–1057.

Schepanski, K., Knippertz, P., Fiedler, S., Timouk, F. and Demarty, J. (2014), "The influence of resolution, initial conditions and boundary-layer setup on the representation of nocturnal low-level jetsover the Sahel in a regional model", *Quarterly Journal of the Royal Meteorological Society* , Vol. Submitted.

Schepanski, K., Tegen, I., Laurent, B., Heinold, B. and Macke, A. (2007), "A new Saharan dust source activation frequency map derived from MSG-SEVIRI IR-channels", *Geophysical Research Letters* , Vol. 34, p. L18803.

Schepanski, K., Tegen, I. and Macke, A. (2012), "Comparison of satellite based observations of Saharan dust source areas", *Remote Sensing of Environment* , Vol. 123, pp. 90–97.

Schultz, D. M. and Doswell, C. A. (2000), "Analyzing and forecasting Rocky Mountain lee cyclogenesis often associated with strong winds", *Wea. Forecasting* , Vol. 15, American Meteorological Society, pp. 152–173.

Schwanghart, W. and Schutt, B. (2008), "Meteorological causes of Harmattan dust in West Africa", *Geomorphology* , Vol. 95, pp. 412–428.

Shao, Y., Wyrwoll, K.-H., Chappell, A., Huang, J., Lin, Z., McTainsh, G. H., Mikami, M., Tanaka, T. Y., Wang, X. and Yoon, S. (2011), "Dust cycle: An emerging core theme in Earth system science", *Aeolian Research* , Vol. 2, pp. 181–204.

Shaw, P. A. (1997), Geomorphology of the worlds arid zones: Africa and Europe., *in* D. S. Thomas, ed., 'Arid zone geomorphology.', Wiley.

Shi, Y., Zhang, J., Reid, J. S., Hyer, E. J. and Hsu, N. C. (2012), "Critical evaluation of the MODIS Deep Blue aerosol optical depth product for data assimilation over North Africa", *Atmospheric Measurement Techniques Discussions* , Vol. 5, pp. 7815–7865.

Simpson, J. (1997), *Gravity currents in the environment and the laboratory*, Cambridge University Press, Cambridge, United Kingdom and New York, NY, USA., Chichester.

Simpson, J. E. and Britter, R. E. (1980), "A laboratory model of an atmospheric mesofront", *Q.J.R. Meteorol. Soc.* , Vol. 106, pp. 485–500.

Skamarock, W. C., Klemp, J. B., Dudhia, J., Gill, D. O., Barker, D. M., Duda, M. G., Huang, X.-Y., Wang, W. and Powers, J. G. (2008), A description of the advanced research WRF version 3, Technical report, NCAR.

Solomos, S., Kallos, G., Mavromatidis, E. and Kushta, J. (2012), "Density currents as a desert dust mobilization mechanism", *Atmos. Chem. Phys.* , Vol. 12, pp. 11199–11211.

Steenburgh, W. J. and Mass, C. F. (1994), "The structure and evolution of a simulated Rocky Mountain lee trough", *Mon. Wea. Rev.* , Vol. 122, American Meteorological Society, pp. 2740–2761.

Sterk, G. (2003), "Causes, consequences and control of wind erosion in Sahelian Africa: a review", *Land Degradation & Development* , Vol. 14, pp. 95–108.

Stocker, T., Qin, D., Plattner, G.-K., Alexander, L., Allen, S., Bindoff, N., Bron, F.-M., Church, J., Cubasch, U., Emori, S., Forster, P., Friedlingstein, P., Gillett, N., Gregory, J., Hartmann, D., Jansen, E., Kirtman, B., Knutti, R., Krishna Kumar, K., Lemke, P., Marotzke, J., Masson-Delmotte, V., Meehl, G., Mokhov, I., Piao, S., Ramaswamy, V., Randall, D., Rhein, M., Rojas, M., Sabine, C., Shindell, D., Talley, L., Vaughan, D. and Xie, S.-P. (2013), Technical summary, *in* T. Stocker, D. Qin, G.-K. Plattner, M. Tignor, S. Allen, J. Boschung, A. Nauels, Y. Xia, V. Bex and P. Midgley, eds, 'Climate Change 2013: The Physical Science Basis. Contribution of Working Group I to the Fifth Assessment Report of the Intergovernmental Panel on Climate Change', Cambridge University Press, Cambridge, United Kingdom and New York, NY, USA.

Storto, A. and Tveter, F. T. (2009), "Assimilating humidity pseudo-observations derived from the cloud profiling radar aboard cloudsat in ALADIN 3D-Var", *Met. Apps* , Vol. 16, John Wiley & Sons, Ltd., pp. 461–479.

Strong, C., Parsons, K., McTainsh, G. and Sheehan, A. (2011), "Dust transporting wind systems in the lower Lake Eyre basin, Australia: A preliminary study", *Aeolian Research* , Vol. 2, pp. 205–214.

Sultan, B. and Janicot, S. (2000), "Abrupt shift of the ITCZ over West Africa and intra-seasonal variability", *Geophys. Res. Lett.* , Vol. 27, pp. 3353–3356.

Sultan, B. and Janicot, S. (2003), "The West African monsoon dynamics. Part II: The pre-onset and onset of the summer monsoon", *J. Climate* , Vol. 16, American Meteorological Society, pp. 3407–3427.

Sultan, B., Janicot, S. and Drobinski, P. (2007), "Characterization of the diurnal cycle of the West African monsoon around the monsoon onset", *J. Climate* , Vol. 20, American Meteorological Society, pp. 4014–4032.

Sultan, B., Labadi, K., Guégan, J.-F. and Janicot, S. (2005), "Climate drives the meningitis epidemics onset in West Africa", *PLoS Med* , Vol. 2, p. e6.

Sutton, L. (1925), "Haboobs", *Quarterly Journal of the Royal Meteorological Society* , Vol. 51, pp. 25–30.

Takemi, T. (1999), "Structure and evolution of a severe squall line over the arid region in northwest China", *Mon. Wea. Rev.* , Vol. 127, pp. 1301–1309.

Takemi, T. (2005), "Explicit simulations of convective-scale transport of mineral dust in severe convective weather", *Journal of the Meteorological Society of Japan. Ser. II* , Vol. 83A, pp. 187–203.

Tan, A. W., Nobes, D. S., Fleck, B. A. and Flynn, M. R. (2010), "Gravity currents in two-layer stratified media", *Environmental Fluid Mechanics* , Vol. 11, pp. 203–223.

Taylor, C. M., de Jeu, R. A. M., Guichard, F., Harris, P. P. and Dorigo, W. A. (2012), "Afternoon rain more likely over drier soils", *Nature* , Vol. 489, Nature Publishing Group, a division of Macmillan Publishers Limited. All Rights Reserved., pp. 423–426.

Thieuleux, F., Moulin, C., Bréon, F. M., Maignan, F., Poitou, J. and Tanré, D. (2005), "Remote sensing of aerosols over the oceans using MSG/SEVIRI imagery", *Ann. Geophys.* , Vol. 23, Copernicus Publications, pp. 3561–3568.

Thompson, G., Field, P. R., Rasmussen, R. M. and Hall, W. D. (2008), "Explicit forecasts of winter precipitation using an improved bulk microphysics scheme. Part II: Implementation of a new snow parameterization", *Mon. Wea. Rev.* , Vol. 136, American Meteorological Society, pp. 5095–5115.

Todd, M. C., Allen, C. J. T., Bart, M., Bechir, M., Bentefouet, J., Brooks, B. J., Cavazos-Guerra, C., Clovis, T., Deyane, S., Dieh, M., Engelstaedter, S., Flamant, C., Garcia-Carreras, L., Gandega, A., Gascoyne, M., Hobby, M., Kocha, C., Lavaysse, C., Marsham, J. H., Martins, J. V., McQuaid, J. B., Ngamini, J. B., Parker, D. J., Podvin, T., Rocha-Lima, A., Traore, S., Wang, Y. and Washington, R. (2013), "Meteorological and dust aerosol conditions over the western Saharan region observed at Fennec supersite-2 during the intensive observation period in June 2011", *Journal of Geophysical Research: Atmospheres* , Vol. 118, pp. 8426–8447.

Todd, M., Washington, R., Lizcano, G., Ragvahan, S. and Knippertz, P. (2008), "Regional model simulations of the Bodélé low-level jet of northern Chad during BoDEx 2005", *Journal of Climate* , Vol. 21, pp. 995–1012.

Toon, O. B. (2003), "Atmospheric science: African dust in Florida clouds", *Nature* , Vol. 424, pp. 623–624.

Torres, O., Bhartia, P., Herman, J., Sinyuk, A., Ginoux, P. and Holben, B. (2002), "A long term record of aerosol optical depth from TOMS observations and comparison to AERONET measurements", *Journal of the Atmospheric Sciences* , Vol. 59, pp. 398–413.

Torres, O., Bhartia, P. K., Herman, J. R., Ahmad, Z. and Gleason, J. (1998), "Derivation of aerosol properties from satellite measurements of backscattered ultraviolet radiation: Theoretical basis", *J. Geophys. Res.* , Vol. 103, pp. 17099–17110.

Torres, O., Tanskanen, A., Veihelmann, B., Ahn, C., Braak, R., Bhartia, P. K., Veefkind, P. and Levelt, P. (2007), "Aerosols and surface UV products from Ozone Monitoring Instrument observations: An overview", *Journal of Geophysical Research* , Vol. 112, p. D24S47.

Trenberth, K. E. and Guillemot, C. J. (1995), "Evaluation of the global atmospheric moisture budget as seen from analyses", *J. Climate* , Vol. 8, American Meteorological Society, pp. 2255–2272.

Urban, J. (2013), Satellite sensors measuring atmospheric water vapour, *in* N. Kämpfer, ed., 'Monitoring Atmospheric Water Vapour', Springer, chapter Satellite Sensors Measuring Atmospheric Water Vapour, pp. 175–214.

Van de Wiel, B. J. H., Moene, A. F., Steeneveld, G. J., Baas, P., Bosveld, F. C. and Holtslag, A. A. M. (2010), "A conceptual view on inertial oscillations and nocturnal low-level jets", *J. Atmos. Sci.* , Vol. 67, American Meteorological Society, pp. 2679–2689.

Vizy, E. K. and Cook, K. H. (2009), "A mechanism for African monsoon breaks: Mediterranean cold air surges", *J. Geophys. Res.* , Vol. 114, p. D01104.

Vohl, O., Mitra, S., Wurzler, S., Diehl, K. and Pruppacher, H. (2007), "Collision efficiencies empirically determined from laboratory investigations of collisional growth of small raindrops in a laminar flow field", *Atmospheric Research* , Vol. 85, pp. 120–125.

Wang, W., Bruyére, C., M., D., Dudhia, J., Gill, D., Lin, H.-C., Michalakes, J., Rizvi, S. and Zhang, X. (2011), *WRF-ARW users guide V3.3*, 3.3 edn, National Center for Atmospheric Research.

Warner, T. T. (2004), *Desert meteorology.*, Cambridge University Press, Cambridge, United Kingdom and New York, NY, USA.

Washington, R., Flamant, C., Parker, D., Marsham, J., McQuaid, J., Brindley, H., Todd, M., Highwood, E., C. Ryder, J. C., Kocha, C., Bechir, M. and Saci, A. (2012), "Fennec: The Saharan climate system", *CLIVAR Exchanges* , Vol. 17, pp. 31–32.

Washington, R. and Todd, M. (2005), "Atmospheric controls on mineral dust emission from the Bodélé depression, Chad: The role of the low level jet", *Geophysical Research Letters* , Vol. 32, p. L17701.

Washington, R., Todd, M., Middleton, N. J. and Goudie, A. S. (2003), "Dust-storm source areas determined by the total ozone monitoring spectrometer and surface observations", *Annals of the Association of American Geographers* , Vol. 93, pp. 297–313.

Winter, M. (2009), '4 dead in dust-storm pileups on I-10 in Arizona.', Online newspaper report. USA Today. Accessed 10/01/11.
**URL:** *http://content.usatoday.com/communities/ondeadline/post/2009/12/4-dead-in-dust-storm-pileup-on-i-40-in-arizona/1.*

Zemach, T. and Ungarish, M. (2013), "The flow of an axisymmetric stratified gravity current into a stratified ambient in a rotating system", *Environmental Fluid Mechanics* , Vol. 13, pp. 337–351.

# Appendix A

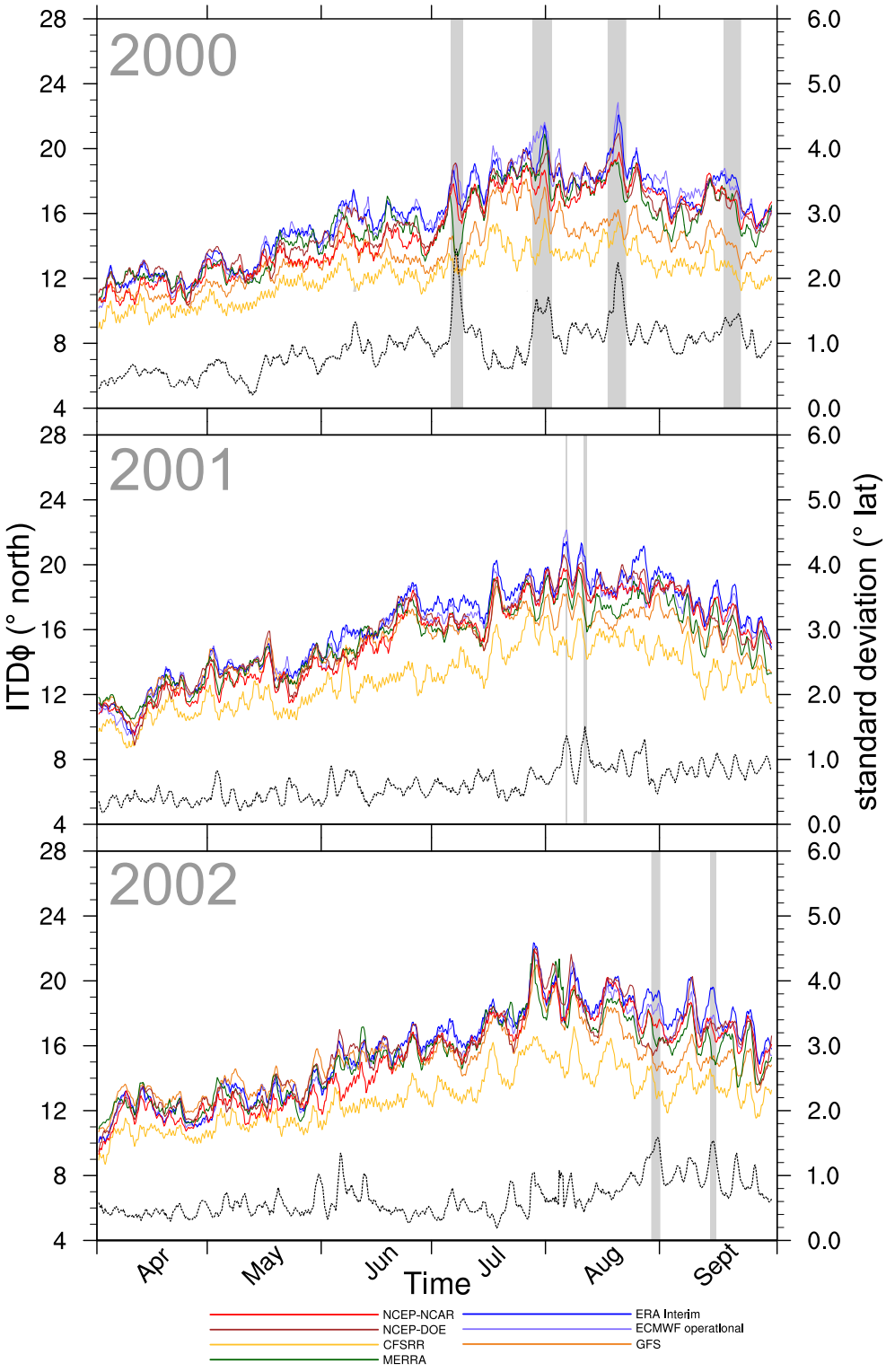


FIGURE 1: Behaviour in monsoon seasons from 2000-2010 of the zonal-mean intertropical discontinuity position (ITDΦ) for all seven (re)analysis products (coloured lines), standard deviation calculated from ITDΦs (excluding CFSR, dashed black line) and periods when the standard deviation exceeds the threshold and is in the top 5% of standard deviation values across all eleven years (grey shading).

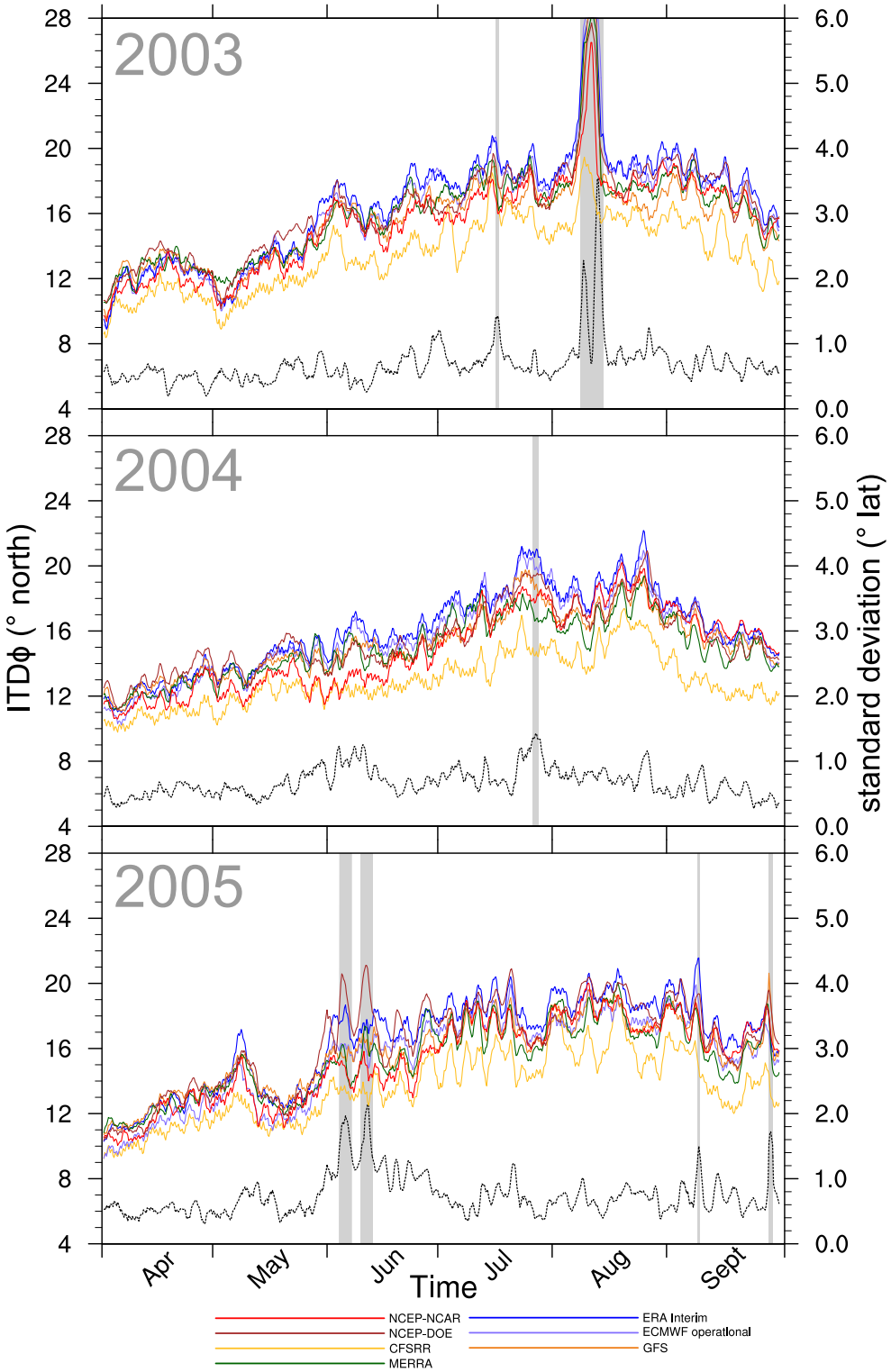


FIGURE 1: Continued

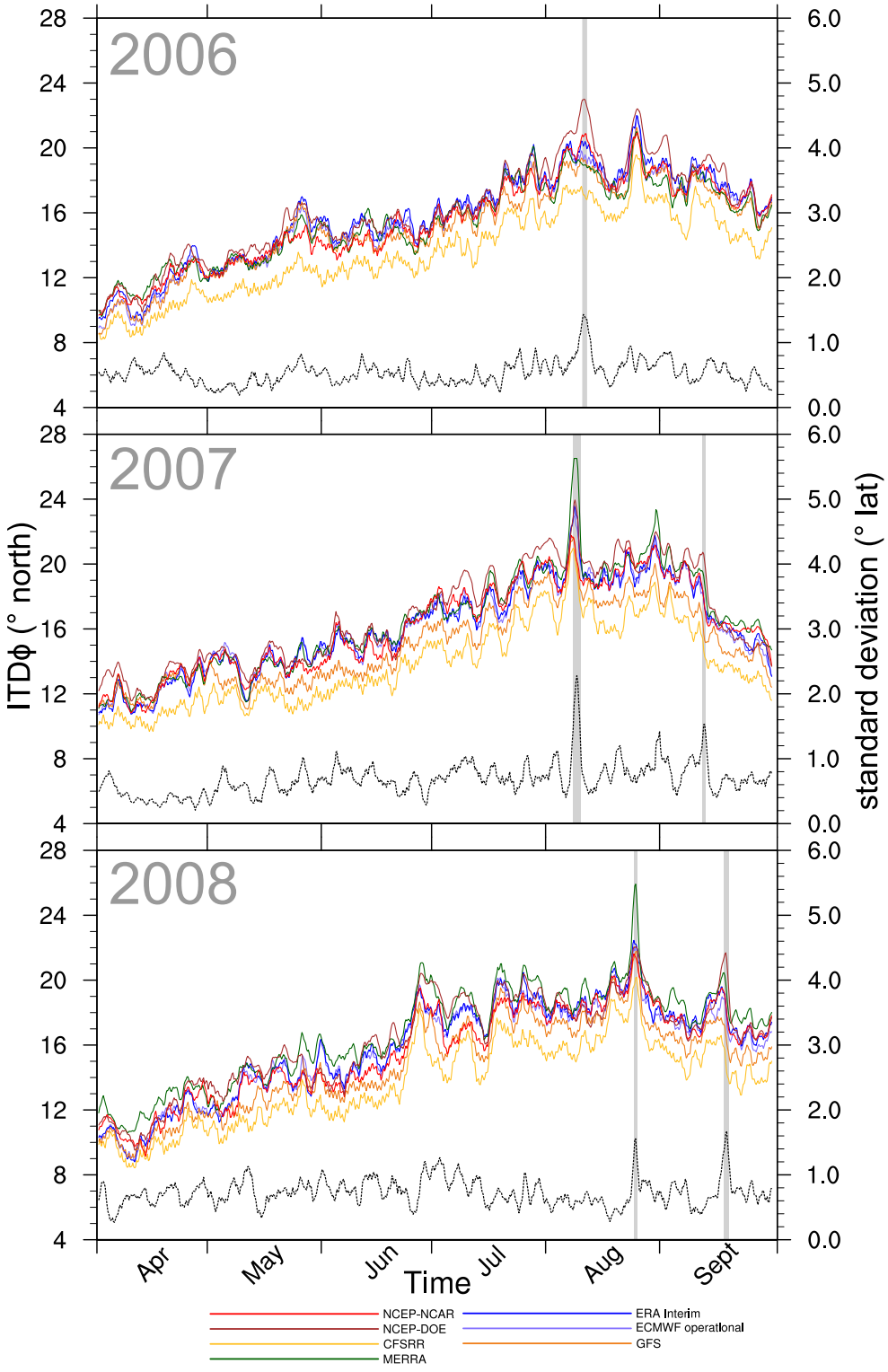


FIGURE 1: Continued

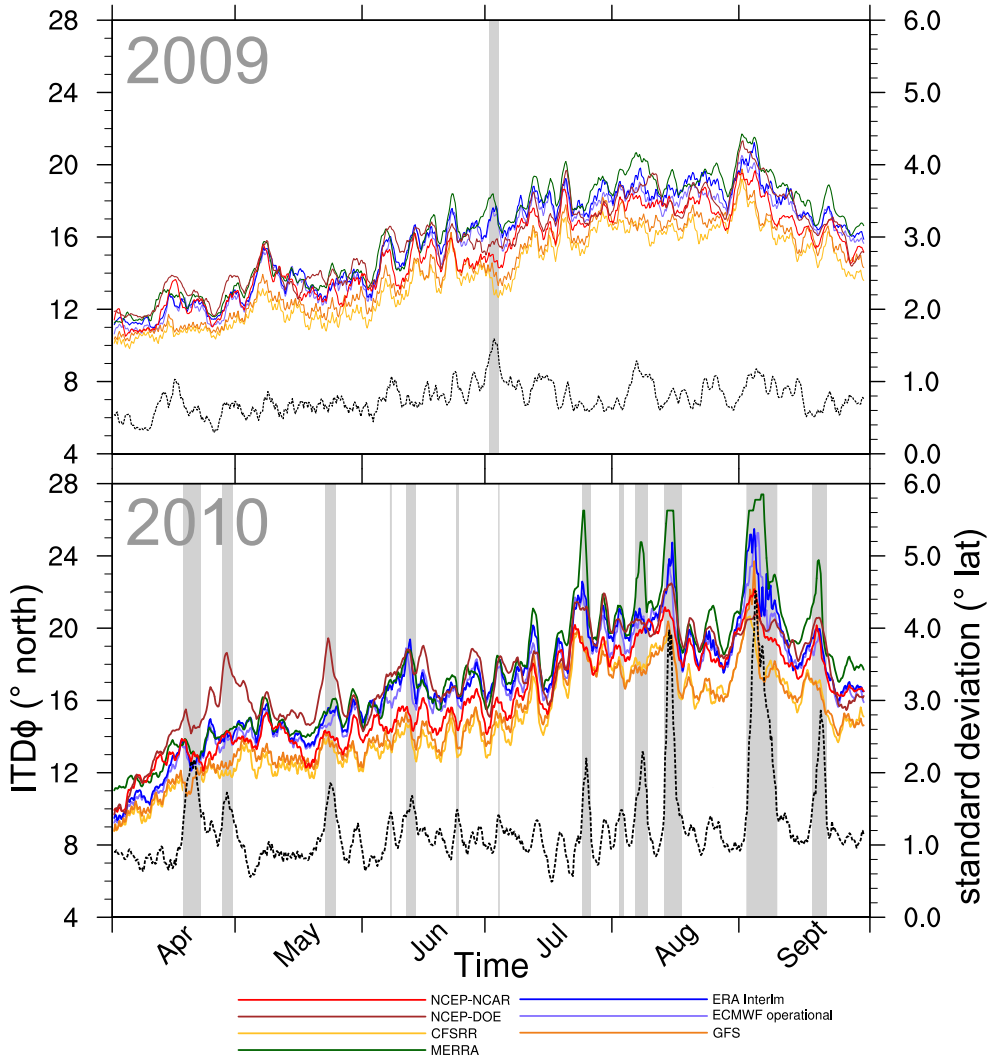


FIGURE 1: Continued

# Appendix B

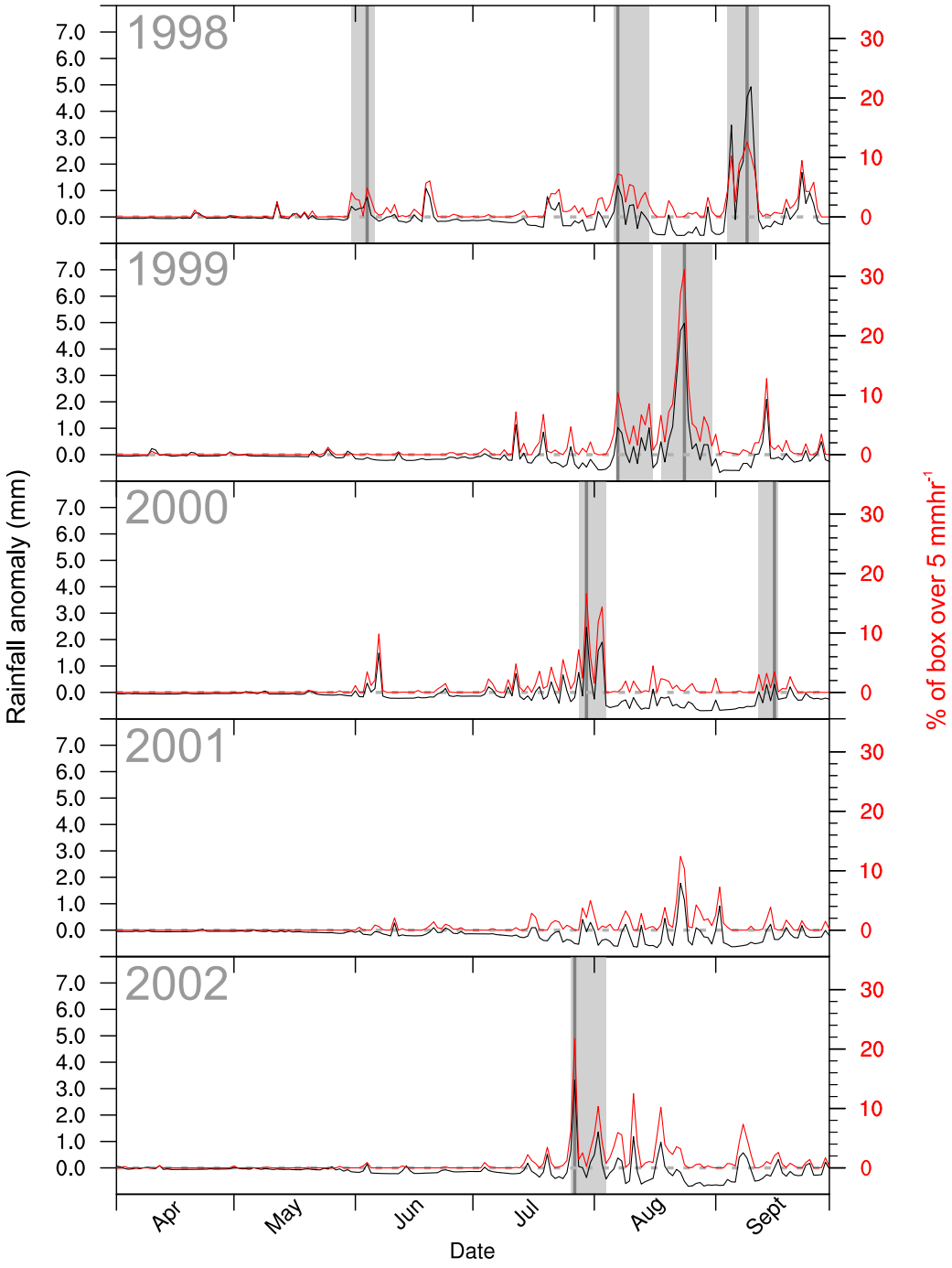


FIGURE 2: Seasonal variation in daily rainfall anomaly (black line) and the proportion of the box being studied with an accumulated daily rainfall in excess of 5 mm (red line) for the monsoon seasons from 1998–2011. Also shown are the anomalous rainy episodes identified (light grey shaded regions) and the day within each of these events with the largest proportion of the box exceeding the 5 mm threshold (dark grey lines).

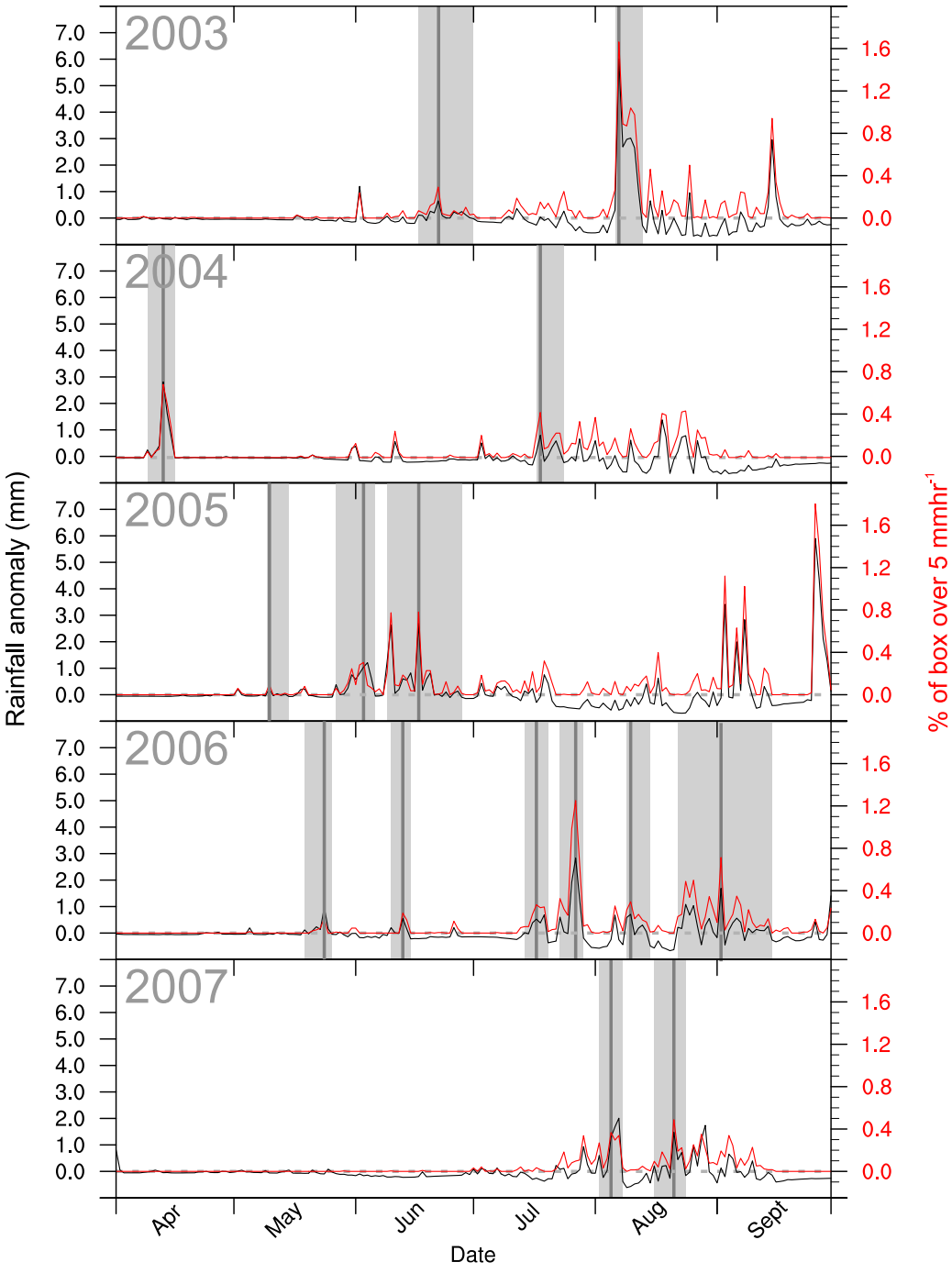


FIGURE 2: Continued

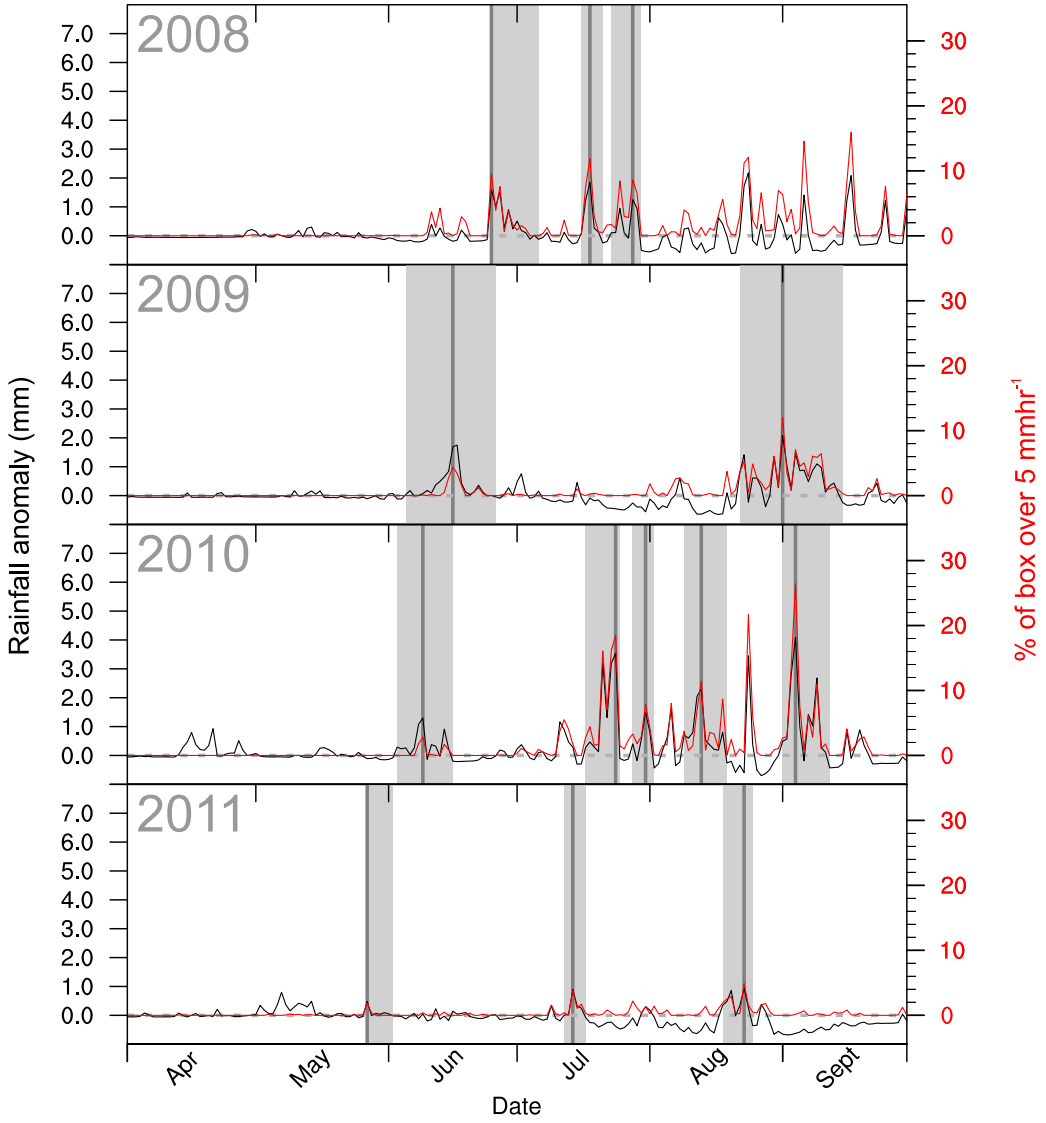


FIGURE 2: Continued